

University of St Andrews



Full metadata for this thesis is available in
St Andrews Research Repository
at:

<http://research-repository.st-andrews.ac.uk/>

This thesis is protected by original copyright

ELECTRICAL PROPERTIES OF THE TWO DIMENSIONAL ELECTRON GAS

by

Mothana H Al-DUBUNI

A thesis submitted for the degree of Doctor of Philosophy

at the

University of St Andrews

ST ANDREWS
December 1987



Th A 700

ACKNOWLEDGEMENTS

My thanks are due to the Head of the Department and to my supervisors for their support and help throughout this project.

I would like to express my thanks to the technical staff for their assistance. I gratefully acknowledge the gift of samples from Professor K E Singer (UMIST), Drs J S Robert and P A Claxton (Sheffield University) and Louise MacPherson for typing this thesis.

I would like to extend my gratitude to Al-Mustansiriyah University for the study leave and the postgraduate scholarship.

DECLARATION

I hereby certify that this thesis is a record of work done by me over three years in the Physical Science laboratory of the University of St Andrews, under the supervision of Dr D M Finlayson and Dr C Sotomayor-Torres.

Mothana H AL-DUBUNI.

We hereby certify that Mothana H AL-DUBUNI has spent nine terms of research work in the laboratories of the School of Physical Sciences, University of St Andrews under our direction and that he has fulfilled the conditions of the Resolution of the University Court, 1967, No1 and that he is qualified to submit the accompanying thesis in application for the degree of Doctor of Philosophy.

Dr D M Finlayson

Dr C M Sotomayor-Torres

(Research Supervisors)

ABSTRACT

A series of samples of GaAs-GaAlAs and InP-GaInAs have been obtained from several laboratories employing molecular beam epitaxy (MBE) and metal-organic-chemical vapour deposition (MOCVD) growth techniques.

Van der Pauw (VdP) and Shubnikov de Haas (SdH) techniques have been employed to measure the properties of the charge carriers over a wide range of temperature and pressure, with and without illumination of the specimen and in varying magnetic fields.

Comparison between experimentally determined mobilities and theoretical predictions were carried out considering a simple triangular well model and including all the major scattering mechanisms. The experimental mobilities obtained were well below the theoretical predictions suggesting that there is room for improvement in growth techniques to reduce, for example, interface roughness.

Shubnikov de Haas measurements were used to identify the 2DEG, to obtain values for the energies of the subbands and for the Fermi level. Fourier analysis was used for samples with more than one subband occupied.

Persistent photoconductivity has been observed in a few samples at low temperature but its origin is not fully understood. The influence of parallel conduction is also considered.

Samples containing a two dimensional hole gas (2DHG) were also investigated. At very low temperatures distinct plateaux were observed and attributed to the quantum Hall effect although the missing levels could not be accounted for easily.

The effects of changing the hydrostatic pressure have been investigated in some detail. In heterostructures both electron density and mobility decreased as the pressure increased. A decrease in mobility resulting from an increase in effective mass might be expected but the decrease in electron density with pressure is not understood in the absence of metastable levels.

LIST OF SYMBOLS

E	kinetic energy
ϵ	electric quantisation
u	external potential
n_s	two dimension electron gas density
ϵ_s	dielectric constant (free space)
F	effective electric field
ϵ_r	semi classical approximation of the energy
\underline{r}	number of zeros of the wavefunction
B or B_H	magnetic field
μ_B	Bohr magneton
g^*	the effective spin-splitting
$2a$	width of square well
m^*	effective mass
n	quantum number
E_f	Fermi energy
ω_c	cyclotron frequency
h	Planck constant
k	k-space (wave vector)
v	velocity of electron
$A(E_f)$	Fermi energy surface
e	electron charge
c	velocity of light 3×10^8 m/s
$\rho(E)$	density of states in 2D
σ	step function
$E_p, E_{p'}$	momentum matrix element connecting the fundamental and higher energy band respectively
V_o	the spin orbit splitting
C	constant in k.p theory
δ	Dirac delta function
ℓ	superlattice periodicity
E_D	donor binding energy
ϵ_∞	optical dielectric constant
ϵ_o	static dielectric constant
μ_H	Hall mobility
R_H	Hall constant
μ^*	high field mobility

q_F	the wave vector on the Fermi surface
q	2D wave vector
s_i	screening constant of i th subband
N_d	uniform remote ionized impurity density
d_i	thickness of spacer layer
z_i	average distance of electronic wavefunction from the heterointerface
F_s	electric field depends on the shape of the potential
d_1	width of depletion layer excluding spacer
$d = d_i = d_o =$	spacer layer thickness
V_o	conduction band energy offset
n_{depl}	the areal concentration of ionized donors in depleted region of S
S_o	screening constant
x	the mole-fraction composition of the ternary alloy
$\langle V \rangle$	the alloy-disorder scattering parameter
Ω	the unit cell volume
$\langle \delta V \rangle$	the strength of the scattering potential = 0.6 eV
ℓ_A	acoustic deformation potential
ρ'	mass density of GaAs
b	the effective width of 2D layers
N_p	the average occupation number of phonon
τ	momentum relaxation time
T	lattice temperature
τ_p	piezoelectric scattering
U_t	velocity of the transverse phonon
h_{iH}	the piezoelectric constant
τ_{io}	intersubband scattering
τ_{po}	optical phonon scattering
τ_{alloy}	alloy disorder scattering
τ_A	acoustic deformation potential scattering
τ_{RI}	remote ionized impurity scattering
τ_{alloy}	alloy-disorder scattering
μ_{po}	mobility due to optical phonon scattering
μ_{alloy}	mobility due to alloy scattering
μ_A	mobility due to acoustic deformation potential
μ_{RI}	mobility due to remote ionized impurity
μ_{BI}	mobility due to background ionised impurity
$\mu_{piezo} = \mu_{PE}$	mobility due to piezoelectric scattering

ELECTRICAL PROPERTIES OF THE 2DEG

CONTENTS

Chapter 1: INTRODUCTION

Chapter 2: PROPERTIES OF THE 2DEG

2.1: Energy Dispersion Relation and Density of States

2.1.1: Kinetic Energy in k_x, k_y plane.

2.1.2: Electric Quantisation .

2.1.3: Magnetic Quantisation.

2.1.4: Density of States.

2.2: Structures Containing 2DEG

2.2.1: Heterojunctions.

2.2.2: Modulation Doped Heterojunctions

2.2.3: Multiple Quantum Wells and Superlattices

2.3: Scattering Mechanisms in the 2DEG

2.3.1: Polar Scattering.

2.3.2: Remote Impurity Scattering.

2.3.3: Residual Ionised Impurity-Scattering.

2.3.4: Alloy-disorder Scattering.

2.3.5: Acoustic deformation potential scattering.

2.3.6: Piezoelectric Scattering.

2.3.7: Intersubband Scattering.

Chapter 4: EXPERIMENTAL METHOD

4.1: Mobility and Carrier Density Measurements.

4.1.1: Determination of μ and n_s .

4.1.2: Preparation, contacting and mounting of sample.

4.1.3: Experimental Apparatus.

4.2: Shubnikov de Haas measurements

4.2.1: Test of two Dimensionality of carriers.

4.2.2: Experimental Apparatus.

4.3: High Pressure Technique

4.3.1: Equipment.

4.3.2: The Pressure Gauge.

Chapter 5: RESULTS AND DISCUSSION

5.1: Samples used in this work

5.2: Temperature dependence of μ and n_s from SdH and Van der Pauw measurements.

5.2.1: Temperature dependence of μ and n_s .

5.2.2: Comparison with theoretical mobilities.

5.3: SdH measurements of 2D systems

5.4: Measurements of Bulk InP

5.5: Persistent Photoconductivity

5.6: High Pressure Transport in 2D systems

5.6.1 Single Quantum Well.

5.6.2 Heterostructure.

5.7: Measurement of 2DHG

5.8: High electron mobility transistors

5.8.1: Experimental Results.

Chapter VI: CONCLUSION AND FURTHER WORK

CHAPTER I INTRODUCTION

The study of semiconductors forms a part of the wider subject known as solid-state physics. Semiconductor materials are of great technological importance, since they are used in electronic, laser and opto-electronic devices and are at the centre of the microelectronics revolution, fast computing and long haul communications systems.

Optical and transport properties are of interest since they provide a guide to the potential applications of a particular material, or material preparation method. From the physics point of view, the interaction of the carriers with the lattice or with photons under the effect of external perturbations such as magnetic field, electric field, temperature, pressure, etc, can be studied to yield information on the form of these interactions and the factors that influence them.

Over the last decade there have been a number of spectacular advances in constructing crystalline semiconductor heterostructures with a specified band gap, which has led to the discovery of the two-dimensional behaviour of electrons as well as to the development of novel electronic and optical devices. Many of these advances are a direct result of the perfection of epitaxial crystal growth techniques, such as molecular beam epitaxy, which allow the growth of layered semiconductors that are perfect on the atomic scale and hence have dimensions comparable to the electron mean free path and the de Broglie wavelength. So there is a need to do experiments to obtain information about electron effective mass, carrier concentration, carrier mobility, electronic and impurity states, quasi-particle interaction and interface quality of the 2DEG which is confined in a 2D potential well

leading to a splitting of three dimensional conduction bands into two dimensional subbands.

The III-V materials have two main advantages. Firstly, the majority of compounds have direct energy gaps at the Brillouin Zone Centre, which tends to simplify the electronic properties due to the absence of the valley degeneracies present in Si and Ge, leading to lower effective masses and hence higher mobilities, and also permits the fabrication of solid state lasers. The second advantage is the great range of different materials available, since all the different compounds used may also be alloyed into one another. This leads to the possibility of growing different materials with similar lattice constants but different energy gaps which vary smoothly over the range of alloy composition. GaAs has a low temperature band gap of 1.52 eV, which is direct at the Zone Centre. Hydrostatic pressure techniques have been employed to study a new field of application of the transport properties of two-dimensional (2D) systems because of its ability to cause a decrease in the 2DEG concentration (n_s) without changing samples. This behaviour is related to the pressure-induced doping of the donor level, which causes a reduction of the charge transfer to the quantum well. GaAs-GaAlAs and InP-GaInAs were studied under hydrostatic pressure upto 12 Kbar at 4.2K and with magnetic fields up to 12T. Because it acts on the band structure, hydrostatic pressure has been used for a long time in optical and transport measurements to determine band parameters of III-V semiconductors.

There is considerable interest in the electrical properties of the two dimensional electron gas (2DEG) which may be confined at a heterojunction interface between two different semiconductors (eg GaAlAs/GaAs or GaInAs/InP) by an electric field or confined between two

very close interfaces which form a quantum well. If the impurities which donate the electrons are well separated from the 2DEG, electron scattering by ionized impurities is greatly reduced. Thus at low temperature where phonon scattering is also low this leads to extremely high mobilities for electrons in GaAs and to the observation of such phenomena as the quantum Hall effect and the fractional quantum Hall effect. In alloys such as (GaInAs) the low temperature effects are less pronounced due to alloy scattering. (Bastard, 1984) and (Basu, 1984.)

The two dimensional hole gas in p-type GaAlAs-GaAs structures has been studied from MBE grown material using beryllium doping to generate the two-dimensional hole gas (OE et al 1986) and (Wang et al 1984). An alternative dopant which is inherent in the MOVPE-grown process is carbon. In addition, the C-doping will extend up to the hetero-interface and should therefore supply a high hole concentration.

Fair agreement between theoretical prediction and experiment has usually been achieved by considering a combination of scattering mechanisms, of which the most important at 4K have been (a) ionised impurity scattering from centres in the doped (Al,As) layer, the undoped spacer layer, the hetero-junction interface and the undoped GaAs, and (b) acoustic phonons, via the deformation potential and piezoelectric interactions. The relative importance of these mechanisms will depend on the details of the structure grown and the quality of the component materials. By the study of the dopant and type of growth we can show qualitatively how the structural and material parameters influence the mobility in different types of sample. Low temperature persistent photoconductivity (PPC) has been observed in a few samples including InP-InGaAs and GaAs-GaAlAs

heterostructures. The common link between all these structures is that electron retrapping or recombination is prevented by a barrier which cannot be overcome at low temperatures. (Kane et al, 1986.)

At room temperature where phonon scattering dominates, modulation doped 2DEG's remain of interest because of the relatively high mobilities attainable in the high density electron gas required for FET (Field Effect Transistor) in which the current between two contacts—source and drain is controlled by the voltage on a third contact - the gate (Vinter, 1984). At room temperature the GaInAs/InP system may be even more attractive for devices than GaAs because the lower electron effective mass leads to a higher mobility despite alloy scattering and because devices may be directly integrated with optoelectronic components of interest for communications.

In this work transport properties of GaAs-GaAlAs and InP-GaInAs heterostructures are determined. In the following pages theoretical considerations including the properties of the 2DEG, structures containing 2DEG, scattering mechanisms in 2DEG and high pressure transport in 2D systems are discussed in Chapter Two. A summary of previous work on relevant systems including design of 2DEG samples, summary of transport measurements in GaAs-GaAlAs, InP-InGaAs systems and parallel conduction and persistent photoconductivity are in Chapter Three. Experimental methods including mobility and density measurements by Hall and Van der Pauw techniques, Shubnikov-de Haas measurements and high pressure techniques are in Chapter Four, Results and Analysis are included in Chapter Five and finally Chapter six contains the Conclusion and Suggestions for further work.

CHAPTER II PROPERTIES OF 2DEG

The first section of this chapter considers the Energy Dispersion Relations and Density of states in two dimensional systems. Electric and magnetic Quantisation are discussed. The next section deals with the 2D gas contained in a variety of quantum well structures. Section 3 goes on to discuss the scattering mechanisms necessary for the subsequent discussions of our 2D measurements. A triangular quantum well has been assumed in the derivations of this section.

The final section considers the influence of high pressure on the transport properties of the 2D gas.

2.1 Energy Dispersion Relation and Density of States.

This part explains the properties of charged carriers in semiconductor space-charge layers, which dynamically behave as if they had two dimensional character, i.e., as a two dimensional electron gas (2DEG); this implies that the electrons or holes have quantized energy levels for one spatial dimension, but are free to move in the other two spatial dimensions. Thus the wave vector is a good quantum number for two dimensions, but not for the third.

However, these systems are not two dimensional in a strict sense, both because the carrier wavefunctions have a finite spatial extent in the third dimension and because electromagnetic fields are not confined to a plane but spill out into the third dimension. The term 2DEG used widely because the spatial confinement occurs over lengths (layer thickness) comparable to the De Broglie wavelength.

In a two-dimensional Coulomb gas (a system of electrons interacting in a strictly two dimensional universe in which electromagnetic fields are confined to a plane) the electrons feel a logarithmic dependence on $1/r$ potential. However, the potential felt by a 2DEG will depend on the shape of the electric field at the interface.

2.1.1 Kinetic Energy in k_x, k_y plane.

When the electron motion is quantized in the z -direction, in the k_x, k_y plane the electron motion will be determined by the parabolic dispersion relation incorporating only k_x and k_y , thus their kinetic energy will be given by:

$$E = \frac{\hbar^2}{2m^*} (k_x^2 + k_y^2) \dots\dots\dots 2.1$$

2.1.2 Electric Quantisation (ϵ)

The electric quantisation of two-dimensional systems for a spherical energy band can be explained as follows: if we consider a moveable electron gas in the presence of an external potential (U) the electronic distribution is described by the Schrodinger equation for the wave function. In order to simplify the problem assume that the effective potential is fixed and consider only the most important idealized cases in this case the Schrodinger equation reads:

$$\left(\frac{p^2}{2m^*} + U\right)\Psi = E\Psi \dots\dots\dots 2.2$$

If the potential is one-dimensional: $U(z)$, hence the solution is in the form:

$$\Psi = A \exp(ik_x x + ik_y y)\phi(z) \dots\dots\dots 2.3$$

which reduces to

$$\left(\frac{1}{2m^*} p_z^2 + U\right)\phi = \epsilon\phi \dots\dots\dots 2.4$$

$$\text{and then } \epsilon = E - \frac{\hbar^2}{2m^*} (k_x^2 + k_y^2) \dots\dots\dots 2.5$$

There are different types of potentials, which define quantum wells for various structures as shown in Fig (2.1). The quantized energies for these wells are given in Table 2.1, where F is an effective electric field and is given by:

$$F = \frac{en_s}{\epsilon_s} \dots\dots\dots 2.6$$

Quantum Well	Quantization energy
Infinite Square Well	$\epsilon_r = \frac{\hbar^2 \pi^2 (r+1)^2}{8m^* a^2}; r = 0, 1, 2, \dots$
Parabolic Well	$\epsilon_r = \hbar\omega(r + \frac{1}{2})$
Asymmetric Triangular Well	$\epsilon_r = \left[\frac{\hbar^2 e^2 F^2}{2m^*} \right]^{1/3} \left[\frac{3\pi r + 3}{4} \right]^{2/3}$
Symmetric Triangular Well	$\epsilon_r = \left[\frac{\hbar^2 e^2 F^2}{2m^*} \right]^{1/3} \left[\frac{3\pi(r + \frac{1}{2})}{4} \right]^{2/3}$

Table 2.1: Quantised Energies for four well shapes.

(Zawadzki, 1984)

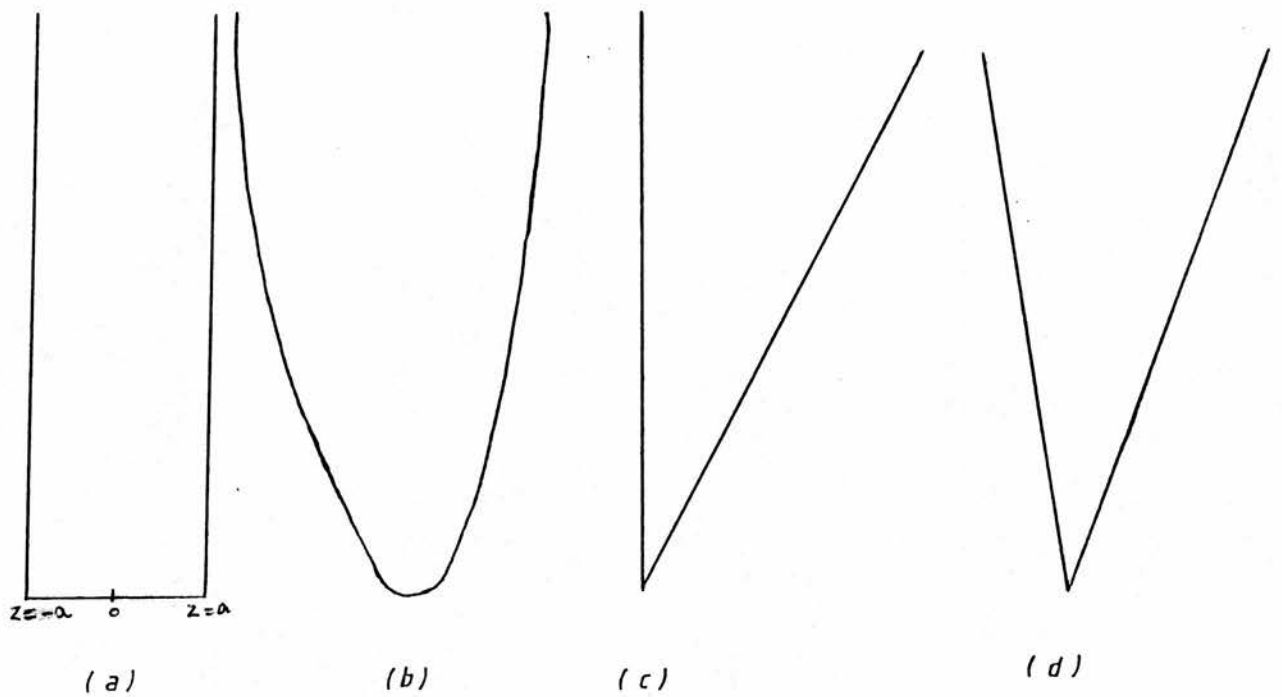


Fig.(2.1) Different Potential Wells :

(a) Infinite Square Well for Heterostructures of different Semiconductors,

(b) parabolic well for n-i-p-i periodically doped crystals,

(c) Triangular asymmetric well for metal-insulator-semiconductor devices and

(d) Symmetric triangular well for bi-crystals.

where n_s is the 2D electron gas density and ϵ_s is the dielectric constant. In the present work structures which can be approximated by the square well and by the asymmetric triangular were used. For these shapes of the electric potential the quantisation of the electronic subbands can be obtained by the simplified Bohr-Sommerfeld quantization conditions (Zawadski, 1984):

$$\int_{z_1}^{z_2} p_z dz = \hbar\pi (r + c_1 + c_2) \dots\dots\dots 2.7$$

where p_z is a non-operator and is given by equation 2.4, z_1 and z_2 are the turning points of the classical motion ($p_z = 0$), c_1 and c_2 are phases to be determined, $r = 0, 1, 2, \dots$ is the number of zeros of the wavefunction.

(i) Infinite Square well:

The potential is $U(z) = 0$ for $|z| < a$

$U(z) = \infty$ for $|z| > a$

From the equations above we observe that if the walls are infinitely high, the wavefunction must vanish at the turning points $z = \pm a$, hence the phases are $c_1 = c_2 = 1/2$. Thus we have:

$$(2m^*\epsilon)^{\frac{1}{2}} \int_{-a}^{+a} dz = \hbar\pi (r + 1) \dots\dots\dots 2.8$$

which gives

$$\epsilon_r = \frac{\hbar^2 \pi^2 (r + 1)^2}{8m^* a^2} \quad r = 0, 1, 2, \dots\dots\dots 2.9$$

Thus the semiclassical quantisation gives here the exact result. The exact wavefunctions for the problem are well known and easy to handle.

(ii) Asymmetric Triangular Well:

The potential is $U(z) = eFz$ For $z \geq 0$

$U(z) = \infty$ For $z < 0$

F is an effective electric field given by equation (2.6). In this case

$c_1 = \frac{1}{2}$ since at the left turning point $z_1 = 0$ the wave function must vanish, and $c_2 = \frac{1}{4}$ since at the right turning point $z_2 = \frac{\epsilon}{eF}$. Equation (2.7) becomes:

$$(2m^*)^{\frac{1}{2}} \int_0^{z_2} (\epsilon - eFz)^{\frac{1}{2}} dz = \hbar\pi(r + \frac{3}{4}) \dots\dots\dots 2.10$$

with $r = 0, 1, 2, \dots$. An elementary integration gives semiclassical energies

$$\epsilon_r = \left(\frac{\hbar^2 e^2 F^2}{2m^*} \right)^{\frac{1}{3}} \left[\frac{3}{2} \pi \left(r + \frac{3}{4} \right) \right]^{\frac{2}{3}} \dots\dots\dots 2.11$$

Formula (2.11) approximates exact eigen values up to a fraction of a percent. In general, the electric field varies with the distance from the interface. The eigenvalues and wave functions for the ground and first excited subbands can be expressed in a simple manner, using one independent parameter related to the electric field within the well.

For the ground subband and excited subband the wave functions are:

$$\Psi_0(\bar{r}, z) = \Phi_{k_x, k_y}(\bar{r}) x_0(z) = \Phi_{k_x, k_y} \frac{2 \exp(-b_0 z/2)}{(b_0^3/2)^{\frac{1}{2}}} \dots\dots\dots 2.12$$

$$\begin{aligned} \Psi(\bar{r}, z) &= \Phi_{k_x, k_y}(\bar{r}) x_1(z) \\ &= \Phi_{k_x, k_y} A(2/b_0^3)^{\frac{1}{2}} z(1 - Bz) \exp(-b_1 z/2) \dots\dots\dots 2.13 \end{aligned}$$

where $\Phi_{k_x, k_y}(\bar{r})$ is the two-dimensional plane wave

$$A = [3b_1^5 b_0^3 / 4(b_0^2 - b_0 b_1 + b_1^2)]^{\frac{1}{2}}$$

$$\text{and } B = (b_0 + b_1)/6.$$

The parameters b_0 and b_1 are evaluated by comparing the roots of the wave functions and their first derivatives for (0) and (1) subbands, given by Equation (2.12) and (2.13) with roots of corresponding wave functions derived from the Airy-function solution for a triangular well. For a given effective mass of the electrons m^* , there is a relationship between b_0 and b_1 . Thus for GaAs it is found that $b_1 \approx 0.754 b_0$ which in turn gives the following relationships: $A = 0.47b_0^3$ and $B = 0.292 b_0$. Therefore, the forms of wave functions 2.12 and 2.13 are determined by the electric field within the well, or equivalently, by the electron gas density, n_s where $n_s' = (N_s + \frac{32}{11} N_{\text{depl}})$, and N_{depl} is the areal concentration of charge in the depleted region of the barrier layer (S_1 of Fig 2.6). From the last two equations, the extent of the wavefunctions for the (0) and (1) subband into the layer containing the 2DEG can be obtained.

2.1.3 Magnetic Quantisation

(i) The 3D case:

Suppose we apply a magnetic field in the z-axis to a sample of cubic symmetry of side L. The field will cause the electrons to rotate in the x-y plane with frequency:

$$\omega_c = Be/m^* \dots\dots\dots 2.14.$$

called the cyclotron frequency where e is the electronic charge and m^* the effective electron mass. In k-space the electron motion in z-direction is unaffected, but in the (x-y)plane they are confined to move in a

circle of constant energy. The quantisation conditions imposed on the electron energy becomes:

$$E = \hbar\omega_c \left(n + \frac{1}{2}\right) + \frac{\hbar^2 (k_x^2 + k_y^2)}{2m^*} \dots\dots\dots 2.15.$$

where k is the wavevector and $n = 0, 1, 2, 3$ etc. The result suggests that the energy of the electron states is expressed as the sum of a translational energy along the magnetic field, together with the quantised energy of the cyclotron motion in the plane perpendicular to the field. The effect in k -space is that the variables k_x and k_y no longer correspond to a definite wavefunction since the electron is no longer represented by specific k values. Instead, the electrons lie on a circle in the $(x-y)$ plane, rotating around it with frequency ω_c . The number of states in a given macroscopic region of k -space, however, remains the same.

Equation (2.14) suggests that the electrons are confined to an area πr^2 , where r is the radius of the cyclotron orbit, instead of extending over the whole area, L^2 of the cube in the $(x-y)$ plane.

$$\text{Area of orbit} = \pi r^2 = \frac{\hbar(n + \frac{1}{2})}{m^* \omega_c} = \frac{\hbar(n + \frac{1}{2})}{Be} \dots\dots\dots 2.16.$$

$$\text{No of electron states in each level} = \frac{L^2 Be}{h} \dots\dots\dots 2.17.$$

These levels are called Landau levels and their degeneracy and separation is dependent on the magnetic field. Returning to k -space we have:

$$\hbar \underline{k}^2 = e(\underline{v} \times \underline{B}) \dots\dots\dots 2.18.$$

If k is the radius of an orbit then $\underline{k} = (\underline{r} \times \underline{B})e/\hbar$ after integration of the above equation. It follows that the area of an orbit in k -space is:

$$A(E_F) = \pi k^2 = 2\pi(n + \frac{1}{2})Be/h \dots\dots\dots 2.19.$$

The orbit in k-space differs in size by $2\pi Be/h$ to that in real space.

(ii) The 2D case ($E_{||}$)

We assume that in addition to an electric field in the z-direction, there exists also an external magnetic field \vec{H} parallel to it. (The treatment below follows closely that of Zawadsky (1984)). The situation in this case is simple, because the electric field affects only the electron motion in the z direction while the magnetic field affects only the motion in x-y plane. In the effective mass approximation for a simple parabolic band the Schrodinger equation without electron spin is

$$\frac{1}{2m^*} (\vec{p} + \frac{e}{c} \vec{A})^2 + U(z)]\Psi = E\Psi \dots\dots\dots 2.20.$$

where \vec{A} is the vector potential of the magnetic field. For $\vec{B}_H = (0, 0, B)$ the vector potential depends only on x and y so that equation 2.20 can be rewritten as:

$$[A_1(x, y) + A_2(z)]\Psi = E\Psi \dots\dots\dots 2.21$$

The solutions are of the form:

$$\Psi(x, y, z) = g(x, y) \phi(z) \dots\dots\dots 2.22$$

we separate the variables in the usual way. The eigenvalue of the equation (2.20) becomes equivalent to two separate equations

$$(\frac{1}{2m^*} p_z^2 + U) \phi(z) = \epsilon \phi(z) \dots\dots\dots 2.23$$

as in section 2.1.2 and:

$$\frac{1}{2m^*} \left[\left(p_x + \frac{e}{c} A_x \right)^2 + \left(p_y + \frac{e}{c} A_y \right)^2 \right] g(x, y) = E_{||} g(x, y) \dots \dots \dots 2.24$$

if electron spin is included, the Schrodinger equations (2.20, and

2.24) should be completed by adding the Pauli term $\mu_B g^* \vec{H} \cdot \vec{\sigma}$ where μ_B is the Bohr magneton, g^* is the effective spin-splitting (Lande factor) and $\vec{\sigma}$ is the Pauli spin operator .

Equation (2.24) gives the magnetic energies:

$$\epsilon_{||} = \hbar \omega_c \left(n + \frac{1}{2} \right) + \frac{1}{2} g^* \mu_B H \dots \dots \dots 2.25$$

The corresponding wavefunctions have spin-up and spin-down components, thus the two dimensional electron gas has an energy given by

$$E_{rnsk_x, k_y} = \frac{\hbar^2}{2m^*} (k_x^2 + k_y^2) + \epsilon_r + \hbar \omega_c \left(n + \frac{1}{2} \right) \pm \frac{1}{2} s g^* \mu_B H \dots \dots \dots 2.26$$

where $\frac{\hbar^2}{2m^*} (k_x^2 + k_y^2)$ is the kinetic (translational) energy, ϵ_r is the electric energy, $\pm \frac{1}{2} s g^* \mu_B H$ the magnetic energy and $\hbar \omega_c \left(n + \frac{1}{2} \right)$ is the cyclotron energy.

2.1.4 The Density of States

In the effective mass approximation for a spherical energy band including electric quantisation, the energy is given by:

$$E_{rk_x k_y} = \epsilon_r + \frac{\hbar^2}{2m^*} (k_x^2 + k_y^2) \dots \dots \dots 2.27$$

where ϵ_r is electrical quantisation explained in Section 2.1. It is of interest to know the corresponding density of electron states. To this end one should sum over all states belonging to the same energy. Introducing polar coordinates and degeneracy, we get for one subband:

$$\rho(E) dE = 2 \frac{2\pi k_{11}}{(2\pi)^2} \frac{dk_{11}}{dE} dE = \frac{m^*}{\pi \hbar^2} \dots \dots \dots 2.28$$

thus each subband contributes the same constant density of states (DOS). This contribution begins at the subband edge ϵ_r of equation (2.27) so that the total density of states is:

$$\rho(E) = \frac{m^*}{\pi\hbar^2} \sum \theta(E - \epsilon_r) \dots \dots \dots 2.29$$

where θ is the step function [$\theta(x) = 0$ for $x < 0$, $\theta(x) = 1$ for $x \geq 0$].

This density of states is shown in Fig (2.2) and Fig (2.3). The system is two-dimensional when one deals with only one electric subband. If more subbands come into play, the situation loses gradually its two dimensional features.

The density of states due to the Landau quantisation can be counted from the number of states belonging to the same energy as in equation 2.28. Consider a sample with dimensions L_x and L_y . Then the allowed k_x values are $(2\pi/L_x) \ell$, where ℓ is an integer. Thus there are $L_x/2\pi$ allowed values of k_x within the unit length of k_x in k space.

The centre of electron oscillations $y_0 = k_x L^2$ should be within the sample, which gives the condition $0 < k_x^2 L^2 < L_y$ hence $0 < k_x < L_y/L^2$

Thus, there are $L_x L_y / 2\pi L^2$ allowed values of k_x in the sample, belonging to each Landau and spin level. Since energies are discrete, the density of states is:

$$\rho(E) = \frac{L_x L_y}{2\pi L^2} \sum_{rns} \delta(E - E_{rns}) \dots \dots \dots 2.30$$

where δ is the Dirac delta function. Equation (2.23) can also be written as:

$$\rho(E) = \frac{m^*}{\pi\hbar^2} \sum \theta(E - \epsilon_r)$$

where θ is the step function. There are various ways of broadening the delta function. The one most popular so far is the Lorentzian model

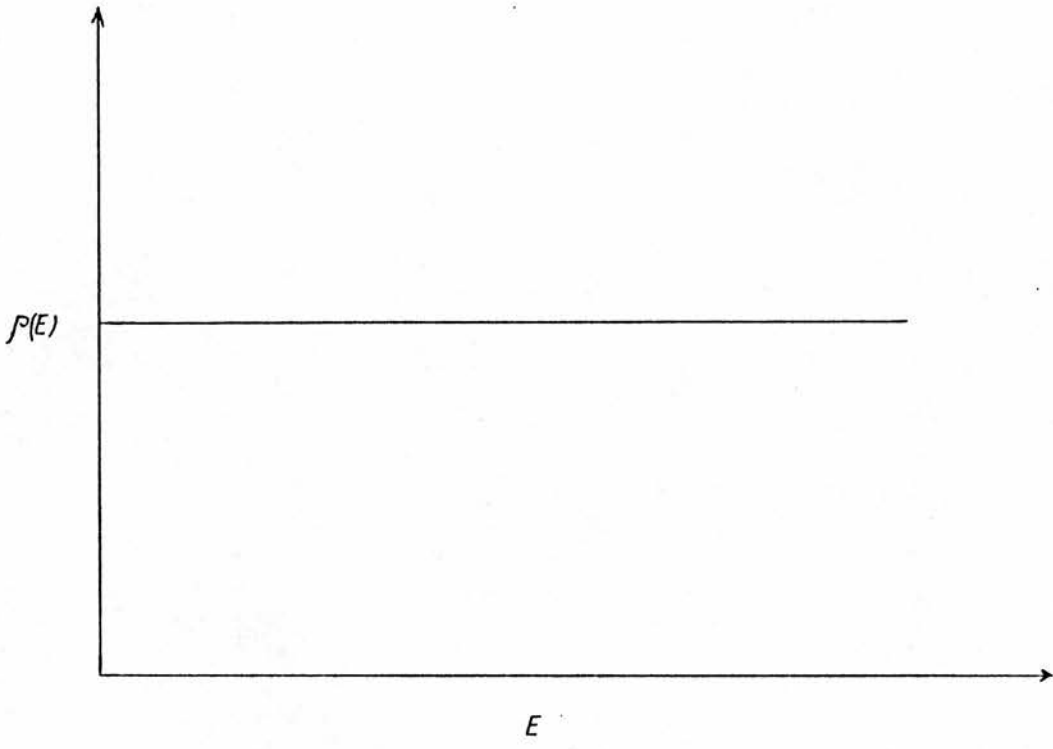


Fig 2.2 Density of state as a function of E for one subband for 2DEG.

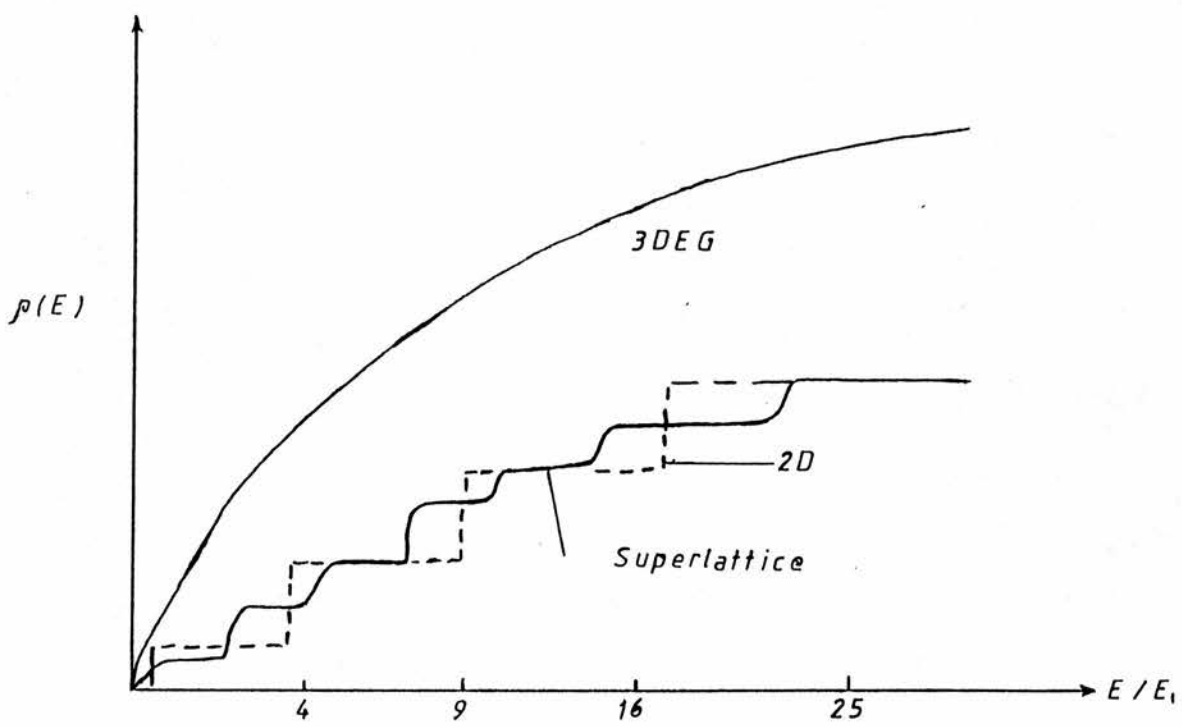


Fig 2.3 Density of states as a function of E/E_1 , for a number of subband for 2DEG and super lattice.

for the density of states.

The main difference between 2D and 3D DOS is shown in fig (2.2) and (2.3) where in two dimension it is a straight line with an intercept on $\rho(E)$ axis for one subband giving a constant DOS for a given energy range between subband energies whereas in the 3D case the DOS varies as $E^{\frac{1}{2}}$ for all energies and it intercepts the origin.

2.2 Structures containing ZDEG

2.2.1 Heterojunctions

Semiconductor quantum well structures and superlattices are the result of the development of epitaxial growth techniques such as molecular beam epitaxy (MBE) and metal organic vapour phase epitaxy (MOVPE), described in Section 3.1. The epitaxial layer is grown on a flat disc of a single crystal substrate of the same lattice constant (lattice matching).

The starting substrate material is usually a simple binary compound (GaAs or InP) with required electrical properties: $\rho \sim 10^7 \Omega\text{cm}$ for semi-insulation. AlAs and GaAs have almost the same lattice constant, hence it is possible to lattice-match the $\text{Al}_x\text{Ga}_{1-x}\text{As}$ system to a GaAs substrate over the full alloy range $0 \leq x \leq 1$, giving a range of band gaps, E_G (at 300 K^o), from 1.4eV ($x = 0$, GaAs) to 2.2eV ($x = 1$, AlAs), while InP has a lattice constant intermediate between those of GaAs and InAs as shown in Fig 2.4. InP lattice-matches the ternary alloy $\text{In}_x\text{Ga}_{1-x}\text{As}$ with composition $x = 0.47$. It has also received considerable attention because of its optoelectronic application as quantum well lasers and photodetectors in the 1.3 - 1.5 μm region. For these purposes a heterojunction involving a semiconductor - semiconductor interface requires a high degree of monocrystallinity achieved by careful lattice-matching which exhibits an abrupt discontinuity in the local band structure.

Away from the interface a gradual band bending occurs reflecting the space-charge distribution or, as explained in Section 2.1.2, the shape of the asymmetric triangular electrostatic potential at and perpendicular to the interface. A typical heterojunction is shown in

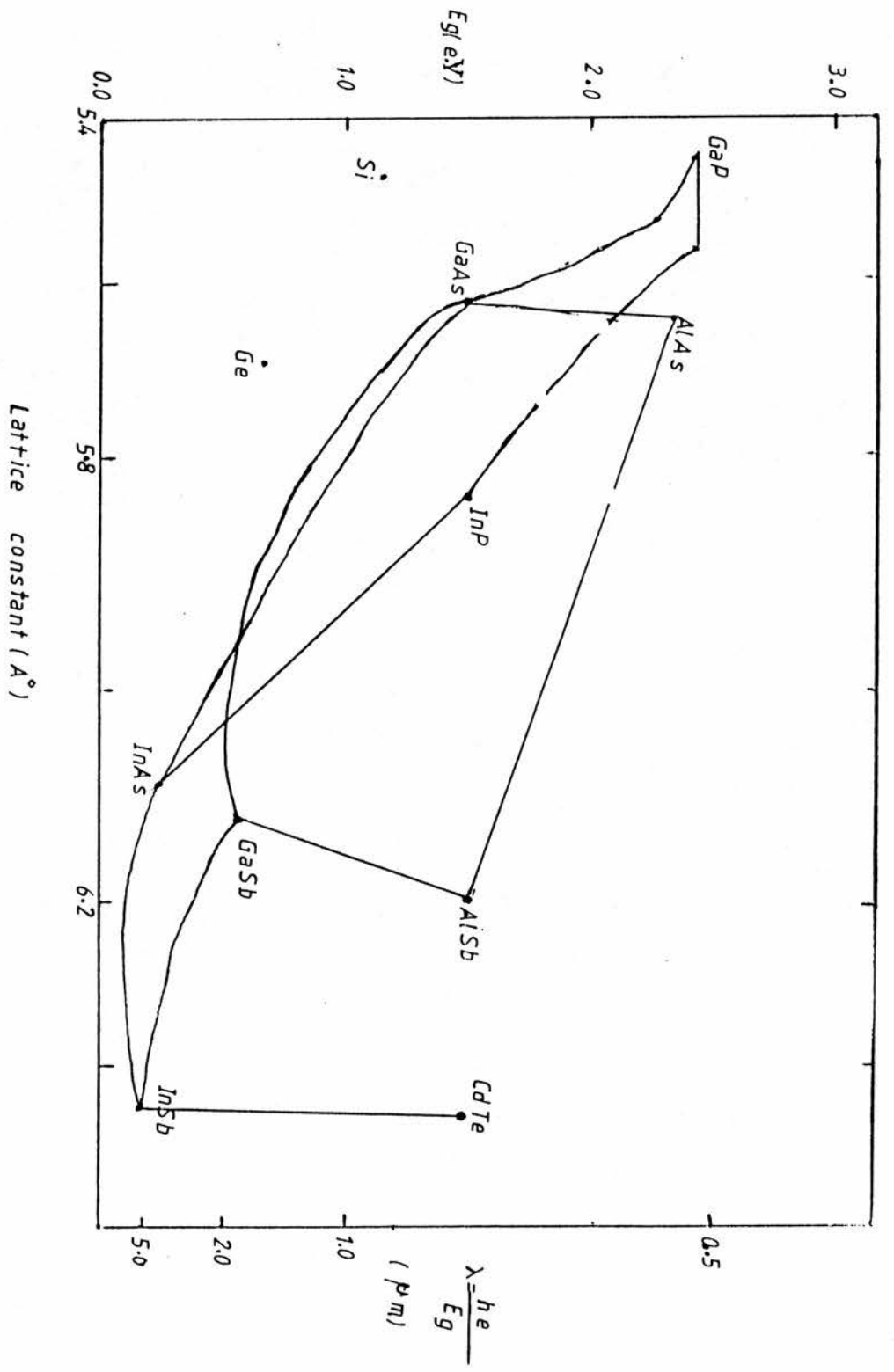


Fig 2.4 the consideration of the degree of lattice matching across various heterojunction.

Fig 2.5 where extra carriers are provided by doping the larger gap material with shallow donors (eg Si in GaAlAs). The donor electron once in the AlGaAs conduction band will feel a lower energy potential in the adjacent layer and will become trapped at the interface.

2.2.2 Modulation Doped Heterojunctions (MDH)

The various scattering mechanisms in a 2DEG are discussed in Section 2.3. However it can be advanced by introducing the role of remote impurities, their concentration and physical position in the structure. Calculations by Price (1982) of the theoretical mobility for a simple structure with (n_{ion}) ion density separated by a distance d from a sheet of conduction electrons yielded:

$$\mu_{ion} = \frac{(16\sqrt{2\pi e})}{h} \frac{(ne^{3/2}d^3)}{n_{ion}} \dots\dots\dots 2.31$$

suggesting that the mobility could be increased if the spacer layer thickness increases. This physical separation reduces the Coulomb field felt by the 2D electrons and reduces the effect of the short wavelength (large wave-vector) potential fluctuations, which are the most important source of scattering by ionised impurities, and falls off with distance from the impurity distribution. This is the idea behind modulation doping.

Consider the single quantum well at the interface of two semiconductors of different electron affinities and band gaps as shown in Fig 2.6. The larger affinity semiconductors (S_1 at $z \geq 0$) is nominally undoped, while the lower affinity semiconductors (S_2 at $z < 0$) is selectively doped, i.e., it contains the undoped region $-d < z < 0$ (commonly referred to as the spacer layer) and the region $z \leq -d$ highly doped with shallow donors. As a result of the electron affinity

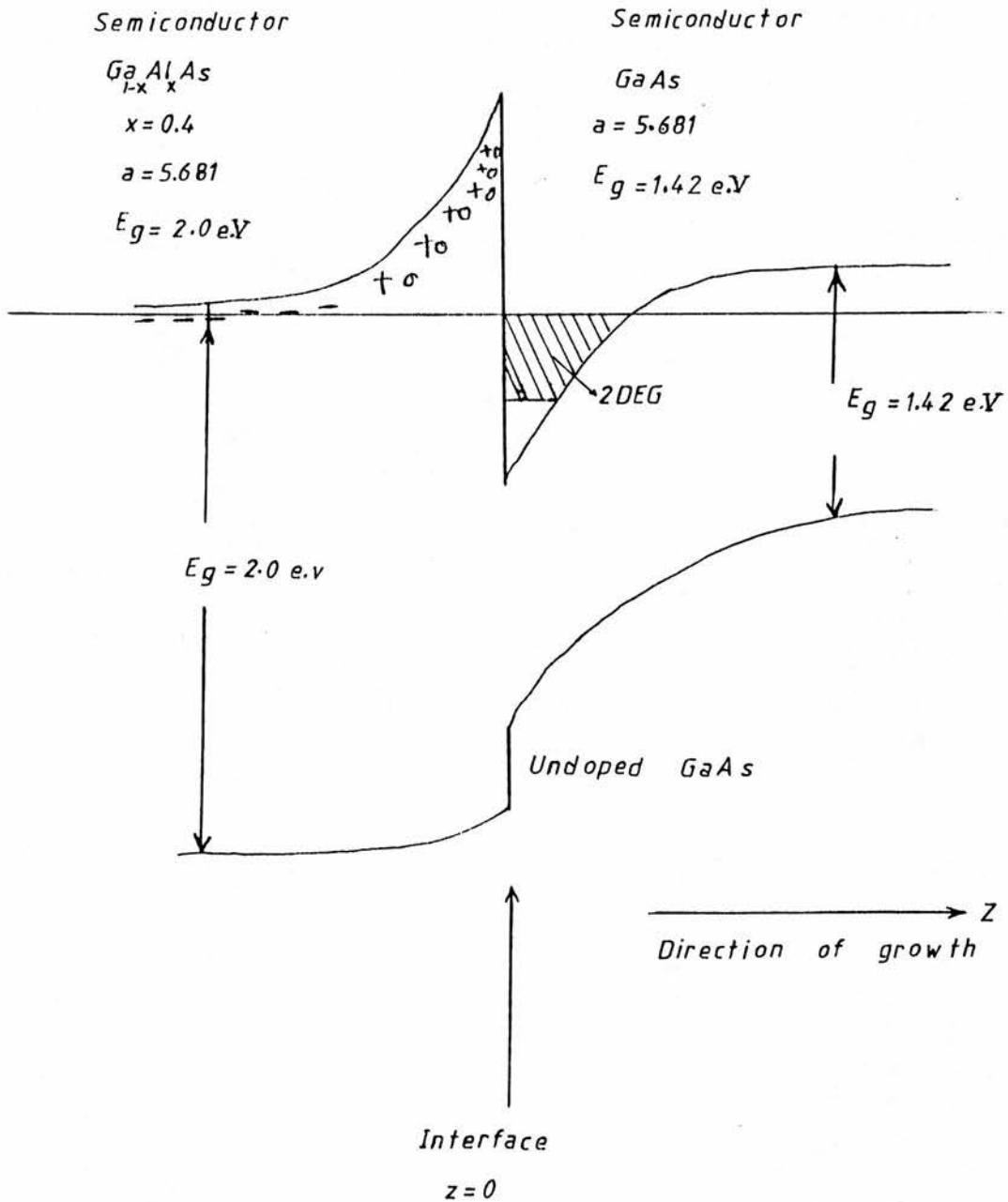


Fig. 2.5 A schematic picture of the GaAs-GaAlAs Heterojunction with Si atoms in the GaAlAs (barrier) layer.

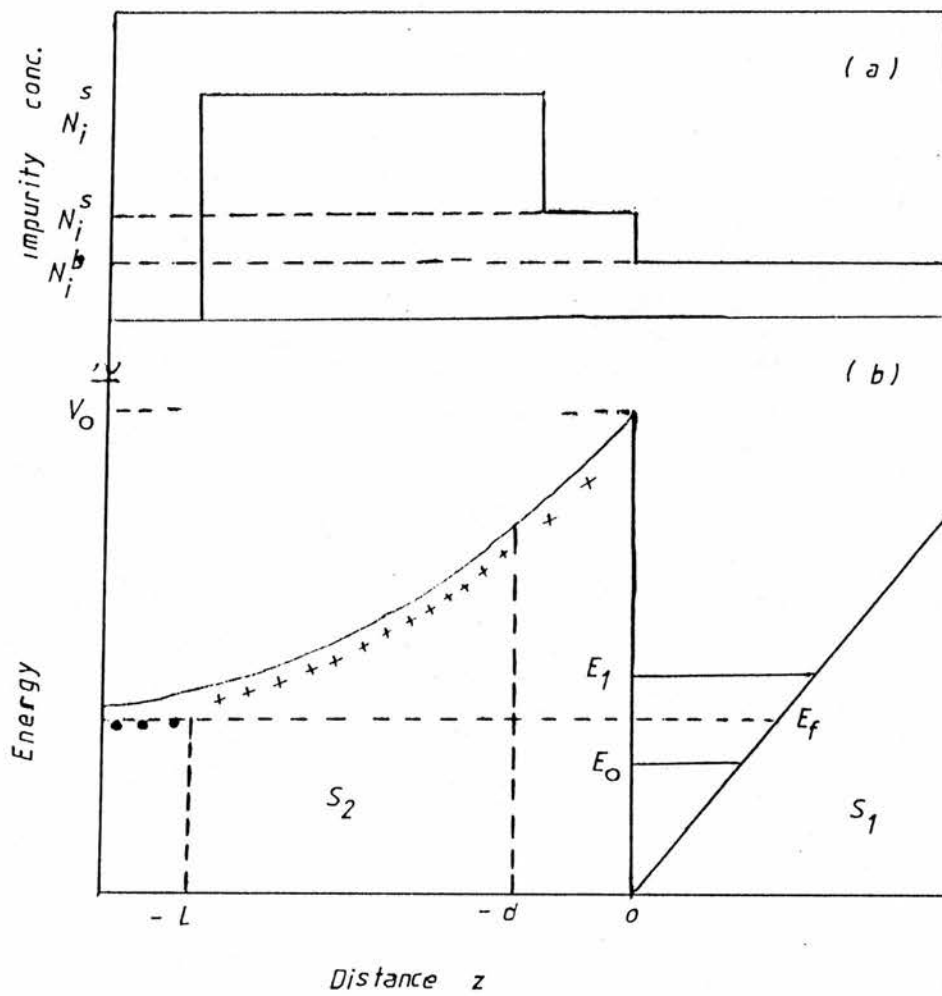


Fig. 2.6 Schematic representation of (a) The doping profile and (b) The energy configuration of a modulation doped heterostructure.

Typically, MDH are doped to $N_D = 10^{18} \text{ cm}^{-3}$ with a spacer layer of typically ~ 50 to 60 \AA . By using the advantage of modulation doping (Roberts et al 1987) in the development of FET.

Recently Tellurium has been used as a dopant in GaAs-GaAlAs MDH the higher energy gap material InP.

GaInAs - InP MDH shown in Fig 2.7. As with GaAlAs, the dopant is in S_1 Another heterojunction system which enjoys popularity is the

electron gas density $n_2(E)$ and the undoped spacer width d . Equation (2.33) is used to calculate the concentration of

barrier height for GaAs = $0.7V$, N_D the doping range (1 to $2 \times 10^{18} \text{ cm}^{-3}$).

permittivity of $\text{Al}^x\text{Ga}^{1-x}\text{As}$, q the elementary charge, Φ_B the surface where w_c is the width of the top GaAs cladding layer, ϵ_1 the

$$w_{\text{depl}} = \left[w_c^2 + \frac{2\epsilon_1}{\epsilon_2} \left(\Phi_B + \frac{q \cdot N_D}{\Delta E_c} \right) \right]^{\frac{1}{2}} - w_c$$

depletion width w_{depl} is (Schubert et al 1984):

regions of S_2 and N_I the ionized impurity concentration. The constant, n_{depl} the real concentration of ionized donors in depleted

energy in the doped part of semiconductor S_2 , ϵ_s the static dielectric where ΔE_c is the conduction band energy offset, E_b the donor binding

$$E_o + E_f = \Delta E_c - E_b - \frac{4\pi e^2}{2\epsilon_s} \left(n_s + n_{\text{depl}} \right) \frac{N_I}{-4\pi e^2} \left(n_s + n_{\text{depl}} \right) \dots \dots \dots 2.33$$

1984):

of the MDH is governed by the following equation (Walukiewicz et al, In equilibrium the transfer electrons from the doped region to the well

$$\Delta E_c = E_{\text{crit}}^F = \frac{\pi^2 \hbar^2}{m^*} n_{\text{crit}}^s \dots \dots \dots 2.32$$

reaches the first excited subband is given by

The critical gas density n_{crit}^s at which the Fermi energy E_f their dependence on the electric field, are discussed in Section 2.1.2.

quantization of the energy band structure. The subband energies and the previous case, results in a strong electric field which leads to a layer S_1 , and accumulate in the vicinity of the interface. This, as in difference, electrons from the donor atoms in S_2 are transferred to

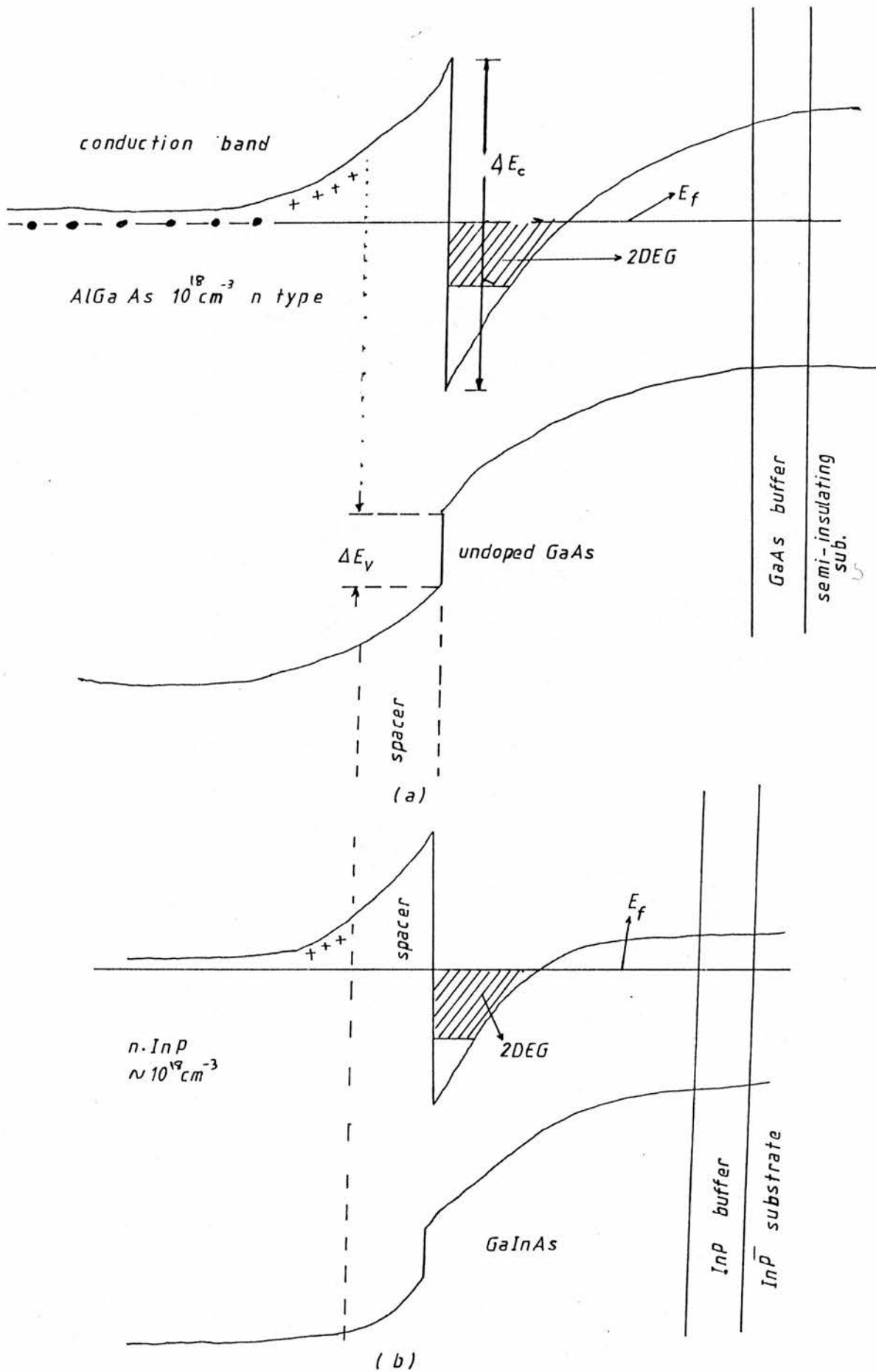


Fig. 2.7 Modulation doped heterojunction (a) GaAs-GaAlAs and (b) GaInAs - InP.

very high electron mobilities can be realised. At liquid helium temperature (4.2K⁰), Hall mobilities in the 2DEG ~ 2 x 10⁶ cm²/Vs or 200m²/Vs have been obtained in GaAs-GaAlAs structures.

2.2.3 Multiple Quantum Wells and Superlattices

(i) Multiple Quantum Wells

GaAs wells which are a few hundred Å thick can result in the quantum confinement of electrons. If two back-to-back "selectively doped" single interfaces are brought progressively closer together they eventually form a single thin GaAs layer sandwiched between two AlGaAs barriers. By coupling many such trilayers together a modulation-doped quantum well structure will result as shown in Fig 2.8. These are also called Multiple Quantum Wells (MQWs).

For thin GaAs layers, $d \leq 2000\text{Å}$, a single 2DEG confined by ΔE_c at both interfaces will exist. The energy of the ground state in the QW is given approximately by:

$$E_{e_1} = \frac{\hbar^2}{2m_e^*} \frac{(2\pi)^2}{\lambda^2}$$

$$\frac{\lambda}{2} = d$$

where d is the thickness of the well. This expression is an abbreviated version of that devised in Section 2.1.2 for square wells. The important feature is the $1/d^2$ dependence of the ground state energy.

MQWs have very important applications in optoelectronic devices. The essential idea is that the energy of the photons

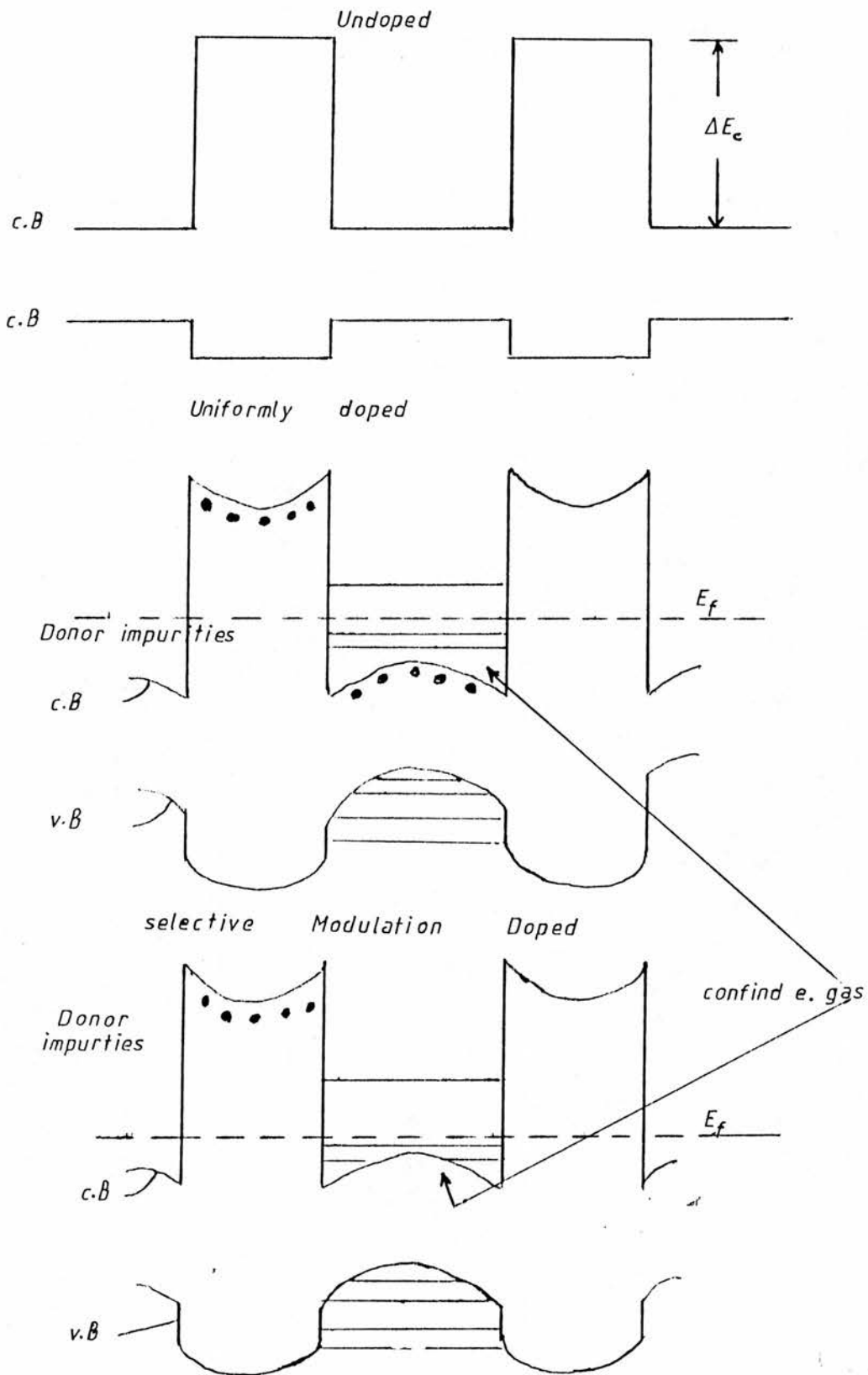


Fig. 2-8 Energy band diagram for undoped uniformly doped and selective (modulation) doped M.Q.Ws of GaAs/AlGaAs

emitted in electron-hole recombination processes can be varied over quite a wide range by using the width of the well to adjust the energy of the localised electron and states, as shown in Fig 2.9, where

$$h\nu = E_G + E_{e_1} + E_{h_1}$$

(ii) Superlattices

In the MQWs above the wave functions of the electrons confined in the individual wells did not overlap, ie, the QWs were decoupled. However, if the barriers become thinner and thinner, then a non-zero overlap of the wavefunction would occur and the wells, provided they have the same thickness (ie the same quantised energy levels), would interact with each other. The extreme case is when the overlap is so significant that the concept of superlattice is needed to describe the motion of the electrons (and holes) perpendicular to the layers.

The basic idea of a superlattice is to introduce a man-made periodicity in one dimension, superimposed on the atomic periodicity of the crystal structure. Consider a superlattice of period l , using the nearly free electron model to generate energy bands and energy gaps such a superlattice will produce an analogous "miniband" and "minigap" structure for conduction band electrons moving along the superlattice z axis as shown in Fig 2.10. If $l = 50a_0$, where $a_0 = 6 \text{ \AA}$ is the lattice constant of GaAs, then the width of the mini (Brillouin) zone of the superlattice along the k_z axis in k -space will be $1/50$ of that of the Brillouin zone of the crystal (see Fig 2.11). The superlattice can be described by the Kronig-Penney model.

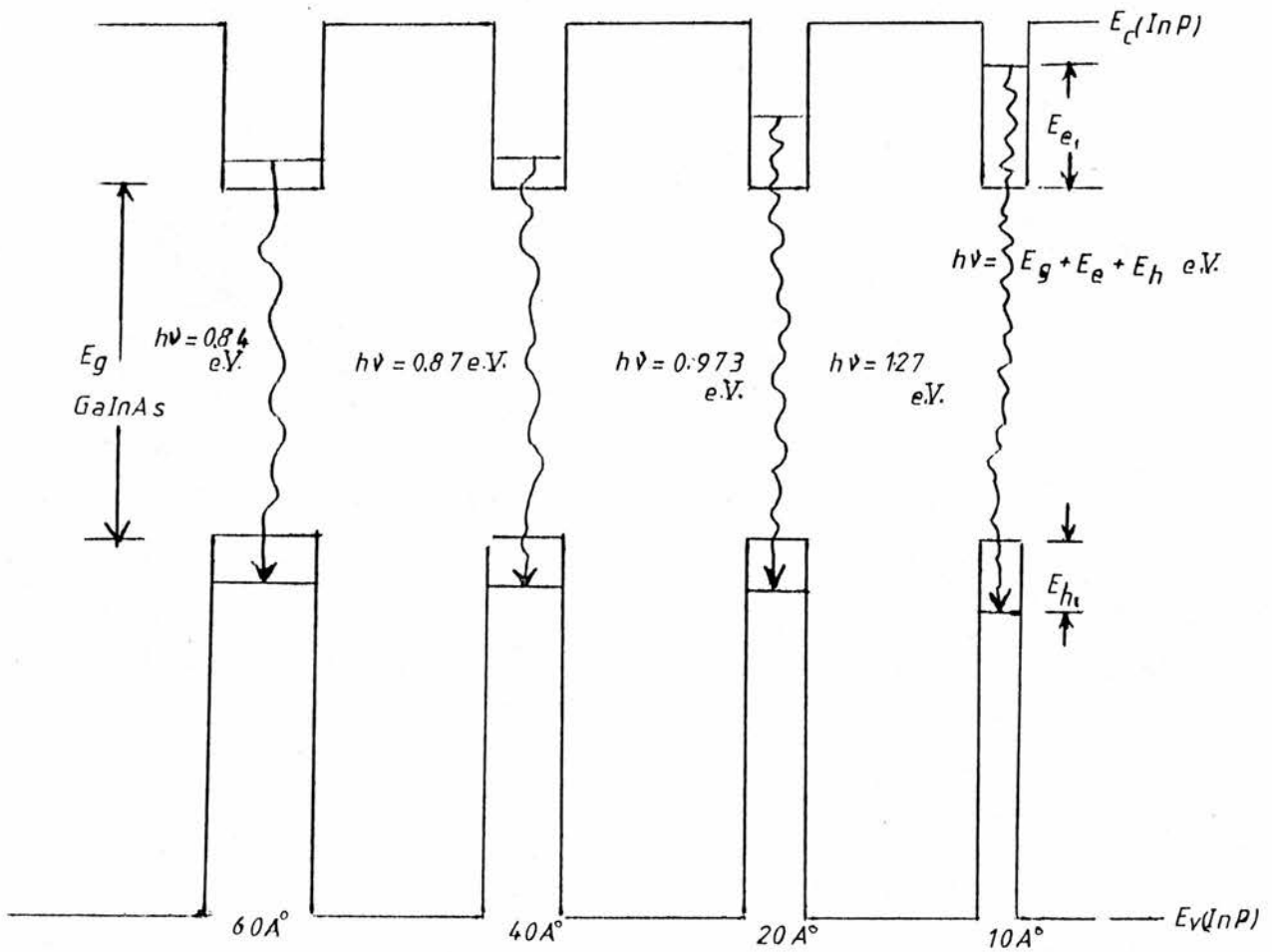
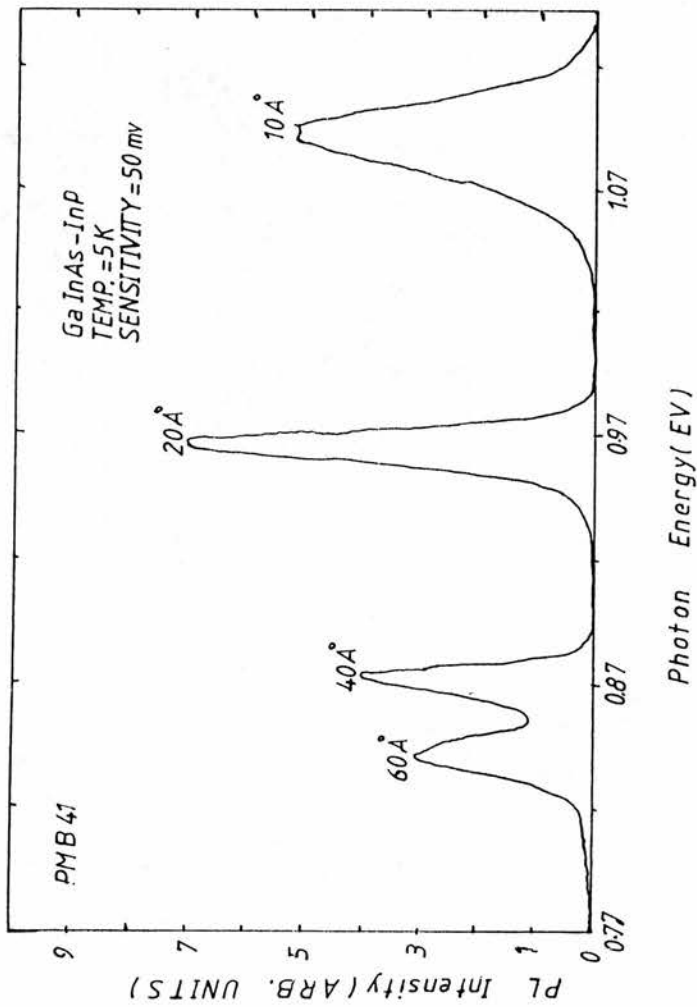


Fig. 2.9a The energies of the ground state in a MQW. InP/InGaAs at 4.2K with four wells of 10Å, 20Å, 40Å, and 60Å grown by M.B.E. at the University of sheffield PM841.



2.9 b Emission spectrum of the MQW structure

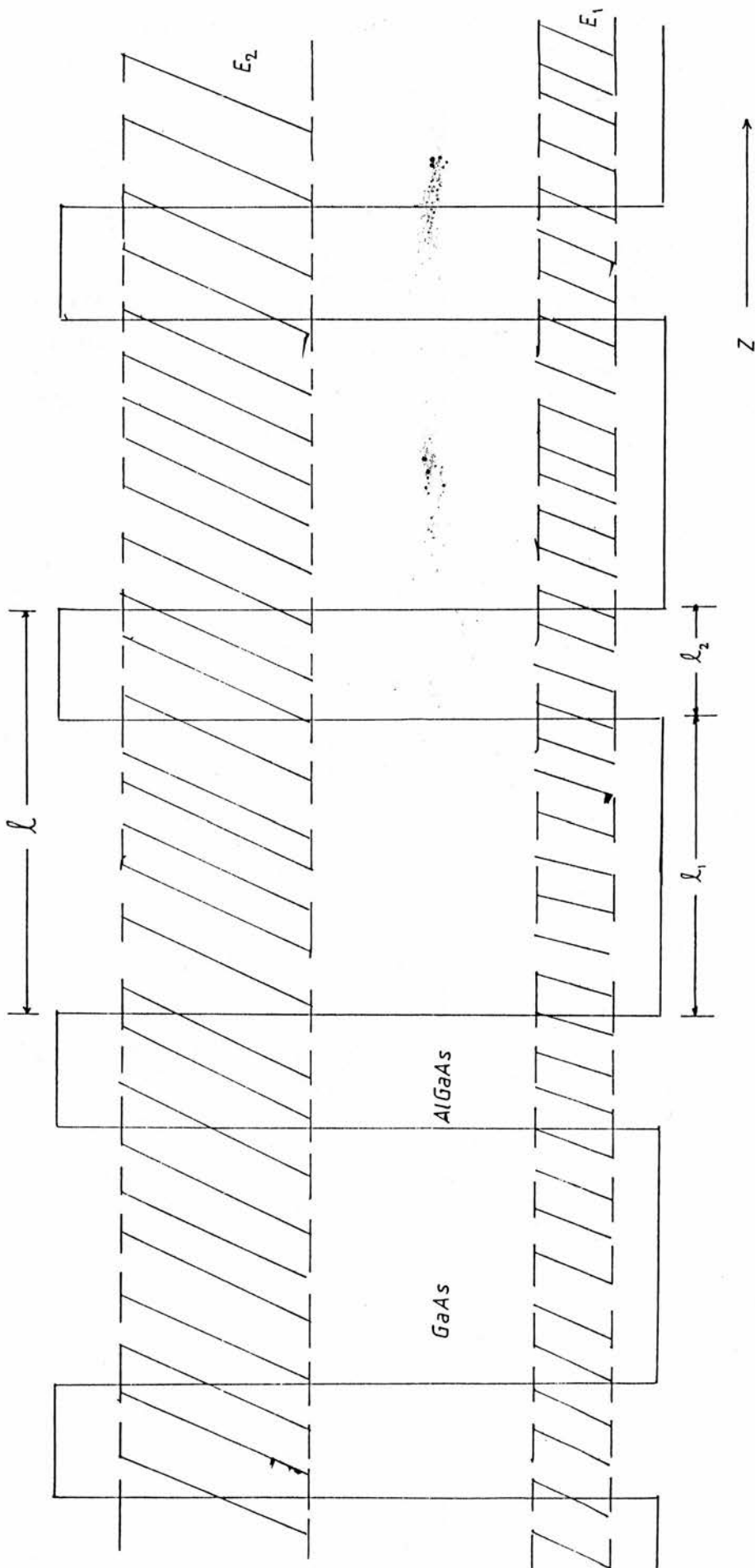


Fig. 2-10 AlGaAs/GaAs superlattice of period $l=l_1+l_2$ showing schematically the mini conduction bands E_1 and E_2 and the first mini gap.

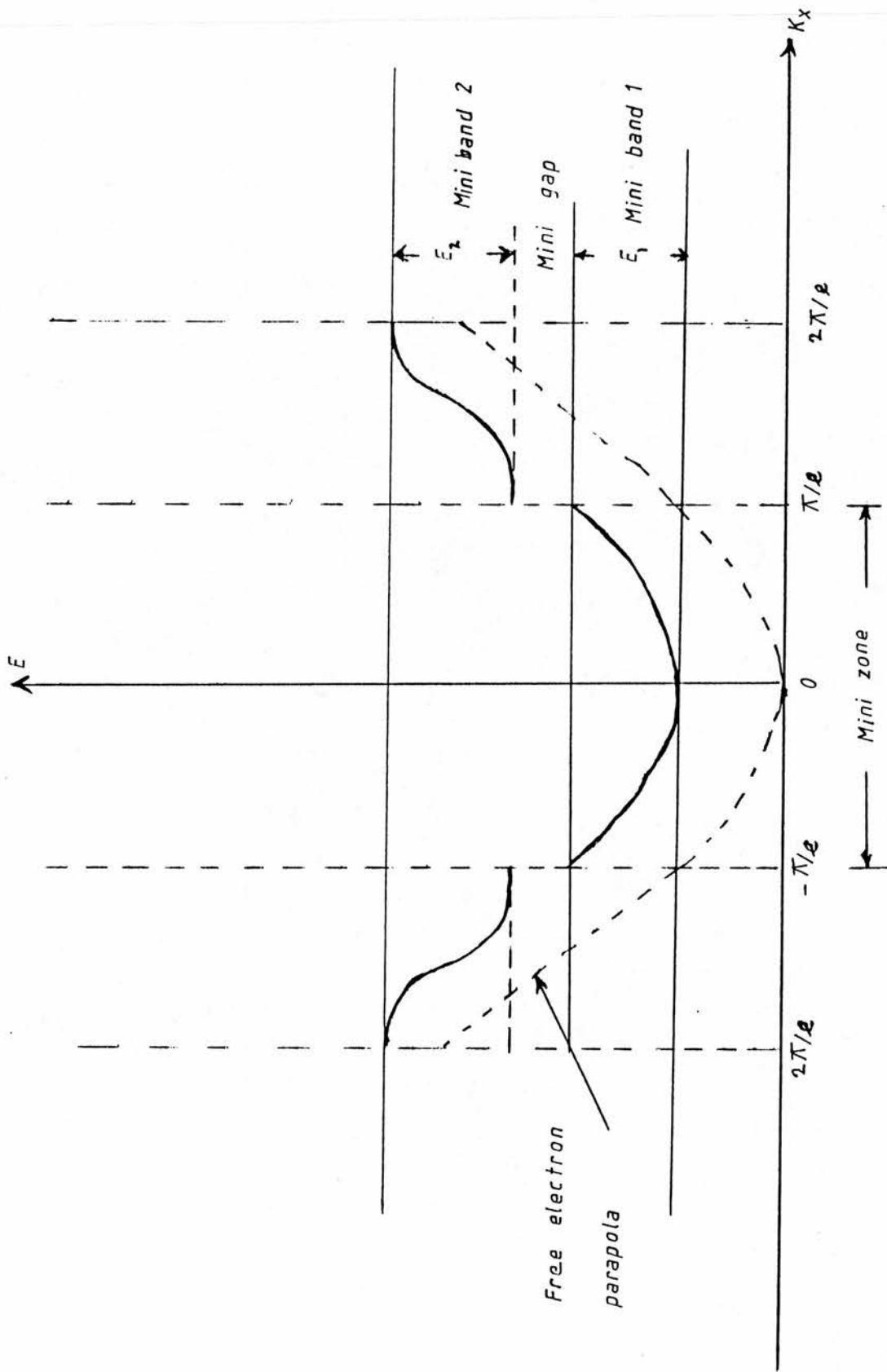


Fig. 2.11 Superlattice Band structure.

2.3 Scattering Mechanisms in the 2DEG

One of the driving forces for research on the 2DEG is quest for improved mobilities in future computer components. To this effect the understanding of the mobility limiting mechanisms is paramount as it is on pure physics considerations that the structures can be tailored to yield a desired distribution of say, Coulomb scatterers.

The range of electron gas densities justifies the use of degenerate-electron statistics at temperature below 60K, therefore the inverse of the total relaxation time $1/\tau_{total}$ can be written as the sum of the scattering rates for the individual processes.

In what follows we will use q_F to denote the wave vector on the Fermi surface where:

$$q_F = (2\pi n)^{\frac{1}{2}} \dots \dots \dots 2.34$$

n is the electron density in 2D and the electron mobility corresponding to the scattering rate is given by:

$$\mu = \frac{e}{m^*} \tau_{total} \dots \dots \dots 2.35$$

and then

$$1/\tau_{total} = \Sigma 1/\tau_i \dots \dots \dots 2.36$$

At temperatures higher than 60K the scattering in 2DEG is dominated by polar scattering. There is the possibility of scattering by interface charges located at the heterojunction interface. These and other mechanisms are treated below. Comparison between theory and experiment for previous work is discussed in sections 3.2 and 3.3.

2.3.1 Polar Scattering

For the polar optical phonon scattering the relaxation time approximation is assumed valid (Lin et al 1984). Since electrons couple only to the longitudinal mode, the electron momentum relaxation time, obtained by using the variational wave function and the Fröhlich Hamiltonian is given by (Lin et al 1984):

$$\tau_{10}^{-1} = \frac{e^2 k_B \theta_D}{8\pi^2 \hbar \epsilon_0} \left(\frac{1}{\epsilon_\infty} - \frac{1}{\epsilon_0} \right) (N_Q + \frac{1}{2} \pm \frac{1}{2}) \times \iiint \frac{|F(q_z)|^2}{q^2 + q_z^2} (1 - \cos\theta) \delta(E_p - E_p \pm \hbar \omega_{LO}) \times q \, dq \, dq_z \, d\theta \dots\dots\dots 2.37$$

where $k_B \theta_D = \hbar \omega_{LO}$ is the longitudinal optical phonon energy, ϵ_∞ and ϵ_0 are the optical and static dielectric constants, respectively, and

$$|F(q_z)| = [b^2 / (b^2 + q_z^2)] \dots\dots\dots 2.37a$$

is the form factor to take into account the variational wave function. Here:

$$b = [12e^2 m^* n_s / E_0 \epsilon_0 \hbar^2]^{1/3} \dots\dots\dots 2.37b$$

and q_z and q are the phonon wave vectors.

The ratio of the 2D polar-optical mobility to the bulk is approximately 1.25 (Hess 1979). Screening was found to be important for polar-optical phonon scattering (Price 1981). All of these lead to a scattering rate that is much more complex than in Eq 2.37. On the other hand the polar-optical phonon scattering has a simpler empirical temperature dependence than the polar-optical mobility deduced for bulk GaAs. The following simple empirical relation for the optical mobility may be used (Drummond et al 1981):

$$\mu_{po} = A/T^2 + B/T^6 \dots\dots\dots 2.38$$

Eq 2.38 may be considered as an interpolation between the temperature dependence of μ near 77K where $\mu_{po} \sim \frac{1}{T^6}$ and the temperature dependence of μ near 300K where $\mu_{po} \sim \frac{1}{T^2}$. The constants A and B are fitted to the theoretical values of the mobility in bulk GaAs limited by polar-optical phonon scattering: $7 \times 10^5 \text{ cm}^2/\text{Vs}$ at 77K (Wolf et al, 1981) and $9000 \text{ cm}^2/\text{Vs}$ at 300K (Rode 1970). The resultant expression for GaAs is:

$$\mu_{po} = 7.95 \times 10^8/T^2 + 1.18 \times 10^{17}/T^6 \text{ cm}^2/\text{Vs} \dots \dots \dots 2.39$$

2.3.2 Remote Ionized Impurity Scattering

In the case of ionized impurities there are two different types of scattering in two dimensions: electrons can be scattered by remote impurities located within the doped region of the S_2 semiconductor as well as by residual background impurities in the S_1 layer of Fig 2.11 (see section 2.3.3). The momentum relaxation of electrons in the i th band (Hess, 1979) is given by:

$$\left(\frac{1}{\tau_{RI}} \right)_i = \frac{(e^4 m^* N_D)}{8\pi \hbar^3 \epsilon^2 q} \int_0^\pi \frac{\exp(-4qL_j \sin \theta)}{2 \sin \theta + S_i} \sin \theta \, d\theta \dots \dots \dots 2.40$$

where m^* = effective mass,

N_D = uniform remote ionized impurity density,

ϵ = dielectric constant of GaAs,

q = 2D electronic wave vector,

S_i = screening constant of i th subband (only intraband scattering assumed),

$$L_i = d_i + Z_i$$

d_i = thickness of the spacer layer,

Z_i = average distance of electronic wave function from the heterointerface.

In fact only donors within the distance

$$L_i = d_i + Z_i + d_1 \dots\dots\dots 2.40a$$

contribute to the scattering. Here $d_i + d_1$ is the distance from the interface of the heterojunction to the boundary between the depleted and neutral donor region. Assuming that only one subband (zeroth) is occupied then the momentum relaxation time becomes (Lee et al 1983)

$$\frac{1}{(\tau_{RI})_0} = \left(\frac{e^4 m^* N_d}{64 \pi \hbar^3 \epsilon^2 q^2} \right) \left(\frac{1}{L_0^2} - \frac{1}{L_1^2} \right) \dots\dots\dots 2.41$$

where

$$q_0 = q_F = (2\pi n_s)^{\frac{1}{2}}$$

$$L_0 = d_i + Z_0$$

$d = d_i = d_0 =$ spacer layer thickness, Z_0 is given by (Stern, 1972).

$$Z_0 = \frac{2E_0}{3eF_s} = \left(\frac{n_s}{10^{12} \text{cm}^{-2}} \right)^{-1/3} \times 55 \text{ \AA} \dots\dots\dots 2.41a$$

where:

$F_s =$ electric field, which depends on the shape of the potential,

$$L'_0 = d + Z_0 + d_1$$

$d_1 =$ width of depletion layer excluding spacer.

Scattering by neutral donors in the AlGaAs (InP) layer, i.e., those in the neutral region separated from the 2DEG by the spacer and depletion layer, can be neglected since the matrix element for this scattering process is weakened by about 10^{-3} with respect to remote ionized impurity scattering (Lee et al, 1983).

2.3.3 Residual Impurity Scattering

There is additional scattering due to residual impurities at the interface. In equilibrium the transfer electrons from the doped region to the well of a MDH is governed by the following equation (Walukiewicz et al 1984):

$$E_o + E_f = V_o - E_b - \frac{4\pi e^2}{2\epsilon_o} \frac{(n_s + n_{depl})^2}{N_i^r} - \frac{4\pi e^2}{\epsilon_o} (n_{\Delta} + n_{depl})d \dots\dots 2.42$$

where V_o is the conduction band energy offset, E_o is the donor binding energy in the doped part of semiconductor S_2 , ϵ_o is the static dielectric constant, and n_{depl} is the areal concentration of ionized donors in depleted regions of S_1 . It should be noted, however, that the contribution of ionized impurities located within the spacer is negligible for densities lower than about $3 \times 10^{15} \text{cm}^{-3}$. Equation 2.36 can be used to calculate the concentration of ionized remote impurities N_i^r as a function of electron-gas density n_s and undoped spacer width d . If d increases it will lead to a decrease in 2DEG density in the well, which has deleterious effect on the electron mobility as will be shown in section 3.2.

The corresponding momentum relaxation time τ_{BI} is given by (Hess, 1979):

$$1/\tau_{BI} = \frac{e^4 m^* N_{BI}}{(8\pi\hbar^3 \epsilon_o^2 \epsilon_s^2 q_F^2)} I_B(\beta) \dots\dots\dots 2.43$$

where N_{BI} is the 2D impurity density in the potential well due to background impurities and/or interface charge and:

$$I_B(\beta) = \int_0^\pi d\theta \sin^2\theta / (\sin\theta + \beta)^2 \dots\dots\dots 2.44$$

$$\beta = S_o / 2q_F \dots\dots\dots 2.45$$

Eq 2.43 is different from those obtained by Soh et al (1972) and Hess (1979) because two-dimensional degenerate Fermi statistics are used here, where as two-dimensional nondegenerate statistics were used previously.

S_0 is the screening constant $S_0 = 2e^2m^*/4\pi\epsilon_0\epsilon_s\hbar^2 = 2 \times 10^6 \text{ cm}^{-1}$ in GaAs. However, the scattering due to the background ionized impurities ($\sim 10^{14} \text{ cm}^{-3}$) in GaAs has been found to be relatively small compared to the remote impurity scattering. The following simplified expression for the GaAs-GaAlAs mobility of Lee et al 1983, due to the interface charges has been used:

$$\mu_{BI} = 1.77 \times 10^6 (n_s / 10^{12} \text{ cm}^{-2}) (10^9 \text{ cm}^{-2} / N_{BI}) \times \frac{1}{I_B(\beta)} \quad (\text{cm}^2/\text{Vs}) \dots 2.46$$

with a quadratic interpolation for $1/I_B(\beta)$ which was found to be quite satisfactory:

$$\frac{1}{I_B(\beta)} = 1.26\beta^2 + 2.21\beta + 0.74 \dots 2.47$$

The mobility μ_{4K} and n_s in the 2DEG are plotted in Fig 2.12 as a function of spacer layer thickness and for two different thicknesses of the doped AlGaAs layers.

2.3.4 Alloy-disorder Scattering

There are two types of heterojunctions. One in which the 2DEG is confined within the alloy. In the other it is within the compound semiconductor. In the first case practically all of the electrons are subjected to alloy disorder scattering while in the second case alloy-disorder scattering affects only the electrons which have penetrated into the alloy. Since both deformation potential acoustic and alloy-disorder scattering result from short range potentials, there is a

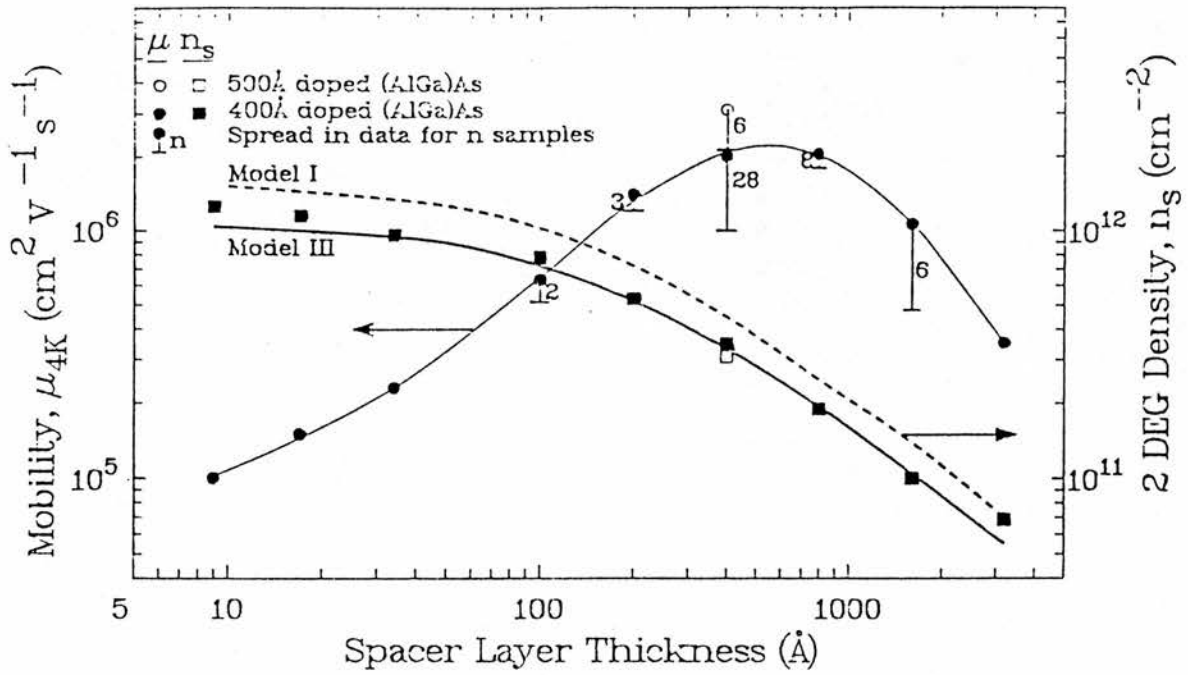


Fig. 2.12 Mobility μ_{4K} and 2DEG density n_s as a function of spacer layer thickness in doped (AlGa)As (J.C Maan et al 1983.)

formal similarity between the relaxation time in both cases.

Thus for intersubband alloy scattering the relaxation time can be written as (Bastard 1983 and Basu 1983):

$$\frac{1}{\tau_{\text{alloy}}^{0,1}} = \frac{m^* x (1-x) \Omega \langle V \rangle}{\hbar^3} I_{\text{alloy}}^{0,1} \dots\dots\dots 2.48$$

where x is the mole-fraction composition of the ternary alloy, $\langle V \rangle$ is the alloy-disorder scattering parameter, and Ω is the unit cell volume.

For electrons within the alloy;

$$I_{\text{alloy}}^0 = \int_0^\infty |x_0(z)|^4 dz = \frac{3}{16} b_0 \dots\dots\dots 2.49$$

$$I_{\text{alloy}}^1 = \int_0^\infty |x_0(z)|^2 |x_1(z)|^2 dz = \frac{3}{16} b_{\text{eff}} \dots\dots\dots 2.50$$

where b is defined in section 2.12 and b_{eff} is given by:

$$b_{\text{eff}} = \frac{2}{3} \frac{A^2}{\alpha^5}, \alpha = 3B \dots\dots\dots 2.50a$$

However for the 2DEG within the compound semiconductor

$$I_{\text{alloy}}^0 = \int_{-\infty}^0 |x_0(z)|^4 dz = \frac{3}{16} b_0 \dots\dots\dots 2.51$$

$$I_{\text{alloy}}^1 = \int_{-\infty}^0 |x_0(z)|^2 |x_1(z)|^2 dz = \frac{3}{16} b_{\text{eff}} \dots\dots\dots 2.52$$

where $x_{0,1}^1(z) = M_{0,1} \exp [-(2m^*V_0/\hbar^2)^{\frac{1}{2}} z]$ for $z < 0$ is the part of the wavefunction for both ground (0), and first excited subband (1), which describes penetration of the electron gas into the alloy.

So for the case of GaInAs-InP assuming the alloy is perfectly random, we obtain at $T = 0\text{K}$ (Bastard 1984):

$$\frac{1}{\tau} = \frac{m^*}{\hbar^3} x(1-x)\Omega_0 |\langle \delta V \rangle|^2 \int_0^\infty x_1^4(z) dz \dots\dots\dots 2.53$$

where $m^* = 0.047 m_0$, $x = 0.47$, $4\Omega_0 = (5.87 \text{ \AA})^3$ and $\langle \delta V \rangle$ is the strength of the scattering potential taken to be 0.6 eV. Alloy scattering in GaAs-GaAlAs is much weaker than in the GaInAs-InP structures because the penetration of the wavefunction in the barrier can be neglected.

2.3.5 Acoustic deformation potential scattering

The matrix element M_A for the acoustic deformation potential scattering in 2D can be written as (Lee et al 1983):

$$M_A^2 = \frac{e_A^2}{A} \hbar \omega_A (2\rho' b A u_\ell^2) (N_p + \frac{1}{2} \pm \frac{1}{2}) \delta_{p, q \pm p} \dots\dots\dots 2.54$$

where e_A is the acoustic deformation potential, ω_A is the acoustic phonon frequency, ρ' is the mass density of the GaAs, A is the area, u_ℓ is the velocity of the longitudinal acoustic phonon, b is the effective width of the 2D layer, P is the wave vector for the phonons, \pm signs denote phonon emission and absorption, respectively. According to conventional time-dependent perturbation theory the probability of a transition between two states of the total system having energy ϵ_1 and ϵ_2 depends on time t as $(t^2 \sin^2 x)/x^2$ where $x = (\epsilon_1 - \epsilon_2)t/2\hbar$. If the mean free time between transitions is large enough, which is the case in the high-mobility materials of interest, the function $\sin^2 x/x^2$ may be replaced by a δ function (Conwell 1967). N_p is the average occupation number of phonons given by

$$N_p = \frac{1}{e^{\hbar \omega_A / kT} - 1} \dots\dots\dots 2.55$$

Even at low temperatures the scattering is elastic because the Fermi energy is much larger than the acoustic phonon energy and the momentum relaxation time τ_A due to the acoustic deformation potential scattering becomes:

$$\frac{1}{\tau_A} = \frac{e^2 m^* K T}{\hbar \rho' b u_\ell^2} I_A(\gamma_\ell) \dots\dots\dots 2.56$$

where T is the lattice temperature and

$$I_A(\gamma_\ell) = \frac{2\gamma_\ell}{\pi} \int_0^{\pi/2} \left(\frac{2}{e^{\gamma_\ell \sin\theta} - 1} + 1 \right) \sin^2\theta d\theta \dots\dots\dots 2.57$$

and $\gamma_\ell = \frac{2\hbar u_\ell q_F}{KT} \dots\dots\dots 2.58$

In GaAs

$$\gamma_\ell = 20.0 \sqrt{n_s / 10^{12} \text{cm}^{-2}} / T \dots\dots\dots 2.59$$

At high temperature ($\gamma \rightarrow 0$) (Stern 1972, Soh et al 1972 and Price 1982):

$$1/\tau_A = \frac{e^2 m^* K T}{\hbar^3 \rho' b u_\ell^2} \dots\dots\dots 2.60$$

is proportional to temperature. But in a low temperature limit ($\gamma \rightarrow \infty$)

$$1/\tau_A = (8/3\pi) (e^2 m^* q_F) / (\hbar^2 \rho' b u_\ell) \dots\dots\dots 2.61$$

which is independent of temperature, since the phonon capture rate is negligible and phonon emission is dominant.

This correction is very important because $\gamma \sim 1$ when $T \sim 20\text{K}$ and $n = 10^{12} \text{ cm}^{-2}$ (see equation 2.59) and hence equation 2.56 instead of equation 2.61 should be used.

It should be noted that T in these equations is the lattice temperature as opposed to the electron temperature which is necessarily greater than zero.

2.3.6 Piezoelectric Scattering

The matrix element for the piezoelectric scattering in a 2DEG calculated by Price (1981) leads to the following expression for the momentum relaxation time:

$$\frac{\tau_A}{\tau_{PE}} = \frac{b}{\pi q} \left[\frac{9}{32} + \frac{13(u_\ell)^2}{32(u_t)^2} \frac{I_A(\gamma_t)}{I_A(\gamma_\ell)} \right] \frac{eh^2}{e_A} \dots\dots\dots 2.62$$

where u_t is the velocity of the transverse phonon, h_{14} is the piezoelectric constant and γ_t is given by equation 2.58 with u_t in the place of u_ℓ . As can be seen from equation 2.62 τ_{PE} is independent of the effective 2D layer thickness b .

2.3.7 Intersubband Scattering

Scattering of electrons between subbands, assisted by optical phonons or electric fields, should occur when more than one electron subband is occupied according to the predictions of Mari et al (1979). The most characteristic signature of this intersubband scattering is an abrupt reduction of electron mobility whenever a subband starts to become populated.

The electron concentration in a modulation-doped GaAs-AlGaAs heterojunctions can be varied over a finite range by an external electric field applied to an electrode attached to the backside of the

specimen (Störmer et al 1981). This together with a properly designed heterojunction allowed Störmer et al (1981) to sweep the carrier concentration and in turn the Fermi level, continuously through the transition from one-subband population to two-subband population.

The intersubband scattering mechanism is illustrated in Fig 2.13 and the effect on mobility is shown in Fig 2.14.

Intersubband scattering would result in an abrupt decrease of the electron mobility for electron concentration exceeding n_s^{crit} . However, since the actual density of states function is broadened, one expects a gradual increase of intersubband scattering for n_s close to n_s^{crit} . We follow the treatment of Walukiewicz et al 1984, including these effects by considering the broadening to be described by a simple Lorentzian function with energy-independent broadening parameter Γ . The relaxation time for intersubband scattering is then modified in the following way:

$$\left| \frac{1}{\tau_i(E)} \right|_{\text{broad}} = \left| \frac{1}{\tau_i(E)} \right|_{\text{unbroad}} \frac{1}{\pi} \left| \frac{\pi}{2} + \tan^{-1} \left[\frac{E - E_1}{\Gamma} \right] \right| \dots 2.63$$

where:

$$\left| \frac{1}{\tau_i(E)} \right|_{\text{broad}} = \text{Relaxation time for intersubband scattering in case of broadening, and}$$

$$\left| \frac{1}{\tau_i(E)} \right|_{\text{unbroad}} = \text{relaxation time for intersubband scattering in case of unbroadening.}$$

$E - E_1 =$ is the difference between two energy levels,

and $\Gamma =$ energy-independent broadening parameter.

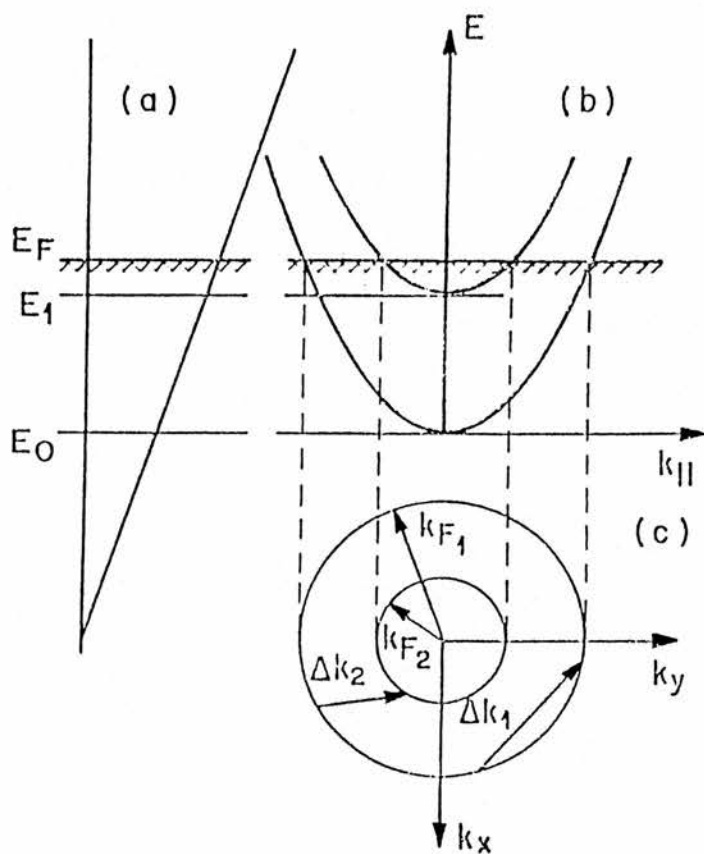


Fig. 2.13 schematic representation of electric subband formation (E_0, E_1) in a triangular potential. (a) In-plane dispersion (b) and Fermi circles (c) of a 2DEG.

E_F is the Fermi level k_{F1} and k_{F2} are Fermi wave vectors of ground subband and excited subband respectively. k_x, k_y and $k_{||}$ are in-plane wave vectors. Two energy conserving electron scattering mechanisms are indicated: standard intra-subband scattering (Δk_1) and the observed inter-subband scattering (Δk_2).

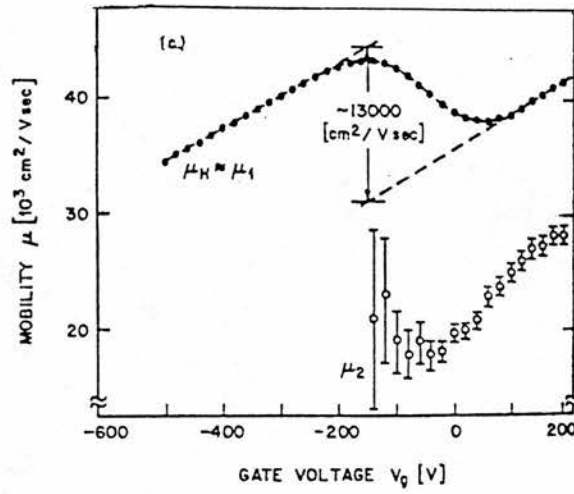


Fig. 2.14 V_g -dependence of the Hall mobility μ_H and the mobilities of the ground subband μ_1 and the excited subband μ_2 . μ_1 and μ_2 are calculated from μ_H where $\mu_H = \frac{n_1 \mu_1^2 + n_2 \mu_2^2}{n_1 \mu_1 + n_2 \mu_2}$, μ_H is Hall mobility of a system consisting two type of carriers having densities n_1 and n_2 and mobilities μ_1 and μ_2 but the same effective mass (Störmer et al 1982)

2.4 High Pressure Transport in 2D System

2.4.1 Modification of Transport Properties by Pressure in 3D III-IV Semiconductors

Hydrostatic pressure, when applied to a semiconductor uniformly and below the phase transition, does not alter the crystal symmetry whereas the semiconductor properties are subjected to variations due to the changes of the interatomic distance.

The effect of hydrostatic pressure on the transport properties are mainly due to changes in the energy band gaps, the energy of electronic states associated with the shallow impurities and of purely electronic states (deep levels).

(i) Effects on band structure

When hydrostatic pressure is applied, the various electronic energy bands shift relative to one another and in some cases carrier transfer may occur. The main effects are to open up the direct energy gap (Γ point) and the indirect gap (L point) typically at rates of 10-15 meV/kbar and 5 meV/kbar, respectively (Aulombard et al, 1987), and to decrease the indirect gap (X point) at a rate 1-5 meV/kbar. Therefore a direct gap semiconductor can be transformed into an indirect gap one under the application of hydrostatic pressure.

A net effect of the variation of the band gap energies is seen in the changes of the effective electron mass (Adams et al, 1986a) since m^* at the bottom of the conduction band at $T = 0K$ is related to the energy gap E by (Herman and Weisbach, 1977):

$$\frac{m_0}{m^*} - 1 = \frac{E_p}{3} \left(\frac{2}{E_0} + \frac{1}{E_0 + \Delta_0} \right) - \frac{E'_p}{3} \left(\frac{2}{E'_0 + \Delta_0 - E_0} + \frac{1}{E'_0 - E_0} \right) + C \dots 2.64$$

where E_p and E_p' are the momentum matrix elements connecting the fundamental and the higher energy bands, respectively. E_0 and E_0' are the energy of the fundamental energy gap and the next conduction band measured both from the top of the valence band, Δ_0 is the spin orbit splitting, and C is a constant representing the contribution of all higher lying bands.

Equation 2.64 is effectively the k.p formula of Kane (1957) also known as the Effective Mass Approximation (EMA). Thus, transport measurements like mobility as a function of hydrostatic pressure can yield information on the relative strength of the various scattering mechanisms because these have different dependence on m^* , as discussed in section 2.3, (Adams et al 1986b and Adams and Shantharama 1986). The application of hydrostatic pressure gives the opportunity to simulate in a continuous manner the effect of alloying whose understanding is still of great interest for many practical problems in the search for optimum materials for a variety of devices.

(ii) Effect on Impurity Levels

Shallow donors are found to follow the conduction band minima with which they are associated as the minima shift with pressure.

In contrast, deep levels move towards or away from the nearest conduction-band edge and are sometimes located too far below this band to be taken into account even as the effective mass and dielectric constant change with pressure. Moreover, some of these deep states could exhibit metastability or persistent photoconductivity at low temperatures.

Transport experiments can help in the classification of impurities into deep or shallow, Γ -, L - or X-like by applying hydrostatic pressure and measuring Hall densities and resistivity (Wasilewski et al 1984) and by far infrared photoconductivity (Sotomayor Torres and Stradling 1987) among other techniques.

2.4.2 High Pressure Transport in 2D Systems

Hydrostatic pressure plays an important role in the understanding of transport properties of 2D systems. For example, it causes a decrease in the two dimensional electron gas concentration in GaAs-GaAlAs (Robert et al 1987). This change was demonstrated to be related to the deepening of the donor level with pressure in the energy gap of the doped layer of heterostructures. Thus hydrostatic pressure reduced the free electron concentration in this layer and the charge transfer to the quantum well. So the application of pressure gives the opportunity to avoid parasitic parallel conduction (see sections 4.1 and 4.3) in doped layers and to study the behaviour of two dimensional electron gas as a function of its density.

The change of 2D electron density with pressure suppresses less important effects of pressure on other parameters which interfere in the description of the quantum well and the 2DEG behaviour. These are, for example, conduction band discontinuity, electron effective mass, the energies and the energy differences between electric subbands. Whereas, in the case when the donor levels in the doped layer are shallow or are placed high enough above the bottom of the conduction band they induce no significant change in the 2D carrier density.

Consider a heterojunction as shown in Fig. 2.15. The doped GaAlAs layer is partially compensated and the donors are not completely ionized. The quantum well is considered triangular. When the pressure increases the shape of the triangular well is modified because as the 2D carrier density decreases the electric field at the interface weakens, the bending of the band decreases and the quantum well becomes shallower bringing closer in energy the electric subbands in the quantum well.

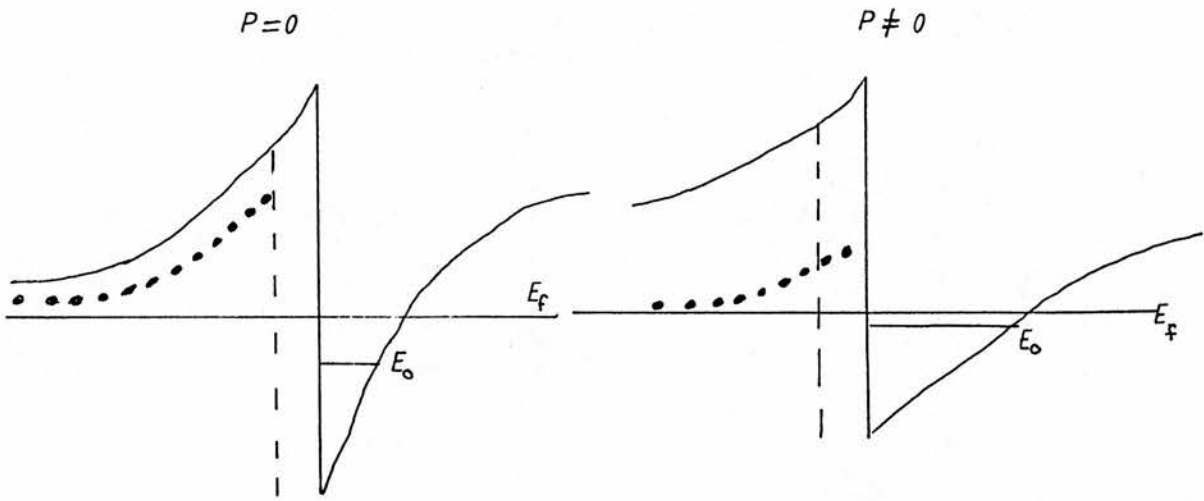
The elimination of parallel conduction by the application of hydrostatic pressure has also been used by Gregoris et al (1987) in GaInAs-AlInAs heterojunctions. As in GaAs-GaAlAs heterojunctions the applied pressure acts upon the shallow donor Si level in the barrier material AlInAs thus reducing the free electron concentration in this layer and decreasing the transfer of carriers to the well.

The work on GaAs-GaAlAs under pressure was extended by Beerens et al (1987) to higher temperatures (non-negligible parallel conduction but much reduced persistent photoconductivity). Their main finding confirmed that the density changes induced by pressure are related to the energy level of the Si donor. Their results were fitted with empirical relations for the activation energy (relative to the Γ - conduction band edge) at 0K as:

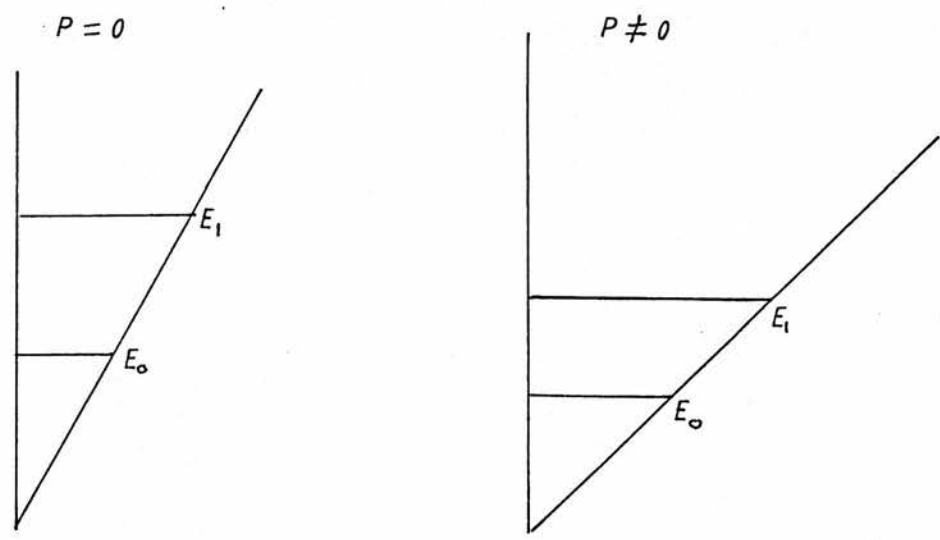
$$E_D (P) = 14 + 110 \times P \text{ meV (P in GPa)}$$

and for the temperature dependence

$$E_D (T) = E_D (T = 0) + 0.75 (E_x(T) - E_x (T = 0K))$$



(a)



(b)

Fig.2.15 a: The variation of the energy diagram of heterojunction under hydrostatic pressure.
 b: The variation of triangular well under hydrostatic pressure (Robert et al 1985).

E_D is the donor binding energy and E_x the X-band energy relative to the Γ - minima. Their interpretation was based on the temperature dependence of the Si donor level, which is still under investigation.

The heterojunction of GaInAs/InP has only shallow impurity levels and other levels which are resonant with the conduction band but which are away from the conduction band minimum energy. As such these states make no contribution to the change of n with pressure (Gauthier et al, 1986). To date, the pressure studies of transport in GaInAs-InP suggest that for a system with three subbands occupied the third uppermost subband remains occupied even at 15 kbar with almost constant density, although the total decrease of carrier is $\sim 12\%$ in 15 kbar. According to the authors, it is the two lowest subbands which loose carriers. Gauthier et al (1986) explained this observation suggesting that the triangular well approximation was not applicable to higher subbands and that only the lowest two feel the effect of the potential.

However, although the densities of the two lowest subbands were determined from low field SdH data, that of the upper subband was obtained from the difference of $n_0 + n_1$ and n_s total. Therefore the density of the uppermost subband has large additive errors.

The GaInAs/InP heterojunction under hydrostatic pressure up to more than 15 kbar reveals that hydrostatic pressure not only lowers the Fermi energy by increasing the donor binding energy in the barrier, thus decreasing the total electron concentration in the quantum well (Gregoris et al 1987), but also decreases considerably the energy separation between electric subbands. This in turn, according to the authors, leads to an observed constant population of third subband despite the fact that the decrease of total electron concentration at up to 15 kbar is about three times higher than the population of the

third subband.

Another observation was the drop of the electron mobility by 30% in 15 kbar. Considerations of the effective mass variation with pressure of $1.9 \pm 0.15\%$ kbar^{-1} in bulk GaInAs (Shantarama et al 1986), of $1 \pm 0.1\%$ kbar in heterojunctions (Gauthier et al 1986) and the fact that the contribution of inter-subband scattering decreases with increasing pressure, other scattering mechanisms such as screening and alloy scattering remain to be considered as responsible for the observed mobility decrease with pressure.

Once these aspects are understood, including the well becoming shallower, hydrostatic pressure could be used to study band-offsets.

CHAPTER III SUMMARY OF PREVIOUS WORK ON RELEVANT SYSTEMS

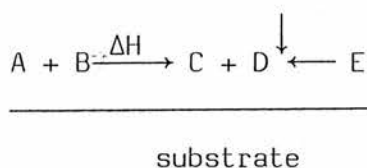
The samples discussed in this work were obtained from a number of sources mentioned at the beginning of Chapter V. Although none of the samples were produced in this laboratory the methods of preparation are very relevant to subsequent discussion and so Section 3.1 gives a summary of the appropriate growth procedures.

Previous transport measurements in GaAs-GaAlAs and GaInAs-InP are then summarised. The next section discusses the complications which have arisen in previous work due to parallel conduction and persistent photoconductivity. The final section is concerned with the behaviour of a 2D hole gas.

3.1 Design of 2DEG Sample

3.1.1 MOVPE

Metalorganic Vapour Phase Epitaxy (MOVPE) is part of a larger family of VPE techniques making use of reactions occurring between the vapours of chemical compounds (A and B) when they are heated together. These reactions produce chemically active species (C and D) that interact either in the vapour phase or on the solid surface of a substrate to produce a corresponding epitaxial film (E):



MOVPE specifically utilises vapours from metalorganic compounds and the hydrides of non-metals.

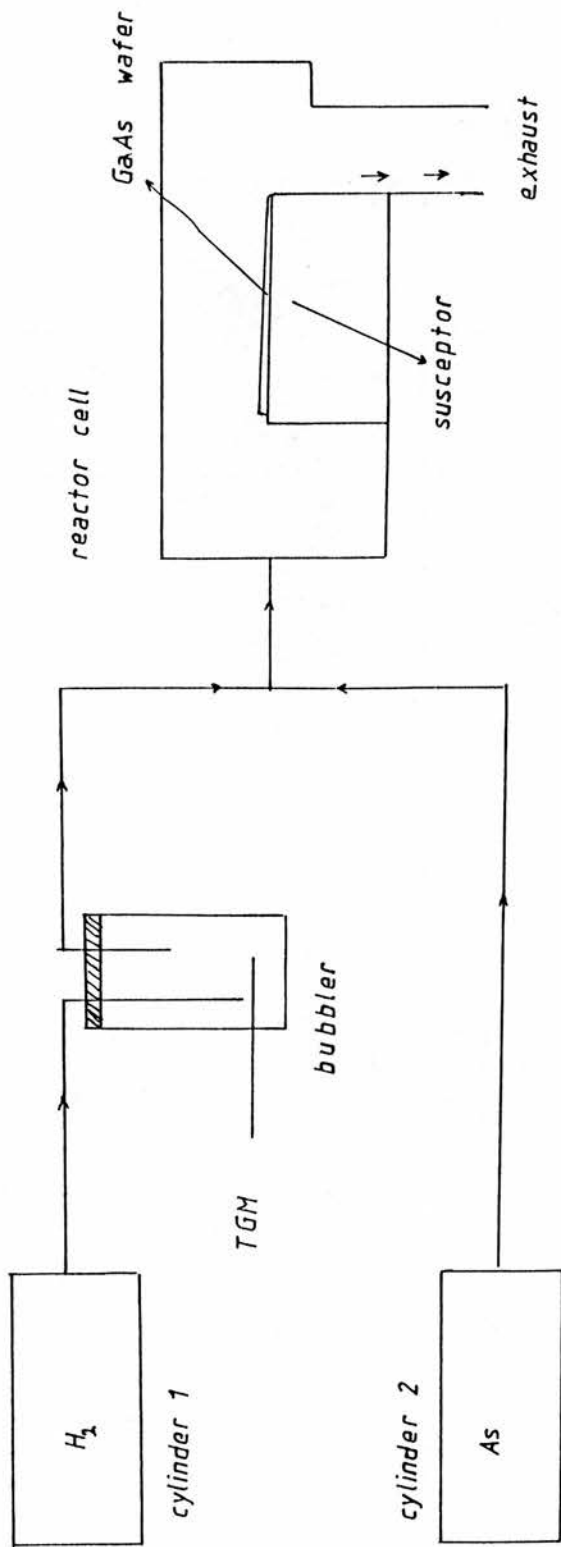
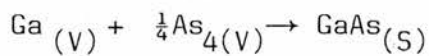
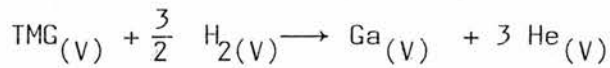


Fig. 3.1 vapour transport to the reaction cell in MOVPE technique.

Typical starting materials are trimethylgallium (TMG) and arsine (AsH_3). TMG is a liquid and is held in a stainless steel bubbler at -10°C through which pure hydrogen is passed to transport the vapour to the reaction cell (see Fig 3.1). The AsH_3 is supplied from a stainless steel cylinder for safety reasons. The two gas streams are intimately mixed and passed over the heated susceptor which holds a GaAs single crystal wafer. The arsine reacts to deposit epitaxial GaAs. AlGaAs is a ternary semiconductor which has either an Al atom or Ga atom on the group III sublattice thus the sublattice can have a range of compositions from 99%Al + 1%Ga to 1%Al + 99%Ga. This is usually denoted by the form $\text{Al}_x\text{Ga}_{1-x}\text{As}$ where x is the number of sites on the group III sublattice which are filled with Al atoms and $1-x$ the number of sites which are filled with Ga atoms, x taking values between 0(GaAs) and 1(AlAs) and all intermediate values. Both dimethylzinc DMZ (liquid in bubbler held at -35°C) and diethylzinc DEZ (liquid in bubbler held at -5°C) are used to dope the material p-type, whilst SiH_4 or H_2Se are used to dope the material n-type. All the compounds are either spontaneously inflammable in air or exceedingly toxic and much of cost of MOVPE systems is taken up with minimizing the chance of accidental exposure of the compounds to either air or operators. The only disadvantage of metalorganics outside the control of the grower are the purity of the source materials and the incorporation of carbon from the methyl groups into the grown layer.

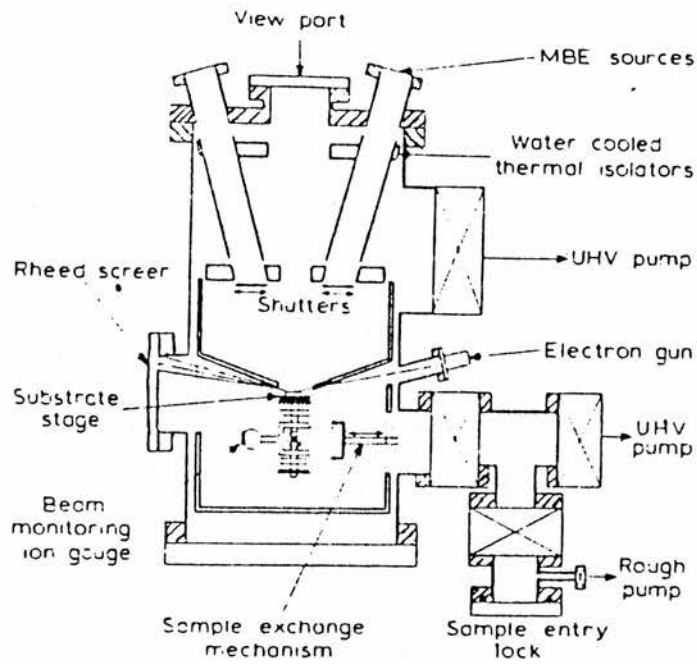
The reaction equation is that the TMG is completely decomposed by homogeneous reaction in the gas phase before reaching the boundary layer. The AsH_3 however decomposes only slowly unless catalysed by solid GaAs



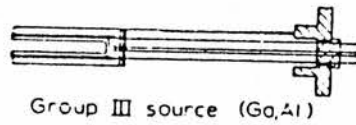
The range of growth rates is between 1 to 5 $\mu\text{m/hr}$. This is because any slower growth rate than that would lead to practical difficulties in getting thick, say 8 μm , structures grown in a reasonable time. The maximum growth rate is a function of the quality of the crystal grown, too fast a growth rate and the epitaxy will be upset even for GaAs. Adding Al to the lattice makes epitaxy of AlGaAs even more difficult and even slower growth rates are advisable (Mason, 1985).

3.1.2 Molecular Beam Epitaxy (MBE)

Epitaxy means "order upon" and is used to describe a process where not only is a film of material deposited on a substrate (chemical vapour deposition (CVD) but it is deposited in such a way as to continue the underlying crystal lattice parameters of that substrate. The substrate may be the same compound as that being deposited (homoepitaxy: GaAs on GaAs) or a different compound but one with a similar lattice constant (heteroepitaxy: GaAs on sapphire). The essential elements of a system suitable for growth of III-V compound films are shown in Fig 3.2. It is based on a two or three chamber of stainless steel in an ultra-high vacuum system, usually ion or cryopumped and incorporates, large areas of liquid-nitrogen cooled panels. The provision of a vacuum interlock, to enable the substrate to be introduced into the growth chamber without breaking the vacuum is



(a)



(b)

Fig. 3.2(a) Schematic diagram of an MBE system showing the essential features required for growth of III-V compound film.

(b) Basic Knudsen cell construction.

essential if films having high electrical quality and optical properties are to be prepared.

The atomic or molecular beams are formed in heated Knudsen effusion cells. An example of such a cell is shown in the lower part of Fig 3.2. The material to be evaporated is contained in a crucible, which is heated by radiation from a separate winding. In the cell the liquid or solid phase and the vapour are in equilibrium. The mean free path of the vapour atoms or moleculars is much larger than the cell orifice, ensuring molecular flow (Knudsen effusion). The inner crucible is made either of reactor-grade graphite or, preferably, pyrolytic boron nitride, so that the possible contamination of the molecular beams is minimised. Beam intensities are controlled by the cell temperatures and for molecular flow are given by:

$$J_i = [aP_i / \pi d^2 (2\pi m_i kT)^{\frac{1}{2}}] \cos \theta \dots \dots \dots 3.2$$

where J_i is the flux per unit area at a distance d from the source, which has an orifice of area a and contains atoms (molecules) of mass m_i having an equilibrium vapour pressure P_i at temperature T (in K) and θ is the angle between the beam and the substrate surface normal. Individual cells are thermally isolated by a succession of heat shields and the flux is regulated by a shutter operating in front of each aperture. A single microcomputer can be used to control all of the cell temperatures (within ± 0.025 K) and all of the shutters to achieve any growth sequence. Fluxes are usually monitored by an ion gauge which can be rotated in and out of the beams.

Other analytical facilities may include a quadruple mass spectrometer for residual gas analysis and leak checking, a reflection high energy electron diffraction (RHEED) arrangement for assessment of

surface structure and an Auger electron spectrometer. A RHEED arrangement consist simply of a 5-20 KeV electron gun and fluorescent screen. The electron beam is incident at a very shallow angle (1° - 4°) to the substrate surface. The diffracted electron beams form a characteristic pattern on the fluorescent screen which provides information on the morphology symmetry and defect structures of the surface. Because of the small incidence angle, the information obtained in RHEED is derived from the first few atomic layers. Temporal variations in the intensity of diffraction features during MBE growth can be related to growth dynamics (Joyce, 1985). It has been shown that with this technique a growth rate variation of <1% could be obtained across a 5 cm substrate, with comparable control of alloy composition.

Growth is initiated by bringing the substrate to the appropriate temperature (typically in the range 500-700°C) in a beam of arsenic and then opening the shutter of the Group III element source. Growth rates are in the range 0.03-3 nm/sec (0.1-10.0 $\mu\text{m/hr}$), corresponding to beam fluxes from $\approx 5 \times 10^{13}$ to 5×10^{15} atoms/cm²s. The arsenic flux is typically 3-5 times greater than that of the Group III element, but it is the latter which determines the growth rate. Dopant beams are also produced from Knudsen effusion cells. The elements used for doping the MBE are principally Be for preparation of p-type films and Si or Sn for the preparation of n-type films. All these elements evaporate as monomers. Free carrier concentrations can be controlled over the range between 10^{14} and 10^{19} cm⁻³.

The relative merits of both techniques MOVPE and MBE are given in table 3.1.

Table 3.1 Relative Merits of MBE and MOVPE

Specification	MBE	MOVPE
Layer area	20 cm ²	500 cm ²
Mobility GaAs	$\mu_{77} = 1.25 \times 10^5$	$\mu_{77} = 1.39 \times 10^5$
Background Doping	10^{14} n-type	5×10^{14} n-type
Complexity	Very Complex	Complex
Morphology	Good	Good
Versatility	Not Versatile	Versatile
$\mu_{4.2k}^{\text{HEMT}}$	$> 2 \times 10^6 \text{ cm}^2 \text{ v}^{-1} \text{ s}^{-1}$	$> 4.5 \times 10^5 \text{ cm}^2 \text{ v}^{-1} \text{ sec}^{-1}$

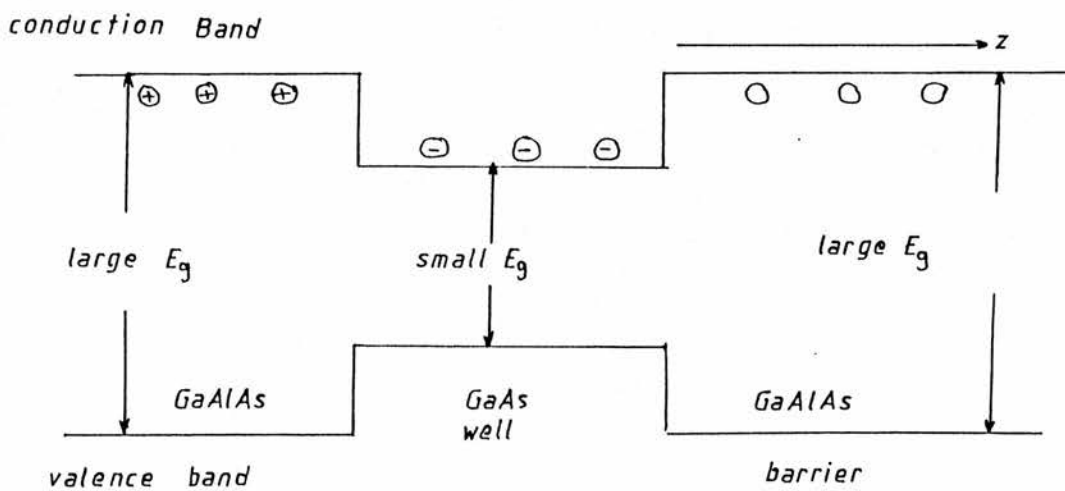
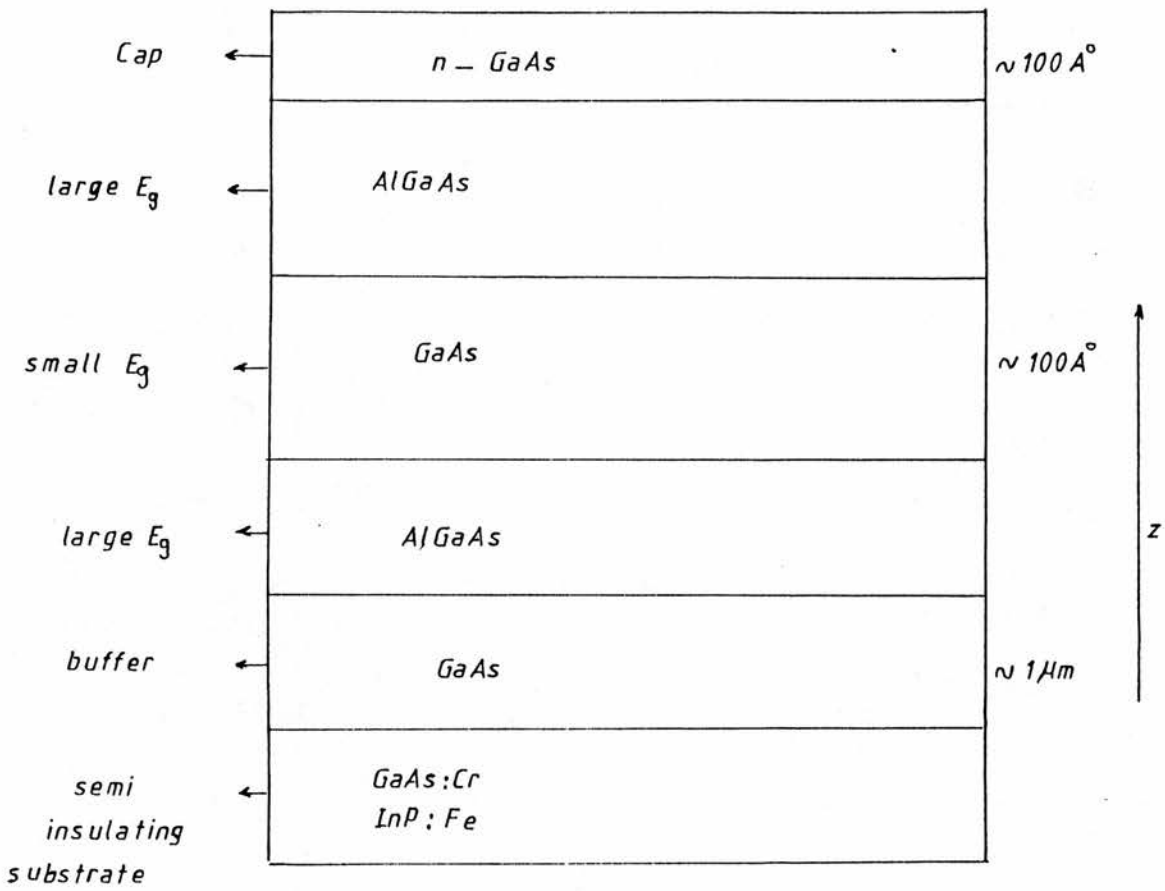


Fig. 3.3 Structure of a GaAs-GaAlAs S-Q.W. indicating direction of growth.

3.1.3 Role of Various Components of Structures

With the development of thin film growth techniques such as MBE and MOCVD during the past decade, high-quality heterojunctions have been produced. The basic structure shown in Fig 3.3 has a buffer layer of typically $1\ \mu\text{m}$ thickness of undoped GaAs.

The role of the buffer layer is to minimise the propagation of dislocations and provide a good starting surface. The large and small gap layers form the single square quantum well. On the surface, an n-type GaAs layer of typically $100\ \text{\AA}$ is grown in order to prevent oxide formation on the GaAlAs and to facilitate the formation of good ohmic contacts.

In a modulation doped heterostructure there is an additional layer of the large gap material adjacent to one side of the small gap layers. This is the spacer layer, it is undoped and typically of $50\ \text{\AA}$ thickness (see Fig 3.4). The role of the spacer layer is that mobile carriers in the conduction channel can be further separated from the ionized impurities by introducing undoped spacer layers in the barriers immediately before the well region. The theoretical prediction is that an undoped layer will progressively decrease ionised impurity scattering with increase separation and this is borne out in practice for a spacer layer thickness of up to $150\ \text{\AA}$ at 4K . The 2D conduction electrons are confined in the wedge-shaped potential well on the undoped GaAs-side of the interface as shown in Fig 3.4, in fact, Poisson's equation has to be solved self-consistently to obtain the form of the potential well in the GaAs. The potential is determined by the charge distribution as explained in section 2.1.2.

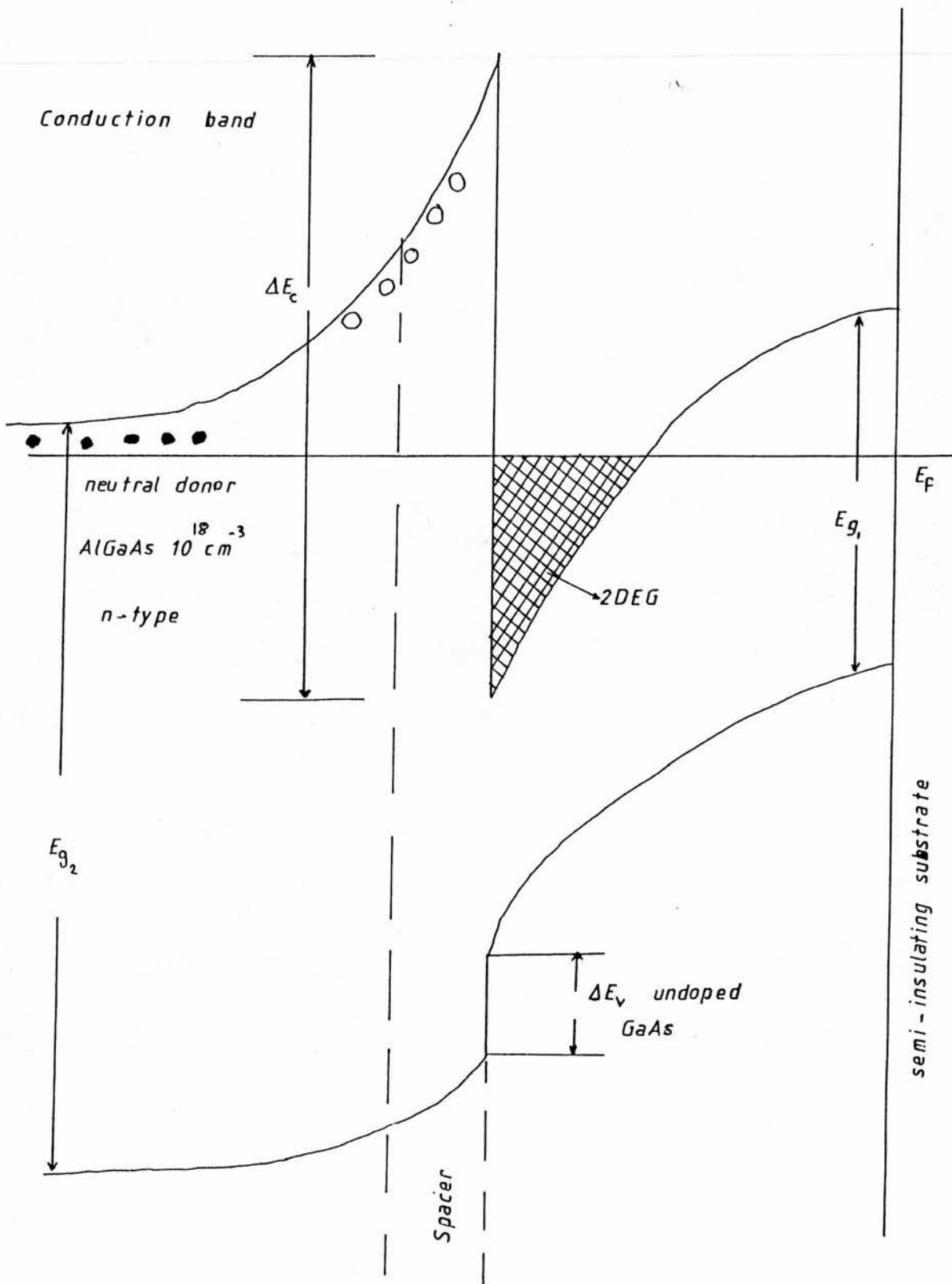


Fig 3.4 Energy band diagram for a AlGaAs MDH .

(a) InP HEMT STRUCTURE (NORMAL).

1	n^+ InP
2	u.d. InP spacer layer
3	u.d. InGaAs 1000 \AA°
4	u.d. InP buffer $\sim 2000 \text{ \AA}^{\circ}$
5	S.I. InP substrate

(b) InP HEMT STRUCTURE (INVERTED).

1	500 \AA° u.d. InP capping layer
2	1000 \AA° u.d. InGaAs
3	u.d. InP spacer layer
4	n^+ InP
5	u.d. InP buffer $\sim 2000 \text{ \AA}^{\circ}$
6	S.I. InP substrate

Fig. 3.5 Two Type of InP HEMT structure (a)Normal and (b)Inverted.

In the energy band diagram, ΔE_c and ΔE_v represent the conduction band and the valence band offset at the interface between the smaller gap semiconductor (E_{G1}) and the larger gap semiconductor (E_{G2}), E_F is the Fermi level, ΔE_G is equal to $E_{G1} - E_{G2}$ as shown in Fig 3.4. Depending on the growth sequence one can differentiate between inverted and non inverted structures (see fig 3.5).

If we take the InP structures as an example one finds that in both cases the range of doping level for the n^+ InP layer ranges typically from 1×10^{17} to $1 \times 10^{18} \text{ cm}^{-3}$ and the thickness chosen to eliminate parallel conduction is about 50 \AA for the spacer and 0.6 \mu m for the n^+ InP layers. When the doped InP layer is grown before the undoped InGaAs one, there are more transferred carriers with higher mobility than when the layers are grown in the reverse order. The differences occur as the result of enhanced interface roughness or of impurity scattering effects.

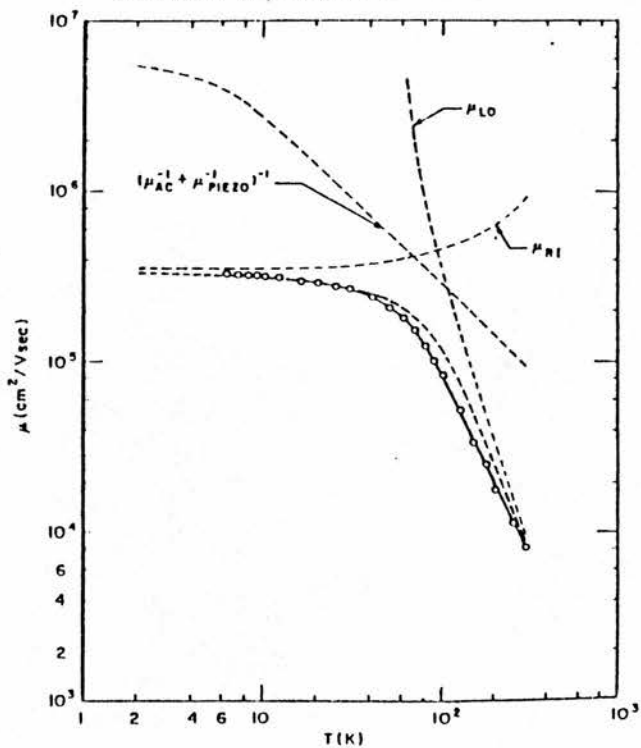
The high mobility structure requires:

1. Absence of scattering centres in the conducting channel,
2. Smooth interfaces,
3. Low trap densities in the confinement regions,
4. Adequate separation of dopant atoms from the conduction channels and
5. Si, Be chosen dopants since they are incorporated readily and diffuse slowly.

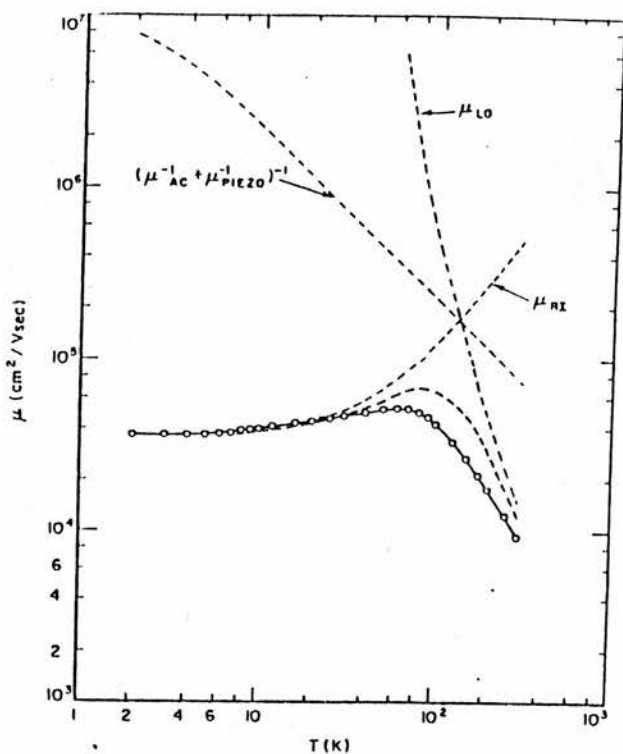
3.2 Transport measurement in GaAs-GaAlAs system

Initially most research work was concentrated in obtaining the highest 2DEG mobility. To this effect a number of theoretical and experimental studies were carried out, most notably by Dingle et al (1978). Since then there have been many reports on the transport of the 2DEG in heterostructures. Most of the earlier work dealt with a specific scattering mechanism in a certain temperature range. More recently, Lee et al (1983) calculated the temperature dependence of the mobility over the temperature range $4.2 < T < 400$ K and achieved good agreement with their experimental data. However, their analysis explained only the lack of temperature dependence at low temperatures, seen in the earlier experiments. It cannot explain the different temperature dependence observed in the more recent experiments (Lin et al, 1984). Their approach is sufficient for device modelling but is satisfactory for the purpose of a fundamental understanding of the physical mechanisms.

The 2DEG confined in GaAs at 4.2 K exhibit electron mobilities of about $2 \times 10^6 \text{ cm}^2/\text{Vs}$ when larger spacer widths ($>350 \text{ \AA}$) are used. The introduction of $1 \times 10^{15} \text{ cm}^{-3}$ background ionized impurities significantly alters this dependence, resulting in a peak mobility at $d \approx 160 \text{ \AA}$ (Walukiewicz et al, 1984). The temperature dependence of the electron mobility has also been studied by Walukiewicz et al (1984) and their theoretical predictions are shown in Fig 3.6. The light dashed lines labelled by μ_{RI} , μ_{LO} , $(\mu_{\text{ac}}^{-1} + \mu_{\text{piezo}}^{-1})^{-1}$ are the calculated mobilities for remote ionized impurity scattering, LO phonon scattering, and acoustic phonon scattering via deformation potential and piezoelectric couplings, respectively. The heavy dashed line is the combined mobility. For $T < 40$ K, there is a decrease of mobility



(a)



(b)

Fig. 3.6 Temperature dependence of 2DEG mobility in a samples (a) High mobility and (b) Low mobility (Lin et al 1984).

with increasing temperature in high mobility samples and an increase in mobility with increasing temperature in low mobility samples. At low temperature the ionized impurities in the $\text{Al}_x\text{Ga}_{1-x}\text{As}$ layer dominate the scattering process of the 2DEG. The most effective scattering centres are the ionized impurities in the depletion region next to the undoped Al_xGaAs (spacer layer) as discussed in section 2.3.1.

The 2DEG density may be continuously varied in a MDH by external means, for example, illumination or temperature; the corresponding mobility changes are very pronounced, and are of practical and fundamental importance. In Fig 3.7 the calculated values of mobilities for individual scattering processes are given as functions of n_s (Walukiewicz et al, 1984). There are two reasons why these processes exhibits n_s dependences: first, direct dependence on the k-vector, and second, dependence on the parameter b_0 in $(\text{cm})^{-1}$. For example, acoustic deformation-potential scattering mobility decreases with n_s solely due to the dependence of b on n . Alloy-disorder scattering exhibits the strongest n_s dependence, which originates from the enhanced penetration of the 2DEG into the alloy with increasing n (Ando, 1982). The alloy-disorder limited mobility values in Fig 3.7 are more than one order of magnitude greater than mobility calculated by Ando (1982), for the same MDH and using the same alloy-disorder potential. The reason for such a large discrepancy is not known at present; however; it cannot be attributed to the approximate description of the penetration of the electron gas into the $\text{Ga}_{1-x}\text{Al}_x\text{As}$.

The increase of the experimental mobility seen in Fig 3.7 with increasing n may be attributed to the presence of background and remote ionized impurities. The mobility due to these scattering mechanisms increases strongly with n_s . Accordingly, as seen in Fig

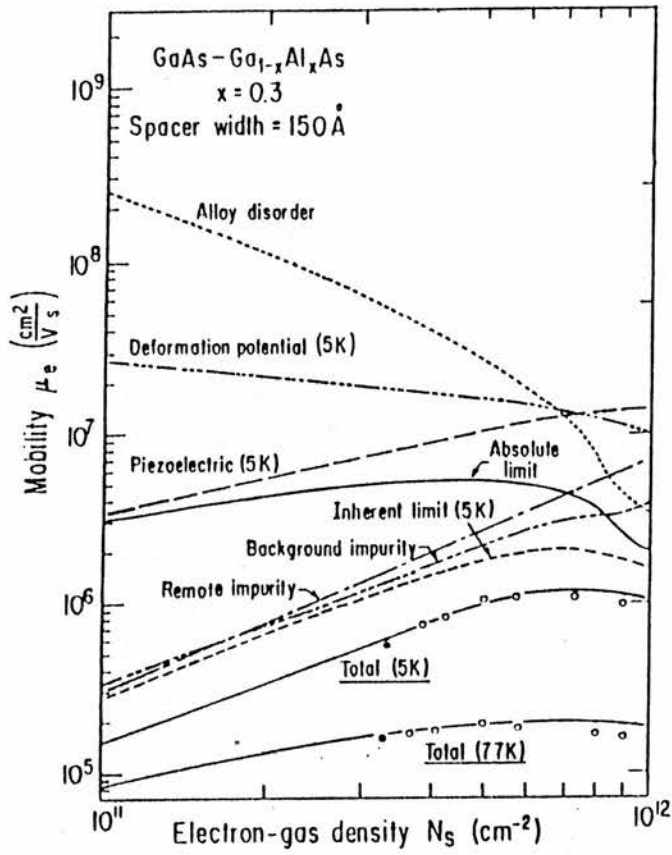


Fig. 3.7 Electron mobility at 5 and 77 K versus interface carrier density (Walukiewicz et al 1984).

3.7, for the MDH with the spacer width $d = 150 \text{ \AA}$, the ionized-impurity electron mobility can be expressed in the form $\mu \propto n_s^\gamma$ with $\gamma = 1.4$ and 1.2 for remote and background impurity scattering, respectively. At higher n_s (values $> 7 \times 10^{11} \text{ cm}^{-2}$), effects of intersubband scattering are important. They result in a lowering of the electron mobility compared with simple intrasubband scattering. The most pronounced drop in the electron mobility is obtained via alloy-disorder scattering: this may be attributed to the large overlap of those parts of the electron wavefunctions for ground (0) and (1) states, which describe the penetration of the 2DEG into the $\text{Ga}_{1-x}\text{Al}_x\text{As}$.

3.3 Transport measurements in GaInAs-InP system

In the case of MDH based on InGaAs lattice matched on to InP the 2DEG is confined within the ternary compound $\text{In}_{1-x}\text{Ga}_x\text{As}$. At room temperature electron mobilities as high as 12,000 cm^2/Vs have been reported by Zhu et al (1985) (see Fig 3.8) and peak electron drift velocity higher than in GaAs-GaAlAs (Walukiewicz et al, 1984). These features make InGaAs especially attractive for high-speed devices. Furthermore its band gap is wide enough for device application at room temperature.

The reports on 2DEG transport in InGaAs/InP heterostructures grown by MOCVD have come mostly from the group at Thomson-CSF (Portal et al, 1983). They used a low-pressure MOCVD system with liquid triethylindium (TEL) as the indium source to get sharp heterointerfaces and to avoid adduct formation. Their highest 77K mobility is 60,000 cm^2/Vs and reported highest 4.2K mobility is 51,000 cm^2/Vs . Other groups are working for high-mobility InGaAs/InP structure grown by VPE. For example Takikawa et al (1983) obtained 2DEG mobilities of 9,400, 71,200 and 106,000 cm^2/Vs at 300, 77 and 4.2K respectively, by chloride transport VPE. SdH experiments are usually performed to determine independently the sheet density and to confirm the 2D nature of the electron gas at the heterointerface. The measured densities are typically in the region of $3.2 \times 10^{11} \text{cm}^{-2}$ (Zhu et al, 1985) to 6×10^{11} (Razeghi et al, 1986). In the latter case three subbands were populated and well defined quantum Hall plateaus were observed with $i = 3$ to 8.

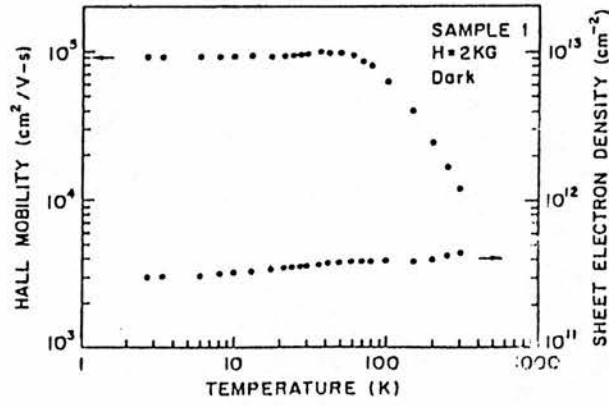


Fig 3.8 Temperature dependence of the electron mobility and sheet-electron density of $In_{0.35}Ga_{0.65}As - InP$ double heterostructure. (Zhu et al 1985).

3.4 Parallel Conduction and Persistent Photoconductivity

3.4.1 Parallel Conduction in GaAs-GaAlAs

Parallel conduction (PC) occurs when the doped region in AlGaAs, InP or AlInAs are not totally depleted. Schubert et al (1984) have noticed the effect of parallel conduction in the $\text{Al}_x\text{Ga}_{1-x}\text{As}$ and shown that this affects adversely the performance of the HEMT. They also noticed that the presence of parallel conduction in $\text{Al}_x\text{Ga}_{1-x}\text{As}$ led to a strong magneto-resistance and to a magnetic field dependent Hall coefficient. Luryi and Kastalsky (1984) have recently found a similar magneto-resistance dependence in a GaAs/ $\text{Al}_x\text{Ga}_{1-x}\text{As}$ heterojunction after illumination at low temperature (4.2K) which they attributed to the creation of a persistent parallel conduction path in the $\text{Al}_x\text{Ga}_{1-x}\text{As}$.

The study of electrical properties of GaAs/ $\text{Al}_x\text{Ga}_{1-x}\text{As}$ heterojunction indicates that parallel conduction paths exist in 2DEG structures at the GaAs/AlGaAs interface and in the undepleted $\text{Al}_x\text{Ga}_{1-x}\text{As}$ doped layer. When the 2D carrier concentration is changed by illumination at 4.2K for a short time, n_s increases possibly due to persistent ionization of the deep impurity state in GaAlAs or to DX centres in the GaAlAs (see section 3.4.2). The PC state at 4.2K results in an artificially high carrier density and low mobility in simple low field measurements (Kane et al, 1986).

By using hydrostatic pressure Beerens et al (1986) have been able to reduce the parallel conduction to negligible values in GaAs-GaAlAs heterostructure as discussed in section 3.2.4.

Because a 2DEG device is a structure inside which a multilayer conduction process is often present, the magneto-transport measurements have to be carefully interpreted (Keever et al 1982, Lee et al 1984,

Look et al 1985). Schubert et al (1984) have shown that the presence of parallel conduction in the bulk layers affects the transport properties of a heterojunction. In a recent paper Kane et al (1985) gives the basis of a high magnetic field method that can be used to analyse transport measurement data. However, it cannot be used in full at high temperatures.

The solution of the Hall problem for two parallel conductive layers leads to two interesting magnetic field regimes (Gregoris et al, 1987). The low magnetic field regime is characterised by $\omega_s \tau_s \ll 1$ and $\omega_b \tau_b \ll 1$:

$$n_H = \frac{1}{eR_H} = \frac{(n_s \nu_s + n_b \nu_b)^2}{(n_s \nu_s^2 + n_b \nu_b^2)} \dots\dots\dots 3.3$$

$$\nu_H = \frac{n_s \nu_s^2 + n_b \nu_b^2}{n_s \nu_s + n_b \nu_b} \dots\dots\dots 3.4$$

The Hall concentration n_H and mobility ν_H are complex functions of the concentrations n_i and mobilities ν_i of the two layers. The indexes s and b refer to 2DEG and the bulk layers, respectively. ω is the cyclotron frequency eB/m^* and τ is the relaxation time. Note that these equations are formally identical to the case of a two band conduction process. The high magnetic field regime is characterised by $\omega_s \tau_s \gg 1$ and $\omega_b \tau_b \gg 1$:

$$n_H^h = \frac{1}{eR_H^h} = n_s + n_b = n_{total} \dots\dots\dots 3.5$$

$$\nu_H^h = \frac{n_s + n_b}{\frac{n_s}{\nu_s} + \frac{n_b}{\nu_b}} \dots\dots\dots 3.6$$

The high field Hall concentration measurement provides, in principle, a way to obtain directly the total electron concentration of the structure. In practice, this can be circumvented by deducing n_s from

the periodicity of the SdH oscillators at low temperature, assuming n_s to be temperature independent. If we define a high field mobility by:

$$\nu^* = R_H^h / \rho_o \dots\dots\dots 3.7$$

it can easily be shown that ν^* is in fact a weighted sum of each layer mobility

$$\nu^* = \frac{n_s \nu_s + n_b \nu_b}{n_s + n_b} \dots\dots\dots 3.8$$

and therefore the high field measurements can be used to get an estimate of how much the conduction is dominated by one of the layers.

McKinnon and Hurd (1986) have reported calculations of the electrical properties of the heterostructure in $Al_x Ga_{1-x} As$ and 2D interface layers under illumination, accounting for the conduction in these layers. Complications arose from this parallel conduction because at low temperatures the mobility in the interface layer may be $10^5 - 10^6 \text{ cm}^2/Vs$ so that even in a modest field (say 5 K Gauss) the electrons at the interface approach the high-field state ($\nu_B > 1$) while those in the parallel $Al_x Ga_{1-x} As$ layer remain in the low-field one ($\nu_B < 1$). Furthermore, the high field state at the interface is destroyed by a sufficient increase in temperature or decrease in the applied magnetic field. The dynamics of the electrons in the interface layer can thus depend strongly on the experimental conditions, and this dependence must be convoluted with that of the electrons in the parallel $Al_x Ga_{1-x} As$ layer to give expressions for the electrical properties of the heterostructure.

Consider the subscripts 1, 2 refer to the interface and $Al_x Ga_{1-x} As$ layers, respectively. The sheet-carrier density in the interface is n_1 , the volume density in the $Al_x Ga_{1-x} As$ layer (of

thickness t) is n_2 . The sheet resistivity matrix of the combination in a magnetic field B is then given by:

$$\rho_{\text{total}} = \begin{vmatrix} (D_1+D_2)(A_1+A_2) \\ -(A_1+A_2)(D_1+D_2) \end{vmatrix} \times \frac{1}{(D_1+D_2)^2+(A_1+A_2)^2} \dots\dots\dots 3.9$$

where

$$D_1 = \frac{n_1 \nu_1 e}{1+(\nu_1 B)^2} \quad \text{and} \quad D_2 = \frac{n_2 \nu_2 e}{1+(\nu_2 B)^2}$$

$$A_1 = D_1 \nu_1 B \quad \text{and} \quad A_2 = D_2 \nu_2 B$$

Following McKinnon and Hurd, if n_m is the effective carrier density derived from the Hall resistivity ρ_H of the heterostructure (ρ_H is the off-diagonal element of ρ_{total} in a field B) then using $n_m = B/\rho_H e$ from equation 3.7:

$$n_m = \frac{B}{e} \left(\frac{(D_1+D_2)^2+(A_1+A_2)^2}{A_1+A_2} \right) \dots\dots\dots 3.10$$

If ν_m is the effective Hall mobility that would be obtained for a pair of conductors then, since $\sigma_m = \sigma_1 + \sigma_2$, we have:

$$\nu_m = (n_1 \nu_1 + n_2 \nu_2 t)/n_m, \dots\dots\dots 3.11$$

where $(n_1 \nu_1 + n_2 \nu_2 t)$ is obtained by measuring the diagonal element of ρ_{total} in zero magnetic field.

To calculate n_m and ν_m for a simulated heterostructure under a given illumination condition and at a given temperature T , first derive $n_1(T) = n_{\text{so}}$ where n_{so} the sheet-carrier density at the interface and $n_2(T) = n_{\bar{c}}$ where $n_{\bar{c}}$ is the volume density in the $\text{Al}_x\text{Ga}_{1-x}\text{As}$ layer of the thickness t (see McKinnon and Hurd, 1987) but $\nu_1(T)$ and $\nu_2(T)$, are also required. As a rough approximation $\nu_2(T)$ can be set as a constant

because in the range 4-300 K it varies by a factor ~ 2 whereas $\nu_1(T)$ varies by $\sim 10^3$. $\nu_1(T)$ can be obtained from the calculation of Lee et al (1983) discussed in section 2.3

3.4.2 Persistent Photoconductivity in GaAs-GaAlAs

Persistent photoconductivity (PPC) in III-V 2DEG heterojunction samples is a complicated phenomena involving photoexcitation and recombination properties of s-like deep donors and defects in a bulk semiconductor, electron-tunnelling through a heterojunction barrier, thermal excitation over such a barrier and properties of the 2DEG at the heterointerface (Nathan, 1986). The 2D carrier concentration can be changed by illumination at 4.2 K: n increases because of persistent ionization of the deep impurity state in GaAlAs which may involve DX centres, since the transfer times to and from the X-associated levels can become extremely long at low temperature due to a barrier associated with lattice relaxation effects and metastable occupancy. A sketch of the direct gap GaAlAs is shown in Figure 3.9 showing the relevant shallow and deep donors.

It has been shown that for a sample kept in different excitation states (dark, illuminated, PPC) at different temperatures (Gennser et al, 1987) the decay of the photoconductivity, after switching off the light, is found to be strongly temperature dependent, i.e., between 70 and 160 K it shows a double character consisting of a temperature independent, fast decay ($\tau \sim 1\text{sec}$), due to direct bulk recombination of ionized deep donors, and temperature independent, slow decay with time constant ranging from months (at 70 K) to seconds (at 150 K) due to thermal excitation of electron from the 2DEG over the heterojunction barrier into the AlGaAs layer. These PPC-decay results support the conclusions drawn from the magnetic field dependence of the Hall coefficient concerning the PPC conduction mechanisms in GaAs/AlGaAs 2DEG heterostructures (Gennser et al, 1987). Their experiments used Van der Pauw structures and a standard Hall configuration with the magnetic

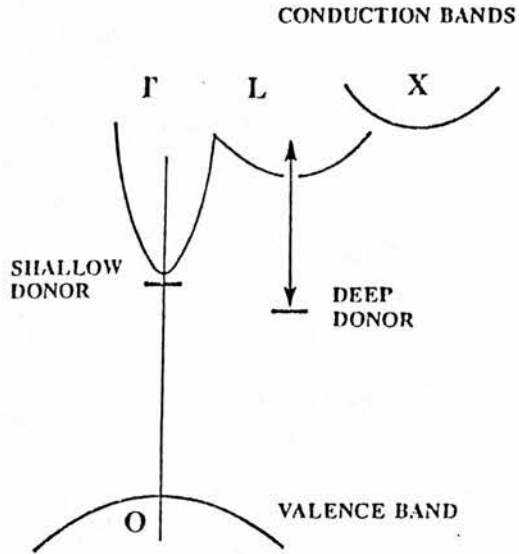
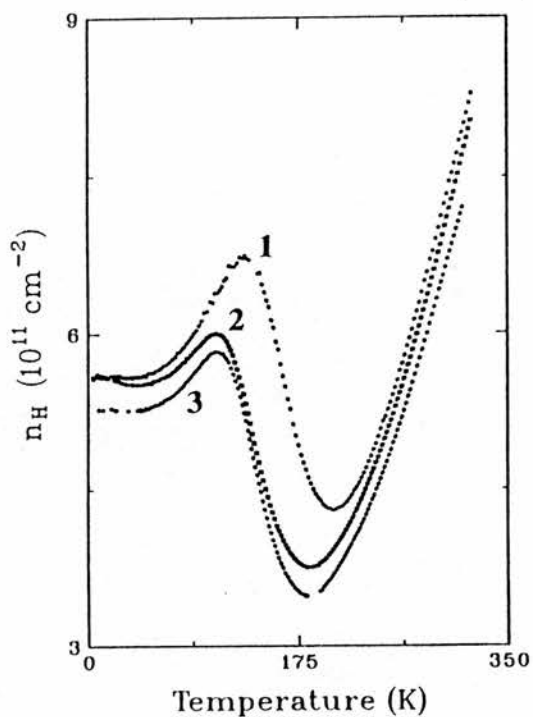


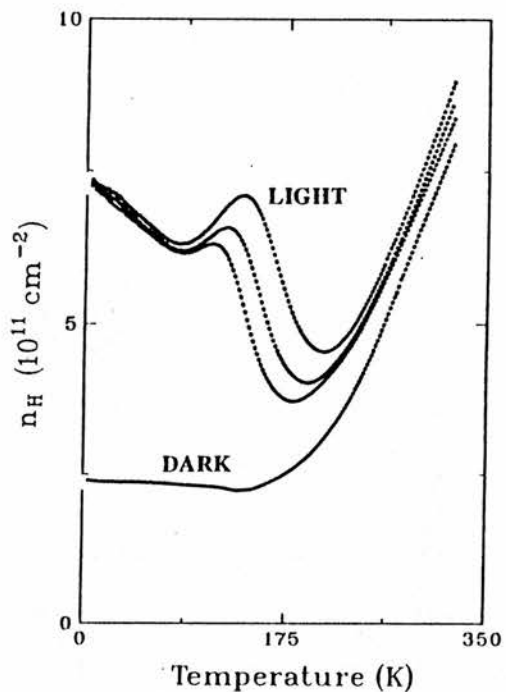
Fig. 3.9 Sketch of the band structure of direct-gap AlGaAs alloy according to Sexena, showing the relevant shallow and deep donors which are expected to be associated with the persistent photoconductivity.

field pointing perpendicular to the layers of the sample. At 17 K the photogenerated increase in conductivity was fully persistent for periods of months or longer while at 88 K the PPC decayed within a few days and at 188 K no PPC was observed. The dependence of the carrier density under different illumination conditions is shown in Figure 3.10.

The energy-band diagrams of Figure 3.11 illustrate three possible physical origins for persistent photoconductivity in GaAs/ $\text{Al}_x\text{Ga}_{1-x}\text{As}$ heterojunctions. An important contribution comes from the well-known deep donor or DX centre which is the dominant trap in n-type $\text{Al}_x\text{Ga}_{1-x}\text{As}$. The activation energy of this donor increases rapidly with Al mole fraction x in the range $0.2 \leq x \leq 0.4$, so that cooling this structure to 4.2 K in the dark results in freeze-out and neutralisation of most donors in the undepleted portion of the $\text{Al}_x\text{Ga}_{1-x}\text{As}$ (Figure 3.11a). This causes an undesirable threshold voltage shift in the transistor. More important, exposing the structure to visible or near visible light photoionizes the centres, pulls the $\text{Al}_x\text{Ga}_{1-x}\text{As}$ conduction band edge below the quasi-equilibrium Fermi level, and increases the electron density in the channel (Figure 3.11b). At low temperatures the effect is persistent since capture to the donor level is thermally activated. Lang et al (1979) have explained the microscopic capture barrier presented by the defect by postulating a large lattice relaxation which depends on the charge state. Another mechanism suggested for persistent photoconductivity is transport of photoexcited carriers across macroscopic potential barriers. Figure 3.11c illustrates the process of electron-hole pair separation by the built-in field in the GaAs buffer layer. Kastalsky and Hwang (1984) have proposed that subsequent hole trapping in the GaAs buffer layer can



(a)



(b)

Fig. 3.10 The empirical dependence of Hall carrier density on temperature for (a) Various light intensities and (b) For various samples under different illumination conditions (Hurd et al, 1987).

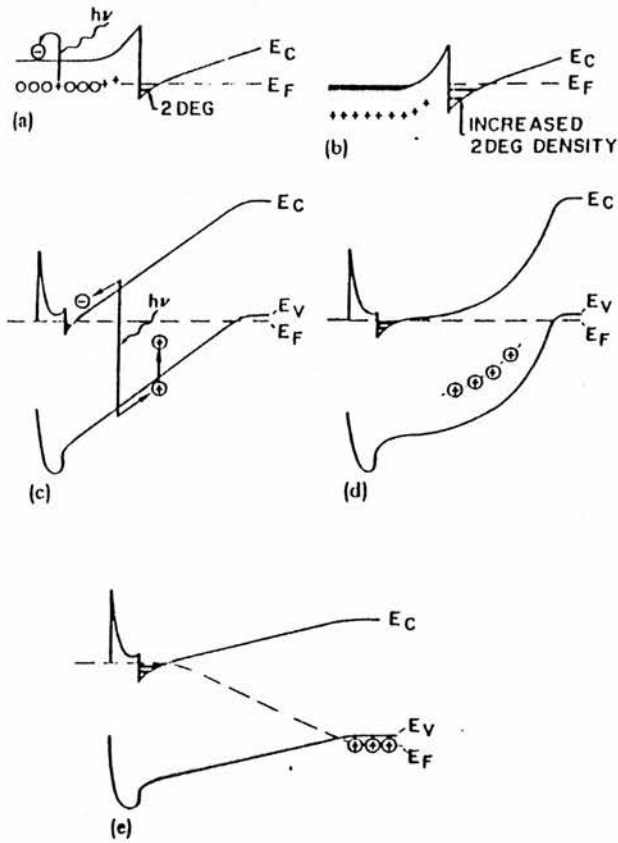


Fig. 3.11 Band diagrams of a modulation-doped GaAs/ $Al_xGa_{1-x}As$ heterojunction illustrating some mechanisms which cause persistent photoconductivity. (a) Photoionization of DX centers. Before illumination the flat-band Fermi level in $n-Al_xGa_{1-x}As$ depends on the depth of the DX center. (b) After illumination all DX centers are ionized and the $Al_xGa_{1-x}As$ conduction band is below the quasi-equilibrium Fermi level. (c) Electron-hole pair separation by the back gate field. After illumination, persistent photoconductivity may result from (d) charge trapping in the buffer layer, or (e) accumulation of charge at the back gate.

(Theis et al 1986.)

bend the bands and alter the channel electron density. These authors have also suggested that electron trapping near the channel and hole trapping in either the GaAs buffer layer or the semi-insulating GaAs substrate may be important. Charge trapping in the substrate can be eliminated by making it conductive. If charge trapping occurs in the buffer layer, the channel electron density will be altered, even if the substrate potential is held constant with respect to the channel (Figure 3.11d). Conversely, if no charge trapping occurs in the buffer layer, but the substrate potential is allowed to float, free holes and electrons will accumulate at the substrate and channel, respectively, until a nearly flat band condition is reached in the buffer layer (Figure 3.11e). This will occur for both conducting and semi-insulating substrates. Subsequent trapping of the accumulated holes is likely in semi-insulating material.

Hurd et al (1987) have been studying the PPC in $\text{Al}_x\text{Ga}_{1-x}\text{As}$ alloys and have associated it with a deep donor level. In the Saxena picture (see Figure 3.9) this deep donor is linked to one of the conduction band minima that lie above the Γ -minima (Saxena, 1982). The PPC arises from electrons that are photoexcited from deep donors and frozen into the conduction band because they have insufficient energy to escape from the Γ -minima and recombine in the donor levels. There are many other approaches to the PPC problem in GaAlAs see, for example, Hjalmasson and Drummond (1986) and Henning and Ansems (1987).

3.4.3 Parallel Conduction in InP/InGaAs

Parallel conduction takes place both in the 2DEG channel and in the InP layer at 4.2 K (Gennser et al 1987). The origin of parallel conduction is a doped region not totally depleted. The presence of parallel conduction led to a strong magneto-resistance and a magnetic field dependent Hall coefficient at 4.2 K in GaAs-GaAlAs quantum wells as discussed in 3.4.1.

The ternary compound $\text{Ga}_{0.47}\text{In}_{0.53}\text{As}$ is a material of rapidly increasing importance for numerous electronic and optoelectronic device applications. The observation of a 2DEG at the interface of $n\text{-Ga}_x\text{In}_{1-x}\text{As}/n^+\text{InP}$ suggests that this material might be an attractive system for the fabrication of 2DEG field-effect transistors operating at room temperature promising an alternative to $\text{GaAs}/\text{Ga}_x\text{Al}_{1-x}\text{As}$. Device performance depends strongly on the presence not only of shallow impurities but also on deep traps in the layer and at interfaces. Reduction of carrier lifetime and occurrence of tunneling processes are two examples of troublesome parasitic effects due to traps (Goetz et al, 1984).

Figure 3.9 shows the presence of parallel conduction in the dark at 4.2 K, while under illumination the parallel conduction channel is eliminated (see Kane et al, 1986). In the fig(3.12) the origin of parallel conduction is shown as incomplete depletion in the InP doped layer. Kane et al (1986) optimised their atmospheric pressure - MOCVD - grown structures by choosing the normal heterostructure configuration, $n^+\text{InP}$ to $1 \times 10^{17} \text{cm}^{-3}$, and spacer layer thickness of around 500 Å. Similarly, in a recent publication Kane et al (1987) reported undoped single (50-200 Å) quantum wells without parallel conduction; the InP barrier and the GaInAs quantum well layers having background impurity

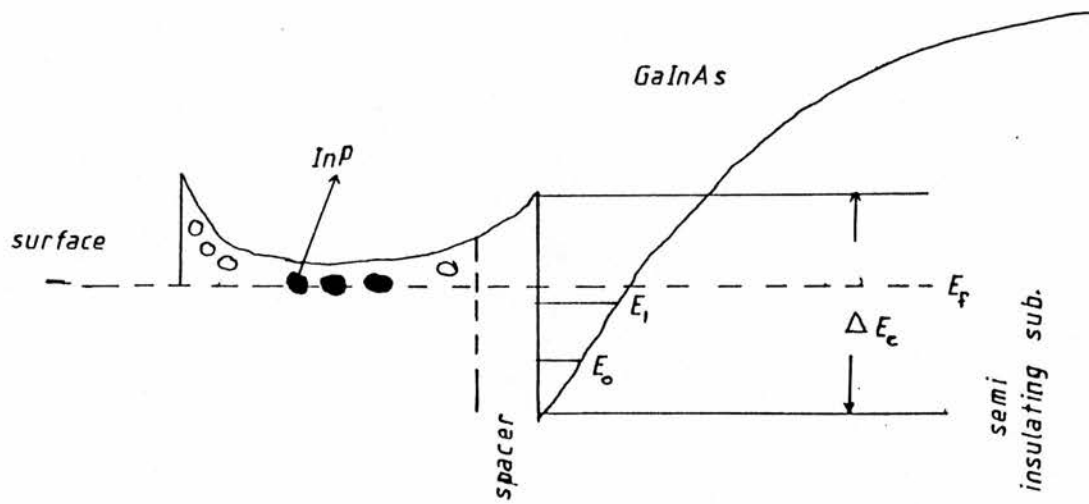


Fig. 3.12 Modulation doped heterostructure InP - InGaAs and the origin of pc.

levels in the low 10^{15} cm^{-3} . Frei et al (1987) reported elimination of parallel conduction in single quantum wells grown by chemical beam epitaxy. They observed PC in thick layer heterostructures where the top layer was 4000 \AA of the InGaAs but eliminated it by growing single quantum wells ($\sim 150 \text{ \AA}$) between thick (1300 and 2000 \AA) InP presumably undoped. They concluded that the origin of PC arose from the n-type GaInAs top layer since the Fermi level of n-GaInAs is not pinned (Brillson et al, 1986) and is strongly affected by the surface conditions.

3.4.4 Persistent Photoconductivity in GaInAs-InP

The persistent photoconductivity effect in InP/InGaAs has been studied by Kane et al (1986, 1987) and Wei et al (1984) among others.

Figure 3.13 shows a plot of (a) n against $1/T$ and (b) μ against T for two InP-InGaAs heterojunctions of Kane et al (1986). Both samples were measured while they were cooled in the dark, one sample showed no variation in carrier density between room temperature and 4.2 K and is an example of a fully optimised structure with no parallel conduction in the InP, while the 2nd sample showed an initial decrease in the carrier density as it was cooled below room temperature before it became temperature independent. Their mobility plots in figure 3.13b exhibited the characteristic temperature independent behaviour. Wei et al (1984) suggested that photoexcited holes were trapped in the InGaAs while the electrons filled up the interface well. To justify the magnitude of the effect they had to invoke a hole trap density in their $1 \mu\text{m}$ thick InGaAs of about $1 \times 10^{15} \text{cm}^{-3}$. Kane et al (1986) found that in InGaAs material this was extremely unlikely and the lack of any persistent effect when a $1.3 \mu\text{m}$ LED was used to illuminate the sample ruled out the possibility of trapping in the InGaAs. Instead they suggested that the photocarriers are excited in the substrate (with photons of 1.42 eV energy) and separated by the field of the heterojunction (see Figure 3.14). The holes are swept into the substrate where trapping is more likely and the redistribution of charge in the system results in a higher 2D electron concentration.

The current picture of PPC in GaInAs-InP is made up by the following observation of Kane et al (1986 and 1987):

- (a) after $1.3 \mu\text{m}$ illumination (ie, across InGaAs band-gap) a "weak" PPC is observed in normal heterostructures. This

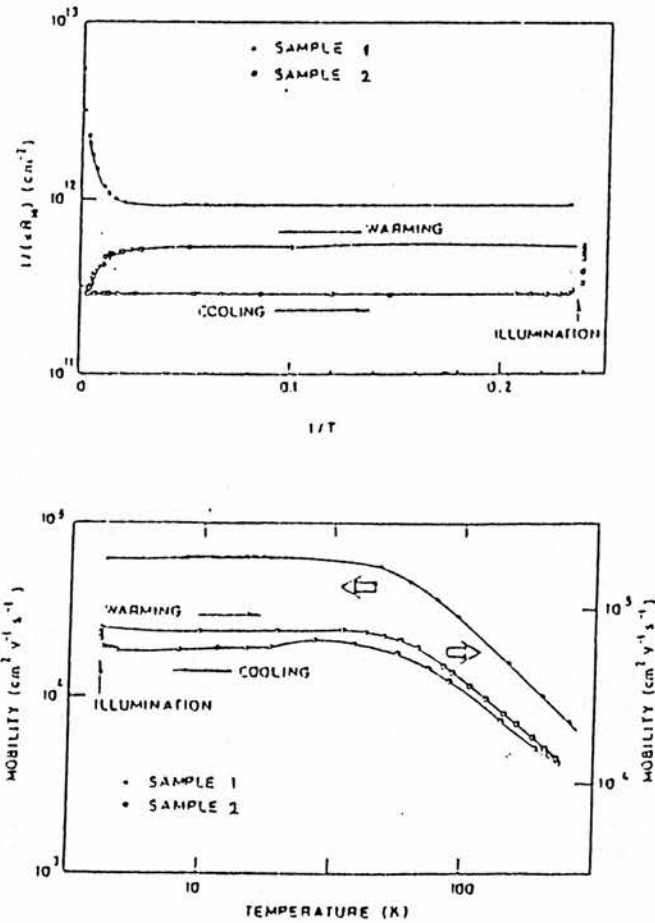


Fig 3.13

(a) $1/eR_H$ vs $1/T$ for typical InP/InGaAs heterojunctions measured on cooling in the dark. Sample 2 is optimised for no parallel conduction, *sample 1 is not*.

(b) μ vs T for the same samples.

The effect of illumination with red LED is shown for *sample 2*.

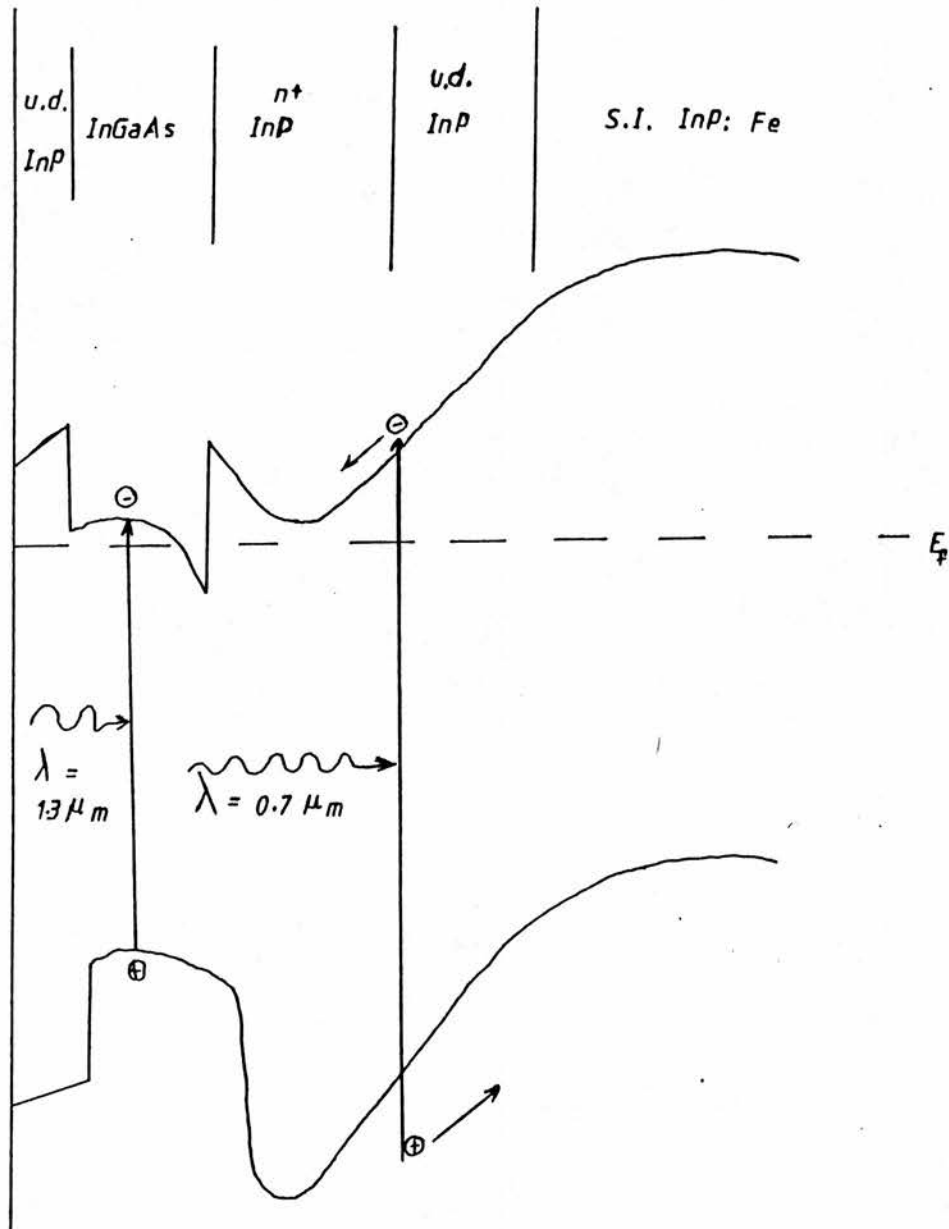


Fig. 3.14 Schematic diagram of band edge profile indicating excitation mechanism for persistent photoconductivity.

may be related to direct excitation of deep levels in the substrate,

- (b) after illumination with light of 0.9 and 0.7 μm a "strong" PPC is observed in normal heterostructures (ie, across the InP gap),
- (c) the photoconductivity persists "indefinitely" below 80 K in heterostructures (MDH),
- (d) in inverted heterostructures the PPC puts electrons in the InP and not in the GaInAs after the InP is depleted: the Hall density increases while the SdH determined density remains unaltered,
- (e) unlike PPC in GaAs/GaAlAs, illumination does not induce strong magneto-resistance (effect associated with the presence of DX centres in the barrier layer of AlGaAs),
- (f) MD single quantum wells behave similar to single heterostructures as far as the strength of the PPC and the onset temperature (150 K) are concerned,
- (g) in undoped single quantum wells the photocreated carrier density relaxes to the dark value at temperatures between 4 and 300 K.

The last two points remain to be clarified as well as the precise origin of the weak PPC observed with 1.3 μm photons.

3.5 Two Dimensional Hole Gas (2DHG) in GaAs-GaAlAs

If instead of shallow donors, the dopant in the higher energy gap layer is an acceptor, the band bending will favour the formation of a potential well at the interface in the valence band. These holes will be trapped and, in an analogy with the 2DEG, will form a 2DHG.

As expected in a 2DHG the effective mass of the carriers will be heavier than the electron mass and as a result they have lower carrier mobilities and smaller Landau-level splittings. Magneto-transport and cyclotron resonance measurements suffered from a small $\omega_c \tau = B \nu$ which made the 2D-hole subband level scheme just about accessible to experiment. This is clearly an unhappy situation since 2D-hole systems have the complex valence band structure of their host material, containing degeneracies and strong anisotropies which are expected to show up as rich structure in spectroscopy experiments. Calculation of the subband structure and Landau level ladder in heterojunctions containing a 2DHG have been carried out by, among others, Fasolino and Altarelli (1984).

In spite of the complexity of 2D-hole subband levels, some general features common to all 2D-hole systems can be deduced from simple symmetry considerations (Störmer et al 1983 and Einstein et al 1984). The most important feature is the lifting of the Kramers degeneracy (Bangert and Landwehr, 1976) of each subband level induced by the absence of inversion symmetry of the roughly triangular potential well. The inversion symmetry plays an important role in solid state physics. It is one of the factors which determines the degeneracies of the energy band away from the high-symmetry points of the Brillouin zone.

In modulation doped samples Störmer et al (1983) performed SdH

and cyclotron-resonance experiments on a 2D hole system based on the GaAs-AlGaAs heterojunction interface. These results showed that the Kramers degeneracy of the lowest two hole subbands is lifted for finite k giving rise to two cyclotron masses. At $k = 0$ both subbands remain degenerate. Their samples had low-temperature mobilities around 40,000 cm^2/Vs and densities around $5 \times 10^{11} \text{ cm}^{-2}$, were Be-doped and grown by MBE.

The band diagram for the (001) interface between a n-GaAs and a p AlGaAs showing a 2DHG is sketched in Figure 2.15 after Ekenberg et al (1983).

The main results on 2DHG can be summarised as follows:

- (a) the valence subband degeneracy leads to two effective hole masses: 0.38 and 0.60 m_0 (Störmer et al, 1983). Comparing them to the light and heavy hole masses of GaAs (0.086 and 0.49 m_0 , respectively) the 2DHG masses have their origin in the bulk heavy hole of GaAs,
- (b) Quantum Hall Effect data in a 2DHG confirmed that this effect is host independent,
- (c) the Fractional Quantum Hall effect was observed (Mendez et al, 1984) in MBE-grown Be-MDH of GaAs-GaAlAs (56% Al) with 4K mobilities of 80,000 cm^2/Vs . Fractional filling factors of $\frac{2}{3}$, $\frac{4}{3}$, $\frac{5}{3}$, $\frac{3}{5}$ and $\frac{2}{5}$ were observed,
- (d) the density of the 2DHG is not altered significantly after illumination at low temperatures in contrast to observations in 2DEG systems of GaAs-GaAlAs.

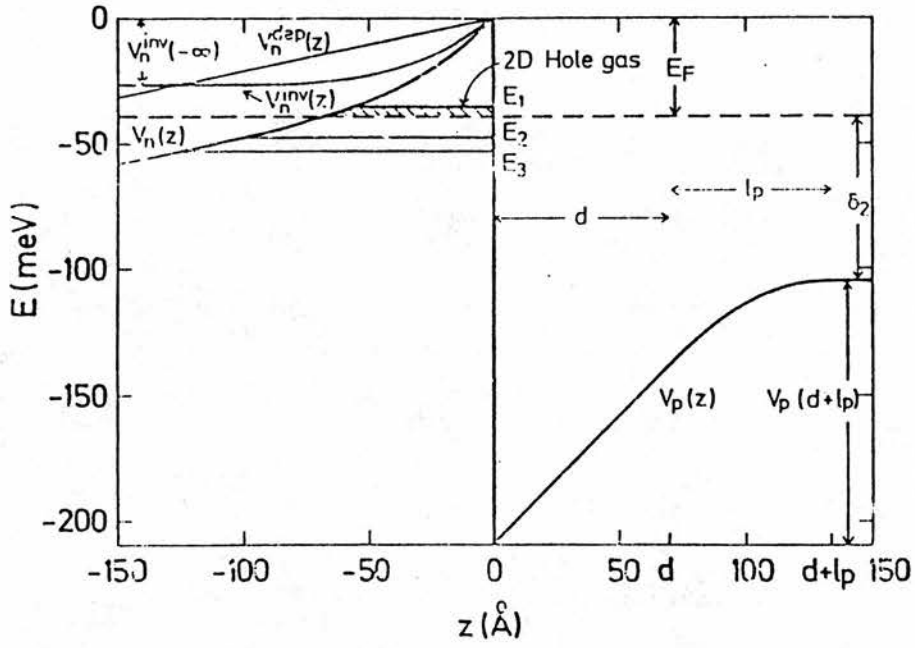


Fig. 3.15 Band diagram for the (001) interface between \bar{n} GaAs and p^+ -Al_{0.5}Ga_{0.5}As (Ekenberg et al 1983).

Recently p-type MDH have been grown by atmospheric pressure MOCVD (Roberts et al, 1987) with Carbon-doping achieving mobilities and carrier densities in the $6000 \text{ cm}^2/\text{Vs}$ and $1.6 \times 10^{12} \text{ cm}^{-2}$, respectively at 2 K. The interest in p-type material is for use in high transconductance p-channel FETs for complementary logic in GaAs.

CHAPTER IV EXPERIMENTAL METHOD

This chapter describes the measurement of mobility and carrier density by the van der Pauw method, Shubnikov-de Haas measurements and the information that can be obtained from them and finally, high pressure techniques.

4.1 Mobility and carrier Density Measurements.

4.1.1 Determination of μ and n_s .

Measurement of μ and n_s can be explained in the light of the work of L J Van der Pauw which provides a method for measuring the specific resistivity and Hall coefficient of flat samples of arbitrary shape, provided that contacts have been made at the circumference and are relatively small. Consider a sample of a regular shape, and homogeneous in thickness as shown in Fig.4.1. Four contacts A, B, C and D are attached to the crystal using alloyed In dots or In:Sn (1:1 ratio).

The only physical dimension required for Hall and resistivity measurement is the sample thickness, d . The Van der Pauw equation determines the value of the resistivity as a function of d , and hence the resistance of the sample.

The value of d is considered unity in 2D. In the equation given below nomenclature $R(ABCD)$ refers to the potential difference $V_C - V_D$ per unit current through the contacts AB.

$$\rho = \pi d (R_{ABCD} + R_{BCAD}) F(Q) / 2 \ln 2 \dots\dots\dots 4.1$$

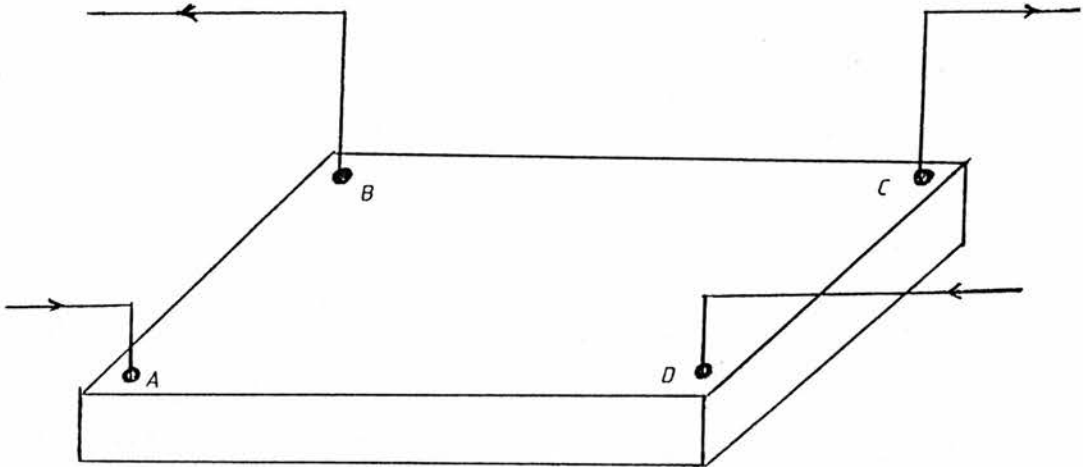


Fig. 4.1 Semiconductor crystal with four dots and copper leads

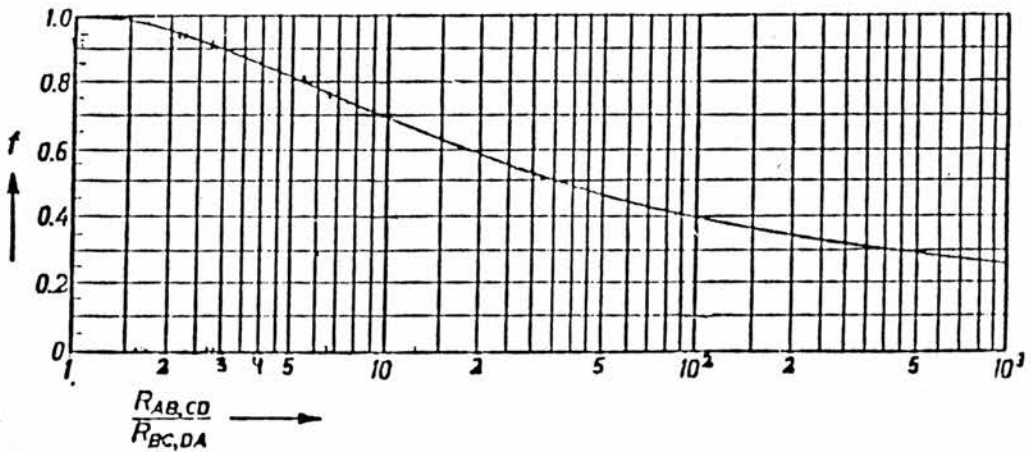


Fig. 4.2 The function f used for determining the specific resistivity of the sample, plotted as a function of $R_{AB,CD}/R_{BC,DA}$.

where Q is the ratio of the two resistances, and $F(Q)$ is a correction factor, the equation and graphical solution of which are shown in Fig.4.2.

The Hall mobility can be determined by measuring the change of the resistance R_{BDAC} when a magnetic field (B) is at 90° to the plane of the crystal.

The Hall mobility is then given by

$$\mu_H = \frac{d}{B} \frac{\Delta R_{BDAC}}{\rho} \dots\dots\dots 4.2$$

where ΔR_{BDAC} is the change of the resistance R_{BDAC} due to the magnetic field. Both electron density and Hall coefficient can be written in the form of

$$n_s = \frac{1}{\rho e \mu_H} \dots\dots\dots 4.3$$

and

$$R_H = \rho \mu_H \dots\dots\dots 4.4$$

where e is the electronic charge.

4.1.2 Preparation, contacting and mounting of sample.

The crystals were cut using a diamond pen in the form of a square or rectangular shape. The approximate dimensions of width and length are around 5mm x 5mm or 4mm x 3mm. Once cut, each crystal was inspected to determine the state of the top surface. All samples were cleaned carefully to remove the top layers of contaminated material. The GaInAs-InP crystals were treated for about thirty seconds in a solution of 5% bromine in methanol. This procedure provided a clean crystal surface, on to which indium dot contacts could be alloyed.

To contact the crystal each surface layer was treated in the following way: (a) clean the surface with toluene to remove wax etc;

(b) repeat with methanol; (c) finally clean the crystal with propanol since methanol inhibits indium adhesion. At this point indium dots were placed on each corner of the sample and then placed on a heater in an atmosphere of 5% H in N . The gas was (regularly) passed through HCl for a short time to help prevent oxides forming at the contact points. The sample was then heated to 160 C for one minute to allow the indium to melt, and then to 350°C to enable it to alloy the crystal surface. Copper wires were then soldered onto the indium to enable the structure as a whole to be mounted on to a probe for measurements of resistivity, mobility, electron density and Hall coefficient. No difficulties were encountered when making contact on to the sample. (See Fig.4.3). The crystal was mounted on probe A and the leads and temperature control wires were connected via a multiconnector type socket at the top of the probe.

The sample was mounted on a probe that was later housed in a Dewar flask to enable low temperatures to be reached.

4.1.3 Experimental Apparatus

Measurements at room temperature, 77K (boiling point of liquid nitrogen) and 4.2K (boiling point of liquid helium) were easily obtained. Measurements between 4.2K and 1.3K were made by pumping on the liquid helium and controlling the vapour pressure of the He gas. For temperatures between 4.2K and 77K and between 77K and room temperature the double can system shown in Fig.4.3 was used. The inner can contained exchange gas at all times to ensure a uniform temperature. To isolate the inner can from the main bath the outer can was pumped to a vacuum of 10^{-4} torr by diffusion pump and backing pump. The temperature of the inner can could then be raised by passing a current through the heater wound on the inner can.

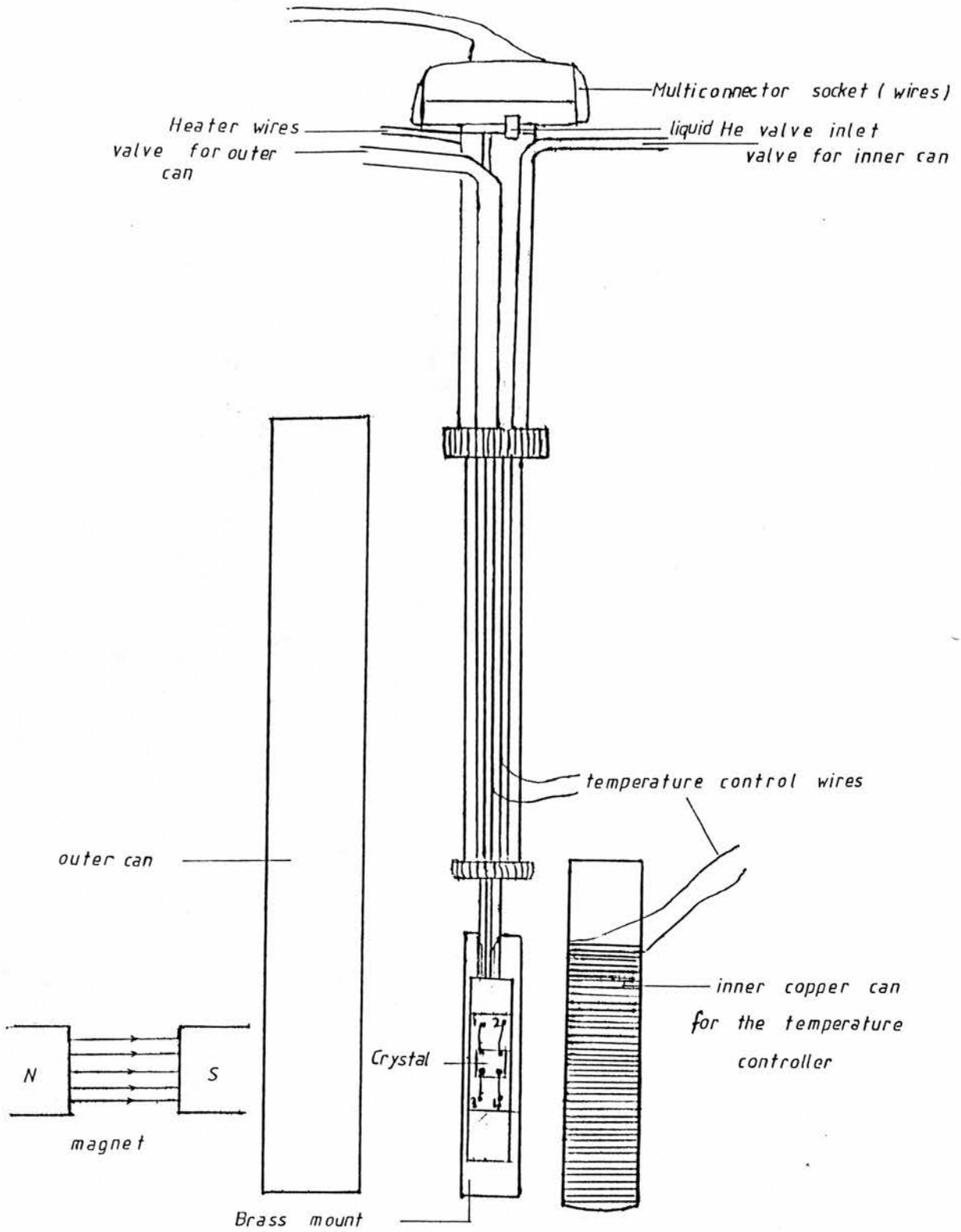


Fig. 4.3 V.d.P. insert used to measure ρ , μ^A and n at different temperature (290~1.3)K.

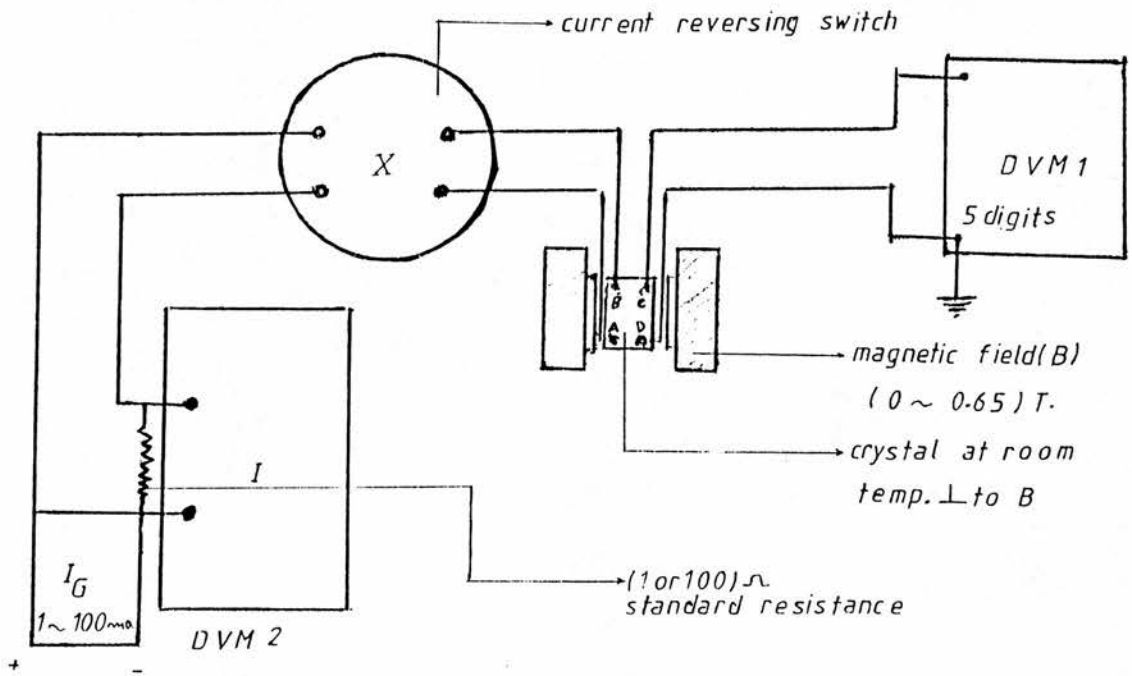


Fig. 4.4 Circuit diagram and apparatus used for Hall effect, resistivity, mobility, measurements at different temperatures by Van der pauw method.

The temperature was measured by a GaAs diode thermometer the voltage from which activated an automatic temperature controller. A constant current of 0.1-10 mA was supplied by a constant current source. Fig.4.4 shows the circuit diagram for the Hall effect, μ and n .

The current was monitored by a Bradley digital multimeter and the potential drop across the crystal with a $5\frac{1}{2}$ Keithley digital voltmeter. Since the current used was usually 1mA, and the DVM was read in mV, the voltmeter gave a direct reading of resistance across the crystal. In this way, resistances R_{ABCD} , R_{BCDA} , and R_{ACBD} were easily measured and from equation 4.1.1 the resistivity could be calculated directly.

The magnetic field applied to the sample was 0.65T from a Mullard electromagnet.

4.2 Shubnikov de Haas measurements:

The Shubnikov de Haas (SdH) effect arises from the movement of sharp maxima in the density of states through the Fermi energy as a changing magnetic field alters the Landau level spacing.

This requires a highly degenerate electron gas and so the SdH effect is found only at very low temperature with an amplitude that declines monotonically upon warming.

The variable $\Delta\rho/\rho_0$ may be used to map the Fermi surface, which is explained theoretically in section 2.13(ii).

In k-space we have:

$$\hbar \underline{k} = e(\underline{V} \times \underline{B}) \dots\dots\dots 4.5$$

If k is the radius of an orbit then $\underline{k} = (\underline{r} \times \underline{B})e/h$ after integration of the above equation. It follows that the area of an orbit in k-space is

$$A(E_f) = \pi k^2 = 2\pi(n + \frac{1}{2})Be/\hbar \dots\dots\dots 4.6$$

The orbit in k-space differs in size by $2 Be/\hbar$ to that in real space. As B is increased the orbits expand in radius and pass through the Fermi surface. Electrons empty into the lower levels and produce an oscillatory density of states at the Fermi surface. This in turn affects properties that are directly related to it (such as resistivity). The conditions for Landau levels to pass through the Fermi surface on successive occasions are:

$$(n + \frac{1}{2}) = \hbar/2\pi B_1 e A(E_f) \dots\dots\dots 4.7$$

and $(n + 1 + \frac{1}{2}) = \hbar/2\pi B_2 e A(E_f) \dots\dots\dots 4.8$

Hence $\Delta(1/B) = 2\pi e/\hbar A(E_f) \dots\dots\dots 4.9$

Consequently, measurements of the period $\Delta(1/B)$ can reveal the cross sectional area of the Fermi surface that is normal to the magnetic field.

By varying the crystallographic orientation it is possible to map the Fermi surface. Furthermore, it is also possible to measure the carrier concentration n. Assuming a spherical conduction band, we have

$$n_s = \frac{e}{\pi\hbar (\Delta 1/B)} \dots\dots\dots 4.10$$

The advantage of this method over that of the Hall effect is that there is no need for a knowledge of the sample thickness.

The two-dimensionality of the electronic system is best demonstrated by the angular dependence of the magnetoresistance.

4.2.1 Test of two Dimensionality of carriers

In two dimensional electronic systems the electrons confined at an interface or in the layer of the quantum well are forced to perform orbited motion in the (x-y) plane of the interface, when the magnetic field is perpendicular to it (z-axis). If the magnetic field is tilted the field that affects the cyclotron motion is the component along the perpendicular z-axis. Thus the magnitude of the magnetic field at which a particular Landau level appeared (crossed the Fermi surface) for an angle between the interface (x-y) plane and the magnetic field, will (see Fig.4.5) increase with the consequent shift of the oscillatory structure in the magnetoresistance to higher fields as

$$B_{\text{tilted}} = \frac{B_{\perp} \text{ layer}}{\sin \theta} \dots\dots\dots 4.11$$

Consequently, the displacement of Shubnikov-de Haas oscillations to higher field as 1/sin θ as the magnetic field is tilted from the perpendicular to the parallel position with respect to the semiconductor interface, is a 2D finger print.

4.2.2 Experimental Apparatus

The power supply and 12.7T superconducting magnet were built by Oxford Instruments. A Keithley 191 DVM gave a reading proportional to the field directly from the control sweep unit.

Fig.4.6 illustrates the two types of insert used in SdH measurements (a) For 90°, i.e. B ⊥ E, fitted with an optical fibre. (b) For different angles in the range of 0° to 90°. The insert for different angles has a gear connected via a spindle to a Vernier scale at the top of the insert that enabled the crystal to be rotated at

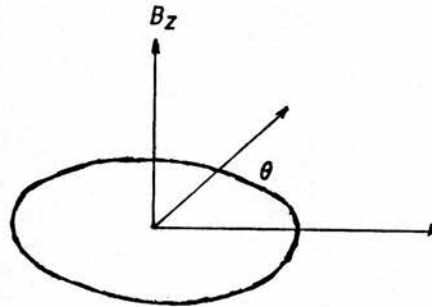
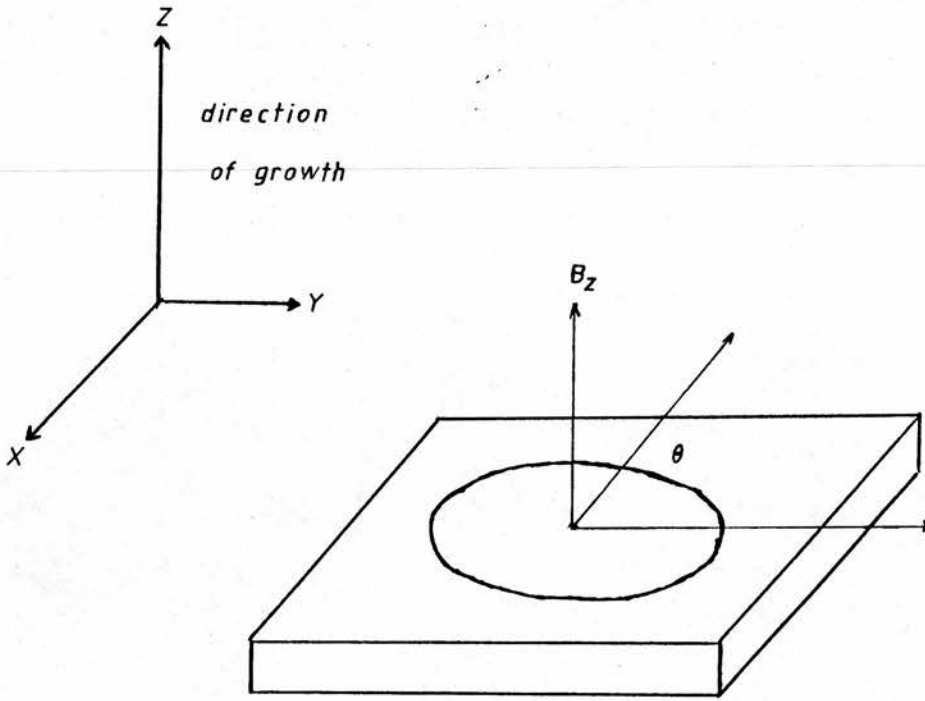


Fig. 45 The magnetic field needed to cross the Fermi energy for a given Landau level under tilted field conditions is $\frac{B_{\perp}}{\sin\theta}$.

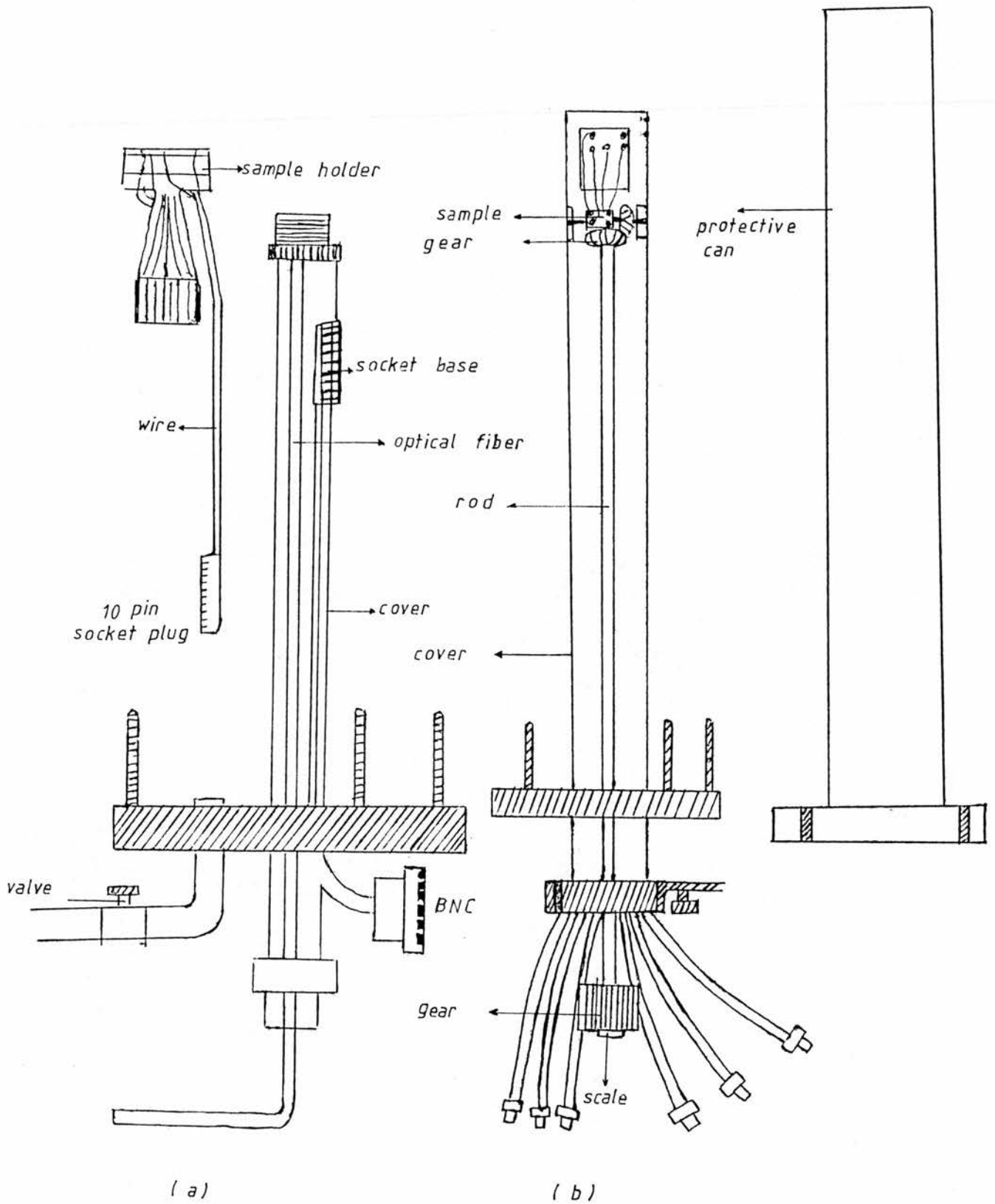


Fig. 4.6 Two types of inserts used in SdH measurements.
 (a) 90° angle with optical fiber and sample holder.
 (b) Different Angles with gear and vernier scale,

will. By this method the precise position of the crystal with respect to the magnetic field was known.

Once mounted, the insert was encased in a protective tube that was designed to provide a gas tight environment for the crystal. By means of a valve at the insert top, the air inside the casing was removed and replaced with He exchange gas.

The casing was lowered into the cryostat sufficiently slowly to allow the temperature of the crystal to change gradually until thermal equilibrium was obtained.

BNC connectors and coaxial cables were connected to the required terminals in order to measure contact resistance and to ensure that the crystal had not shattered. All the measurements were made with the samples cooled (a) in the dark and (b) under illumination using an optical fibre.

Measurements have to be conducted in high magnetic fields and at low temperatures in order to satisfy the conditions

$$\begin{aligned} \omega_c \tau &> 1 \\ \hbar\omega_c &> kT \\ E_f &> kT \dots\dots\dots 4.12 \end{aligned}$$

where τ is the mean relaxation time.

The circuit diagram and apparatus used for the SdH effect is shown in Fig 4.7. The magnetic field B was swept from 0 to 12T.

The Vernier scale on the head of the insert is calibrated as shown in Fig 4.8, as a function of the angle between the field direction and the sample surface, where each 1.8° represents 1 division on the insert dial. Circuit diagrams for the current source and differentiator are shown in Fig 4.9 and Fig 4.10, respectively.

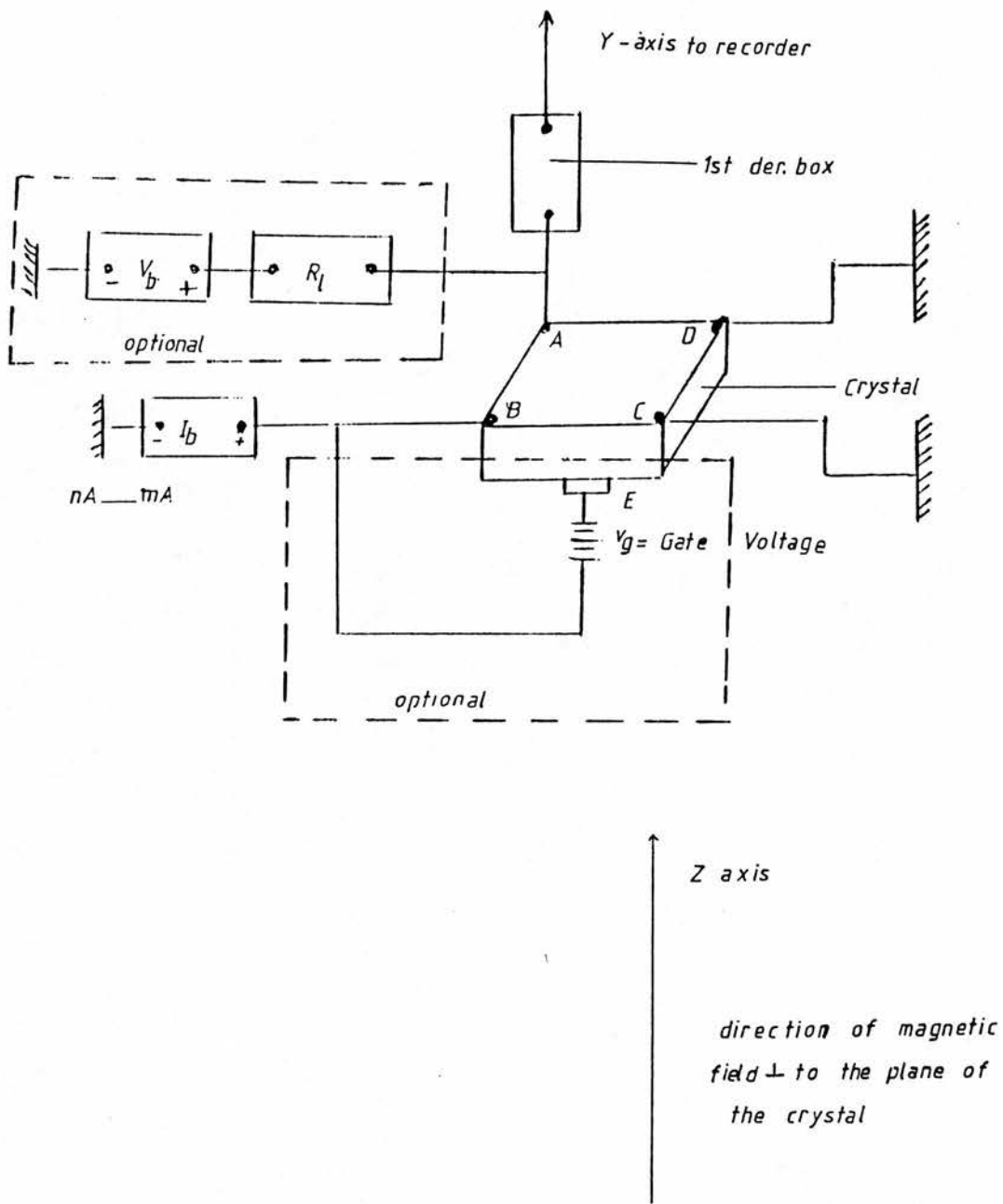


Fig 4.7 Circuit diagram used for S.d.H. method

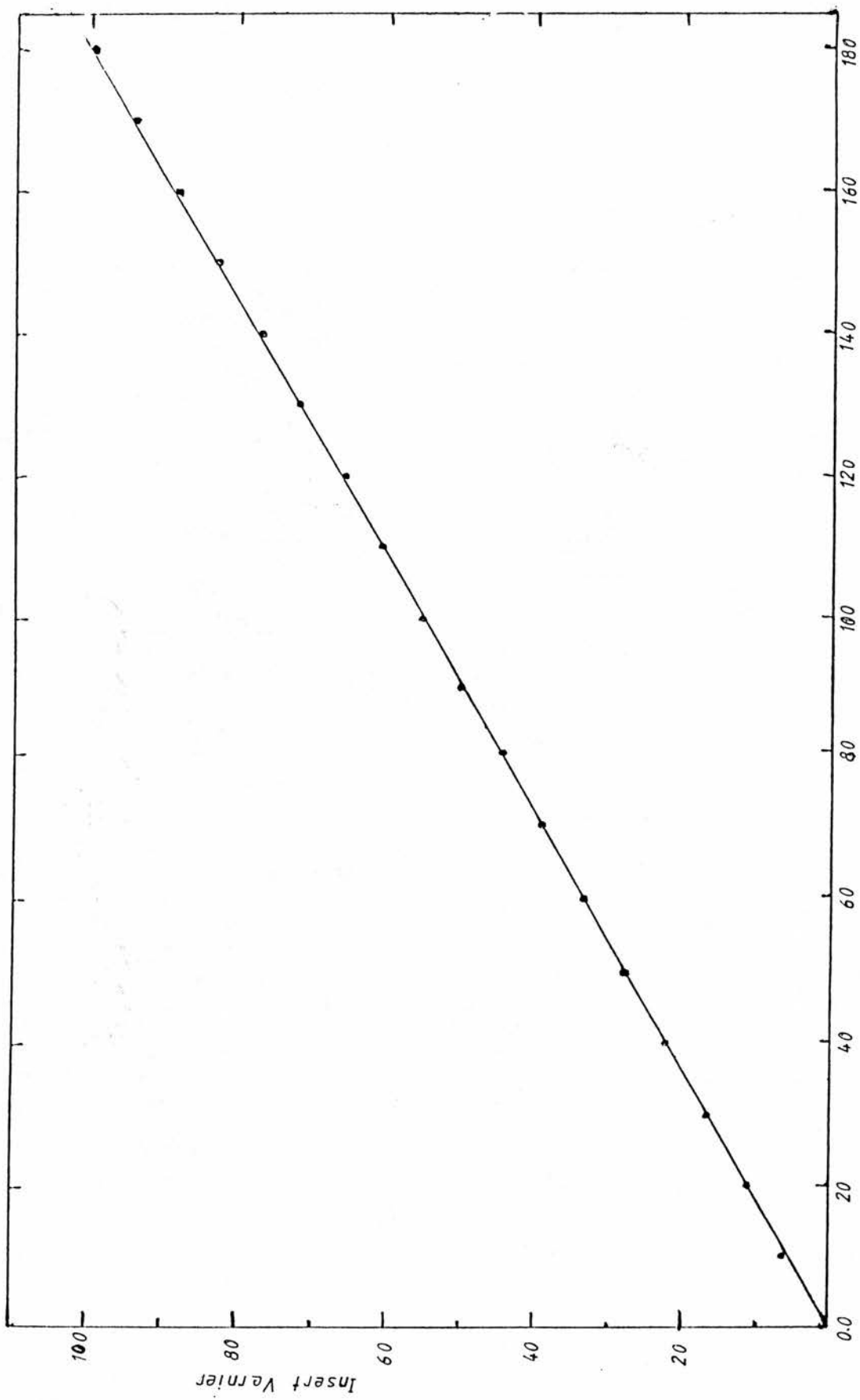


Fig. 4-8 Vernier read out versus angle

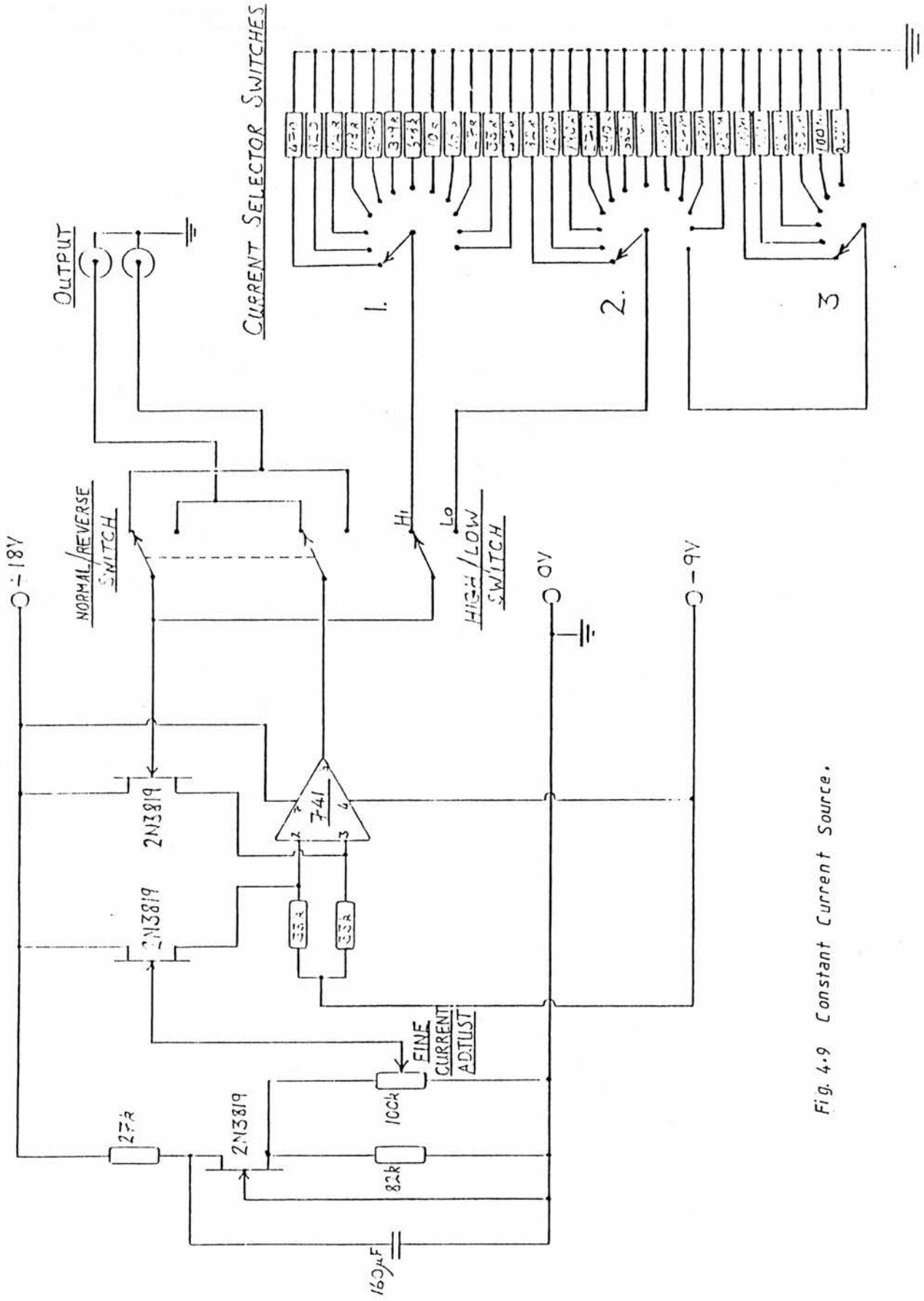


Fig. 4.9 Constant Current Source.

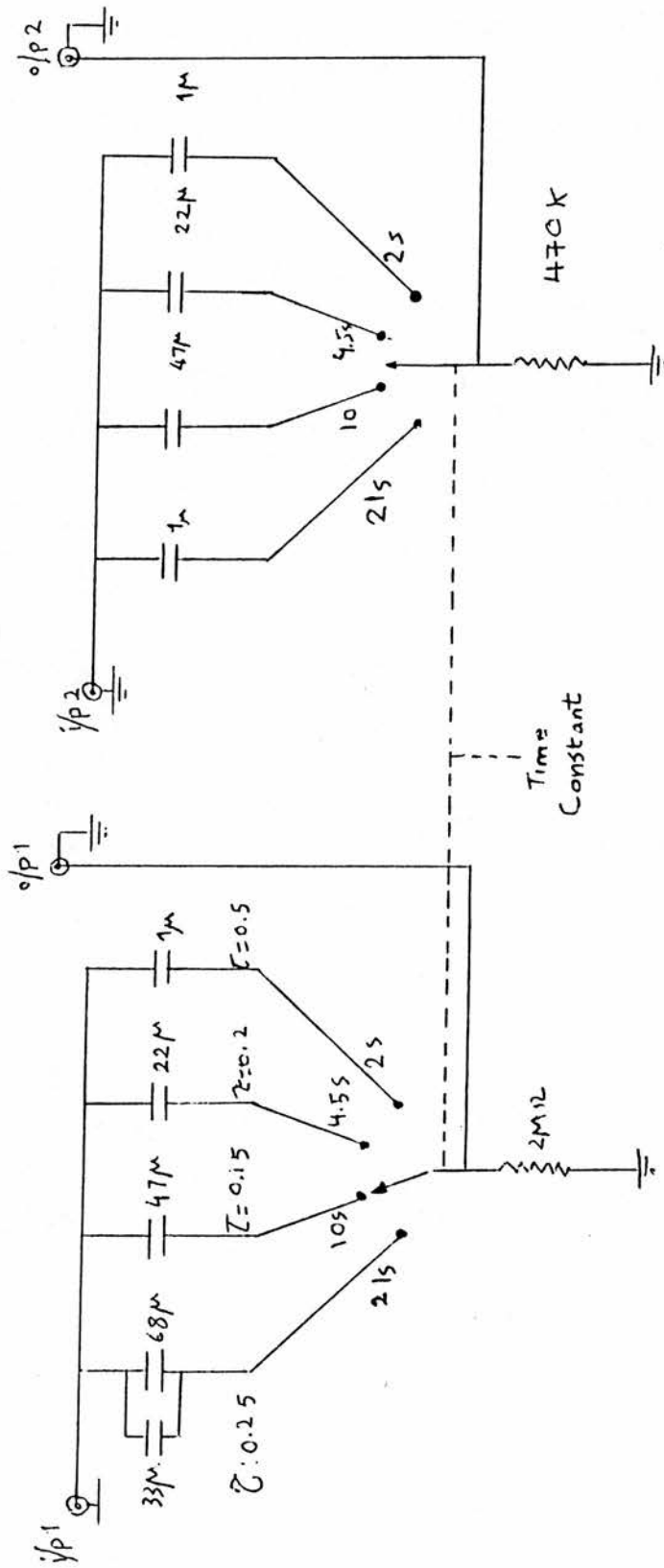


Fig. 4.10 Differentiation box.

4.3 High Pressure Technique

4.3.1 Equipment

The tool used to generate a high pressure on the semiconductor samples is the Copper Beryllium liquid filled clamp cell as shown in Fig 4.11 and Fig 4.12, manufactured by UNIPRESS.

The parts of the cell are cleaned very well with toluene and then with acetone. Then these are placed on the clean white sheet of paper because small pieces are likely to be lost. The work is done with care to avoid damaging of the cell. The steps followed to pressurise the cell are given below (these are a revised version of those given in the cell manual):

1. The optical plug (see Fig 4.13) is cylindrical and should be cleaned all over especially the two bases. Avoid any particles on the two surfaces since even the dust can scratch the surface when you put the window on it.
2. Take a new pair of rubber and brass gaskets, place them on the optical plug as shown in Fig.4.13b.
3. Apply a very small amount of silicon vacuum grease on the surface of the window and place the window on the top surface of the optical plug and press the window hard against the surface as shown in Fig 4.13c.
4. Take a nail enamel and using a thin wire apply it around the joint of the window and the plug (see Figs 4.13d and 4.13e). Use a microscope to make sure all the joints are covered.

It is very important to avoid the enamel contacting the rubber gasket; then leave them to dry.

HIGH PRESSURE CELL

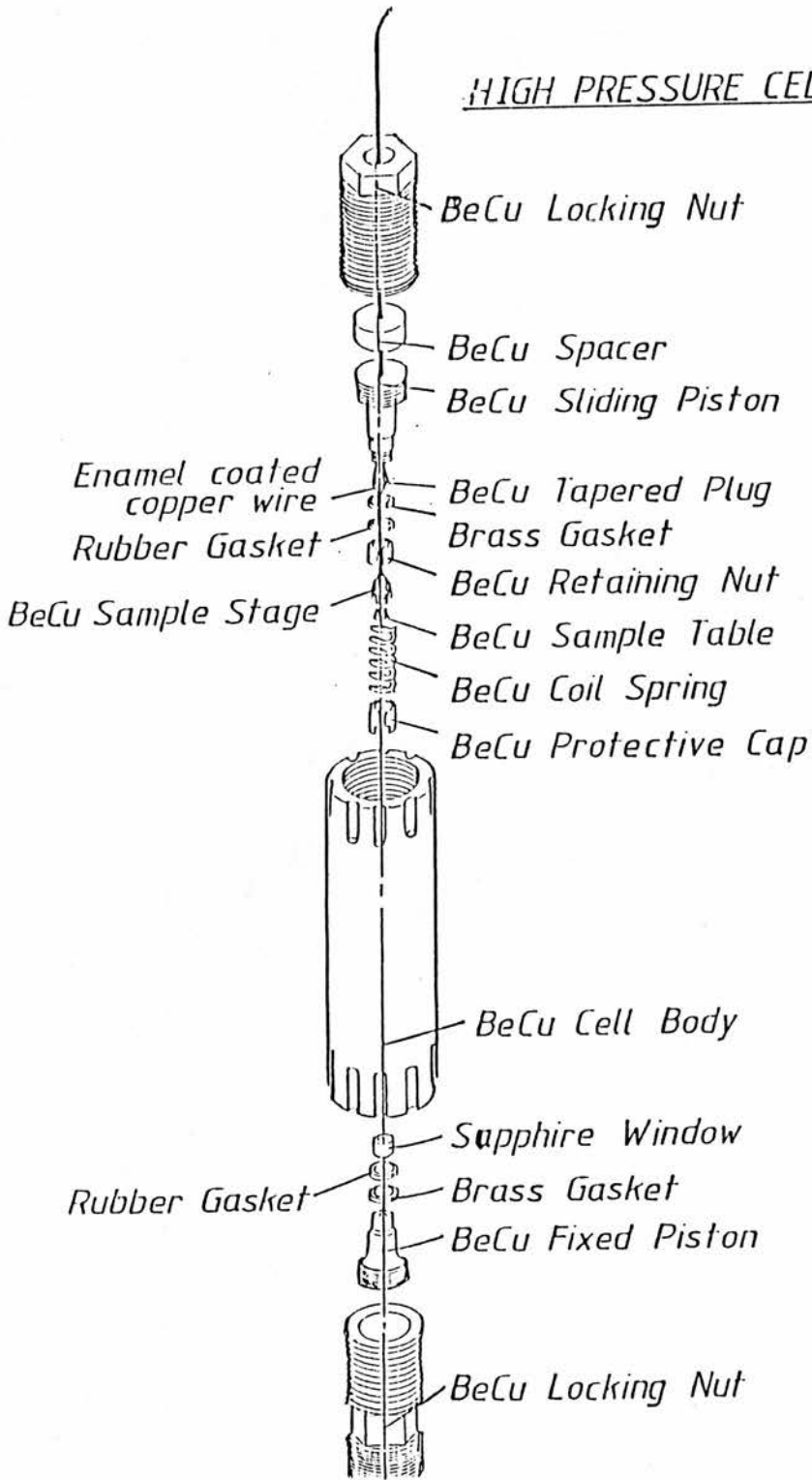


Fig 4.11 High pressure cell sketch diagram.

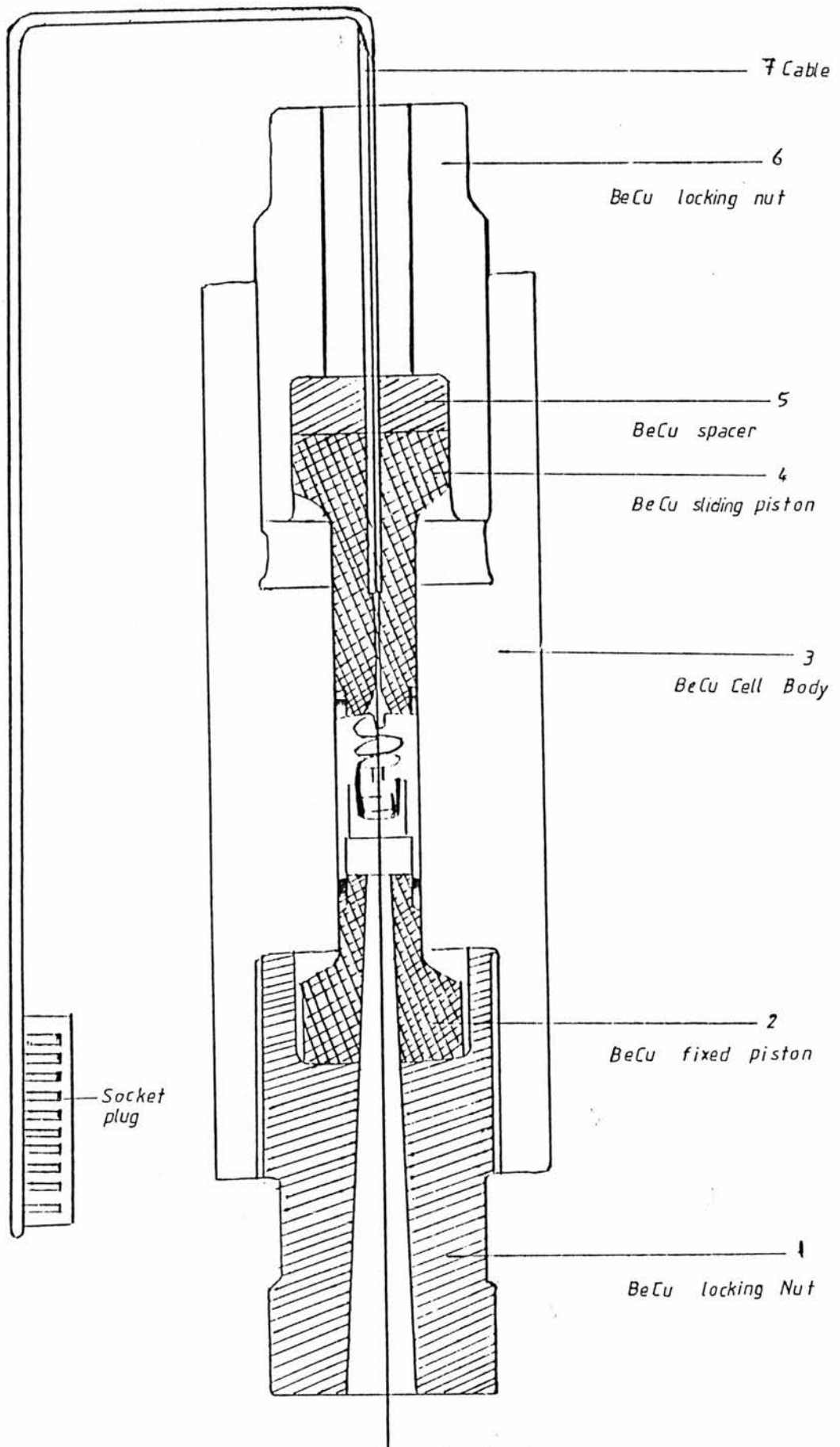


Fig. 4.12 High pressure cell longitudinal diagram .

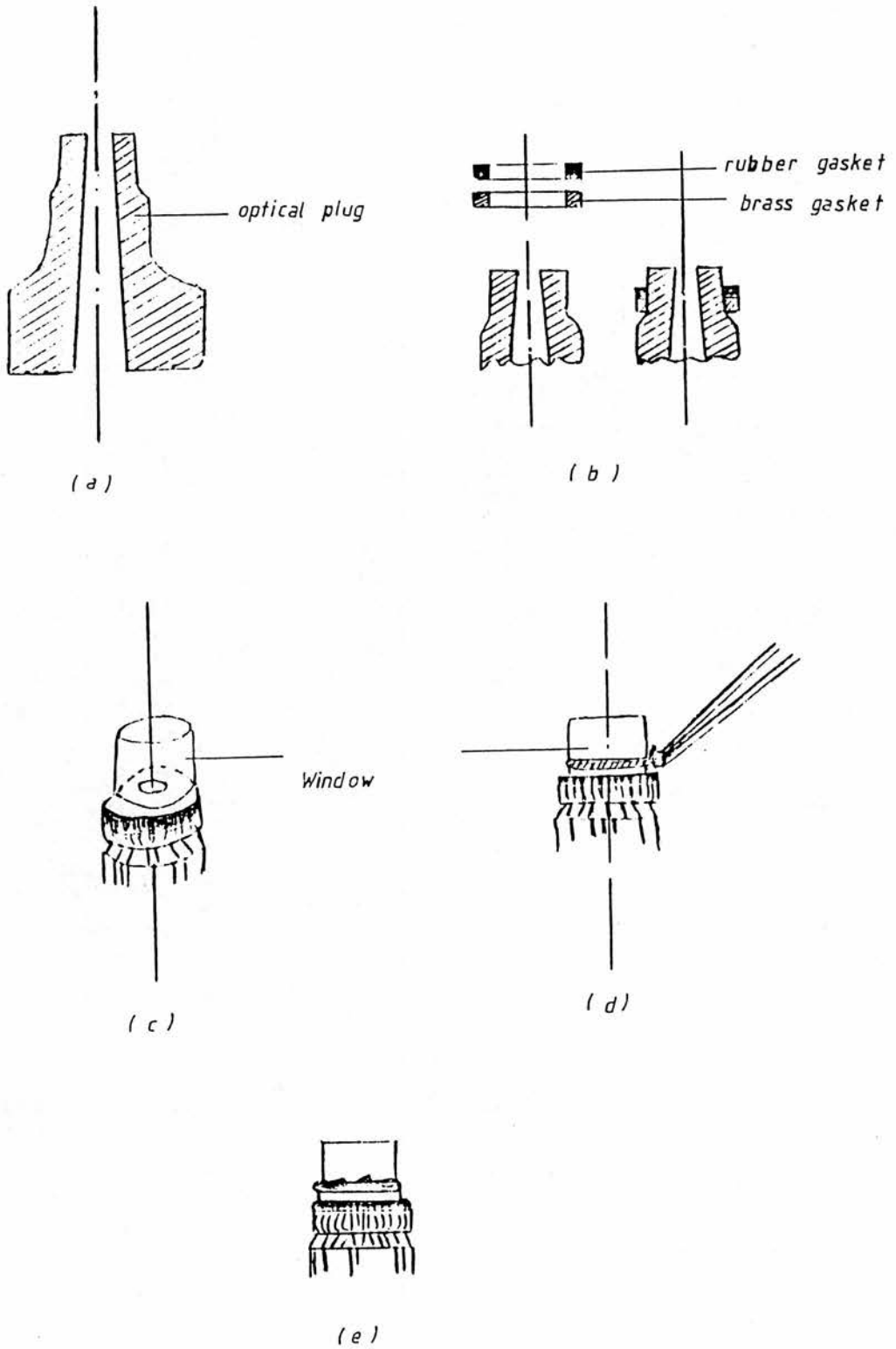


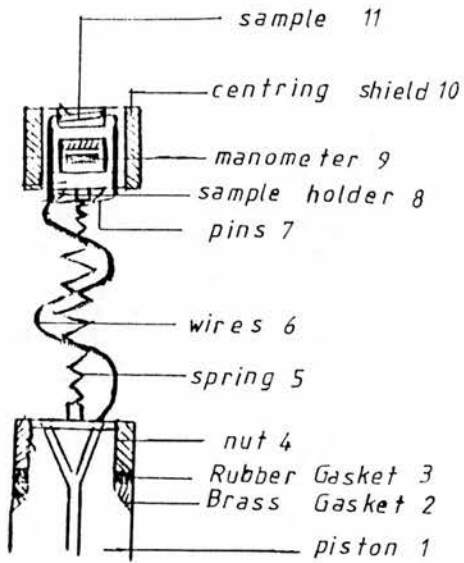
Fig. 4.13 optical plug parts of pressure cell (side view)

b. Assembling the piston and the sample holder

1. Remove the old gaskets. (See Fig 4.14). Unscrew the nut (4) (see Fig 4.14a) and take it out through the lowest part of the spring (5) and straight part of the wires (6) (see Fig 4.14b), stretch the rubber gasket on to the brass gasket (see Fig 4.14c), remove the centering shield (10), remove the gaskets (2) and (3) taking them out through the sample holder (8).
2. Position the new gaskets. Take a pair of rubber and brass gaskets, put them in their proper positions by inserting them through the sample holder (see Fig 4.14c) and put the nut back on its place (4).
3. Solder the sample to the sample holder, soldering should be done with a clean and hot soldering iron. It should be done quickly to avoid overheating the pins. If necessary a very small amount of flux can be applied to the pin tips but it is important to avoid polluting the other parts of the sample holder with the flux.
4. Replace the centering shield (10). Its position can be adjusted to suit the sample geometry. A small amount of wax can be applied on the side surface of (8) to give a stronger fit.

Assembling the Cell

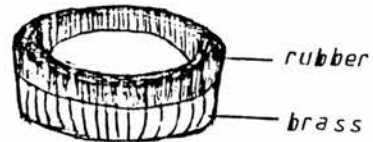
1. Adjust the optical plug (2) into the screw (1) (See Fig. 4.12).
2. Holding the cell (3) in the left hand in a vertical position screw the screw (1) into the cell with your right



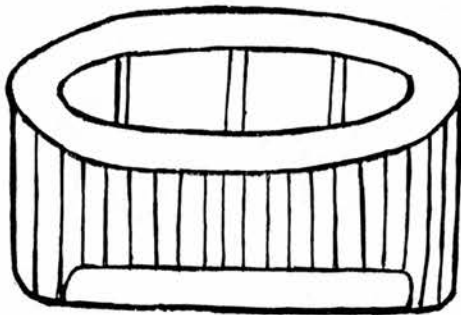
(a) pressure cell holder



(b) spring



(c)



(d) dedicated spanner

Fig. 4.14 Assembling the piston and sample holder of the pressure cell.

hand. Use an appropriate spanner for the last few turns. Both threads of the cell (3) have the same diameter but one of them is shorter than the other. The shorter is supposed to accommodate the screw with the optical plug. Take care to keep the optical plug with the window concentric with the cell.

3. Take the dedicated spanner (See Fig.4.14d) and clamp it in the vice.
4. Insert the cell into the spanner with the open part upwards.
5. Prepare all the necessary equipment for monitoring the pressure in a position near the hydraulic press. (See Section 4.3.2).
6. Calibrate the (InSb) manometer at atmospheric pressure by measuring its resistance at room temperature, $77K^{\circ}$ and $4.2K^{\circ}$ and feed these values to a computer program (See Appendix A).
7. Pour into a small glass a few cc of the pressure transmitting medium (Petroleum spirit of 0.72 g/ml at 20°C).
8. Pour the petrol into the cell right to the upper edge of the inner bore. Immerse the sample holder into the pressure medium in the glass and shake it a little bit in order to get rid of air bubbles.
9. Gently introduce the sample holder into the bore of the cell and subsequently the top part of the piston. Press the piston in with your fingers.
10. Stretch the cable (7) allowing the washer (5) to sit on the piston, make a few turns of the screw (6) with your

hand and then put on it the dedicated spanner (1) (See Fig.4.15).

11. Connect the cable to the Digital voltmeter through the bridge resistance and monitor the pressure changes then rotate screw (6) with the dedicated spanner, press the piston further into the cell. If the vice is firmly mounted around 2 kbar is achieved by this means. If there is no sealing problem then the above pressure should be achieved after few turns.
12. Plot the position of the piston as a function of the number of turns of the screw (6). From this one can carefully follow the piston position and avoid smashing the sample holder if the cell is leaking.
13. Disconnect the cell from the equipment and take out the dedicated spanner (1).
14. Put the cell into the shields and assemble the set; protect the cable always through the whole process of pressuring.
15. Put the cell in the hydraulic press and make sure that the cell is positioned concentrically on the piston of the press, connect the cell to the pressure monitoring set-up then apply the load.
16. When increasing the load one should watch carefully the reading of the press manometer and simultaneously the reading of the InSb manometer through the digital voltmeter.
17. With the piston made of Be-Cu never apply a load bigger than 5.3 Tons; with 0.5 Ton of friction and possible

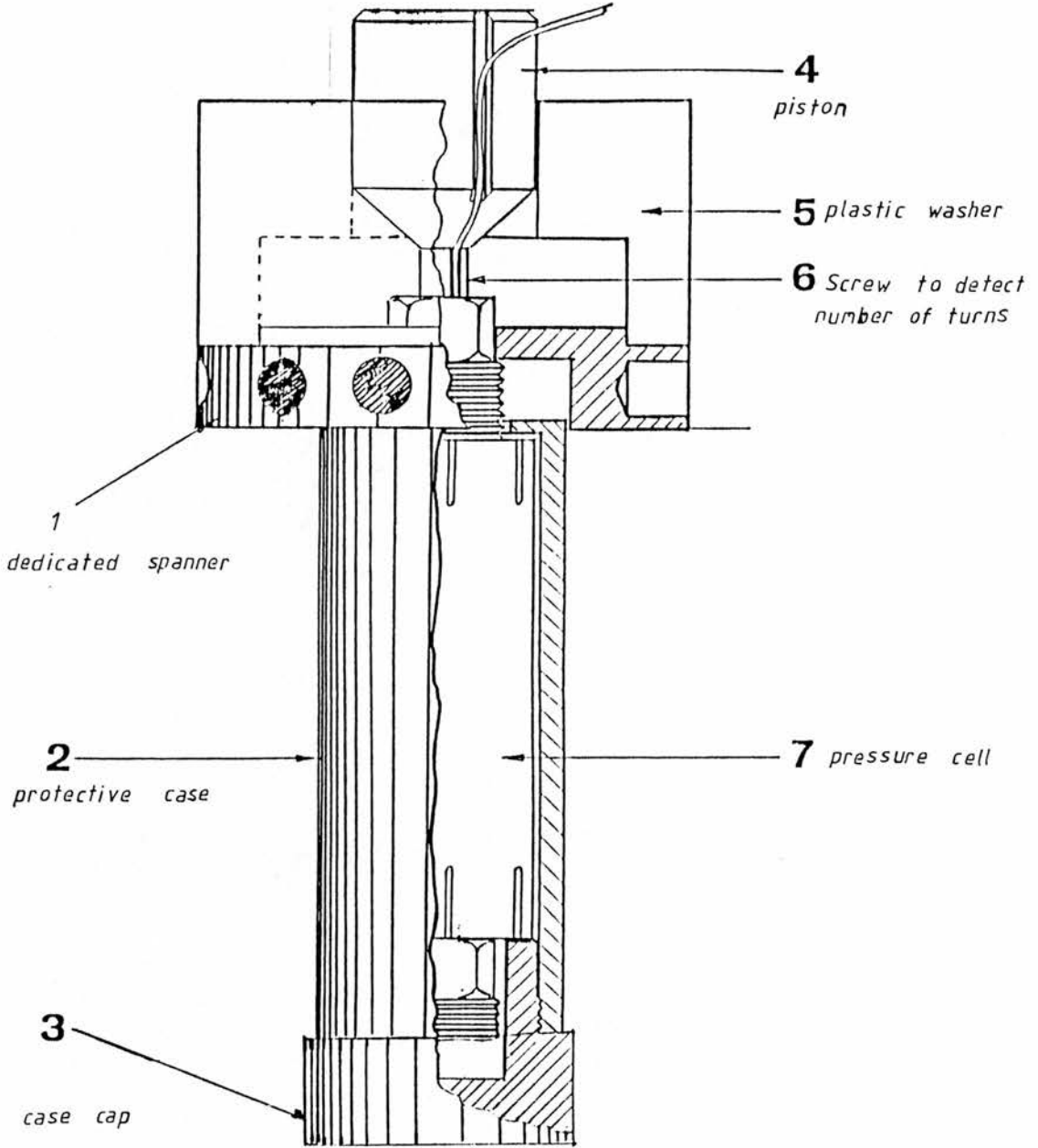


Fig. 4.15 The pressure cell in the protective case.

losses while removing the load should give around 12.0 kbars at 300K.

18. Remove the cell from the shield, assemble it on the insert and connect the plug; finally encase in a protective tube, remove the air and replace with He gas from the connected He line.

Removing the pressure

1. Make sure that the piston of the press is at least 8 mm above its lowest position.
2. Apply a load approximately equal to the last load when putting on the pressure.
3. Turn out the fixing screw around two turns. Slowly open the valve of the press allowing the load to drop, watch carefully the readings of the press manometer and InSb manometer. The pressure should be released slowly.

When the pressure in the cell stops dropping then close the valve of the press, increase the load a bit and unscrew the locking screw further.

When the load on the press drops down to around 1 Ton unscrew the locking screw around three additional turns and release the load to zero.

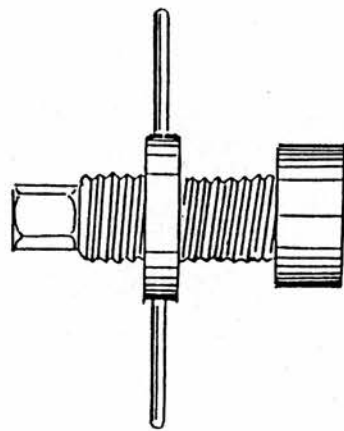
4. Take the cell out of the shield and unscrew the locking screw (6); if this is too hard to do by hand insert the cell into the dedicated spanner (See Fig.4.15) (clamped previously in the vice) and use the top dedicated spanner (1) to unscrew the locking screw.
5. Take the piston out of the cell using the tool (a) shown

in (Fig 4.16), unscrew the other screw (the one fixing the optical plug), and take the optical plug out of the cell; be careful not to lose the window.

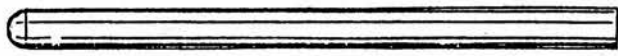
6. If the brass gasket is in the cell remove it by knocking it out with the steel rod .b. (See Fig.4.17). The flat surface of the rod is to be inserted into the cell from the "piston side". The cell should be positioned vertically on the flat surface. The rounded end of the rod should be hit with a hammer. Before doing this make sure the window is not in the cell. Clean the cell with toluene and then with acetone.

4.3.2 The Pressure Gauge

The pressure is monitored by a highly doped crystal of InSb placed in the pressure cell. A typical resistance of the manometer at room temperature and atmospheric pressure is 4.3Ω . The manometer dimensions are typically $10 \times 1 \times 1$ mm. Four electrical contacts of alloyed Indium are made onto the manometer: two for the current and two for the voltage. The manometer is extremely brittle and must be treated with care. To calibrate the manometer and monitor the pressure a datron digital multimeter with the ratio option and constant current (100 mA) source are used. The current is passed through the manometer and through a 0.1Ω standard resistor and the ratio of the voltage drop across them obtained at these temperatures 296, 77 and 4.2K. The semiconductor gauge resistance increases non-linearly with increasing pressure. A computer program is then used to calculate the expected ratio of voltages for a desired room temperature pressure and to estimate the pressure change when the cell is cooled down to 4.2K. (See Appendix A).



a



b

Fig. 4.16 (a) the extractor used to depressurise the cell.
(b) steel rod used to remove the old brass gasket.

CHAPTER V - RESULTS AND DISCUSSION

This chapter begins with a note of the characteristics, architecture and origin of the samples used in this work. The next two sections discuss Van der Pauw and Shubnikov de Haas measurements in the light of existing theories. Some measurements on bulk InP are similarly treated. The next section deals with persistent photoconductivity and the final section reports and interprets measurements at high pressures.

5.1 Samples used in this work

The samples used in this work were grown by MBE and MOCVD (MOVPE) at the SERC Central Facility for III-V semiconductors, Sheffield, at RSRE, Malvern, at UMIST Electronics and Electrical Engineering Department, at Plessey and at Glasgow University Department of Electronics and Electrical Engineering. Their characteristics and architecture are shown in Tables 5.1 and 5.2. Some of the GaAs/AlGaAs samples were obtained from an early stage of production and consequently the mobilities of these samples are lower than that now obtainable.

5.2 Temperature Dependence of μ and n_s from SdH and VdP measurements

A summary of mobility and carrier density in samples containing a 2DEG (2DHG) at RT, 77K and 4.2K is given in Table 5.3. The VdP measurements were all carried out with the samples in the dark. The SdH measurements were done with the samples both in the dark and after illumination with white light.

5.2.1 Temperature Dependence of μ and n_s .

The results shown in Table 5.3 indicate that for some samples the measured carrier density of the 2DEG at the same temperature (4.2K) depends on whether the technique of the VdP or SdH is used to obtain n_s . An example is provided by the samples KES422 and KES427: $4.9 \times 10^{16} \text{ m}^{-2}$ compared to 4.5×10^{15} and 5.8×10^{15} compared to $5 \times 10^{15} \text{ m}^{-2}$, respectively. One of the reasons for this discrepancy is probably due to the fact that when using the VdP technique a strong contribution to the voltage drop and sample resistance comes from carriers with 3D character, ie, not at the 2DEG interface; whereas using the SdH technique the 3D carrier contribution is manifested in the form of a rising background in the magnetoresistance and in the width of the SdH

Sample and name	Origin and growth method	R.T. $\mu\text{cm}^2\text{v}^{-1}\text{s}^{-1}$ $n_3\text{cm}^{-3}$	77K° $\mu\text{cm}^2\text{v}^{-1}\text{s}^{-1}$ $n_3\text{cm}^{-3}$	4-2K° $\mu\text{cm}^2\text{v}^{-1}\text{s}^{-1}$ $n_3\text{cm}^{-3}$	Thickness of epitaxial layer μm	Substrate
InP 233	Glasgow M.B.E	2,750 1.8×10^{16}	26,900 0.86×10^{16}	7,300 0.45×10^{16}	2.9	InP (Fe)
InP 232	Glasgow M.B.E	2,530 2.24×10^{16}	24,900 1.11×10^{16}	5,000 0.57×10^{16}	2.9	InP (Fe)
InP 236A	Glasgow M.B.E	2,120 1.85×10^{16}	13,440 0.6×10^{16}	895 2×10^{16}	2.1	InP (Fe)
InP PMB106	Sheffield MBE	3,450 3.61×10^{15}	43,340 2.1×10^{15}	2,100 0.68×10^{15}	2.5	InP (Fe)
GaInAs PMB112	Sheffield M.B.E	3,960 1.5×10^{16}	12,000 0.9×10^{16}	1,300 1.9×10^{16}	2.5	InP (Fe)

Table 5.1 30 samples used in this work and results.

Sample and Name	Origin and growth method	$\mu\text{cm}^2\text{V}^{-1}\text{s}^{-1}$ $n_s\text{cm}^{-2}$ at 77K ^o	x%	Structure
GaAs-GaAlAs MV116	Sheffield MOVPE	(a) 8,600 (a) 9.9×10^{11}	25 Al	100Å:GaAs 500Å:GaAlAs:Si 10^{18}cm^{-3} 100Å:GaAlAs 7000Å:GaAs GaAs: s/i
GaAs-GaAlAs MV134	Sheffield MOVPE	(a) 6,250 (a) 5.3×10^{11}	30 Al	9000Å:GaAs: 10^{14}cm^{-3} 150Å:GaAlAs 350Å:GaAlAs: 10^{18}cm^{-3} 100Å:GaAs GaAs: s/i
InP-InGaAs PMB 41	Sheffield MBE M.Q.W	(b) 1,754 (b) 3.11×10^{12}	47 Ga	1000Å: InP 10Å: InGaAs 1000Å: InP 20Å: InGaAs 1000Å: InP 40Å: InGaAs 1000Å: InP 60Å: InGaAs 5000Å: InP : InP sub.
GaAs-GaAlAs KES427	Umist MBE	(a) 64,000 (a) 2.7×10^{11}	35 Al	450Å:GaAs:n 1865Å:GaAlAs:Si 86Å:GaAlAs undoped GaAs sub,undoped
GaAs-GaAlAs KES422	Umist MBE	(b) 7,555 (b) 5.9×10^{12}	38 Al	830Å:GaAs:Si 1867Å:GaAlAs:Si 90Å:GaAlAs 20000Å:GaAs sub.
InP-InGaAs PMB 121	Sheffield MBE s.l.	(b) 11,940 (b) 1.25×10^{11}	47 Ga	1000Å: InP 25Å: 50 periods GaInAs q.w. 100Å: InP barrier InP subs: Fe doped

Table 5.2 for 2DEG samples used in this work:

(a) By the grower. (b) Our data.

Sample and Name	Origin and growth method	$\mu\text{cm}^2\text{V}^{-1}\text{s}^{-1}$ $n_s\text{cm}^{-2}$ at 77K ^o	x%	Structure
InP-InGaAs PMB116	Sheffield MBE Q.W. 160	(b) 3,660 (b) 3×10^{11}	47 Ga	500Å:InP 160Å:GaInAs InP InP:sub; Fe doped
InP-InGaAs PMB78	Sheffield MBE S.Q.W	(b) 10,680 (b) 2.5×10^{12}	47 Ga	2000Å:InP 160Å:GaInAs 2000Å:InP InP:Fe
InP-InGaAs PMB79	Sheffield MBE S.Q.W	(b) 986 (b) 2.8×10^{12}	47 Ga	2000Å:InP 50Å:GaInAs 2000Å:InP InP:Fe
InP-InGaAs PMB80	Sheffield MBE S.Q.W	(b) 12440 (b) 5×10^{12}	47 Ga	2000Å:InP 10Å:GaInAs 2000Å:InP InP:Fe
GaAs-GaAlAs OC-117	Plessey MOCVD	(b) 4903 (b) 3.8×10^{12}	30 Al	N ⁺ :500Å:GaAs: 2.3×10^{18} 200Å:GaAs graded N ⁺ :500Å:GaAlAs: 1×10^{18} 20Å:GaAlAs undoped 8000Å:GaAs 10^{16} undoped
InP-GaInAs SJB5507	RSRE MOCVD M.D. S.Q.W	(b) 1135 (b) 1.65×10^{12}	47 Ga	300Å:InP: 3×10^{17} 100Å:InP: undoped 100Å:InP: undoped 100Å:InP: undoped 200Å:InP: 3×10^{17} 180Å:InP: undoped S.I.sub.

Table 5.2 (continued) 2DEG samples used in this work.

(a) By grower. (b) Our data.

Sample and Name	Origin and growth method	$\mu \text{ cm}^2 \text{ v}^{-1} \text{ s}^{-1}$ $n_s \text{ cm}^{-2} \text{ at } 77 \text{ K}^\circ$	x %	Structure
GaAs-GaAlAs HEMT# 1	Plessey MOCVD	(b) 27840 (b) 0.86×10^{12}	30 Al	N^+ :500Å:GaAs: 23×10^{18} 200Å:GaAs graded N^+ :500Å:GaAlAs: 1×10^{18} 20Å:GaAlAs undoped 8000Å GaAs 10^{18} undoped
InP-InGaAs PMB137	Sheffield MBE	(a) 104000 (a) 1×10^{12}	47 Ga	5000Å:InP: 5×10^{17} Si 100Å:InP undoped 10000Å:InGaAs 25Å:InP; undoped InP:Fe subs.
Hole gas cpm157G	Sheffield MOVPE	(a) 2500 (a) 2×10^{12}	60 and 45 Al	100Å:GaAs:cap 1000Å:Al _{0.6} Ga _{0.4} As: $p > 2 \times 10^{17}$ 2500Å:GaAs: n type 4500Å:AlGaAs: $p = 10^{17}$ S.I:sub
Hole gas cpm161G	Sheffield MOVPE	(a) 2232 (a) 1.9×10^{12}	60 Al	100Å:GaAs:cap 1000Å:Al _{0.6} Ga _{0.4} As $p > 2 \times 10^{17}$ 2500Å:GaAs n type 2500Å:Al _{0.6} Ga _{0.4} As $p > 2 \times 10^{17}$ S.I:sub

Table 5.2 (continued) 2DEG samples used in this work;

(a) By the grower. (b) Our data.

Sample	R.T.		77K		4.2K dark		SdH 4.2K	
	$n_s \text{ m}^2$	$\mu \text{ m}^2 \text{ v s}^{-1}$	$n_s \text{ m}^2$	$\mu \text{ m}^2 \text{ v s}^{-1}$	$n_s \text{ m}^2$	$\mu \text{ m}^2 \text{ v s}^{-1}$	dark	light
MV116	13.2×10^{15}	0.094	3.0×10^{15}	0.366	5.14×10^{15}	0.0624	4.1×10^{15}	—
MV134	13.0×10^{15}	0.167	9.0×10^{15}	1.313	6.0×10^{15}	1.330	5.2×10^{15}	—
PMB 41	6.3×10^{16}	0.0044	3.1×10^{16}	0.1754	2.45×10^{16}	0.1032	4.7×10^{15}	—
KES427	10.98×10^{15}	0.221	16.6×10^{15}	0.6120	5.75×10^{15}	2.060	5.0×10^{15}	—
KES422	3.12×10^{16}	0.1043	5.9×10^{16}	0.7555	4.9×10^{16}	1.0024	4.5×10^{15}	—
PMB121	4.4×10^{15}	0.2490	12.5×10^{15}	1.1940	1.1×10^{15}	0.7585	0.88×10^{15}	1.57×10^{15}
PMB116	2.9×10^{16}	0.1280	0.9×10^{16}	0.3870	1.4×10^{16}	0.0900	0.12×10^{16}	0.13×10^{16}
PMB78	3.2×10^{16}	0.1173	2.54×10^{16}	0.1068	4.2×10^{16}	0.0334	—	—
PMB 79	22.1×10^{16}	0.0810	28×10^{16}	0.0986	6.3×10^{16}	0.0189	4.1×10^{15}	—
PMB80	7.2×10^{16}	0.0947	4.97×10^{16}	0.1244	7.9×10^{15}	0.0541	—	—
OC-117	5.3×10^{16}	0.2228	3.8×10^{16}	0.4903	4.0×10^{16}	0.2931	12×10^{16}	—
SJB5507	1.3×10^{16}	0.0619	1.65×10^{16}	0.1135	2.2×10^{16}	0.0930	0.86×10^{16}	12×10^{16}
HEMT#1	1.6×10^{16}	0.3490	0.86×10^{16}	2.7840	0.84×10^{16}	4.1710	0.8×10^{16}	—
PMB137	1.5×10^{16}	0.9750	0.88×10^{16}	6.1520	0.74×10^{16}	8.1880	0.5×10^{16}	0.5×10^{16}
CPm157G, hole gas	5.6×10^{16}	3.83×10^{-3}	1.8×10^{16}	53.4×10^{-3}	1.7×10^{16}	120.4×10^{-3}	12×10^{16}	1.2×10^{16}
CPm161G, hole gas	5×10^{16}	1.33×10^{-3}	1.2×10^{16}	15×10^{-3}	0.98×10^{16}	23.1×10^{-3}	0.66×10^{16}	0.66×10^{16}

Table 5.3 Van der Pauw and SdH measurements of μ and n in samples with a 2D system at 4.2K, 77K, and R.T. in the dark and after illumination.

oscillations. In addition, the features in the SdH oscillations which are purely 2D are separated out and identified when oscillations recorded at various tilted angles as discussed in section 2.1.3(ii). This point is reinforced when the results for HEMT No.1 are inspected. Here the difference between the measured densities is the smallest (about 5%). In this sample the area of doped AlGaAs layer where the ohmic contacts were made had been etched off thus removing the 3D contribution in the VdP measurements.

It is also of interest to note the role of the spacer layer and its effect on carrier mobility. The data for samples MV116 and MV134 shown in figure 5.1 indicates that μ is higher for MV134 and that for MV116 the mobility shows a decrease at low temperature typical of 3D structures due to ionised impurity scattering. Although in MV116 there is a spacer layer of 100\AA of AlGaAs the 2D interface was not reached. Thus the mobility of the carriers at the interface between the cap layer and the doped AlGaAs is measured: effectively an unmodulated heterostructure. On the other hand, in MV134 the 2D carriers are found at the interface between the cap layer of GaAs and the undoped layer of GaAlAs which acts as the spacer separating from the GaAs layer the doped AlGaAs layer. However the overall low temperature mobility is very poor. This may be due to contributions from carriers at other interfaces and layers with much lower mobilities, ie, parallel conduction.

Another feature of the data in Table 5.3 is the difference in carrier density at 4.2K measured with SdH technique with the sample in the dark and after it has been illuminated with white light. This is best illustrated by samples PMB121, PMB116 and PMB137. In the former sample the 2D density doubles after illumination whereas in the two

latter samples the differences are negligible. The behaviour is explained by the existence of persistent photoconductivity in sample PMB121 and its absence in the other two. The PPC will be discussed in Section 5.6. However, the possibility of this effect being due to different substrates has been ruled out since all these samples were grown on substrates belonging to the same batch.

The temperature dependence of the mobility in the dark for the three samples mentioned above and for a multiple quantum well (PMB41) of GaInAs is shown in figure 5.2.

In the case of the multiple quantum well (PMB41) the mobilities measured at various temperatures are in the low end of 3D values for GaInAs. This is due to the fact that in this early sample the In concentration was higher than expected by about 1 to 2% (Roberts, 1986) leading to lattice mismatches in the structure which in turn may have caused serious lattice defects. On the other hand, the emission spectrum of this sample shows reasonable optical quality (See Fig 2.9b). Samples containing a single quantum well (PMB116) and multiple thin wells (PMB121) exhibit a quasi 3-D behaviour indicating a charge contribution from bulk carriers (mobility decreases below 100K). The mobility of PMB116 is much lower than that of PMB121 possibly due to improvements in the growth reactor since cooled shutters were installed in the MBE Sheffield reactor after PMB116 and before PMB121 were grown. By contrast the contribution of improved growth methods and sample architecture (PMB137 is a MDH) yielded a very good mobility for the GaInAs-InP system limited by alloy scattering at low temperatures (see discussion in next section).

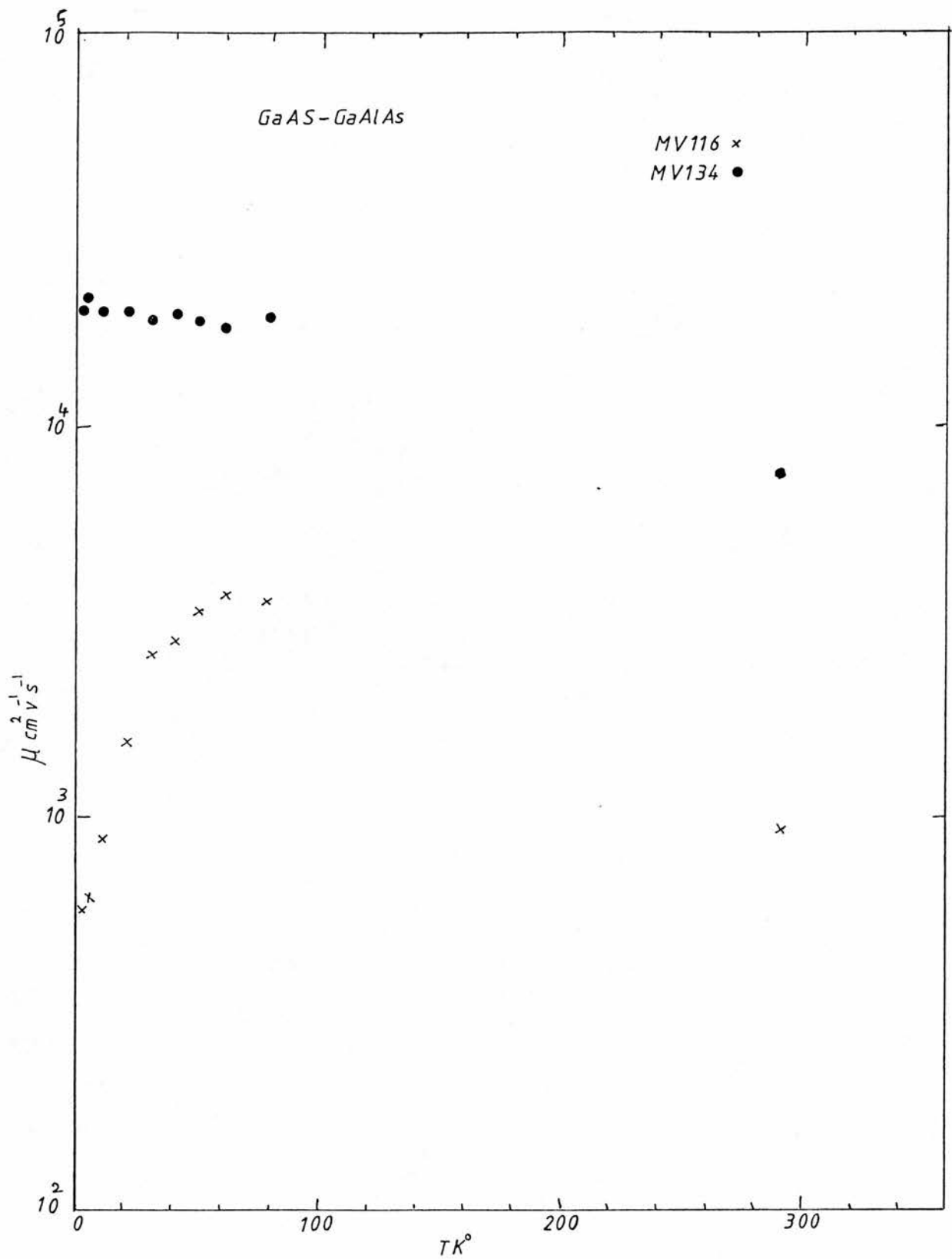


Fig 5.1 μ versus T for samples MV116 and MV134.

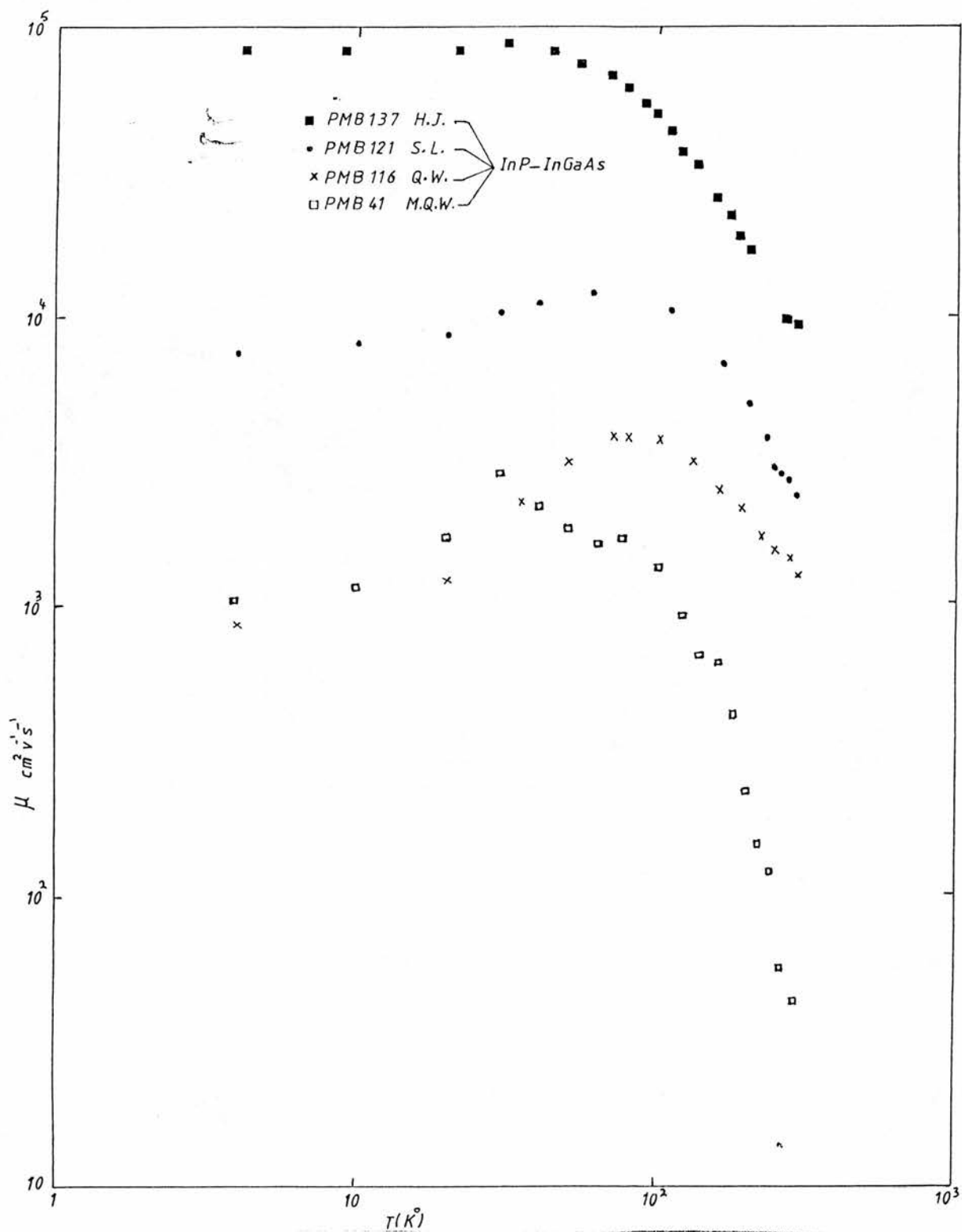


Fig 5-2 μ versus T for samples PMB121, PMB116, PMB137, and PMB41.

5.2.2 Comparison with theoretical mobilities

For the purpose of comparison between the theoretical and experimental mobilities for heterojunction samples KES422, MV134 of GaAs-GaAlAs and PMB137 of InP-InGaAs, the various scattering mechanisms which are taken into account in the calculation are: optical phonon μ_{PO} , acoustic phonon μ_A , piezoelectric μ_{PE} , ionized impurity μ_{RI} and background ionized impurities μ_{BI} scattering. The total mobility is calculated from Mathiessens rule:

$$\frac{1}{\mu_{TO}} = \frac{1}{\mu_{RI}} + \frac{1}{\mu_{BI}} + \frac{1}{\mu_{PO}} + \frac{1}{\mu_A} + \frac{1}{\mu_{PE}} \dots\dots\dots 5.1$$

The total theoretical mobility μ_{TO} for samples KES422 and MV134 GaAs-GaAlAs as a function of temperature are plotted in Fig 5.3 and Fig 5.4 indicating the contributions from different scattering mechanisms. We have used the following expressions (Lee et al, 1983): μ_{PO} is calculated from equation (2.39) and μ_A is found from:

$$(\mu_A)_{T \rightarrow \infty} = 4.77 \times 10^7 / T (10^{12} \text{ cm}^2 / n_{SO})^{\frac{1}{2}} \text{ cm}^2/\text{Vs} \dots\dots\dots 5.2$$

$$(\mu_A)_{T \rightarrow 0} = 5.50 \times 10^6 (10^{12} \text{ cm}^2 / n_{SO})^{5/6} \text{ cm}^2/\text{Vs} \dots\dots\dots 5.3$$

The piezoelectric scattering μ_{PE} is found from:

$$\mu_{PE} = 7.95 \times 10^7 / T (10^{12} \text{ cm}^{-2} / n_{SO})^{\frac{1}{2}} \dots\dots\dots 5.4$$

μ_{RI} is found from

$$\mu_{RI} = \frac{1.28 \times 10^5 (n_{SO} / 10^{12} \text{ cm}^{-2})^{3/2} (10^{18} \text{ cm}^2 / N_d)}{(100A^\circ / L_o)^2 - (100A / L'_o)^2} \dots\dots\dots 5.5$$

and ν_{BI} is found from equation (2.46).

For GaInAs-InP PMB137, ν_{PO} is found from:

$$\nu_{PO} = 6.9 \times 10^8/T^2 + 1.1 \times 10^{17}/T^6 \dots\dots\dots 5.6$$

where the constants are calculated from a fit to the experimental mobilities at various temperatures above 4.2K of bulk GaInAs (Kastalsky A et al, 1982). ν_{RI} is found from equation (2.41) in which the parameters for GaInAs are given in Table 5.7. The expression used is:

$$\nu_{RI} = \frac{8.4 \times 10^4 (n_{SO}/10^{12} \text{ cm}^{-2})^{3/2} (10^{18} \text{ cm}^2/N_d)}{(100A^\circ/L_o)^2 - (100A/L'_o)^2}$$

The alloy disorder scattering contribution to the mobility is taken from Takeda et al (1981) who calculated it taking in to account the effective mass correction for non-parabolicity at low temperatures and a scattering potential of 0.53 ev. This potential is about 10% smaller than the one used by Bastard (1984) and thus may underestimate the total contribution. We approximate the dependence on temperature as $\log \nu \propto T^{-1}$ taking ν equal to 3×10^5 , 1.8×10^5 and $8 \times 10^4 \text{ cm}^2/\text{Vs}$ at 4.2, 77 and 300K respectively, as the reference point. This is plotted in Fig 5.6. The total mobility of InGaAs-InP is calculated from

$$\frac{1}{\nu_{TO}} = \frac{1}{\nu_{PO}} + \frac{1}{\nu_{RI}} + \frac{1}{\nu_{alloy}}$$

Fig 5.5 shows the various contributions to the total mobility as a function of temperature. The experimental results agree well with the calculated mobilities. The calculated mobilities are given in Table

5.4, 5.5 and 5.6 for KES422, MV134 and PMB137, respectively. The measured mobility for KES422 and MV134 at different temperatures are much lower than the theoretical values as shown in Fig 5.3 and 5.4. To obtain the μ_{2D} for MV134 and KES422 we refer to equation 3 (Chapter 3):

$$\mu_{vdp} = \frac{n_s \times \mu^2 + n_{bulk} \mu_{2D}^2}{\mu_s \mu_{2D} + n_{bulk} \mu_{3D}}$$

All the above parameters except μ_{2D} can be taken from Table 5.3 where μ_{vdp} is Van der Pauw mobility, n_s is the electron density at 4.2K from SdH. Both n_{bulk} , μ_{bulk} are electron density and electron mobility of the AlGaAs layer at 300K measured by the VdP technique, the use of the room temperature VdP value for n follows from the analysis of Kane et al (1985) which shows that there are approximately the same number of electrons in the AlGaAs at low and room temperatures. It is also observed, by Kane et al (1985), that the mobility of electrons in the AlGaAs varies little with temperature between 300K and 4.2K.

From equation (3.4) we obtain values of 1.8×10^4 and 3.1×10^4 cm^2/Vs for μ_{2D} in MV134 and KES422 respectively. Comparing them to the theoretical estimate Table 5.4 and Table 5.5 μ_{2D} is approximately 20 times and 13 times smaller than expected. Factors not included in the theoretical estimate such as interface roughness and Si donor migration may account for this discrepancy. This suggests that these factors may play a crucial role in achieving mobilities closer to the theoretical limit.

TK°	μ_{Po}	μ_A	μ_{PE}	μ_{RI}	n_{scm}^{-2}	μ_{Po}^{-1}	μ_A^{-1}	μ_{PE}^{-1}	μ_{RI}^{-1}	μ_{To}^{-1}	μ_{ex}	μ_{BI}	μ_{BI}^{-1}	μ_{To}^{-1}	μ_{To}
4	2.9×10^{13}	8×10^6	2.5×10^7	7.4×10^5	6.4×10^{11}	3.5×10^{-14}	1.3×10^{-7}	4×10^{-8}	1.4×10^{-6}	1.6×10^{-6}	1.3×10^4	1×10^6	9.7×10^{-7}	2.6×10^{-6}	3.9×10^5
10	12×10^{11}	7.4×10^6	95×10^6	7.7×10^5	7×10^{11}	8.5×10^{-12}	1.4×10^{-7}	1.1×10^{-7}	1.2×10^{-6}	1.5×10^{-6}	2×10^4	1.7×10^6	5.8×10^{-7}	2.1×10^{-6}	4.8×10^5
20	1.8×10^9	7.4×10^6	4.8×10^6	7.7×10^5	7×10^{11}	5.4×10^{-10}	1.4×10^{-7}	2.1×10^{-7}	1.2×10^{-6}	1.6×10^{-6}	2×10^4	1.7×10^6	5.8×10^{-7}	2.2×10^{-6}	4.6×10^5
30	1.6×10^8	7.4×10^6	3.2×10^6	7.7×10^5	7×10^{11}	6.2×10^{-9}	1.4×10^{-7}	3.2×10^{-7}	1.2×10^{-6}	1.7×10^{-6}	1.8×10^4	1.7×10^6	5.8×10^{-7}	2.3×10^{-6}	4.4×10^5
40	2.9×10^7	7.4×10^6	2.4×10^6	7.7×10^5	7×10^{11}	3.4×10^{-8}	1.4×10^{-7}	4.2×10^{-7}	1.2×10^{-6}	1.8×10^{-6}	1.9×10^4	1.7×10^6	5.8×10^{-7}	2.4×10^{-6}	4.2×10^5
50	7.9×10^6	7.4×10^6	1.9×10^6	7.7×10^5	7×10^{11}	1.3×10^{-7}	1.4×10^{-7}	5.3×10^{-7}	1.2×10^{-6}	2×10^{-6}	1.8×10^4	1.7×10^6	5.8×10^{-7}	2.6×10^{-6}	3.9×10^5
60	2.8×10^6	7.4×10^6	1.6×10^6	7.7×10^5	7×10^{11}	3.6×10^{-7}	1.4×10^{-7}	6.3×10^{-7}	1.2×10^{-6}	4.3×10^{-6}	1.7×10^4	1.7×10^6	5.8×10^{-7}	2.9×10^{-6}	3.5×10^5
78	6.6×10^5	5.5×10^6	1×10^6	9.8×10^5	1×10^{12}	1.5×10^{-6}	1.8×10^{-7}	9.8×10^{-7}	1×10^{-6}	3.7×10^{-6}	1.3×10^4	2.2×10^6	4.7×10^{-7}	4.2×10^{-6}	2.4×10^5
291	9.6×10^3	1.8×10^5	2.4×10^5	1.2×10^6	1.3×10^{12}	1.0×10^{-4}	5.6×10^{-6}	4.2×10^{-6}	8.3×10^{-7}	1.1×10^{-4}	1.7×10^3	2×10^6	5.1×10^{-7}	1.1×10^{-4}	9×10^3

Table 5.4 calculated mobilities limited by various scattering mechanisms at different temperature. The carrier density is also indicated. The total theoretical mobility μ_{To} excluding ionized impurity scattering μ_{BI} is compared to the experimental values. μ_{BI} is the theoretical mobility including μ_{BI} . For samples MV134 GaAs-GaAlAs.

TK°	μ_{po}	μ_A	μ_{PE}	μ_{RI}	$n_s \text{ cm}^{-2}$	μ_{po}^{-1}	μ_A^{-1}	μ_{PE}^{-1}	μ_{RI}^{-1}	μ_{TO}^{-1}	μ_{TO}^3	μ_{ex}	μ_{BI}	μ_{BI}^{-1}	μ_{TO}^{-1}	μ_{TO}
4	2.9×10^{13}	15×10^6	9×10^6	95×10^5	4.9×10^{12}	35×10^{-14}	6.8×10^{-7}	11×10^{-7}	1.1×10^{-6}	1.9×10^{-6}	5.3×10^5	1×10^4	2.3×10^7	4.3×10^{-8}	1.9×10^{-6}	5.2×10^5
64	1.9×10^6	1.3×10^6	5.3×10^5	2.5×10^6	5.6×10^{12}	5.2×10^{-7}	7.6×10^{-7}	1.9×10^{-6}	3×10^{-7}	3.5×10^{-6}	2.9×10^5	8.2×10^3	1.7×10^7	5.8×10^{-8}	3.6×10^{-6}	2.8×10^5
77	7×10^5	1.3×10^6	4.3×10^5	2.5×10^6	5.9×10^{12}	1.4×10^{-6}	7.8×10^{-7}	2.4×10^{-6}	4.1×10^{-7}	5×10^{-6}	2×10^5	7.5×10^3	1.7×10^6	5.8×10^{-7}	5.6×10^{-6}	1.8×10^5
90	3.2×10^5	1×10^6	3.3×10^5	3.3×10^6	7.2×10^{12}	3.1×10^{-6}	9.8×10^{-7}	3×10^{-6}	31×10^{-7}	7.4×10^{-6}	1.4×10^5	5.7×10^3	2.8×10^5	3.6×10^{-6}	1.1×10^{-5}	9.1×10^4
100	2×10^5	9.5×10^5	2.8×10^5	3.9×10^6	8×10^{12}	5.1×10^{-6}	1×10^{-6}	3.6×10^{-6}	2.6×10^{-7}	9.9×10^{-6}	1×10^5	4.8×10^3	1.1×10^7	9×10^{-8}	1×10^{-5}	1×10^5
110	1.3×10^5	8.3×10^5	2.4×10^5	4.6×10^6	9×10^{12}	7.6×10^{-6}	1.2×10^{-6}	4.2×10^{-6}	2.2×10^{-7}	1.3×10^{-5}	7.6×10^4	4×10^3	1.8×10^7	5.7×10^{-8}	1.3×10^{-5}	7.7×10^4
120	9.5×10^4	1.1×10^6	2.1×10^5	5.7×10^6	1×10^{13}	1.1×10^{-5}	9.2×10^{-7}	4.8×10^{-6}	1.8×10^{-7}	1.7×10^{-5}	5.9×10^4	3.5×10^3	2.4×10^7	4.3×10^{-8}	1.7×10^{-5}	5.9×10^4
220	1.8×10^4	7.6×10^4	7.5×10^4	8.6×10^7	2.3×10^{13}	5.7×10^{-5}	1.3×10^{-5}	1.3×10^{-5}	1.2×10^{-8}	8.3×10^{-5}	1.2×10^4	1.5×10^3	5.7×10^7	1.8×10^{-8}	8.3×10^{-5}	1.2×10^4
296	9.3×10^3	5.1×10^4	4.8×10^4	2.6×10^7	3.1×10^{13}	1.1×10^{-4}	2×10^{-5}	2.1×10^{-5}	3.9×10^{-8}	1.5×10^{-4}	6.6×10^3	1×10^3	6.4×10^7	1.5×10^{-8}	1.5×10^{-4}	6.6×10^3

Table 55 calculated mobilities limited by various scattering mechanisms at different temperature. The carrier density is also indicated. The total theoretical mobility μ_{to} excluding ionized impurity scattering μ_{BI} is compared to the experimental values. μ_{to} is the theoretical mobility including μ_{BI} . For sample KES422 GaAs-GaAlAs.

TK°	μ_{Po}	μ_{RI}	μ_{Allo}	n_{scm}^{-2}	μ_{ex}	μ_{po}^{-1}	μ_{RI}^{-1}	μ_{Allo}^{-1}	μ_{To}^{-1}	μ_{To}
4.2	2×10^{13}	3.3×10^5	2.8×10^5	7.4×10^{11}	8.2×10^4	5×10^{-14}	3×10^{-6}	3.6×10^{-6}	6.6×10^{-6}	1.5×10^5
21	1.3×10^9	3.3×10^5	2.6×10^5	7.4×10^{11}	8.2×10^4	7.7×10^{-10}	3×10^{-6}	3.9×10^{-6}	6.9×10^{-6}	1.5×10^5
54	4.7×10^6	3.8×10^5	2.3×10^5	6.8×10^{11}	7.5×10^4	21×10^{-8}	2.6×10^{-6}	4.4×10^{-6}	7.2×10^{-6}	1.4×10^5
68	1.3×10^6	3.8×10^5	2.2×10^5	6.8×10^{11}	6.9×10^4	7.7×10^{-7}	2.6×10^{-6}	4.6×10^{-6}	8×10^{-6}	1.3×10^5
78	6×10^5	4×10^5	2.1×10^5	8.8×10^{11}	6.2×10^4	1.7×10^{-7}	2.5×10^{-6}	4.8×10^{-6}	9×10^{-6}	1.1×10^5
88	3.3×10^5	4×10^5	2×10^5	8.9×10^{11}	5.5×10^4	3.0×10^{-7}	2.5×10^{-6}	5×10^{-6}	1.1×10^{-5}	9.5×10^4
96	2.2×10^5	4.1×10^5	1.9×10^5	9.1×10^{11}	4.9×10^4	4.6×10^{-6}	2.4×10^{-6}	5.3×10^{-6}	1.2×10^{-6}	8.1×10^4
106	1.4×10^5	4.1×10^5	1.8×10^5	9.2×10^{11}	4.3×10^4	7.1×10^{-6}	2.4×10^{-6}	5.6×10^{-6}	1.5×10^{-5}	6.6×10^4
201	1.9×10^4	5.8×10^5	1.2×10^5	1.2×10^{12}	1.7×10^4	5.3×10^{-5}	1.7×10^{-6}	8.3×10^{-6}	6.3×10^{-5}	1.6×10^4
292	8.3×10^3	7.6×10^5	7.8×10^4	1.5×10^{12}	9.8×10^3	1.2×10^{-4}	1.3×10^{-6}	1.3×10^{-5}	1.3×10^{-4}	7.5×10^3

Table 5.6 calculated mobilities for various scattering mechanism for sample PMB137 InP-InGaAs μ_{ex} is the experimentally determined value at different Temp. T.

Parameters	MV134	KES422	PMB137
ϵ_0 static dielectric constant.	12.9	12.9	13.8
m^* electron effective mass.	$0.076 m_0$	$0.076 m_0$	$0.05 m_0$
d_0 thickness of spacer layer	150 \AA	90 \AA	100 \AA
N_D doping densities	10^{18} cm^{-3}	10^{18} cm^{-3}	$5 \times 10^{17} \text{ cm}^{-3}$

Table 5.7 Constants used to calculate μ (Walukiewicz et al 1984).

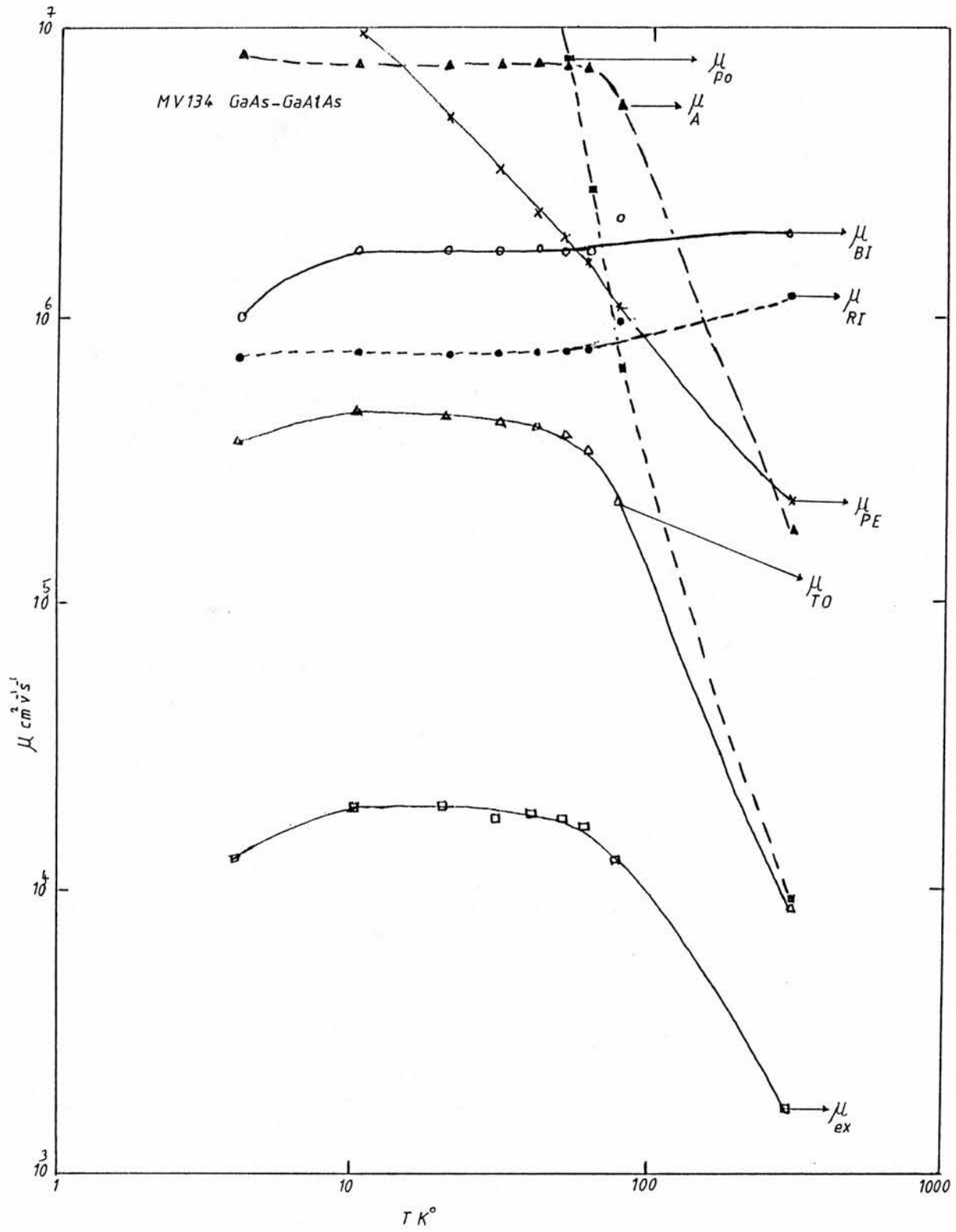


Fig 5.3 μ for different scattering mechanisms versus T for the MV134 GaAs-GaAlAs Heterostructure.

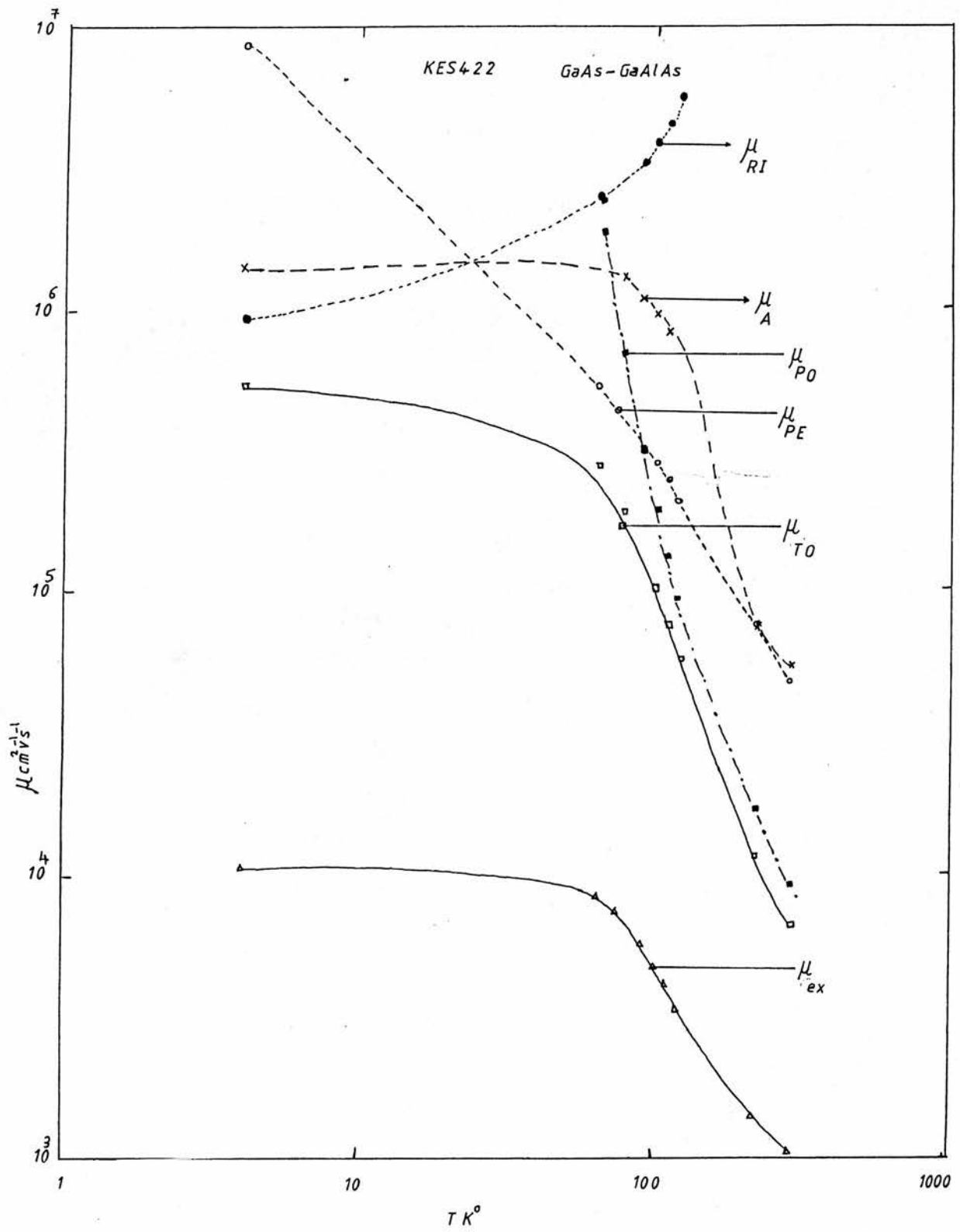


Fig 5.4 μ of different scattering mechanisms versus T for the KES422 sample.

InP-InGaAs
PMB137

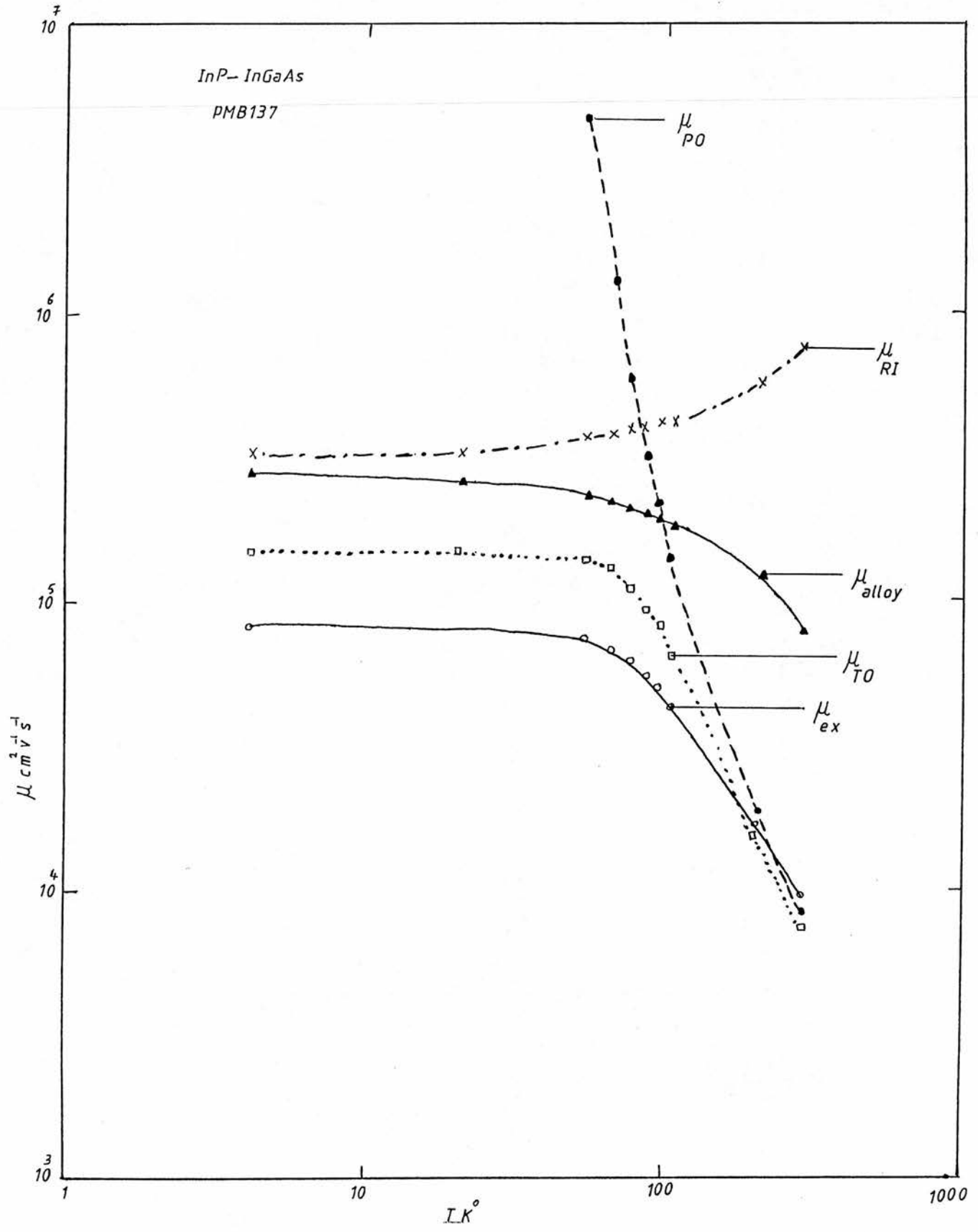


Fig.5.5 μ dependence on T for InP-InGaAs Heterojunction PMB137

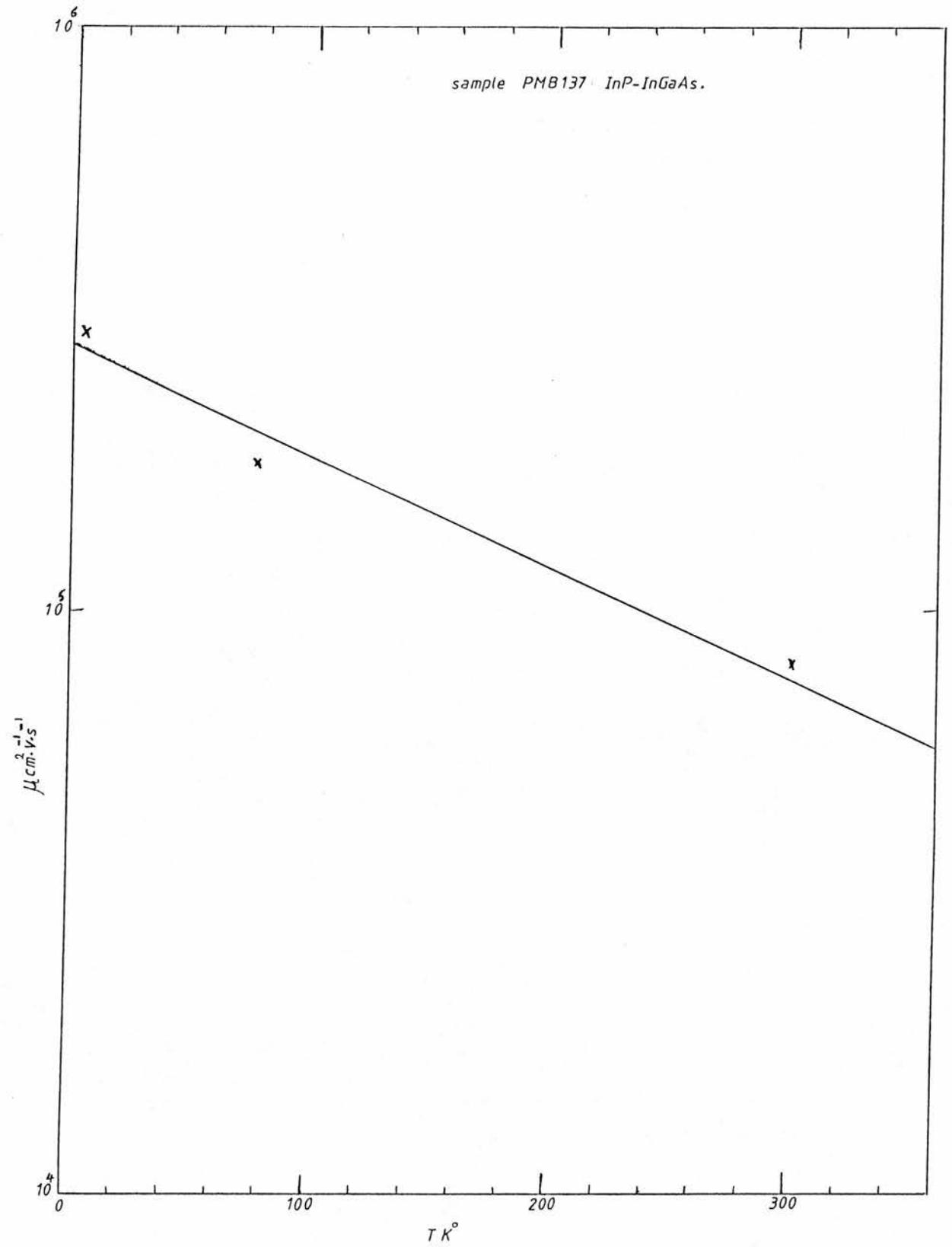


Fig 5.6 Extrapolated graph of μ versus T (from Takeda et al 1981) to calculate alloy scattering

5.3 Shubnikov de Haas measurements of 2D systems

The SdH oscillations for samples GaAs/GaAlAs (MV134) InP/InGaAs (PMB137, PMB41, PMB121) and GaAs/GaAlAs HEMT (OC117 and HEMT #1) are shown in Figs 5.7, 5.8a,b, 5.9, 5.10 and 5.11a,b,c. From the peak positions of the oscillations the periodicity upon $1/B$ can be obtained. The electron density n_s of the 2DEG in each sample can be calculated from SdH traces recorded with B and E perpendicular to each other using equation (4.10).

In Fig 5.7 the traces obtained from GaAs-GaAlAs MV134 show the first derivative of the magnetoresistance as a function of the field.

The oscillations are observed down to fields as low as 0.5T. As the angle θ increased the oscillations moved to higher fields as $B_\theta = B_{\theta=90} \cos \theta$ proving the two dimensionality of the carriers. n_s has been found to be $4.5 \times 10^{11} \text{ cm}^{-2}$. Fourier analysis of the magnetoresistance against $1/B$ for this sample reveals that only one subband is occupied. The fundamental field is $B_f^0 = 11.1\text{T}$ and from it we obtain an electron density n_0 of $5.4 \times 10^{15} \text{ m}^{-2}$.

The energy of the ground state E_0 is 72.8 meV. The expression for an asymmetric triangular well is given in table 2.1 and is of the following form:

$$E_0(\text{meV}) = 61.15 \left(0 + \frac{3}{4} \right)^{2/3} \left(\frac{n_s}{10^{12} \text{ cm}^{-2}} \right)^{2/3} \times \left(\frac{11.5}{t_0} \right)^{2/3} \left(\frac{0.916m_0}{m_z} \right)^{1/2} \dots\dots\dots 5.1$$

where m_z is m^* perpendicular to the interface; for GaAs $m^* = m_z = 0.067 m_0$ and $\epsilon_0 = 13$, (Ando et al 1982). The Fermi energy is 19.3 meV and is calculated from equation (Ando et al 1982):

$$E_F \text{ (meV)} = 6.3 \left(\frac{n_s}{10^{12} \text{ cm}^{-2}} \right) \left(\frac{Z}{g_v} \right) \left(\frac{0.19 m_0}{m} \right) \dots\dots\dots 5.2$$

where g_v is the valley degeneracy and for GaAs $g_v = 1$.

The average distance of the electron from the interface with only one subband occupied is calculated from:

$$Z_0 = \left(\frac{9\epsilon_0 \epsilon \hbar^2}{4m_z e^2 N^*} \right)^{1/3} \dots\dots\dots 5.3$$

where $\epsilon =$ dielectric constant, ϵ_0 static dielectric constant and $N^* = N_{\text{depl}} + \frac{11}{32} n_s$, since N_D is too small $N^* = n_s \times \frac{11}{32}$. Simplifying the above equation

$$Z_0 \text{ (nm)} = 2.283 \left(\frac{32 \times 10^{12} \text{ cm}^{-2}}{11 n_s} \right)^{1/3} \times \left(\frac{13}{11.5} \right)^{1/3} \left(\frac{0.916}{0.067} \right)^{1/3} \dots\dots\dots 5.4$$

and for MV134, $Z_0 = 175 \text{ \AA}$.

Fig 5.8a shows the SdH traces for sample PMB137 (InP/InGaAs heterostructure) up to 12T. In Fig 5.8b the second derivative of magnetoresistance is shown for the same sample expanded up to 5T. The oscillations start at 0.5T, n_s is found to be $0.5 \times 10^{12} \text{ cm}^{-2}$ using equation 4.10.

At 3.2T and $\theta = 90^\circ$ a small peak appears as θ the field was tilted away from the perpendicular position.

This peak changes its shape and moves to higher field probably indicating spin splitting. Fourier analysis has been done on the SdH oscillations for PMB137; it reveals that two subbands are occupied with fundamental fields $B_f^0 = 9.34\text{T}$, $B_f^1 = 6.73\text{T}$ and $n_o^0 = 4.6 \times 10^{15} \text{ m}^{-2}$, $n_o^1 = 3.2 \times 10^{15} \text{ m}^{-2}$.

The energy of the ground state E_0^0 is 73.96 meV and E_0^1 is 61.64 meV. The total electron density of 7.4×10^{15} compares well with VdP measurements; the Fermi energy for the ground state is 22.02 meV and for the higher subband is 15.32 meV.

The peak appearing at 3.2T is possibly due to spin splitting of the $n' = 1$ because $B_+ - B_-$ is 0.6T or

$$\Delta h\nu_c = \frac{\hbar e B}{m^*} = \frac{6.6 \times 10^{-34} \times 1.6 \times 10^{-19} \times 0.6}{2\pi \times 0.05 \times 9.1 \times 10^{-31}} = 2.22 \times 10^{-22} = 1.39 \text{ meV}$$

$$\Delta s = g^* \mu_B B; \quad g^* = 10 \quad \text{for IrGaAs and } \mu_B = 9.3 \times 10^{-24} \text{ JT}^{-1}$$

$$\frac{10 \times 9.3 \times 10^{-24} \times 0.6}{1.6 \times 10^{-19}} = 34.9 \times 10^{-5} = 0.35 \text{ meV}$$

Fig 5.9 shows the SdH traces for a MQW sample of GaInAs-InP (PMB41) as a function of field B. The oscillations start at 1.5T approximately, n has been found to be $4.7 \times 10^{11} \text{ cm}^{-2}$. Fourier analysis has not been used for this sample because at 90° there are not sufficient oscillations and it is not clear whether they are a set of square wells or triangular wells from back to back heterojunctions.

Despite the poor quality of the oscillations tilting the field shows that they are two dimensional in character.

Fig 5.10 shows the SdH traces up to 11T for sample PMB121 InP-InGaAs superlattice in the dark.

Fourier analysis for sample PMB121 in the dark shows one subband with electron density $n = 0.56 \times 10^{15} \text{ m}^{-2}$ and a fundamental field $B_f^0 = 1.12\text{T}$ and the energy of ground state $E_0^0 = 4.88 \text{ meV}$. The Fermi energy E_f^0 is found to be 2.68 meV and Z_0 the average distance of electron from the interface with only one subband occupied is 234\AA .

n_{SdH} is $1/2 n_{\text{VdP}}$; there are few oscillations and a very broad low μ , near bulk mobility; hence the electron transport is seriously affected by 3D effects.

This sample shows a 2DEG from the series of recordings of the SdH effect taken with different angles of the magnetic field with respect to the plane of the sample. Fig 5.11a, 5.11b and 5.11c GaAs-GaAlAs (HEMT #1 and OC117) shows SdH traces at different angles proving a 2DEG with electron density of $1.2 \times 10^{12} \text{ cm}^{-2}$ and $0.8 \times 10^{12} \text{ cm}^{-2}$. Fourier analysis of sample HEMT #1 GaAs-GaAlAs reveals two subbands of two fundamental fields $B_F^0 = 4.1\text{T}$ and $B^1 = 15.25\text{T}$ where the electron density n_0 is $7.4 \times 10^{15} \text{ cm}^{-2}$ and n_1 is $1.9 \times 10^{15} \text{ cm}^{-2}$ and E_0^0 is 90 meV and E_F^0 is 26.4 meV and E^1 is 6.8 meV. The average distance of electrons from the interface with only one subband occupied is 88\AA and with two subbands is 176\AA . The data analysis of OC117 is very similar to that of HEMT #1.

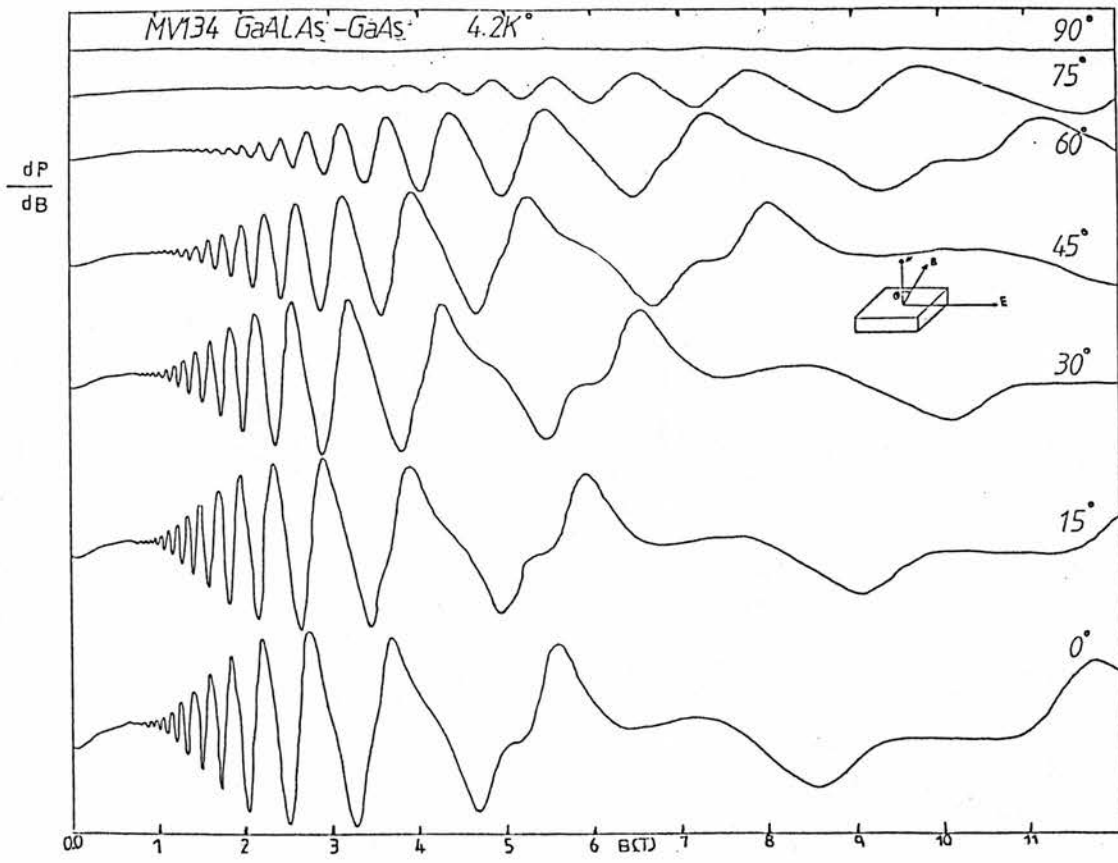


Fig 5.7 First derivative of the magnetoresistance against magnetic field for a heterostructure of GaAs GaAlAs MV134 as a function of the angle between the electric and magnetic field.

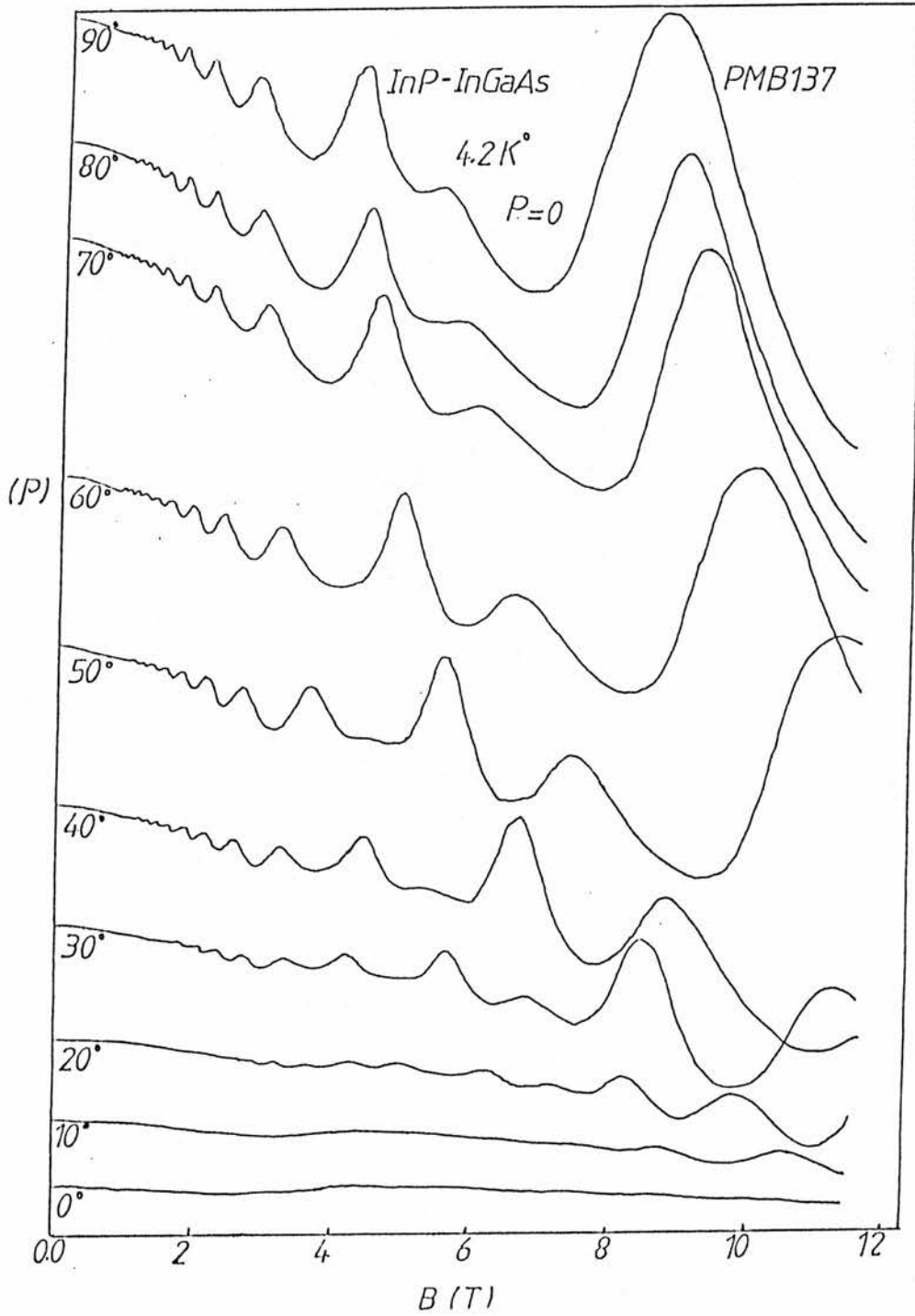


Fig 5.8a Magnetoresistance against magnetic field for sample PMB137 (GaInAs-InP H.J.) at different angles.

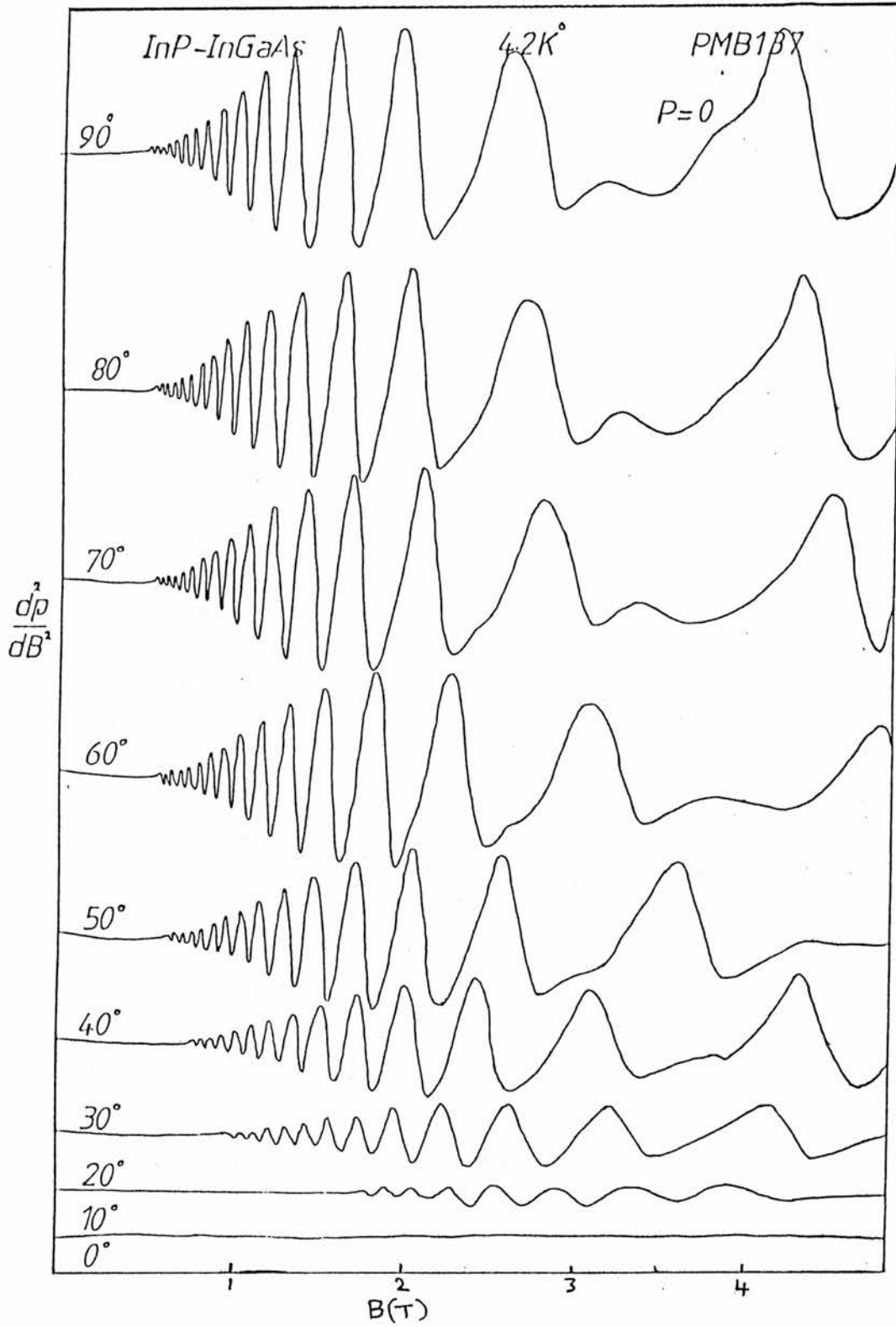


Fig 5.8b Second derivative of the magnetoresistance against magnetic field for sample PMB137 GaInAs-InP H.J. at different angles.

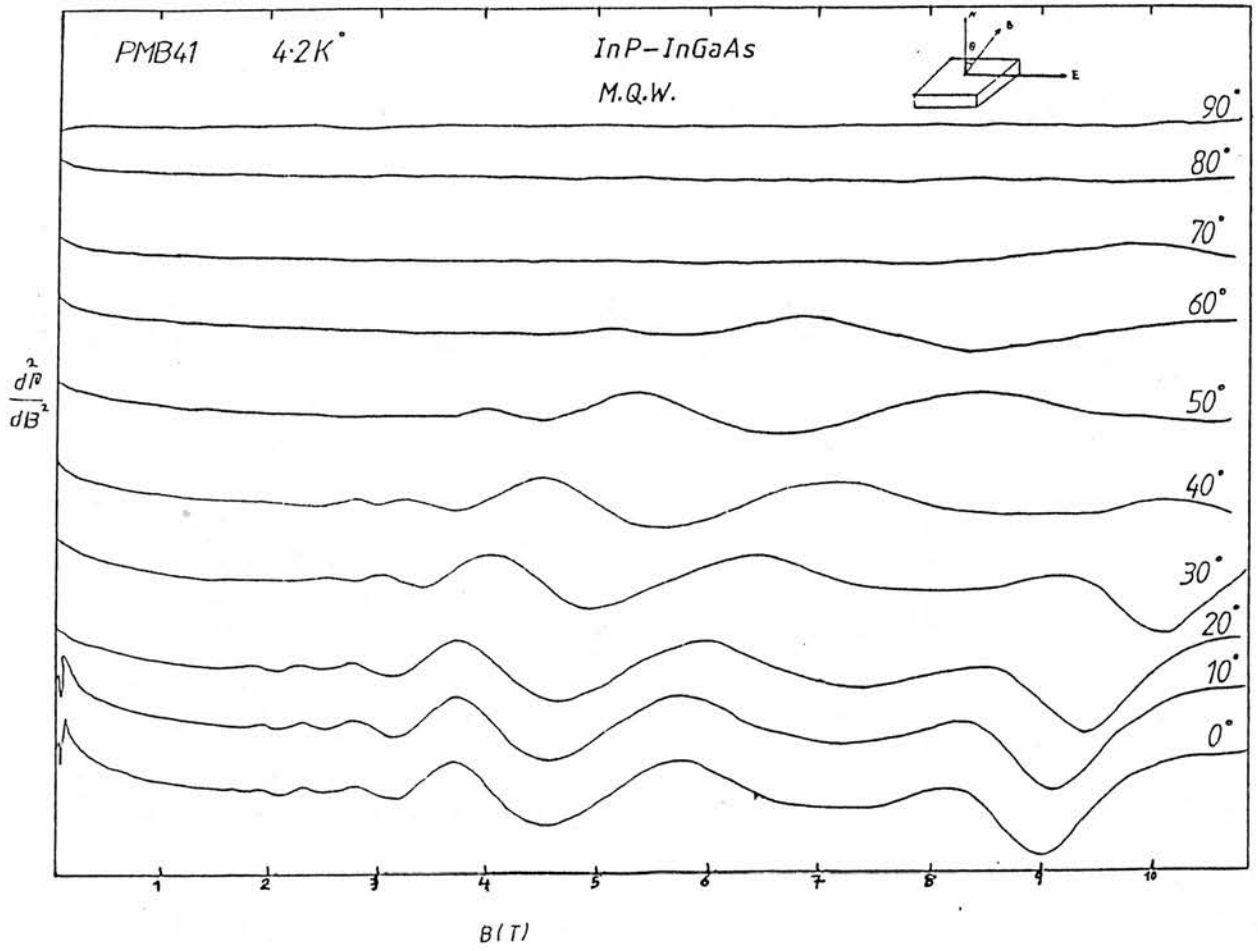


Fig. 5.9 Second derivative of the magnetoresistance against magnetic field for sample PMB41 M.Q.W. at different angles.

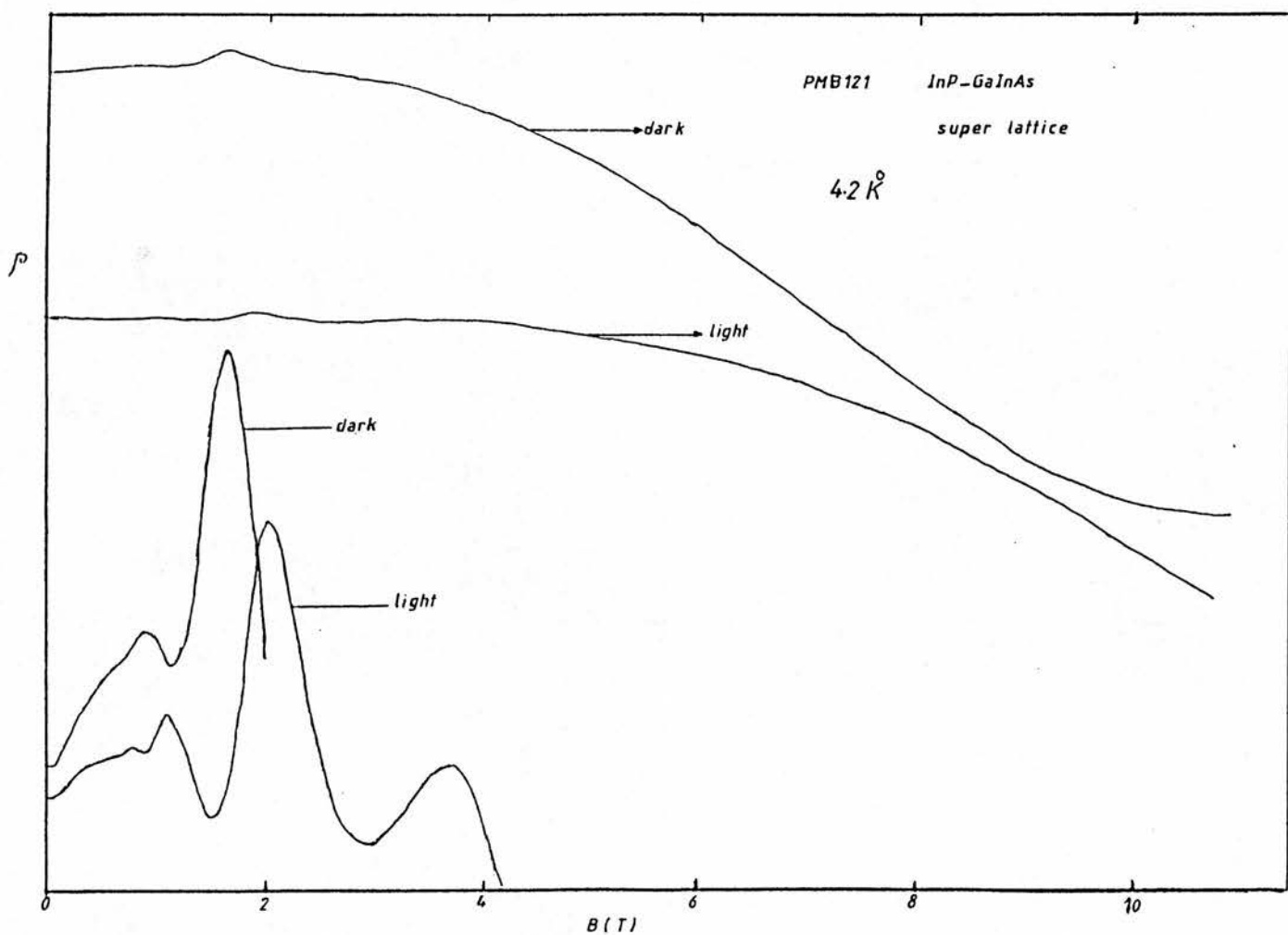


Fig 5.10 Magnetoresistance against magnetic field for sample PMB121 super lattice at 90 degree angle .

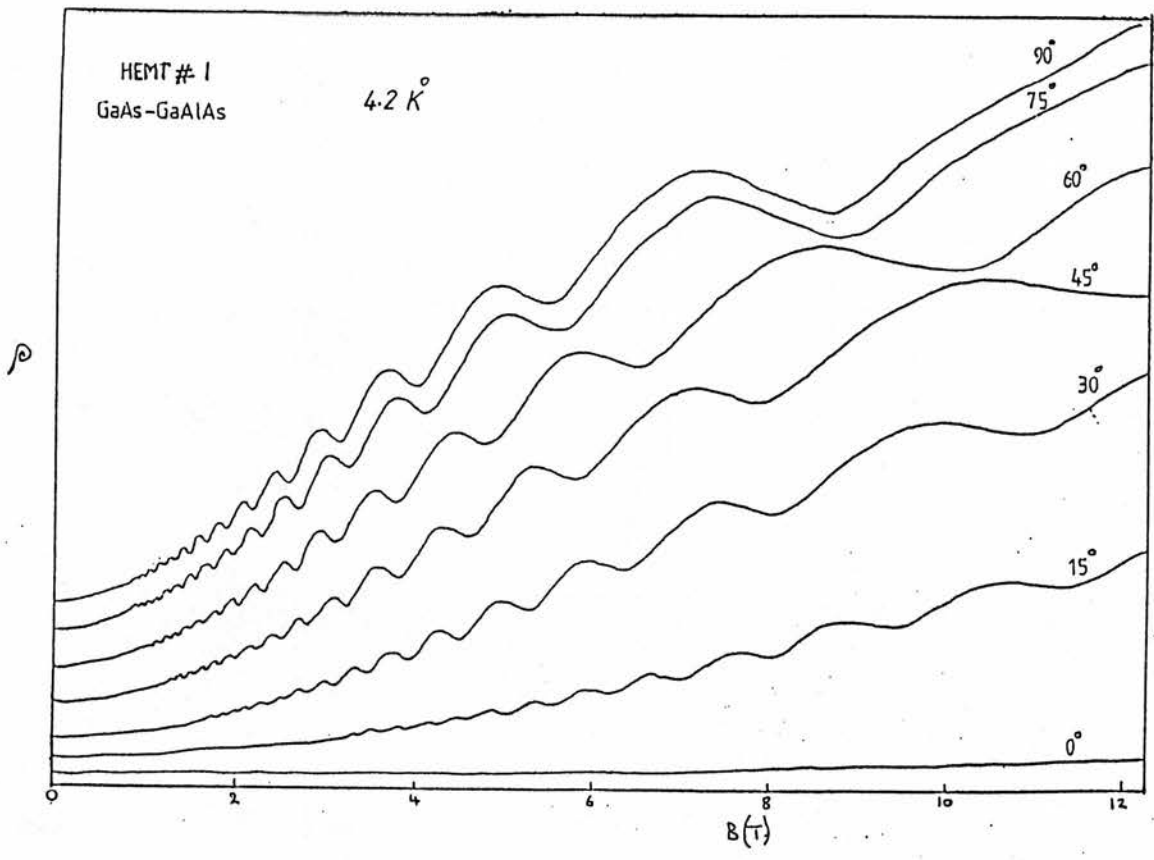


Fig.5.11a Magnetoresistance against magnetic field for sample HEMT#1 at different angles.

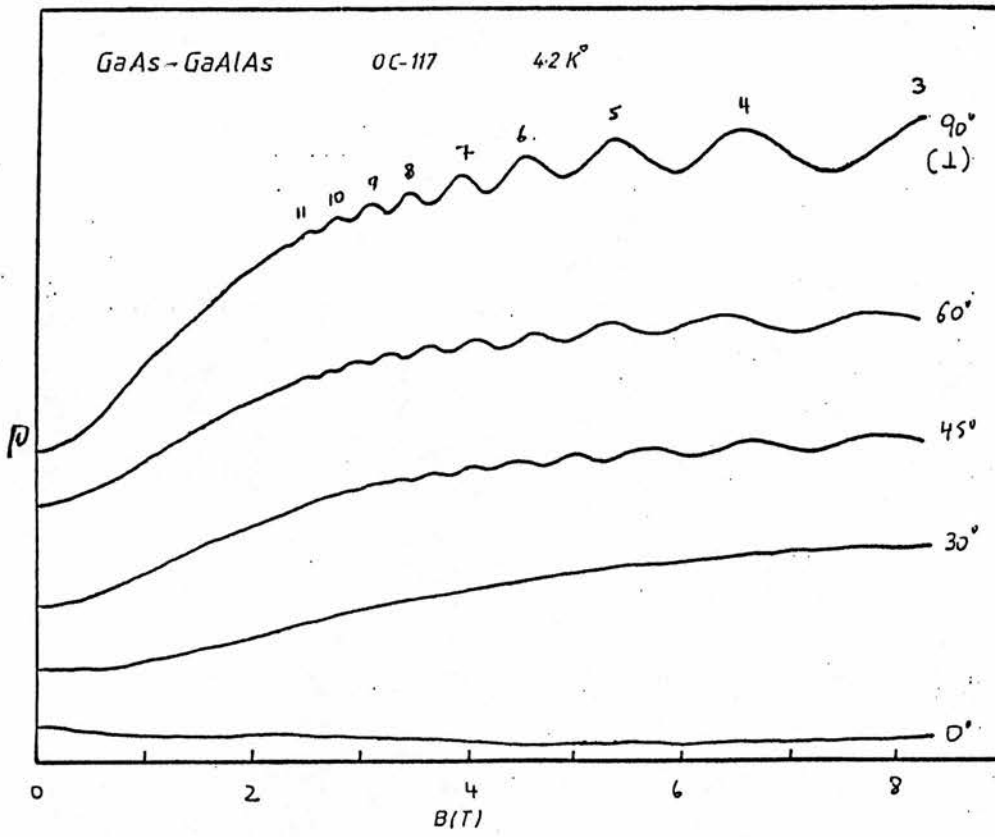


Fig 5.11b Magnetoresistance against magnetic field for sample 0C117 at different angles.

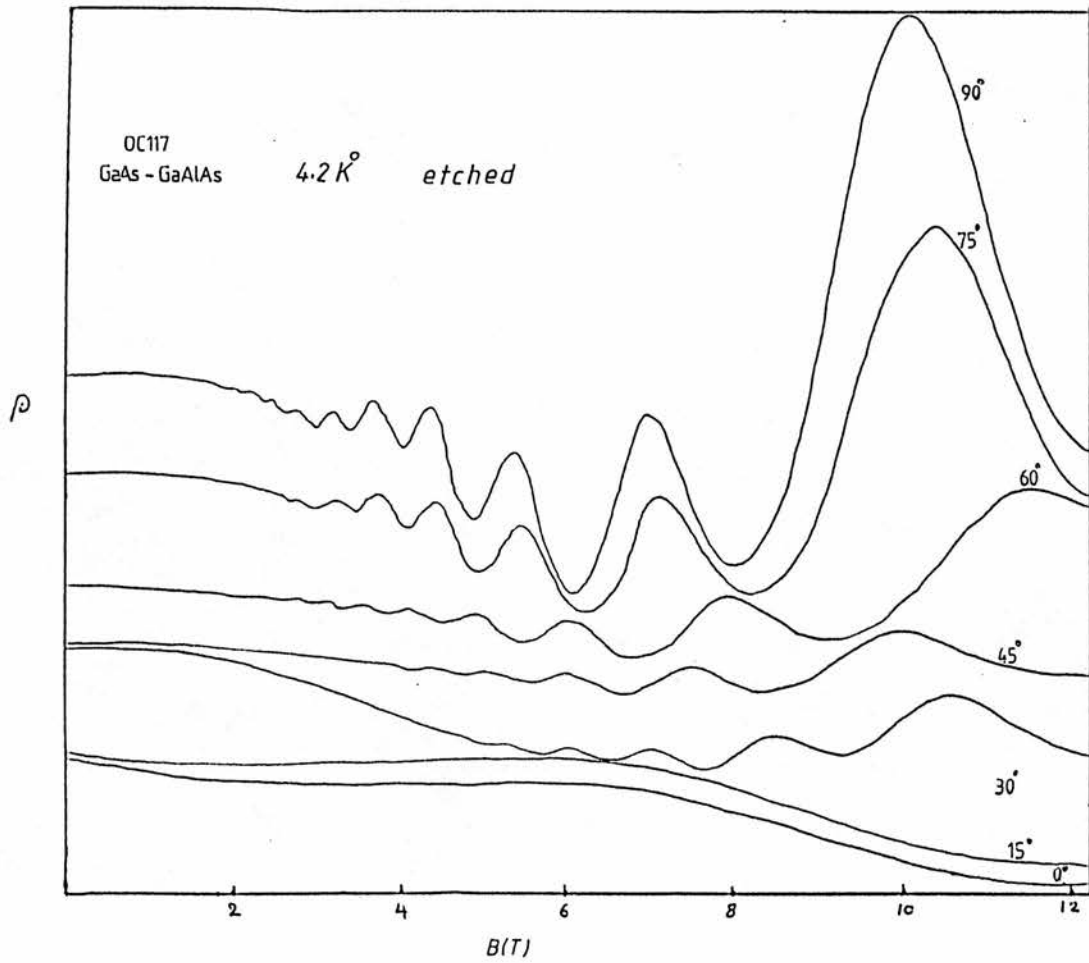


Fig 5.11c Magnetoresistance against magnetic field for sample OC117 at different angles.

5.4 Measurements of Bulk InP

3D Samples InP232, InP233 and PMB106 were grown by MBE. The first two samples show similarity in both mobility and electron density, the mobility increased sharply and shows a high value at 80 K equal to $2.5 \times 10^4 \text{ cm}^2/\text{V.s}$ and drops down to a room temperature value around $2.5 \times 10^3 \text{ cm}^2/\text{V.s}$. The electron density increases starting from $4.5 \times 10^{15} \text{ cm}^{-3}$ at 4K up to $(1.8-2.5) \times 10^{16} \text{ cm}^{-3}$ at room temperature. Sample PMB106 exhibits a maximum mobility of $4.2 \times 10^4 \text{ cm}^2/\text{V.s}$ at 80 K while the electron density increases gradually up to $3.5 \times 10^{15} \text{ cm}^{-3}$. (See figure 5.12, 5.13 and 5.14.) Donor concentration for InP samples have been calculated by the Mansfield formula. (Proc Phys Soc B69, 1956, p76.)

$$x = \frac{\bar{n}(kT)^{\frac{1}{2}}\epsilon, h}{e^2(2m^*)^{\frac{1}{2}}F_{\frac{1}{2}}(J^*)} \dots\dots\dots 5.1$$

where $\epsilon = \frac{12.4}{9 \times 10^9} = 1.38 \times 10^9 \text{ MKs}$

$h = 6.6 \times 10^{-34} \text{ J.S}$

$m^* = 0.082 \times 9.1 \times 10^{-31} \text{ kgm}$

$k = 1.38 \times 10^{-23} \text{ J.K}^{-1}$

$e = 1.6 \times 10^{-19} \text{ Coul.}$

J^* is the reduced Fermi level E_F/kT . $F_2(J^*)$, $F_{\frac{1}{2}}(J^*)$ are Fermi Dirac integrals. \bar{n} can be obtained from Mansfield. The value of $f(x)$ can be found from

$$f(x) = \ln(1 + x) - x/(1 + x) \dots \dots \dots 5.2$$

And from σ_I the conductivity formula N can be calculated

$$ne\mu = \sigma_I = \frac{32e^2m^*(kT)^3F_2(J^*)}{Ne^2h^3f(x)} \dots \dots \dots 5.3$$

The Fermi-Dirac integrals were obtained from tables.

Where $n_s = n_{LT} + 2N_A$, n_{LT} = electron density at 4.2 K^o and then
 $N_D = n_{RT} + N_A$, n_{RT} = electron density at 300 K^o

N_A : No of acceptors

N_D : No of Donors (residual donors)

$$K = \frac{N_A}{N_D} \text{ compensation ratio}$$

The calculated N_A , N_D , K, n_{3D} and μ_{3D} are shown in table 5.8

Table 5.8 shows that InP sample 233 has the highest mobility of the three and the lowest compensation ratio.

Sample	$N_A \text{ cm}^{-3}$	$N_D \text{ cm}^{-3}$	K	$n_{30} = N_D - N_A$	$\mu = \frac{1}{\rho e n_{30}} \text{ cm}^2 \text{ v}^{-1} \text{ s}^{-1}$
InP232	0.86×10^{22}	3.1×10^{22}	0.3	2.24×10^{22}	0.1288
InP233	0.48×10^{22}	2.3×10^{22}	0.21	1.82×10^{22}	0.1793
InP106	0.79×10^{22}	1.5×10^{22}	0.69	0.36×10^{22}	0.0389

Table 5.8 N_A , N_D , K , n_{30} and μ_{30} for InP samples.

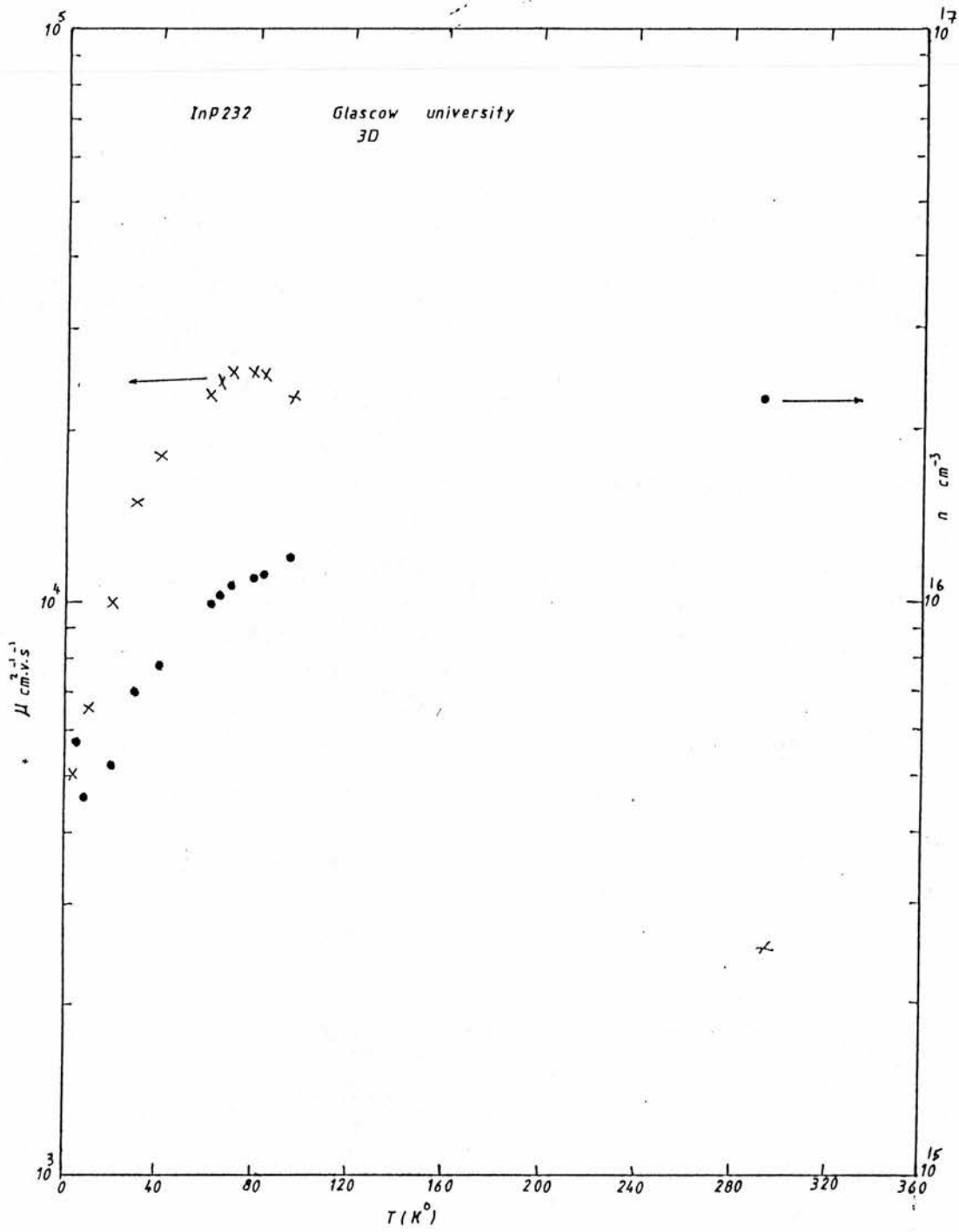


Fig 5.12 μ, n versus T of sample 232 3D InP.

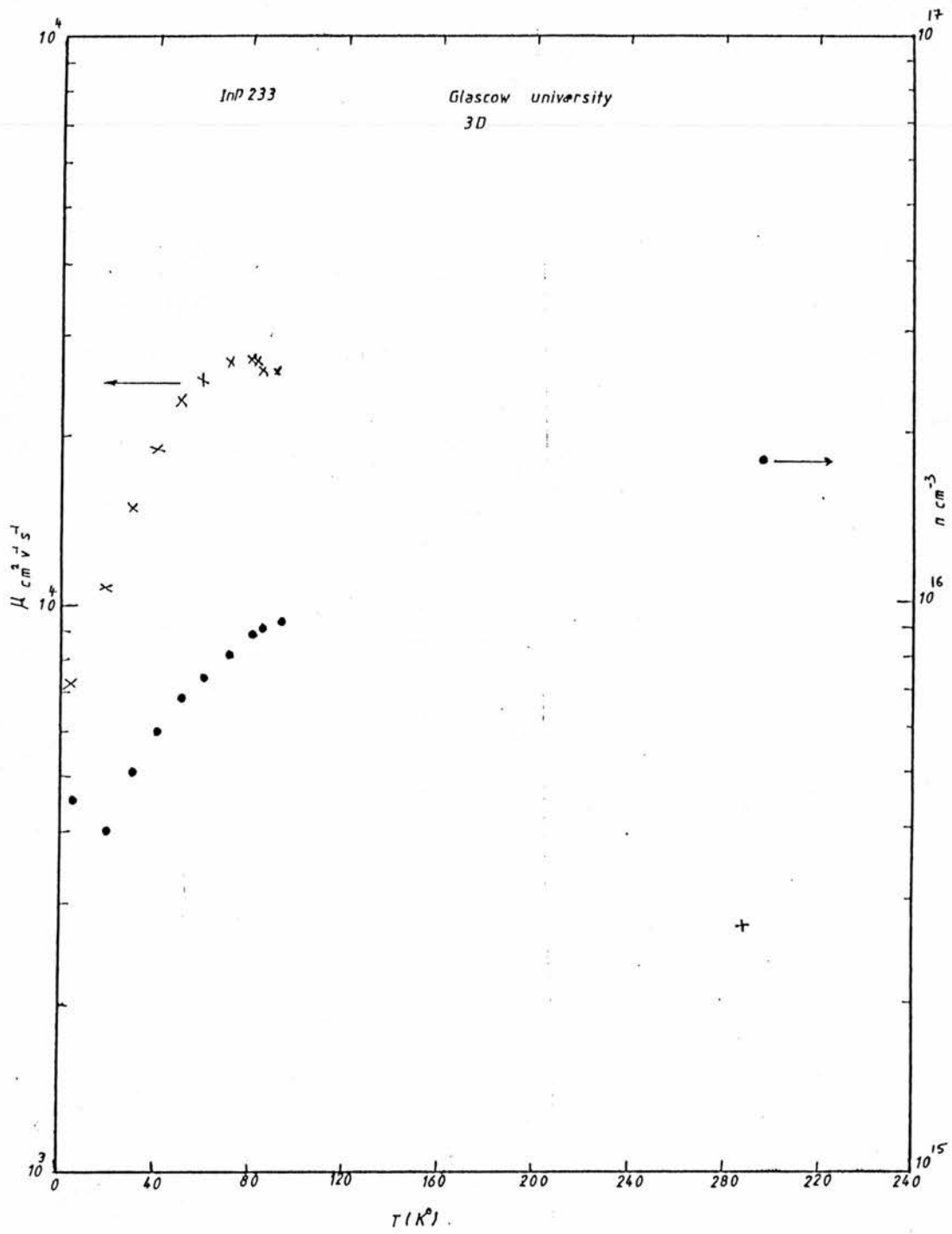


Fig 5.13 μ, n versus T of sample 233 3D InP.

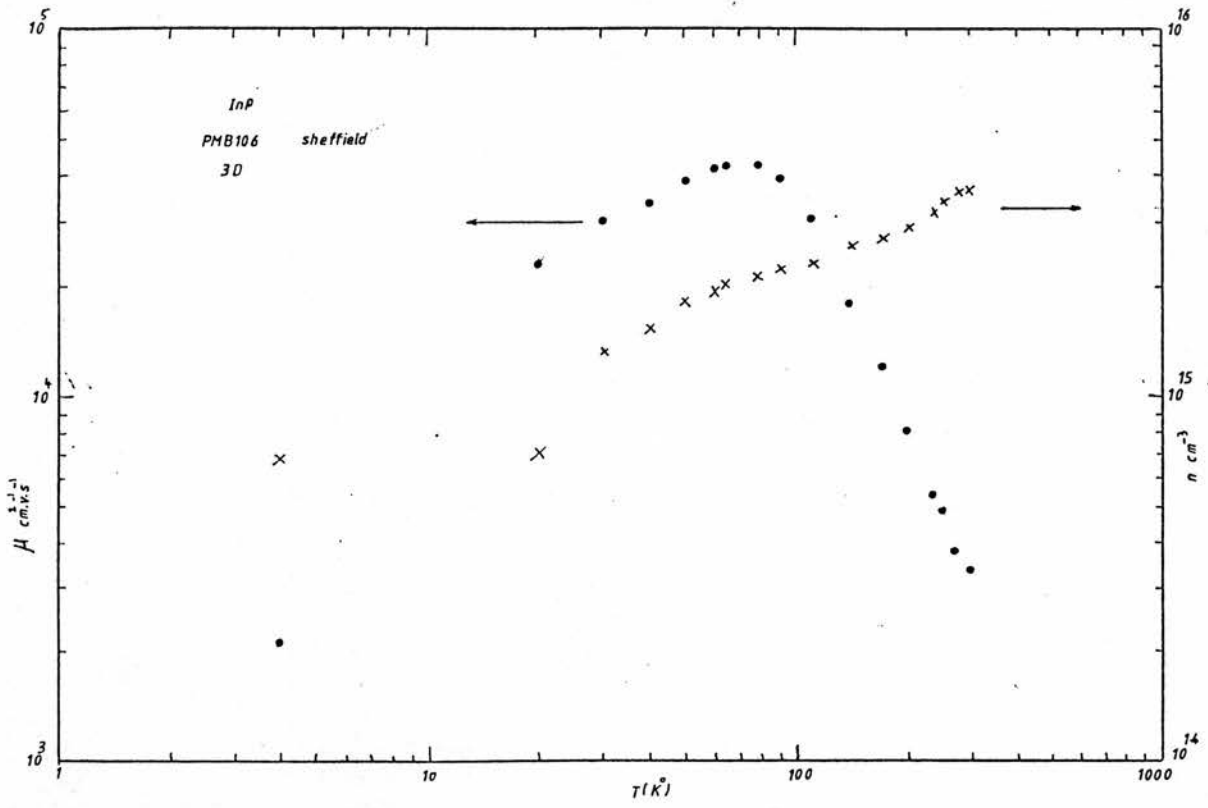


Fig 5.14 μ, n versus T of sample PMB106 3D InP.

5.5 Persistent photoconductivity in InP-InGaAs

Persistent photoconductivity in this system is not fully understood. Agreement as to whether the photocreated hole is trapped in the substrate and the electron drawn towards the interface quantum well by the function field is still to be reached.

In the single square quantum well PMB78 SdH traces were recorded with sample after illumination with different wavelengths around the energy gap of InP at 4.2K° are 1.423 eV (equivalent to 871 nm) and 0.78 eV (equivalent to 1590 nm), respectively.

It was not possible to identify any particular photon energy as being responsible for the persistent photoconductivity in the range from 880 to 940 nm, 1.41 to 1.32 eV, respectively. Therefore these results suggest that the PPC level is within 10 meV of the InP energy gap since after white light illumination the PPC was observed. The effect of band gap illumination is clearly shown in Fig 5.16 where within the experimental error the density in the dark and after illumination remains constant for pressures up to 6.5 kbar, ie, the level involved in the PPC is not affected by increasing both energy gaps by approximately 60-70 meV assuming that the InP energy gap pressure coefficient is 11 meV/kbar. Fig 5.17 shows traces of SdH oscillations at atmospheric pressure and at 6.5 kbar before and after illumination, from which the data points in Fig 5.15 were obtained. Sample PMB137 InP-InGaAs shows no significant change of electron density under illumination (see table 5.3). There remains the possibility that there was insufficient photon flux impinging on the sample when light of 940 nm was used because the transmission of the optical fibre had a dip near this wavelength and optimum coupling was not achieved. However, this was not the case for 880 nm.

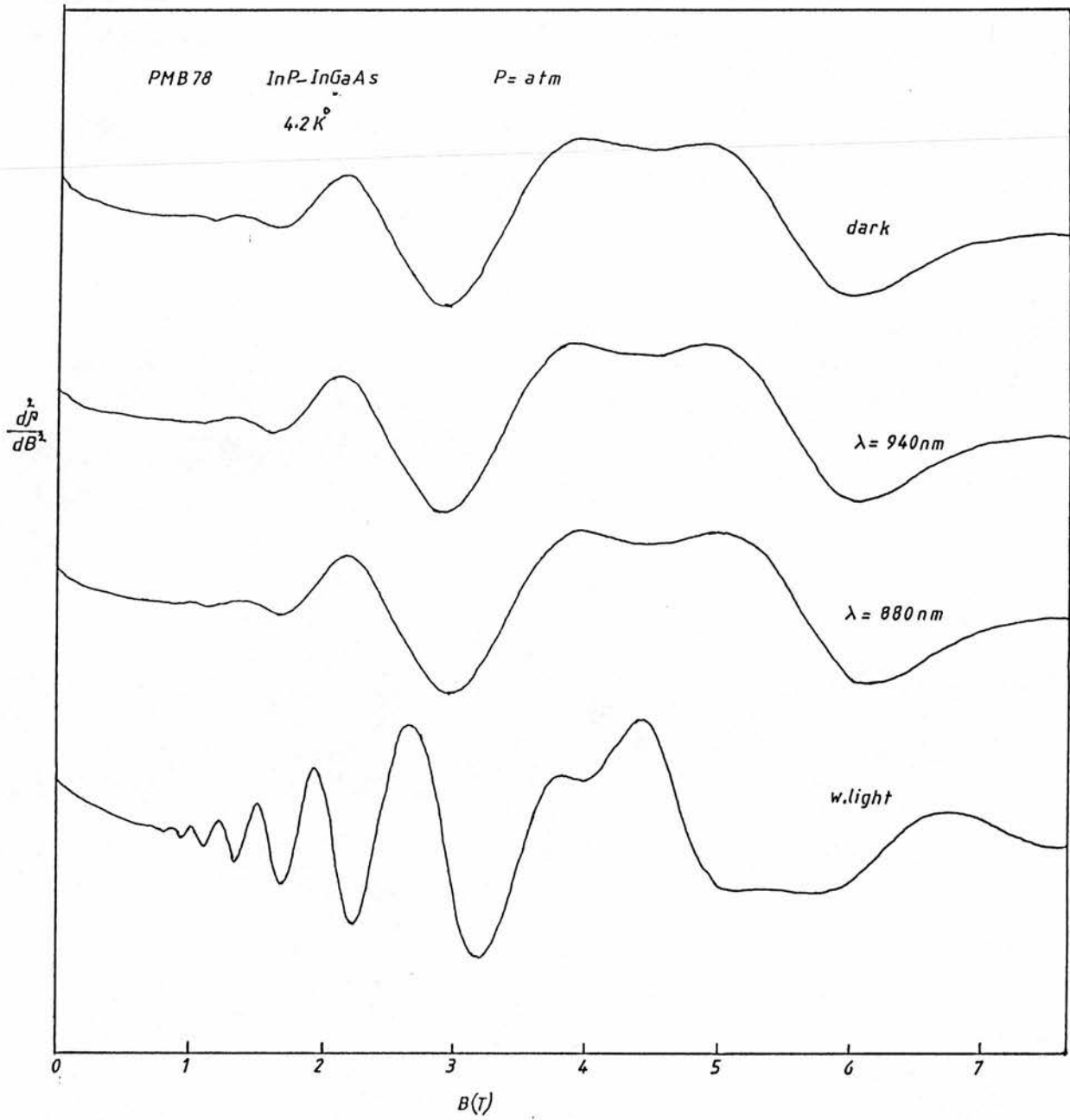


Fig 5.15 SdH oscillation $\frac{dR}{dB}$ versus B for sample PMB78 at $P=atm$ with different wave length.

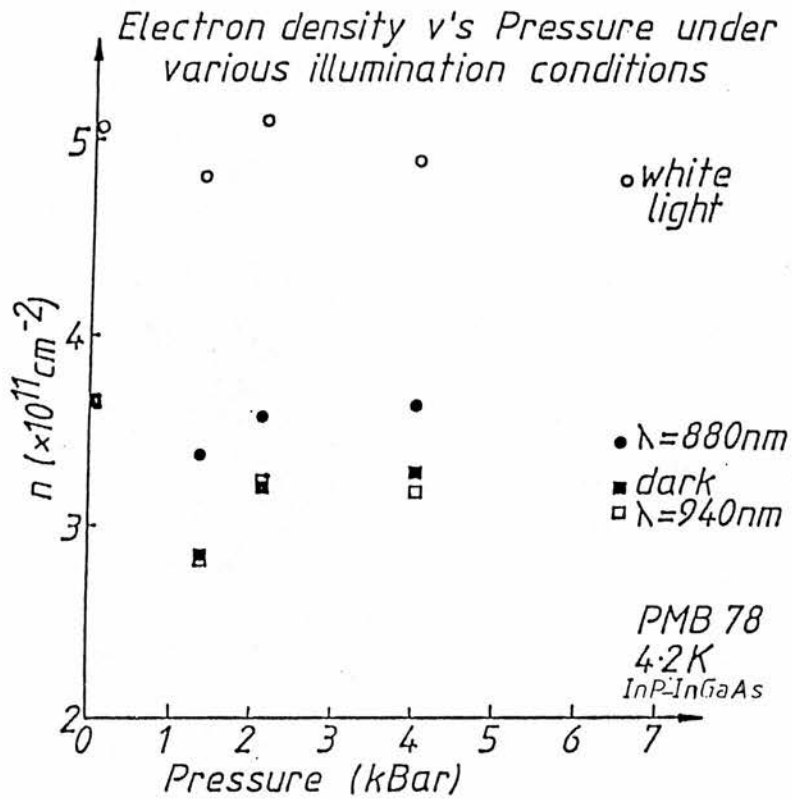


figure 5.16 shows the density of the 2DEG after the sample has been illuminated with light of the indicated wavelengths. It is shown that for persistent photoconduction to occur photons of energy less than 940nm are required.

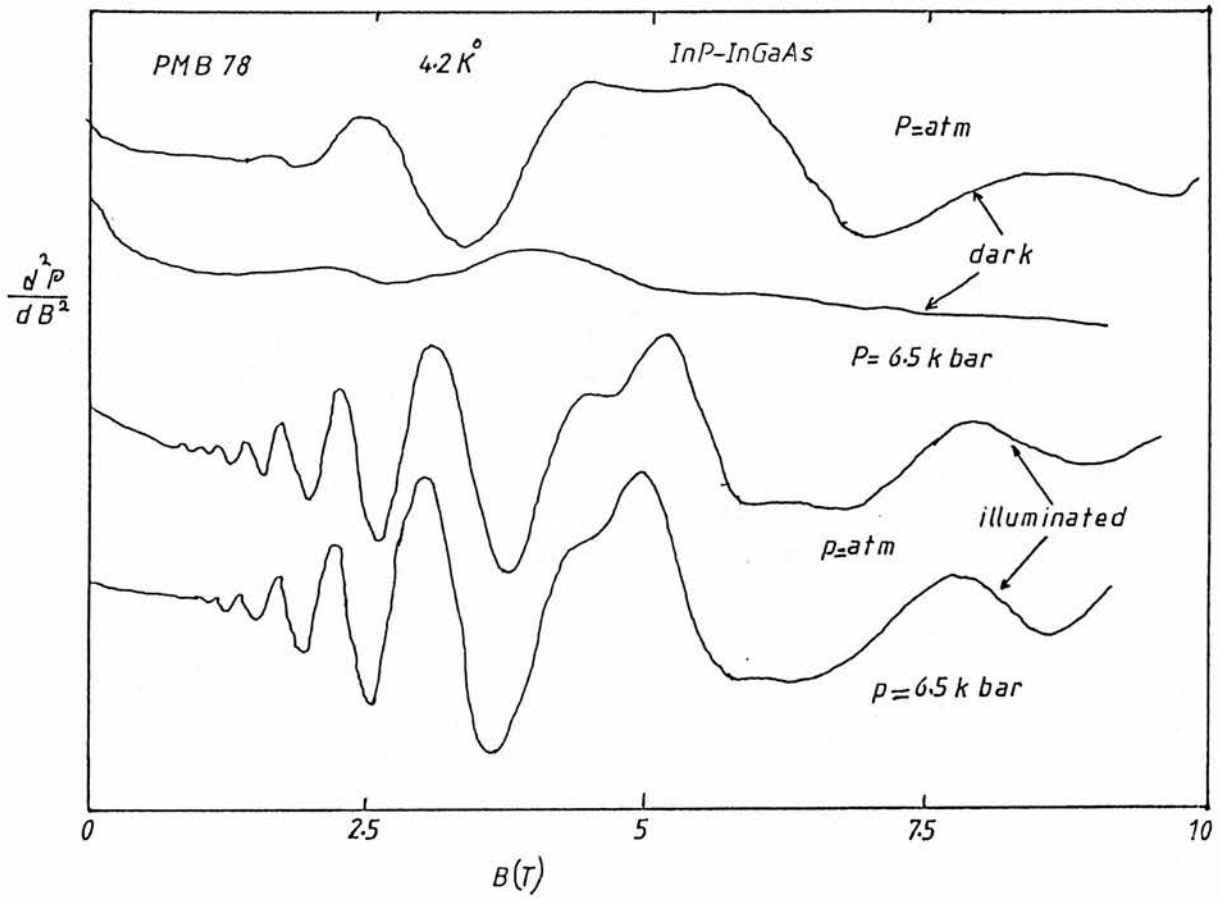


Fig 5.17 SdH oscillations at atmospheric pressure and at 65Kbar before and after illumination for sample PMB78.

5.6 High Pressure Transport in 2D System

5.6.1 Single Quantum Well

The Van der Pauw and SdH measurements on the single quantum well of GaInAs-InP (PMB78) are very anomalous (the same behaviour was observed in three pieces of the same sample). The Hall mobility and electron density showed a dependence on pressure both with and without illumination (see Fig 5.18a and 5.18b). At around 2kbar a sudden jump occurs in n_H and μ_H and this possibly suggests the presence of a 3D impurity effect or poor contacts. The quality of this sample is below average since during growth a higher indium flux was used compared to the one for lattice matched InP (Robert, 1986). One consequence might have been the reaction of dislocations in the crystal since the SdH traces were very similar for all pressures indicating a smooth decrease in carrier density.

5.6.2 Heterostructure

By contrast the pressure measurements on the heterostructure of InP-InGaAs (PMB137) were free from strong 3D effects.

SdH traces were recorded at atmospheric pressure ($P=0$ kbar) and up to 11.5 kbar.

From the results in Figure 5.19a, b it is calculated that the 2DEG density decreases about 10% over 12 kbar. As shown in section 5.5.1 this sample does not exhibit persistent photoconductivity.

The SdH results for electron density at different pressures are shown in Fig 5.20a in the dark and after illumination.

The VdP results for electron density and mobility at different pressures are shown in Fig 5.20b, c in the dark and after illumination.

All the above results show a decrease of both mobility and electron density at higher pressure (see Table 5.9). At 4.2K the Fermi energy of the lowest subband can be obtained from the equation given in Section 5.3. From the Fourier analysis of the atmospheric pressure SdH traces the relative occupations are found to be $n_g = 4.6 \times 10^{15} \text{m}^{-2}$ for the electron density of the ground state and $n = 3.2 \times 10^{15} \text{m}^{-2}$ for the electron density of the first excited state with $E_F^0 = 22.02 \text{ meV}$ and $E_F^1 = 15.32 \text{ meV}$ relative to the subband energy. The effect of pressure on both materials InP and GaInAs is very similar with $dE/dP = 10.7 \text{ meV/kbar}$ for GaInAs. (Gauthier et al 1986.)

Even in the case of very shallow donor levels or those placed high enough above the bottom of the conduction band they do not seem to contribute to the change of the electron concentration with pressure. At present we do not understand the mechanism whereby the carrier density decreases with pressure in the heterostructure.

The rate of change of carrier density with pressure measured by SdH (see Fig 5.20a) and VdP (see Fig 5.20d) is 1.3 and 0.7%/kbar, respectively.

In both Figs 5.20a and Fig 5.20c the change in n with pressure is with respect to the atmospheric pressure value. The VdP measurements give a lower pressure coefficient than SdH. It would appear that although weak, the 3D channel is masking the decrease of the 2D carrier density. Fig 5.20 shows the decrease of electron mobility in GaInAs with a pressure coefficient of 1.4%/Kbar. The mobility at low temperature is governed mostly by alloy and remote ionized impurity scattering. Both scattering mechanisms depend

strongly on m^* (eg $\mu \propto (m^*)^{-2}$ for remote ionized impurity scattering, and a similar power dependence for the alloy scattering). Thus the dependence of m^* upon pressure was calculated assuming $dm^*/dP \approx 1\%/kbar$ (see Section 2.4.2). The dependence of the mobility upon n_s for μ_{alloy} and μ_{RI} exhibits opposite trends although μ_{alloy} decreases slightly more with increasing n_s than μ_{RI} increases (see Fig 3.7). Over the density range observed in our experiments we estimate that these opposing trends roughly cancel each other out.

It can be seen in column 7 of Table 5.9 that the calculated pressure dependence of μ_{RI} including the increase in m^* and the decrease of n_s is negligible. By contrast assuming that $\mu_{\text{alloy}} \propto (m^*)^a$ with $a = -1.5$, a drop in mobility of 15% is obtained. Thus considering $a = -1.5$ as an upper limit, most of the mobility decrease with pressure may be ascribed to alloy scattering. A proper analysis ought to include the effect due to an expected decrease in inter-subband scattering. However the complexity of the calculation, as that of an analytical form for the alloy scattering, were beyond the scope of this thesis.

1	2	3	4	5	6	7
P Kbar	$n_{vdp}^{cm^{-2}}$	$n_{sdH}^{cm^{-2}}$	$\mu_{exp}^{cm^2Vs^{-1}}$	$\frac{m^*}{m_0} - 1\%$	$\frac{\mu_{RI}(P)}{\mu_{RI}(P=0)}$	$\frac{\mu_{Alloy}(P)}{\mu_{Alloy}(P=0)}$
0.0	6.28×10^{11}	3.93×10^{11}	2.4×10^4	0.0485	1.0	1.0
0.32	6.25×10^{11}	3.78×10^{11}	2.4×10^4	0.0496	0.97	0.96
2.39	6.16×10^{11}	3.78×10^{11}	2.34×10^4	0.0497	0.97	0.96
5.78	6.0×10^{11}	3.69×10^{11}	2.21×10^4	0.0513	1.07	0.92
7.82	5.9×10^{11}	3.58×10^{11}	2.15×10^4	0.0523	0.98	0.89
11.53	5.88×10^{11}	3.45×10^{11}	2.08×10^4	0.0541	1.0	0.84

Table 5.9 two dimension electron density and mobility dependence on pressure. Columns 5 to 7 show the values used in the estimates of the pressure coefficients.

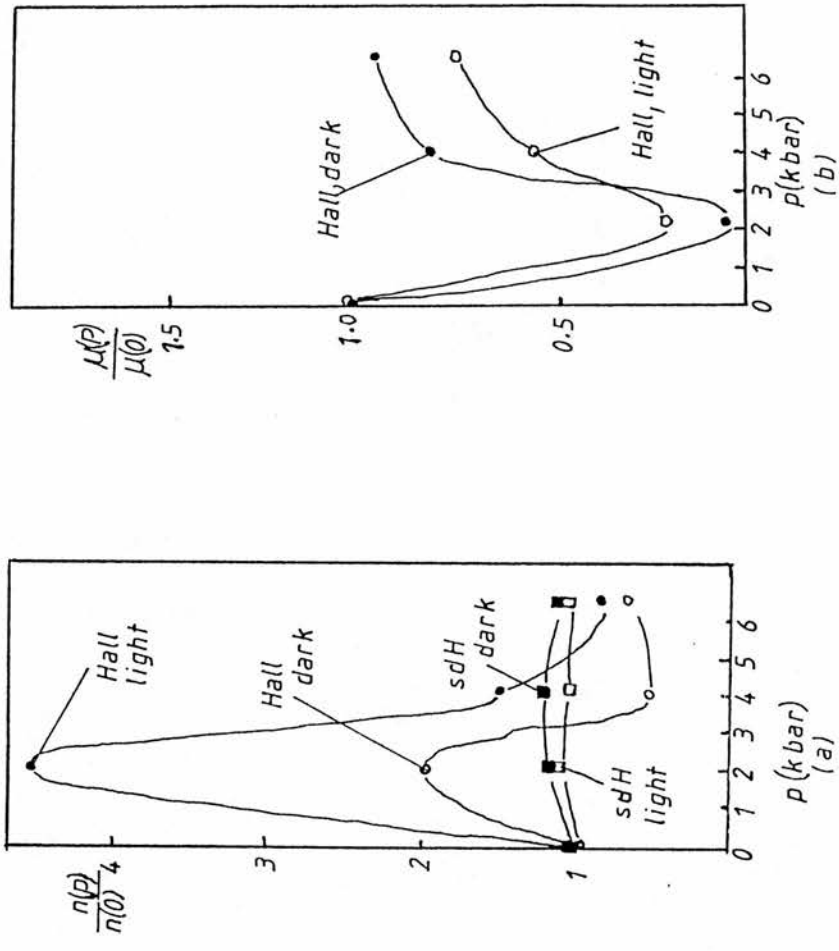


Fig 5.18 SdH and VdP measurements for sample PMB78 S.Q.W. (a) $\frac{n(P)}{n(0)}$ versus pressure P in the dark and after illumination. (b) $\frac{\mu(P)}{\mu(0)}$ versus pressure in the dark and after illumination

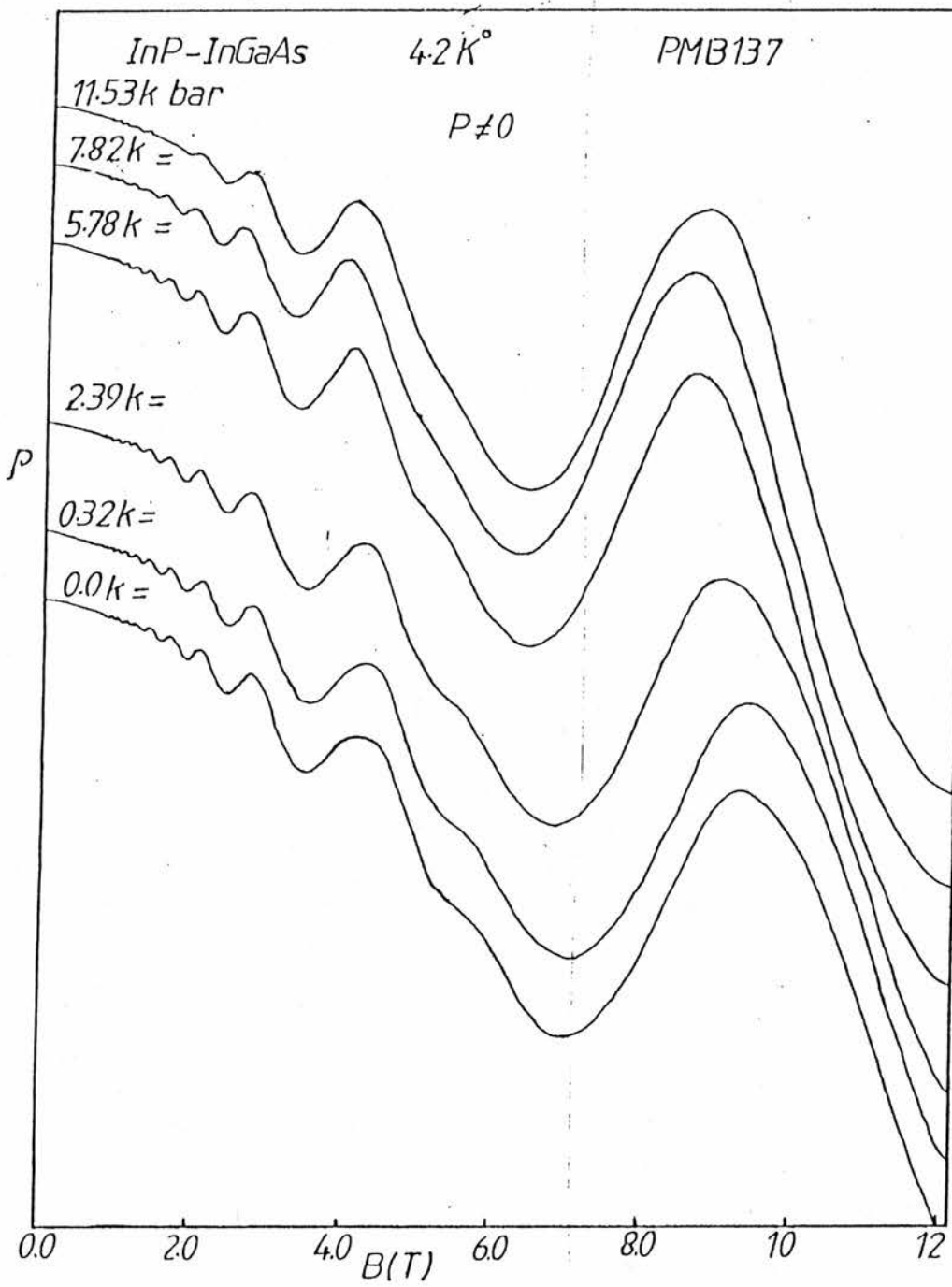


Fig5.19a SdH oscillations (ρ) versus (B) for sample PMB137 at high pressure and at angle 90° between E and B .

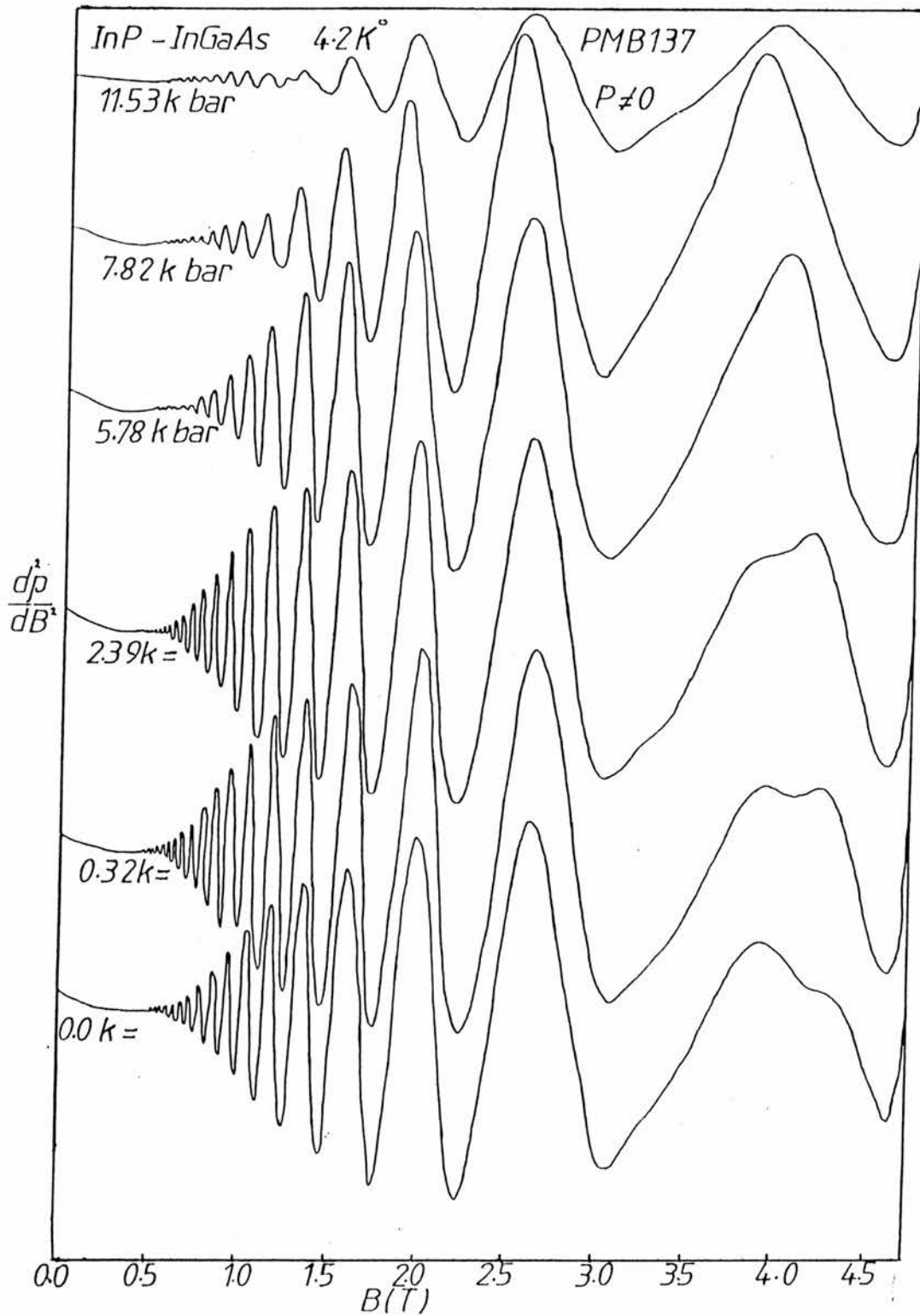


Fig.5.19b SdH oscillations $\frac{d^2\rho}{dB^2}$ versus B for sample PMB137 at high pressure and at angle 90° between E and B .

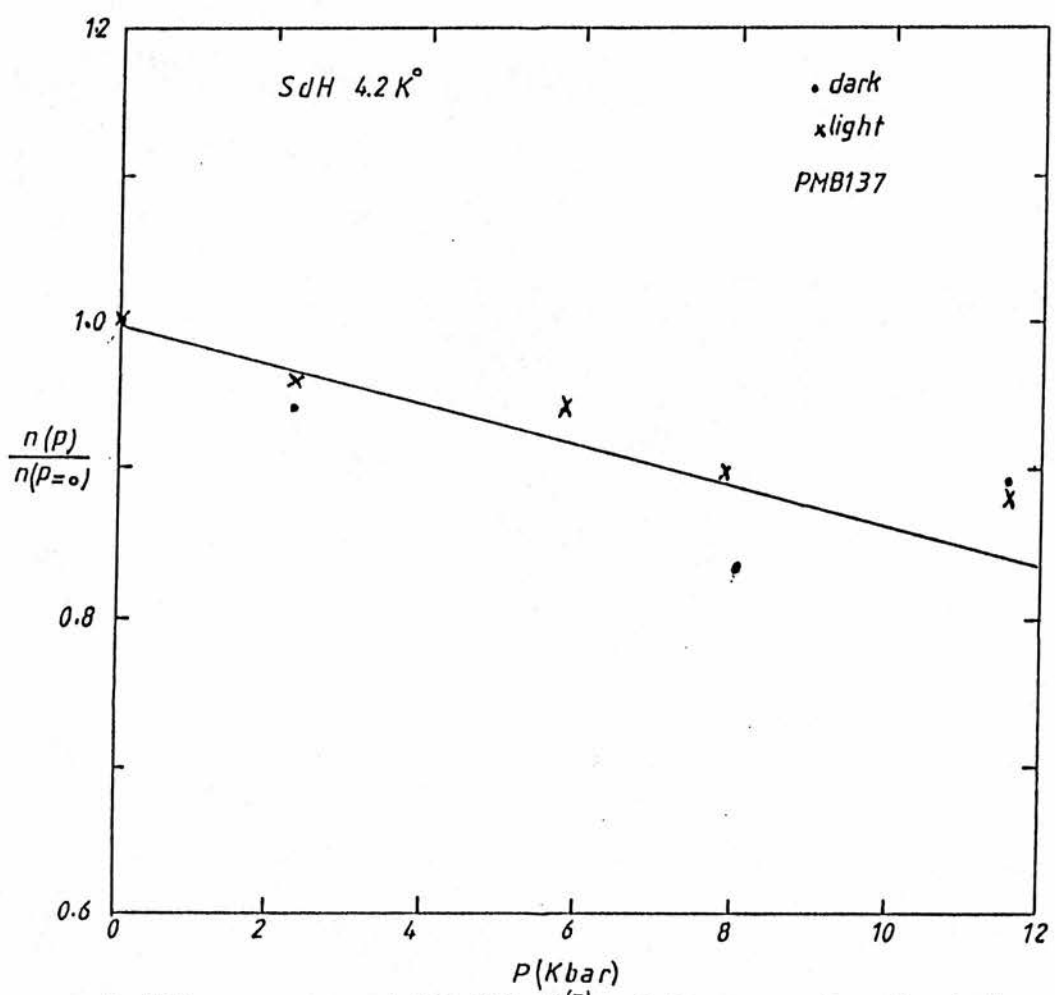


Fig.5.20a Sample PMB137 H.J. $\frac{n(p)}{n(p=0)}$ SdH versus P in the dark and after illumination $n(p=0) = 7.4 \times 10^{15} \text{ cm}^{-2}$.

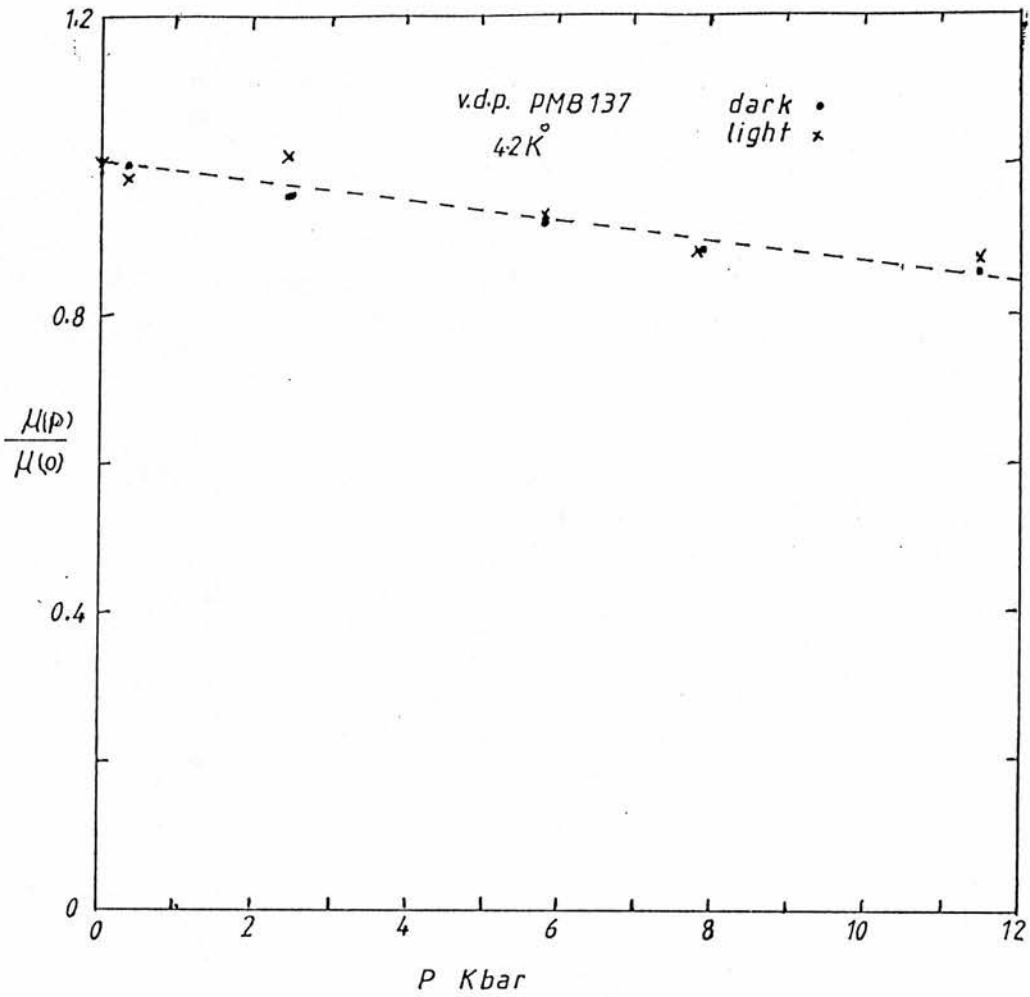


Fig. 5.20b Sample PMB137 H.J. $\frac{\mu(p)}{\mu(0)}$ VdP versus p in the dark and after illumination.

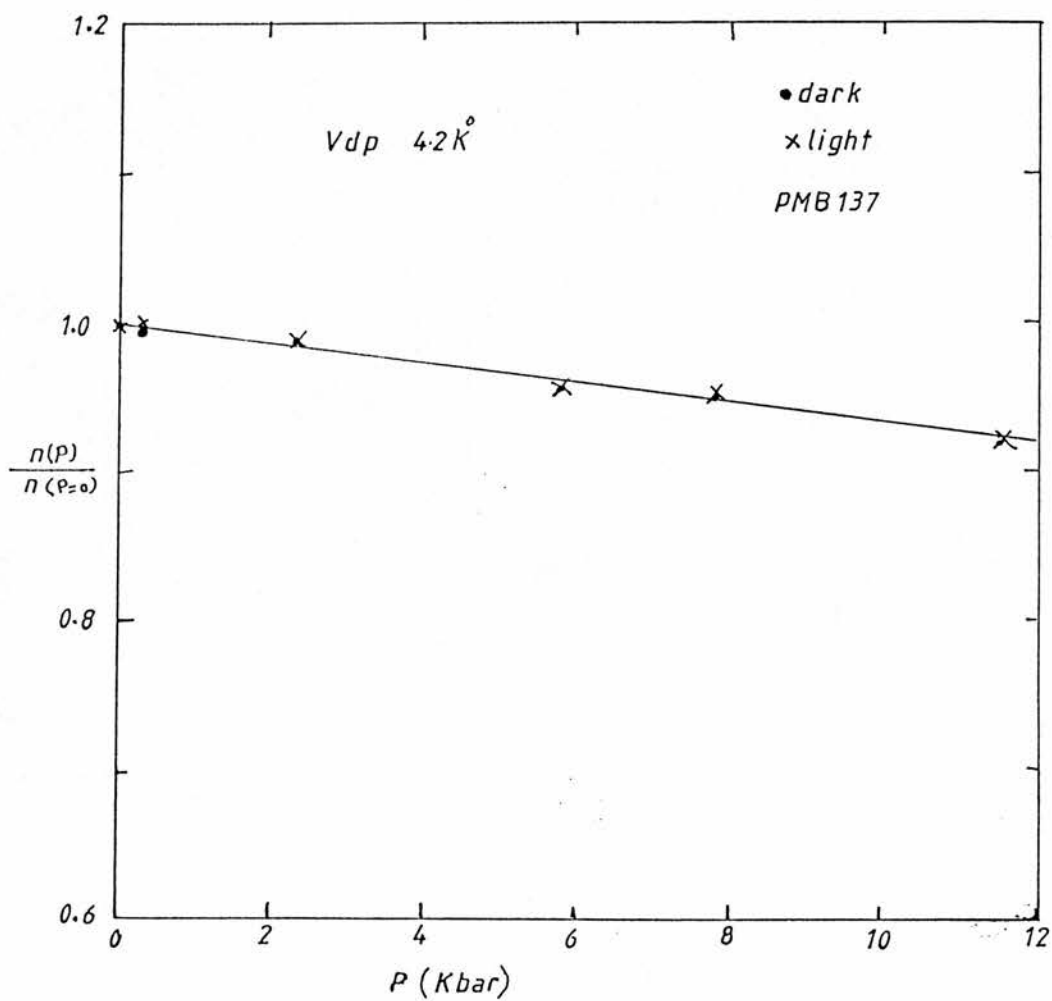


Fig.520c Sample PMB137 H.J. $\frac{n(p)}{n(p=0)}$ v_{dp} versus (P) in the dark and after illumination $n(p=0) = 7.4 \times 10^{15} \text{ cm}^{-2}$.

5.7 Measurement of 2DHG

5.7.1 Mobility and density measurements

The aim of these experiments is to characterise two samples containing a 2DHG (CPM157G, CPM161G) at different temperatures. The samples are p -type AlGaAs heterostructures grown by MOVPE at Sheffield using carbon doping to generate the 2DHG (see Section 5.1). The samples were cut in Hall bar geometry and contacted using indium dots on the Au/Zn/Au pads. The dc impedance between contacts at room temperature was anomalous for currents below $100\mu\text{A}$.

The current used for these measurements was $120\mu\text{A}$. The Hall measurements for sample CPM157G are shown in Fig 5.21. Cooling from 298 to 10K° causes the sheet hole density to decrease sharply from $6 \times 10^{12}\text{cm}^{-2}$ to $1.6 \times 10^{12}\text{cm}^{-2}$ remaining essentially flat down to 2K . The hole mobility smoothly increased from 200 to $1500\text{cm}^2/\text{Vs}$ on cooling from 298 to 2K , although the maximum value could be influenced by the resistivity of the ohmic contacts when these are temperature cycled.

The principle application of p -modulation-doped AlGaAs/GaAs is the p -MODFET device operating close to room temperature; consequently parallel conduction paths have to be eliminated. From the magnitude of the carrier concentration change on cooling, the dominant conduction path parallel to the 2DHG, was identified as the $\text{Al}_{0.45}\text{Ga}_{0.55}\text{As}$ buffer layer. The second structure CPM161E consisted of semi-insulating GaAs substrate of $0.25\mu\text{m}$ with $2 \times 10^{17}\text{cm}^{-3}$ p -type $\text{Al}_{0.6}\text{Ga}_{0.4}\text{As}$ (see Section 5.1.) The reduction in the $\text{Al}_{0.6}\text{Ga}_{0.4}\text{As}$ buffer thickness was expected to reduce parallel conduction effects.

The Hall data (see Fig 5.22) recorded over the temperature range 2 to 90K^o showed a concentration of $1 \times 10^{12} \text{ cm}^{-2}$ up to 60K which increased up to $5 \times 10^{12} \text{ cm}^{-2}$ at 298K . The mobility increased from 14 to $200 \text{ cm}^2 \text{ V}^{-1} \text{ s}^{-1}$ upon cooling down to 40K. The 2DHG concentrations are very similar for both structures. Results of n for both samples CPM157G and CPM161G hole gas can be seen from table 5.3 at 4.2K where n_s is $1.2 \times 10^{16} \text{ m}^{-2}$ and $0.66 \times 10^{16} \text{ m}^{-2}$ in dark and after illumination respectively. This indicates that sample CPM161G is better than CPM157G.

Fig 5.23 and Fig 5.24 show SdH for both CPM157G and CPM161E. Samples at different tilted fields as the angle changes the position of the peaks move toward the high magnetic field following the relation $B_\varphi = B_1 \sin\varphi$ at 4.2K^o. This confirms the two dimensionality of the hole gas. In these samples to estimate the number of 2D energy levels likely to be filled by holes, the positions of the Fermi level, and the Landau level energies, the following equation for the asymmetric well has been used (see Table 2.1).

$$E_r = \left(\frac{\hbar^2 e^2 F^2}{2m^*} \right)^{1/3} \left(\frac{3\pi}{2} \left(r + \frac{3}{4} \right) \right)^{2/3}$$

where m^* is the effective mass of carriers in the well material, which will be of the order $m_h^* = 0.5 m_0$ and $m_L^* = 0.09 m_0$ (Stormer et al 1983) and (Medez et al 1984).

$$F = e \frac{n_s + N_{\text{depl}}}{E_s}$$

where $E_s = 11 E_0$ for GaAs and N_s is the areal hole density in the well and N_{depl} is the areal hole density in the depletion layer; N_{depl} is unknown but it can be neglected.

$$\therefore F = e \frac{n_s}{E_s}$$

$$\text{or } E_r = \left(\frac{\hbar^2 e^4}{2m_0 E_s^2} \right)^{1/3} n_s^{2/3} \left(\frac{m_0}{m^*} \right)^{1/3} \left(\frac{3\pi}{2} \right)^{2/3} \left(r + \frac{3}{4} \right)^{2/3}$$

The value of $\left(\frac{\hbar^2 e^4}{2m_0 E_s^2} \right)^{1/3} = 1.33 \times 10^{-9}$

The effect of subband energy for heavy holes is smaller than the effect of energy for light holes because heavy holes gives low mobility and the 2DHG is not a normal band (see Fig 3.15). Therefore the predicted 2D energy levels for sample CPM157G hole gas for $m^* = 0.09m_L$ is $E_0 = 357.8 \text{ meV}$ at $r = 0$.

If all the carriers are in a single parabolic band then the Fermi energy will be at

$$E_f = \frac{\pi \hbar^2}{m^*} n_s$$

$$\therefore E_f \text{ is } 127 \text{ meV}$$

while at $r = 1$ E_1 is 629.4 meV.

For sample CPM161G hole gas E_0 at $r = 0$ is 243.5 meV, E_f is 70 meV and E_1 at $r = 1$ is 426 meV.

Beryllium doping is used in MBE material ρ -type AlGaAs/GaAs to generate the two-dimensional hole gas.

An alternative dopant which is inherent in the MOVPE-grown process is carbon. Unintentionally doped $\text{Al}_x\text{Ga}_{1-x}\text{As}$ shows ρ -type conduction for $x = 0.25$ which increases with x . As an example $\rho = 5 \times 10^{17} \text{ cm}^{-3}$ for $x = 0.6$. At this high aluminium fraction, which is necessary to obtain a high carbon doping, the valence band offset between the AlGaAs and GaAs will be large and should be suitable for a high-density hole gas. In addition, the C doping will extend up to the heterointerface and should therefore supply a high hole concentration.

The classical expression for the Hall voltage U_H of a 2DEG with a surface carrier density n_s is:

$$U_H = \frac{B}{n_s \cdot e} I$$

where I is the current through the sample. A calculation of the Hall resistance

$$R_H = U_H/I$$

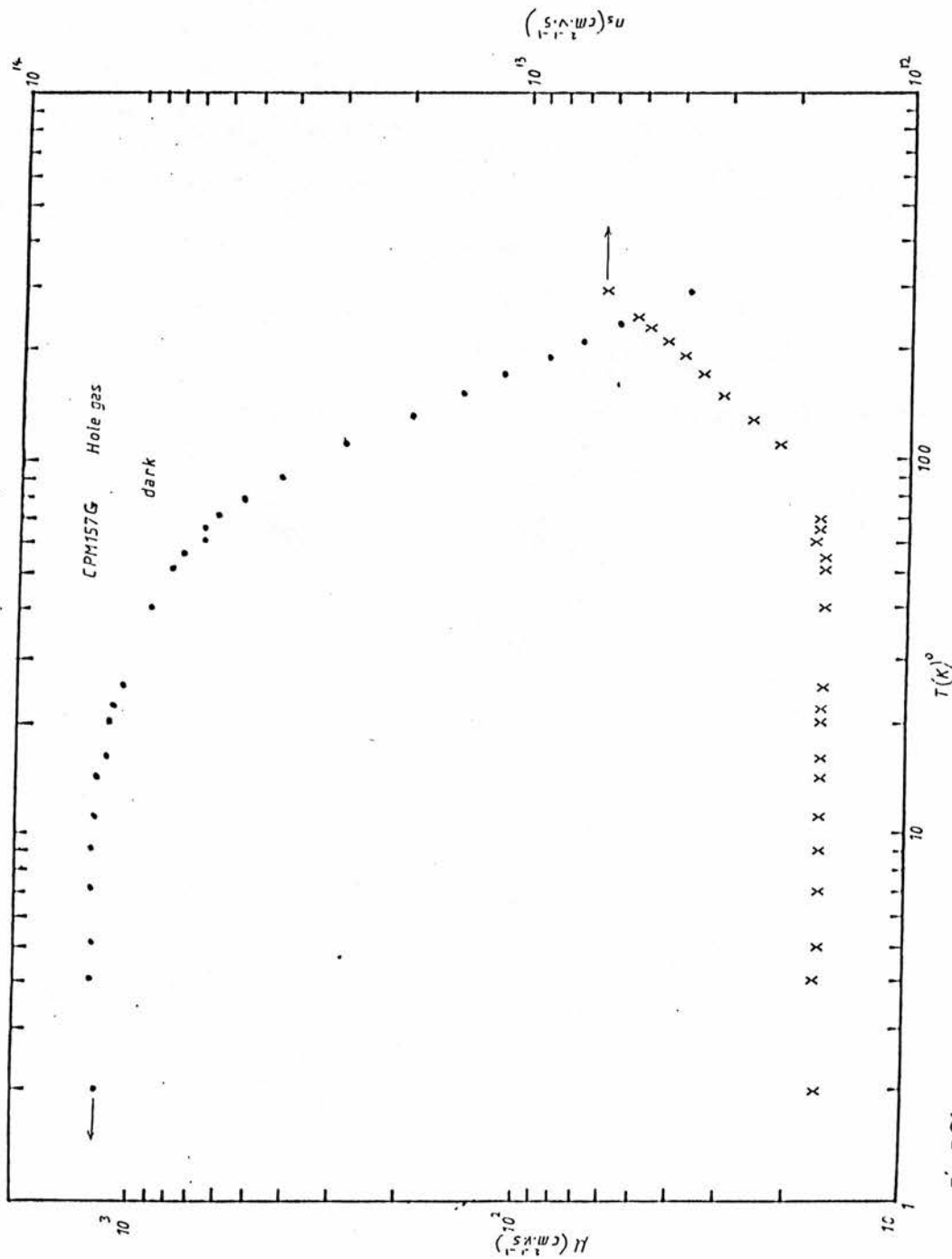
Under the condition that energy levels are fully occupied ($n_s = iN$), leads to the expression for the quantised Hall resistance, where N is the degeneracy factor per unit area.

$$R_H = \frac{B}{iN \cdot e} = \frac{h}{ie^2} = \frac{25812.8}{i} \text{ where } i = 1, 2, 3, \dots$$

A quantised Hall resistance is always expected if the carrier density n_s and the magnetic field B are adjusted in such a way that the filling factor i of the energy levels given in equation (2.25) $i = \frac{n_s}{e\beta/h}$ is an integer.

The variation of ρ_{xy} and ρ_{xx} with magnetic field for CPM157G held at $1.6K^0$ is shown in Fig 5.25. Distinct resistance plateaus at 4071Ω and 2655Ω were observed indicative of the quantum Hall effect with integer values $i = 6$ and 10 , respectively $R_H(\rho_{xy}) = (25812.8/i)\Omega$.

The 2DHG concentration calculated from these resistivity plateaus has a value of $1.6 \times 10^{12} \text{ cm}^{-2}$ ($2DHG = ieB/h$, where B is the field corresponding to the plateau. We note that plateaus for $i = 6$ and 10 are clearly visible; presumably intermediate values are too small for observation.



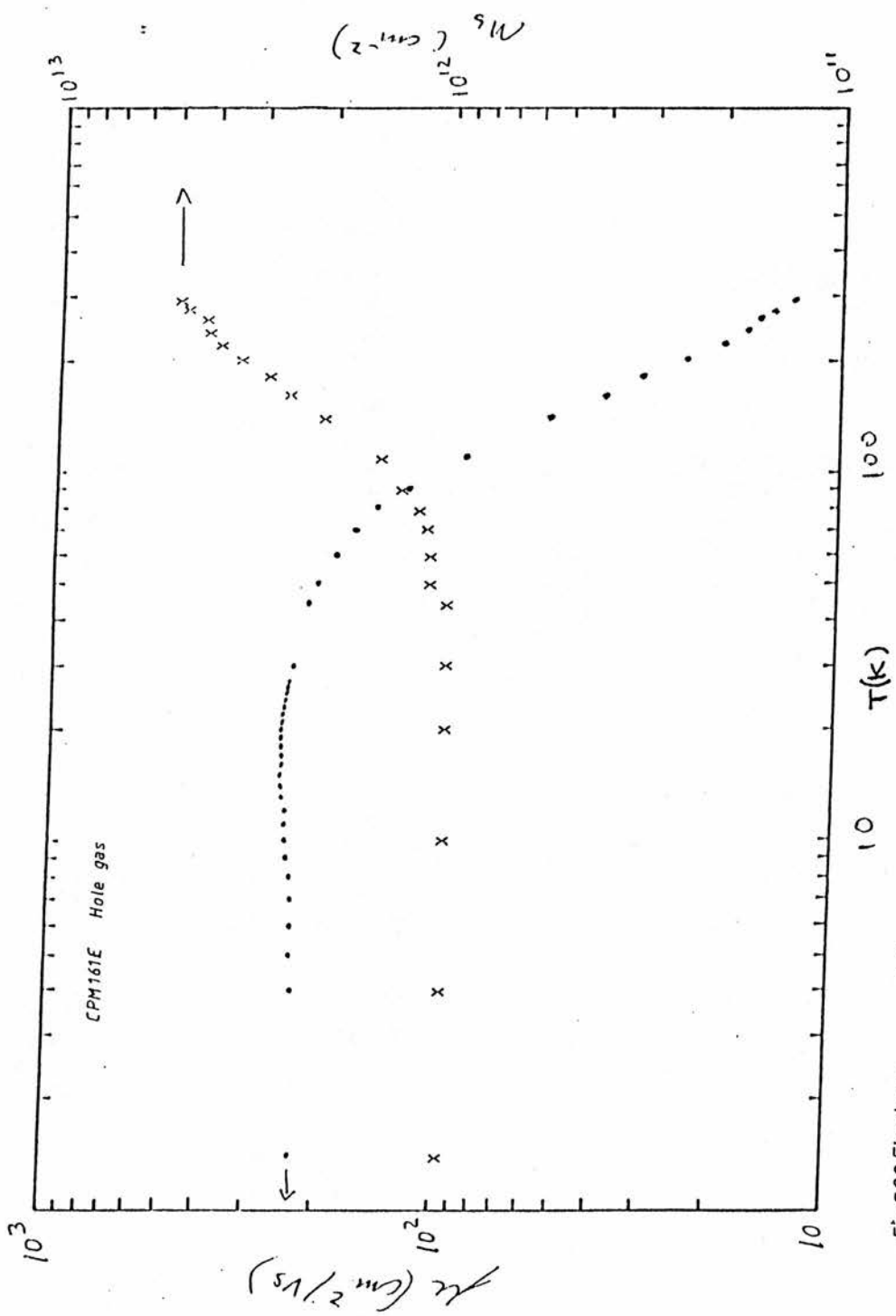


Fig.522 Electron mobility and density as a function of temperature for sample CPM161E Hole gas GaAs-GaAlAs.

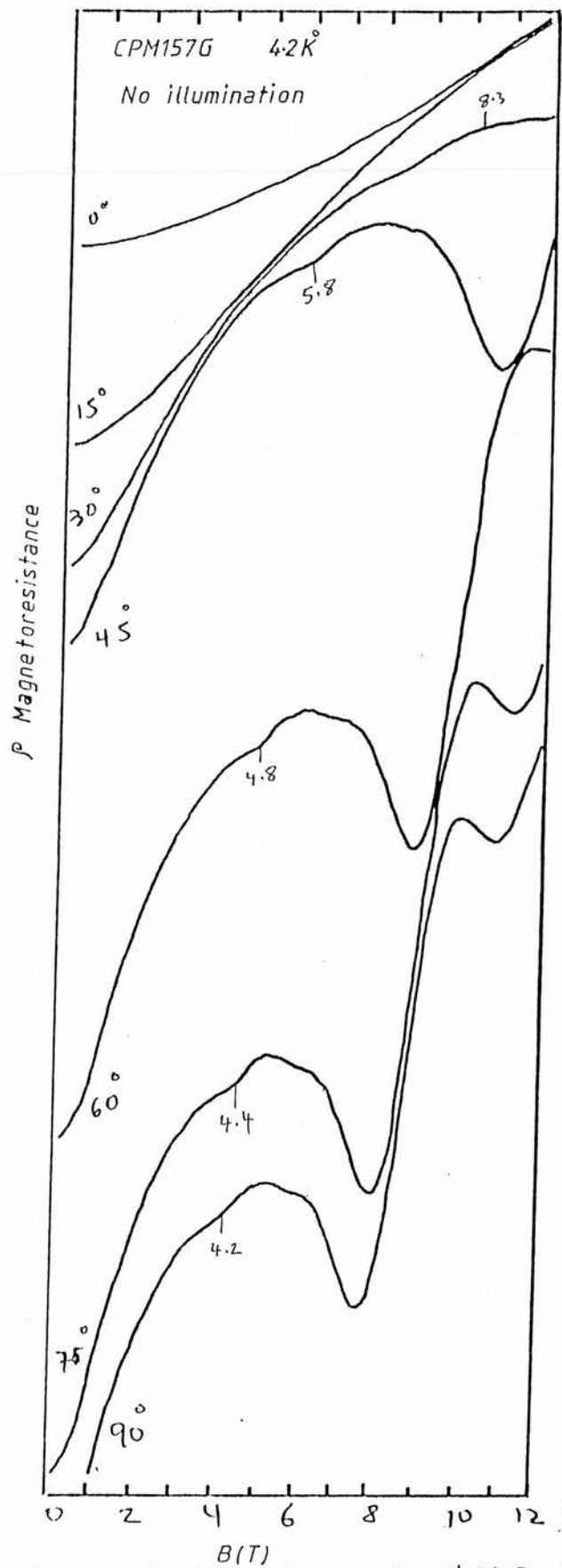


Fig.5.23 Magnetoresistance ρ as a function of magnetic field B at different angle for sample CPM157G Hole gas GaAs-GaAlAs. at dark.

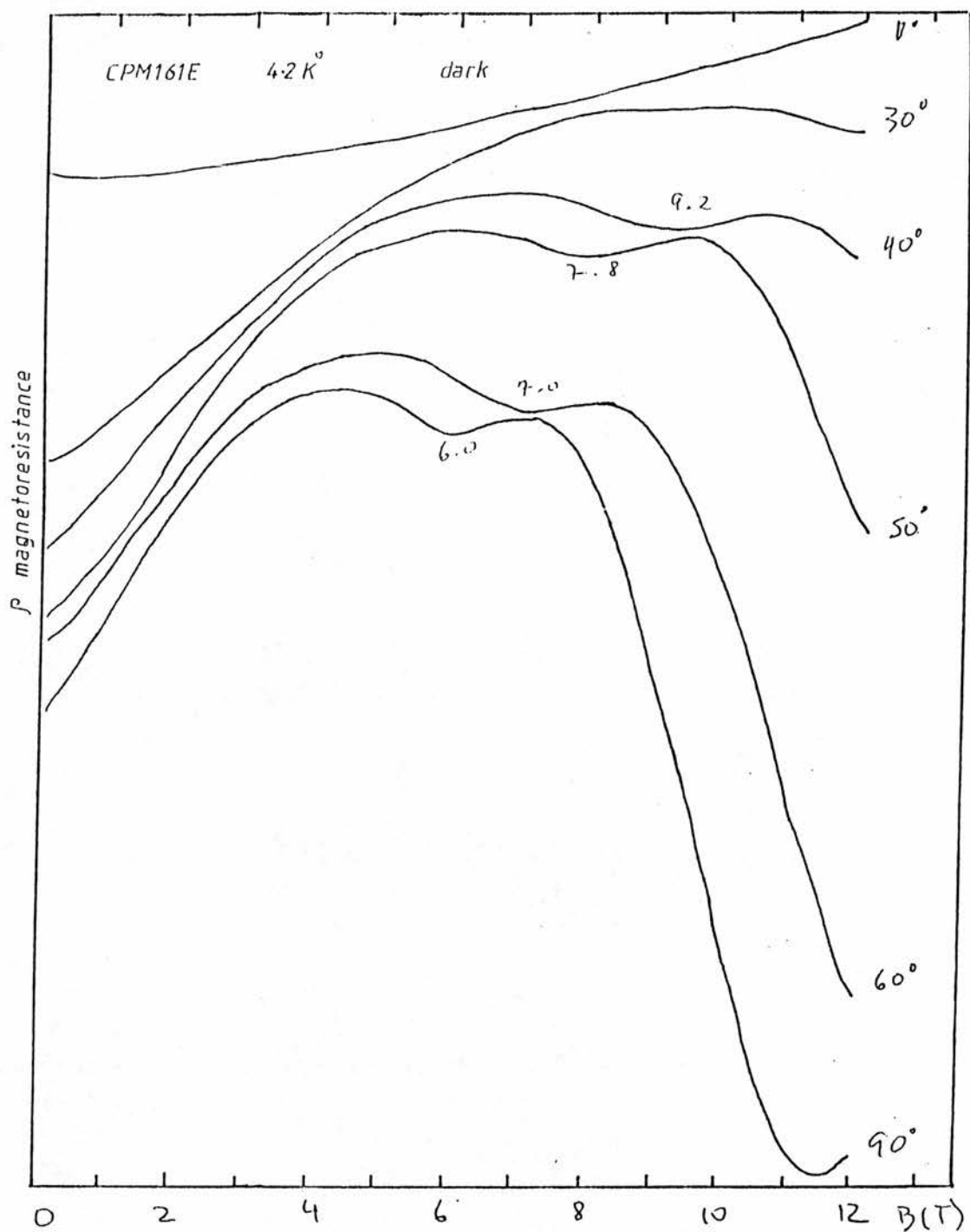


Fig.5.24 Magnetoresistance P as a function of magnetic field B at different angle for sample CPM161E Hole gas GaAs-GaAlAs at dark.

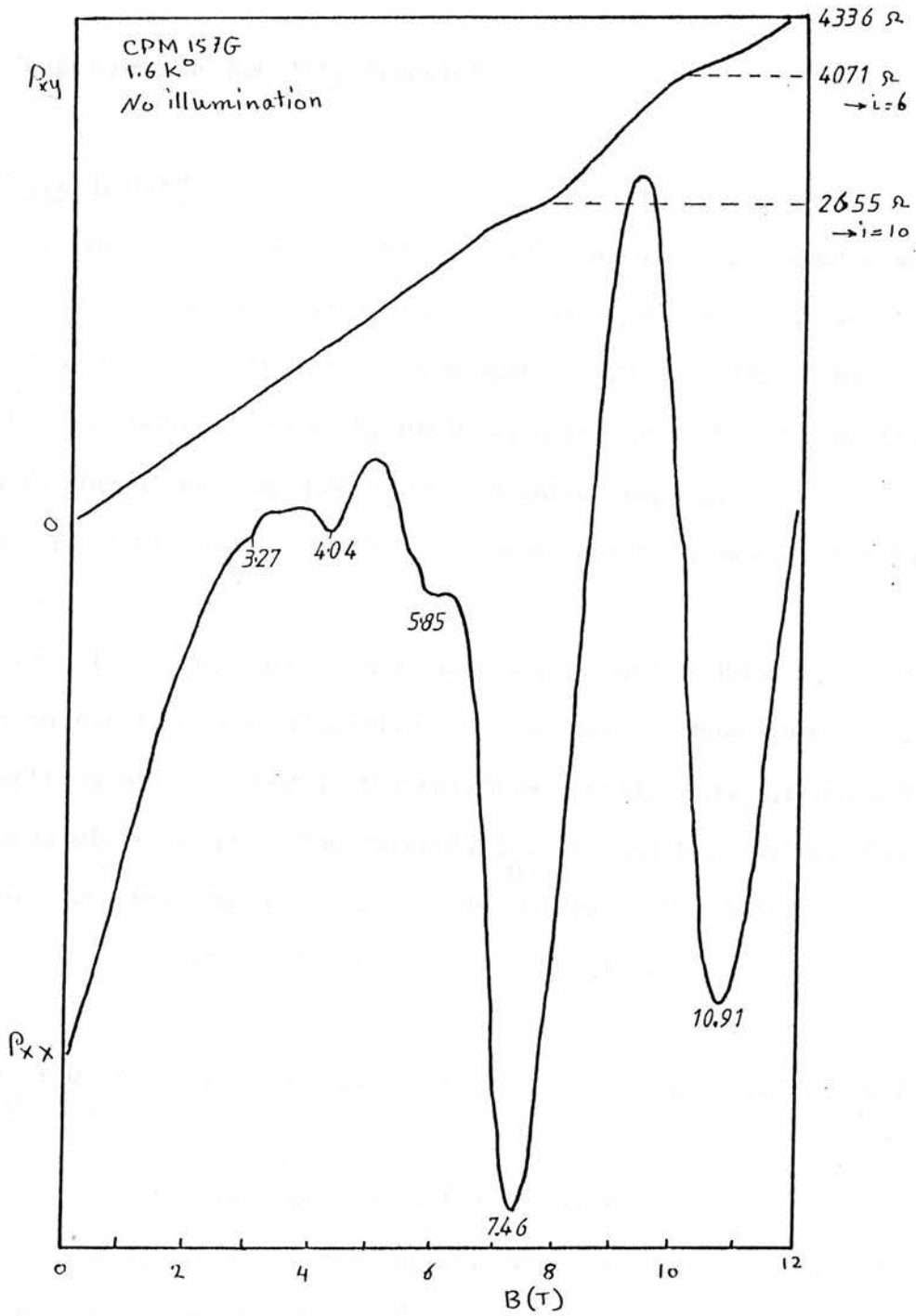


Fig5.25 Hall resistance R_{xy} (top curve) and magnetoresistance R_{xx} (lower curve) for sample CPM157G as a function of magnetic field applied perpendicularly to the 2DHG.

5.8 High Electron Mobility Transistor

5.8.1 2DEG in HEMT

The difference between HEMT material and ordinary quantum wells is primarily the high mobilities eg $\mu = 10^6 \text{ cm}^2 \text{ v}^{-1} \text{ s}^{-1}$ at 4K^0 , which is larger than that of a bulk film by almost a factor of 10. This high mobility has been achieved by minimising the effect of scattering centres in the conducting channel by modulation doping, as discussed in section 2.2, and by improving the interface quality growing at optimum temperature.

The structure, band diagram and charge distribution of a two-dimensional electron gas field-effect transistor is shown in Fig (5.28). The electrons are confined in the potential well, thus giving a two-dimensional electron gas. The current, I_D , through the channel between the ohmic contact source (S) and drain (D) is controlled by a third electrode, the gate (G). The current is defined by

$$I_D = Q_s \cdot V_s \cdot W \dots \dots \dots (5.4)$$

where W is the channel width V_s is the electron drift velocity and $Q_s = Q_s$. Here, n_s is the sheet carrier concentration per unit area.

The control of the sheet carrier concentration n_s and hence the current I_D by the gate voltage V_{Gs} is explained as follows. The AlGaAs layer below the gate is depleted a) by the transfer of electrons into the 2DEG and b) by the charge distribution at the metal-semiconductor contact such that an overall charge neutrality exists.

An undesirable conductivity in the (AlGa)As is avoided by choosing its thickness such that both the contact depletion region and the hetero-interface depletion region touch. Then at $V_{Gs} = 0$ V the maximum value of n_s is obtained (depletion-type normally-on). By decreasing the (AlGa)As layer thickness the 2DEG channel is depleted, while the charge on the gate electrode remains constant. It is thus possible to deplete the channel completely at $V_{Gs} = 0$ V. A negative gate voltage ($V_{Gs} < 0$ V) decreases n_s and I_D while a positive gate voltage increases both n_s and I_D . The drain voltage ($V_{Ds} > 0$ V) creates an electric field in the channel which accelerates the electrons.

In addition it modifies the potential drop across the heterostructure and the distribution of n_s along the channel. From these principles of operation the device characteristics can be deduced. A more simplified consideration assumes that the space charge in the (AlGa)As layer is always constant (all donors are ionized). If it is further assumed that the electron drift velocity has reached its saturation value v_s the current-voltage characteristic is given by:

$$I_{Ds} = k' (V_{Gs} - V_T) \dots\dots\dots(5.5)$$

where: I_{Ds} = current in the saturation regime, independent of V_{Ds}

$$k' = \frac{\epsilon_0 \epsilon_r w_s V_s}{d_{eff}} = c_s V_s w_s \text{ with } d_{eff} = d + 8\text{nm}$$

d = thickness of the AlGaAs layer

c = gate capacitance per unit area

V_T = threshold voltage.

Equation (5.5) is a good approximation for a two-dimensional electron gas FET. Especially if parallel conduction in the AlGaAs layer occurs.

The transconductance g_m can be written as:

$$g_m = \frac{\partial I_{Ds}}{\partial V_{Gs}} = k' = c \cdot V_s; g_m \propto n_s \mu_w$$

or normalised to unit gate width:

$$g_m^* = \frac{g_m}{v} = \frac{\epsilon_0 \epsilon_r \cdot V_s}{d_{eff}} = c \cdot V_s \dots \dots \dots (5.6)$$

The upper frequency limit can be described by the transit frequency f_T which is approximately given by

$$f_T = \frac{g_m}{e\pi C_{Gs}} = \frac{V_s}{2\pi L} \text{ with } c \cdot W \cdot L \approx C_{Gs}$$

Equations (5.5) and (5.6) show the important influence of the maximum drift velocity V_s , the gate length L and the carrier concentration n_s on the device performance. Experiments indicate that the effective maximum drift velocity for GaAs at room temperature is $V_s = (1.8 - 2.5) \times 10^7$ cm/s and increases towards lower temperature. The optimum thickness d for maximum n_s is around 45 nm for doping of $N_D = (1-2) \times 10^{18-3}$ cm⁻³. For a 1μm gate two dimensional electron gas FET at 300 K one obtains:

$$g_m^* = (300-400) \text{ ms/mm}$$

Equations (5.5) and (5.6) lead to the conclusion that the low field mobility does not have any influence on the device performance.

Indeed, more detailed calculation show that this is approximately true for transconductance and frequency limit if the low-field mobility is higher than $3000 \text{ cm}^2/\text{Vs}$.

HEMTs exhibiting intrinsic DC transconductances as high as 295 ms/mm at room temperature have been fabricated using $\text{Al}_{0.45}\text{Ga}_{0.55}\text{As}/\text{GaAs}$ material grown by atmospheric pressure MOVPE (Parker et al, 1982). High Al mole fraction, Se doping and high material quality are said to be directly responsible for the improvement in performance. 1 μm -gate length high-transconductance $\text{AlInAs}/\text{GaInAs}$ HIFET has been fabricated using a selectively doped $\text{AlInAs}/\text{GaInAs}$ heterostructure grown by atmospheric pressure MOCVD (Kamado et al, 1987). The HIFET showed a transconductance as high as 530 ms/mm at room temperature. This is possibly the highest value reported to date in this system. These results are promising for the use of $\text{AlInAs}/\text{GaInAs}$ HIFETs for high-speed devices. Another approach to optimising g_m is to shorten the gate width. The improved performance is due to the very high carrier density as a result of good confinement within the active channel (Lee et al 1986).

5.8.2 Experimental Results

The experiments were carried out on two pieces from the same wafer grown by MBE (see Section 5.1). The wafer was grown according to the specification of the HEMT group at Plessey, Caswell.

On one unetched piece (Sample OC117) SdH and VdP measurements were made as a preliminary assessment. These are shown in Fig 5.11b.

The SdH oscillation showed clearly the existence of a 2DEG. The oscillation has a fundamental field given by $B_n = \frac{nh}{2e}$ where n is the Landau level index. An analysis of the oscillations yields a

fundamental field $B = 26.43 \text{ T}$ which in turn gives a 2D density of $1.3 \times 10^{12} \text{ cm}^{-2}$.

From the slope of the magnetoresistance, as the field increases, the pressure of a strong parallel conduction channel is detected.

From VdP measurements (see Fig 5.26) it is seen that the mobility does not reach $10,000 \text{ cm}^2/\text{Vs}$ at any temperature and that it decreases below 77K suggesting a strong impurity scattering mechanism present.

A recent paper by Hawi et al (1986) suggests that for a spacer layer of 20 \AA the theoretical mobility at 4.2K is about $1.5 \times 10^5 \text{ cm}^2/\text{Vs}$ limited by remote impurity scattering, the carrier density varies between 5 and $3 \times 10^{12} \text{ cm}^{-2}$.

These measurements suggest that the most active layer has 3D character and is likely to be the n^+ GaAs Cap. However that SdH traces clearly show the presence of a 2DEG possibly at the lower interface.

Another piece of the wafer was etched for 4 minutes in 1000cc H_2O , 30cc H_2O_2 (20%) and 7cc H_4OH . The etch rate was taken to be $150 \text{ \AA}/\text{min}$ for GaAs and about $200 \text{ \AA}/\text{min}$ for GaAlAs with low Al concentration according to information supplied by Plessey. The n^+ GaAs layer and most of the graded GaAlAs layer were removed. The first attempt was not successful since the resistance between any two pairs of contacts increased by a factor of 10. The second attempt was successful as is illustrated by the clear SdH oscillation. See Fig 5.11c for various different angles.

The 2DEG is still present and from the periodicity in $1/B$ the 2D density was determined to be $1.9 \times 10^{12} \text{ cm}^{-2}$. This density compares well with the previous SdH measurements. The band edge profile with depth is shown in Fig 5.27b.

This profile was taken at Plessey, Caswell using an electrochemical profiler on sample HEMT #1 which had the gate recessed to leave 4.500 Å of GaAlAs below. On this sample the VdP measurements (see Fig 5.27a) revealed that 3D electrons still contributed to the conduction processes.

The HEMT #1 SdH data shown in Fig 5.11a also points to the presence of parallel conduction but clearly identifies a 2DEG at an interface on the structure. The low mobility is likely to be due to the very narrow spacer layer (see Fig 2.12) and to some residual parallel channel considering that the difference in carrier density obtained from VdP and SdH measurement is only 5%.

Since no better quality material was available at the time this preliminary work on HEMT material was concluded at the material characterisation stage.

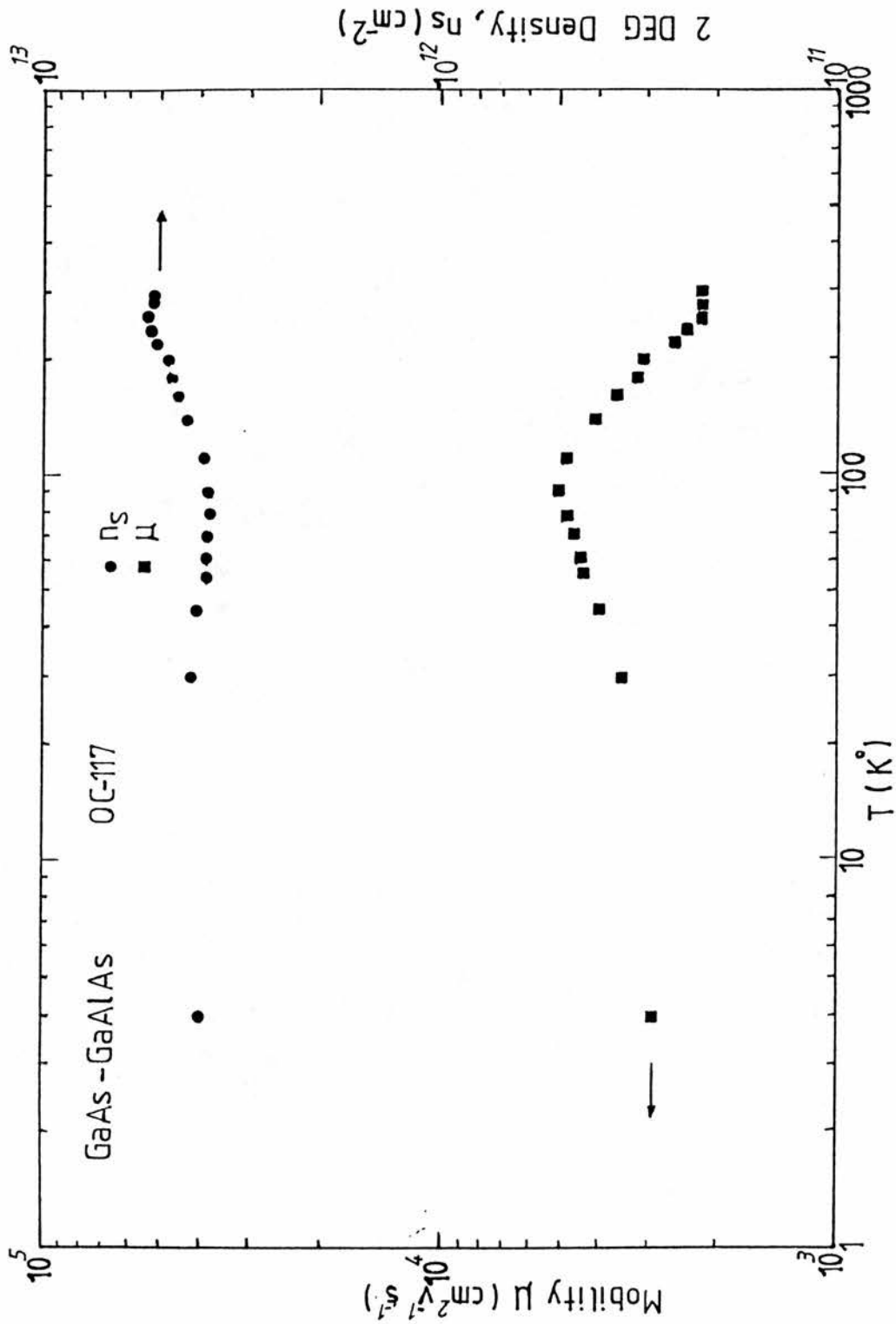


Fig. 5.25 Electron mobility and density as a function of temperature for sample OC117 GaAs-GaAlAs.

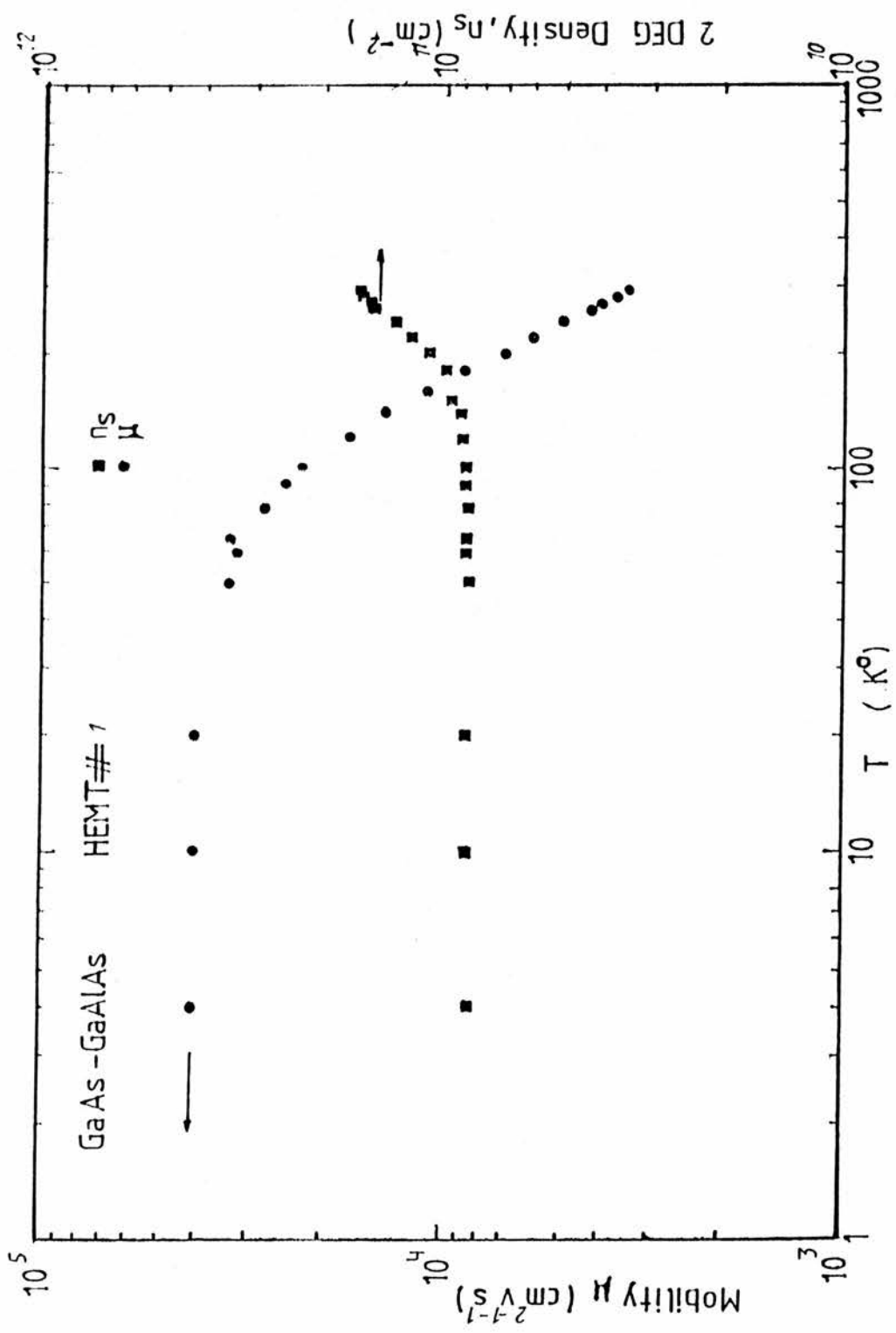


Fig.5.27a Electron mobility and density as a function of temperature for sample HEMT#1 GaAs-GaAlAs.

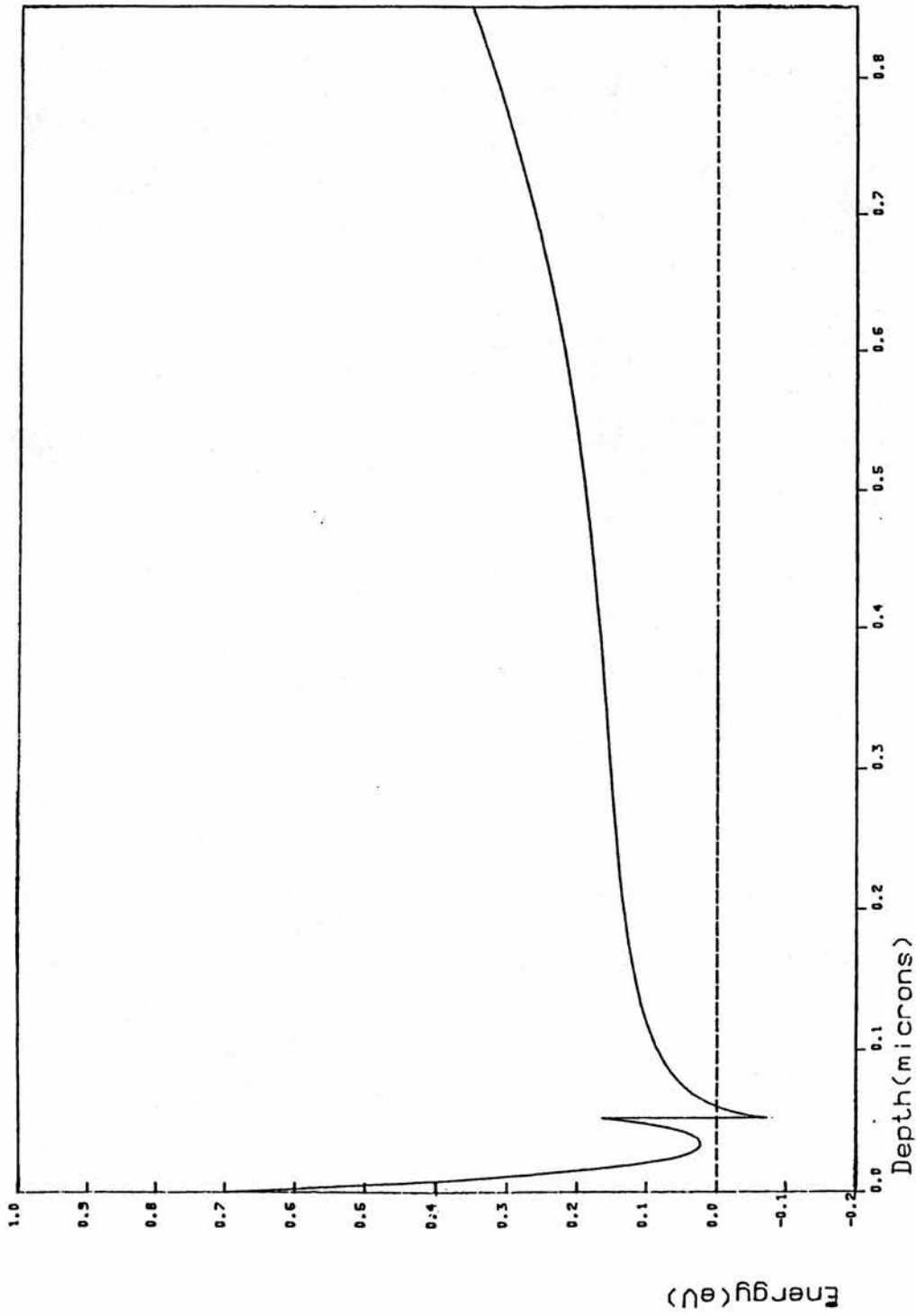


Fig.5.27b Band edge profile as a function of depth for GaAs HEMT #1.

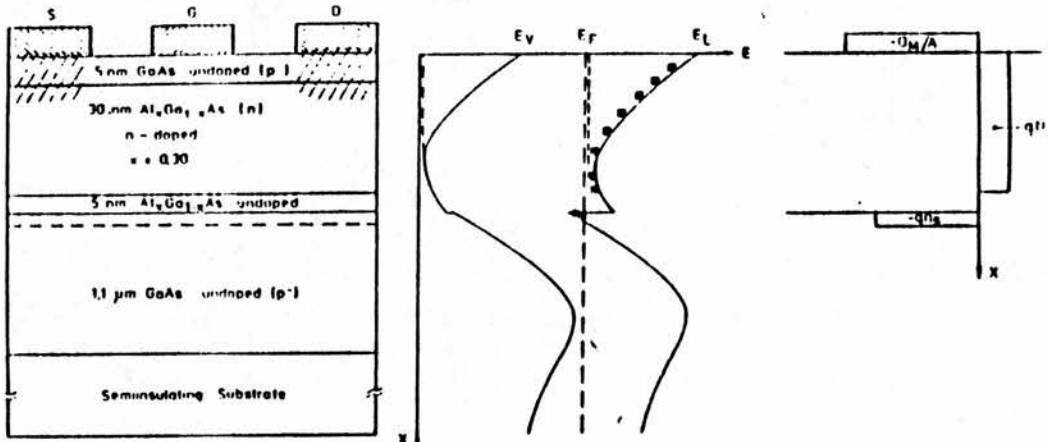


Fig.5.28, Structure, band diagram and charge distribution of a 2DEGFET.

6.1 Conclusion

The transport properties of semiconductor samples containing a 2D electronic system have been studied. They varied significantly in quality and this was borne out in the course of this research. Comparisons between experimentally determined mobilities and theoretical prediction were carried out considering a simple model of a triangular well with infinite walls. All the major scattering mechanisms were included such as polar optical phonon scattering acoustic deformation potential and piezoelectric scattering, ionized impurity scattering, remote impurity scattering and alloy disorder scattering. The comparison covered the temperature range from 4 to 300 K^o.

These simple calculations provided an upper limit on the electron mobilities in the best sample of a given type (normal and inverted GaAlAs-GaAs and GaInAs-InP structure). In both systems the inherent mobility limit increased with decreasing temperature. For the design of the GaAs-based structures studied the maximum expected low temperature mobility was about 500,000 cm²/Vs. However the measurements were a factor of 13-20 down indicating that other factors such as interface roughness and Si migration seriously affected the transport properties. For the GaInAs-InP the theoretical limit of about 150,000 was calculated but only 82,000 cm²/Vs was measured. This suggests that the alloy scattering mechanism estimate, which is the strongest at low temperatures, needs to be revised.

Mobilities μ have been calculated for sample KES422 and MV134 GaAs-GaAlAs at different temperatures and show a lower mobility than the theoretical value about 20 times from MV134 and 13 times from KES423. This discrepancy comes from the interface roughness and Si donor migration factors; the InP-InGaAs sample PMB137 shows better agreement with the theoretical values.

Shubnikov-de Haas measurements have been employed on most of the samples. This is very suitable for identifying the 2DEG from the oscillations recorded at various tilted angles and must follow $B_{\varphi} = B_{\perp} \sin \varphi$ where φ is the angle between E and B. The electron density of each 2DEG sample is given in table 5.3. The SdH measurement reveals the energy of the ground state subband and the excited state subband, the Fermi energy and the average distance of electrons from the interface of the subband as well.

The range of n_s calculated by SdH has been found to be $(10^{11} \sim 10^{12}) \text{ cm}^{-2}$ at 4.2K° in both 2DEG systems of GaAs-GaAlAs and InP-InGaAs.

VdP measurements exhibit a range of n_s between $(10^{11} \sim 10^{12}) \text{ cm}^{-2}$ in GaAs-GaAlAs heterojunctions and the same in InP-InGaAs heterojunction systems over a broad range of temperature $(4 \sim 300)\text{K}^{\circ}$ (see table 5.3 and 5.2).

The persistent photoconductivity has been noticed in a few samples at low temperature such as PMB78 and PMB121 InP-InGaAs samples. This leads to an electron density increase and is still not fully understood. Sample CPM157G hole gas structure shows a better mobility at 4.2K° than the other structure CPM161G hole gas (see Table 5.3). These samples need improvement to get better results. MOVPE has been used to prepare $\text{Al}_{0.6}\text{Ga}_{0.4}\text{As-GaAs}$ heterostructures which support the

2DHG quality. The ρ -doping for the $\text{Al}_{0.6}\text{Ga}_{0.4}\text{As}$ was the residual carbon associated with the use of the reagent trimethylaluminium. At 1.6K° distinct resistance plateaus at 4071 and 2655 were observed; indicative of the quantum Hall effect with integer values $i = 6$ and 10 , respectively.

The effect of hydrostatic pressure has been investigated for sample PMB137 InP-InGaAs. This shows a decrease in the electron density n_s of the 2D electron gas and changes in the electron effective mass.

Scattering mechanisms such as alloy scattering and ionized impurity scattering are responsible for the observed mobility decreasing with pressure.

For 3D samples InP232, InP233 and PMB106 grown by MBE, it has been shown that the mobility increased sharply and shows a high value at 80K of $2.5 \times 10^4 \text{cm}^2/\text{Vs}$ and drops down to a room temperature value around $2.5 \times 10^3 \text{cm}^2/\text{Vs}$. The electron density increases starting from $4.5 \times 10^{15} \text{cm}^{-3}$ at 4K up to $(1.8-2.5) \times 10^{16} \text{cm}^{-3}$ at room temperatures.

If we refer to table 5.8 we can conclude that InP samples 233 has the highest mobility of the three and the lowest compensation ratio. MBE grown InP seems as good as InP grown by more traditional techniques. The problems found in heterostructures, are probably associated with interfaces.

Finally, sample HEMT # 1 reveals a good mobility of $41,710 \text{cm}^2 \text{v}^{-1} \text{s}^{-1}$ and electron density of $1.7 \times 10^{12} \text{cm}^{-2}$ at 4.2K° and has a good agreement with the value of electron density found by SdH of $1.2 \times 10^{12} \text{cm}^{-2}$ at 4.2K . This indicates a good quality and well grown sample compared with the other samples used throughout this work.

6.2 Future Work

On the experimental set up aspects, recording of experimental data in digital form, particularly for the delicate and time-consuming high pressure experiments, is absolutely essential. This is especially important for studying systems with more than one subband occupied since digitizing data from chart papers produces several errors to the detriment of a Fourier analysis to determine the population of each subband. In some cases extension to fields well above 12T would have been helpful to *distinguish* the contribution of each subband to the SdH oscillations closer to quantum limits.

With respect to the experimental techniques one area needs particular attention, namely the persistent photoconductivity studies under hydrostatic pressure. Light transmission characteristics of the pressure transmitting medium at low temperatures are required to determine the relative photon flux reaching the sample through the optical fibre at various pressures.

Similar precautions are necessary for a study of the mobility dependence on pressure. In our work, both mobility and carrier density changed with increasing pressure. In any further work it would be advisable to keep the carrier density constant by controlling the sample illumination conditions.

Some of the unresolved questions need further attention. When calculating the subband structure a simple infinite triangular well approach is used. This model is very simplistic and becomes fairly inaccurate at high carrier densities when more than one subband is occupied. Complementary experiments such as electronic Raman scattering can give intersubband energy separations but still do not give information on the extent or penetration of the wave function for

carriers in the ground and excited states. this issue can be resolved by self-consistent variational calculations and its resolution is essential to understand, for example, the pressure dependence of the carrier density of the 2DEG in GaInAs-InP.

On the persistent photoconductivity issue the evidence suggests that there are different origins for this effect in GaAlAs-GaAs and GaInAs-InP. The DX centre is involved in the former but not in the latter. We suggest that a search for the origin of the PPC effect in GaInAs-InP include a systematic study of dn/dP in the controlled photon flux for a given photon energy and lattice temperature. In this way the pressure coefficient will indicate its symmetry (X, Γ , or L); the temperature and photon energy will give its binding energy.

The work on the 2DHG needs to be extended to both higher fields and lower temperatures (mK region). It is not clear why some intermediate filling factors are not observed but we suspect that some non-negligible contribution either from a second heavy hole subband or the light hole subband may blurr the Quantum Hall plateaus. To optimise both mobility and carrier density further study of this system is required. Ideally a p -type heterostructure with transport properties mainly due to the light hole is wanted.

An analytical expression for the alloy scattering is highly desirable although we do not underestimate the magnitude of the task. However, since most technologically useful heterostructure devices involve an interface in which one alloy (GaAs-GaAlAs, GaInAs-InP, InAsSb-InAs. etc) or two alloys are involved (AlInAs-GaInAs, GaAlAs-GaInAs) this scattering mechanism may become increasingly important.

APPENDIX A

```
2 for i=1 to 5
4 @""
6 next i
10 @"MANOMETER PRESSURE CALCULATIONS"
20 @""
30 @"Break in to change any parameters"
40 @""
50 input "Manometer number? ",m
55 input "Temperature (R/(I)/N/H)? ",T$
60 if m=1 then goto 110
70 if m>6 then goto 50
80 A=4.05e-10
81 B=1.908e-5
83 C=0.9996
85 if m=2 then gosub 1000
90 if m=3 then gosub 1500
91 if m=4 then gosub 1600
92 if m=5 then gosub 1700
93 if m=6 then gosub 1800
100 goto 200
110 A=5.7004E-10
120 B=3.7724E-5
125 C=1
130 R0=15.831
140 IF T$="N" THEN R0=16.219
150 IF T$="R" THEN gosub 2000
200 @ "A=";A;" B=";b;" C=";c;" R0=";R0
210 IF T$="R" THEN GOTO 2100
```

```

220 INPUT "Manometer reading? ",r
230 p=(-b+(b*b+4*a*(r/r0-C))0.5)/(2*a)
240 @""
250 @"Bomb pressure = ";p/1000
260 if t$="R" then gosub 2200
270 @""
280 goto 55

1000 if T$="R" then r0=126.1
1010 if T$="N" then r0=112.95
1020 if T$="H" then r0=119.38
1030 return

1500 if T$="R" then r0=134.9
1510 if T$="N" then r0=122.18
1520 if T$="H" then r0=119.38
1530 return

1600 if T$="R" then r0=19.20
1610 if T$="N" then r0=16.160
1620 if T$="H" then r0=15.700
1630 return

1700 if T$="R" then r0=8.91
1705 if T$="I" then r0=8.694
1710 if T$="N" then r0=6.938
1720 if T$="H" then r0=6.483
1730 return

1800 if T$="R" then r0=14.564
1810 if T$="N" then r0=12.034
1820 if T$="H" then r0=9.229

```

```
1830 return
2000 a=6.0712e-10
2010 b=3.3891e-5
2020 r0=19.6
2030 return
2100 Input "Do you wish to find the required manometer reading (Y/N)? ",A$
2110 IF A$="N" THEN 220
2120 INPUT "Room temperature pressure required? ",p1
2125 P=P1*1000
2130 r1=r0*(a*p*p+b*p+c)
2135 @""
2137 @"Required manometer reading = ";r1
2150 gosub 2200
2160 @""
2170 goto 55
2200 p1=P/1000
2250 P2=1.223*P1-5.674
2300 @"Anticipated He Pressure = ";p2
2310 return
```

REFERENCES

- Adams A R, Shantharama L G, Nicholas R J and Sarkar C K, (1986) *Physica B* 139 and 140, 401.
- Adams A R, and Shantharama L G, (1986) *Physica B* 139 and 140, 419.
- Adams A R, Fisher M A, Lancefield D and Gunney B J, (1986b) *Physica B* 139 and 140, 423.
- Ando T, *J Physics Soc Japan* 51, 3900 (1981).
- Ando T, Fowler A B and Stern F, (1982), *Rev Mod Phys* 54, 437.
- Ando T and Murayama Y, (1985) *J Phys Soc Japan* 54, 1519.
- Aulombard R L, Kadiri A and Zitouni, (1987) in: "Optical Properties of Narrow Gap Low Dimensional Structures", (Eds: Sotomayor Torres C M, Portal J C, Maan J C and Stradling R A) Plenum, New York 1987, 299.
- Bangert E and Landwehr G, (1976), *Surf Sci* 58, 138.
- Basu P K and Nag B R, (1980), *Phys Rev*, B22, 4849.
- Basu P K and Nag B R, (1984), *Surface Science* 142, 256.
- Bastard G, (1984) *Surf Sci*, 142, 284.
- Beerens J, Gregoris G, Ben Amor S, Portal J C, Mendez E E, Chang L L and Esaki L to be published.
- Beerens J, Gregoris G, Portal J C, Mendez E E, Chang L L and Esaki L, to be published.
- Brum J A and Bastard G, *Inst Phys Conf Ser No 74 chapter 5* 384, (1984).
- Brummell M A, Nicholas R J, Portal J C, Cheng K Y and Cho A Y, (1983) *J Phys* C16, L579.
- Brummell M A, Hopkins M A, Nicholas R J, Harris J J and Foxon C T, to be published.
- Chang L L, Sakaki H, Chang C A and Esaki L, (1977), *Phys Rev Letters* 38, 148.
- Conwell E M, (1967) *Solid State Physics, Supplement 9*, (Academic Press, New York) 108.
- Das Sarma S, (1983) *Phys Rev* B27, 2590.
- Dhar S, Hong W P and Bhattacharya P K, (1986) *J Vac Sci Technol* B4(2), 546.

- Dingle R, Stormer H L, Gossard A C and Wiegmann W, (1980) Surface Science 98, 90.
- Drummond T J, Markoc H, Cho A, (1981) J Appl Phys 52, 1380.
- Eisenstein J P, Stormer H L, Narayanamuri V, Gossard A C and Wiegman W, (1984) Phys Rev Lett 53, 2579.
- Englert T, Tsui D C, Portal J C, Beerens J and Gossard A, (1982) Solid State Comm 44, 1301.
- Englert T H, Maan J C, Remenyi G, Kunzel H, Ploog K and Fischer A, (1984), Surface Science 142, 68.
- Esaki L, (1985) in "Molecular Beam Epitaxy and Heterostructures", (Eds Chang L L and Ploog K, Martinus Nijhoff Publ, Dordrecht).
- Fasolino A and Altorelli M, (1984) in: "Two Dimensional Systems, Heterostructures and Super Lattices", (Eds: Bawer G, Kuchar F, Heinrich H). Springer Series in Solid State Science 53, 179.
- Foxon C T, Harris J J, Wheeler R G and Lacklison D E, (1986) J Vac Sci Technol B4(2), 511.
- Frei M, Tsui D C and Tsang W T, (1987) Appl Phys Lett 50, 606.
- Gauthier D, Dmowski L, Ben Amor S, Blondel R, Portal J C, Razeghi M, Maurel P and Omnes F, (1986). Semicond Sci Tech 1, 105.
- Gennser U I F, and Zurcher P, (1987). To be published.
- Goetz K H, Bimberg D, Brauchle K A, Jurgensen H, Selders J, Razeghi M and Kuphal E, (1985) Appl Phys Lett 46(3) 277.
- Gregoris G, Beerens J, Ben Amor S, Dmowski L, Portal J C, Sivco D L and Cho A Y, (1986), J Phys C, Solid State Phys 20, 425.
- Gregoris G, Beerens J, Ben Amor S, Portal J C, Alexandre F, Sivco D L and Cho A Y, to be published.
- Guldner Y, Vieren J P, Voisin P, Voos M, Razeghi M and Poisson M A, (1982) Appl Phys Lett 40, 877.
- Henning J C M, Ansems J P M, de Nijs A G M, (1984) J Phys C17, L915.
- Herniann C and Weisbuch C, (1977) Philip Rev 13, 822.
- Hess K, (1979) Appl Phys Lett 35, 484.
- Henning J C M and Ausen J P M, (1987) Semicond Sci Technol 2, 1.
- Hirakawa K, Sakaki H, and Yoshino J, (1985) Appl Phys Lett, 46, 412.

- Hjal Marson H P and Drummond T J, (1986) Appl Phys Lett 48, 656.
- Hong W-P, Bhattacharua P K and Singh J, (1987) App Phys Lett 50(10), 618.
- Hopkins M A and Nicholas R J, to be published.
- Hopkins M A, Nicholas R J, Brummel M A, Harris J J and Foxon C T, to be published.
- Hurd C M, McAlister S P, McKinnon W R, Falt C E, Day D J, Miner C J and Spring Thorpe A J, (1987) J Appl Phys 61, 2244.
- Iwasa Y, Miuro N, Takeyama S and Ando T, (1987) in Proc Int Conf on the Application of High Magnetic Fields in Semiconductor Physics - Wurzburg 1986. (Ed Landwehr G, to be published by Springer Verlag).
- Kane E O, (1957) J Phys Chem Solids 1, 249.
- Kane M J, Anderson D A, Taylor L L and Bass S J, (1986) J Appl Phys 60 657.
- Kane M J, Apsley N, Anderson D A, Taylor L L and Kerr T, (1985) J Phys C 18 5629.
- Kane M J, Anderson D A, Taylor L L and Bass S J, (1987) Superlattices and Microstructures 2, 369.
- Kastalsky A and Hwang J C M, (1984) Sol Stat Commun 51, 317.
- Kastalasky A, Dingle R, Cheng K Y and Cho A Y, (1982) Appl Phys Lett 41(3), 274.
- Kido G, Miura N, Ohno H and Sakaki H, (1982) J Phys Soc Japan 51, 2168.
- Kido G and Miura N, (1983) J Phys Soc Japan 52, 1734.
- Kittel (1986), Introduction to solid state physics. Wiley 5th edition Chapter 4,5.
- Konczykowski M, Baj M, Szafarkiewicz E, Konczewicz L, Porowski S, (1978) Proc Int Conf High Pressure and Low Temperature Physics, Cleveland, Ohio 1977 (Plenum Press, New York), 523.
- Lee K and Shur M S J, (1983) J Appl Phys 54, 5432.
- Lee K and Shur M S J, (1983) J Appl Phys 54, 6432.
- Lin B J F and Tsui D C, (1984) Appl Phys 45 695.
- Maan J C, Englert T H, Vihelm C H, Knuzel H, Loog K and Fischer A, (1983) J Vac, Science Technol B1 289.

- Mason N J, 17th Sept (1985), "Basic MOVPE", Low dimensional structure, SERC Summer School, Nottingham.
- Mendez E E, Wang W I, Chang L L and Esaki L, (1984) Phys Rev B 30, 1087.
- Mendez E E, (1986) Surf Sci 170, 561.
- McKinnon W R and Hurd C M, (1987) J Appl Phys 61, 2250.
- Morris S and Ando T, (1979), Phys Rev B19, 6433.
- Morris S and Ando T, (1980) J Phys Soc Jap 48, 865.
- Nicholas R J and Brummell M A (1984), Appl Phys Lett 44(6) 629.
- Oe K and Tsubaki K, J appl Phys (1986), 59 pp 3527-3531.
- Portal J C, Nicholas R J, Brummell M A, Brunel L C, Huant S, Razeghi M and Laviro M (1986), Semicond Sci Technol 1, 3.
- Portal J C, Nicholas R J, Brummell M A, Cho A Y, Cheng K Y and Pearsall T P, (1982) Sol Stat Commun 43, 907.
- Portal J C, Nicholas R J, Brummell M A, Razeghi M and Poisson M A, (1983) Appl Phys Lett 43, 293.
- Price P J, (1982) Surf Sci 113, 199.
- Price P J, (1981) J Vac Sci and Technol. 19, 599.
- Putley E H (1960), "Hall effect and related phenomena", Butterworth London.
- Razeghi M, Duchemin J P, Portal J C, Dmowski L, Remeni G, Nicholas R J and Briggs A, (1986) Appl Phys Lett 48, 712.
- Razeghi M and Hirtz J P, Appl Phys Lett 43 (6), 585.
- Reed M A, Kirk W P and Kobiela P S (1986), IEEE Journal of Quantum Electronics, Vol QE-22 No9, 1753.
- Rude D L, (1970) Phys Rev B2, 1012.
- Robert J L, Raymond A, Bousgreet C and Konczewicz L, (1985) Unpublished paper presented at Polish-French meeting on high pressure research in semiconductors.
- Robert J L, Raymond A and Bousgreet C, (1987) Optical Properties of Narrow Cap Low Dimensional Structures (Eds: Sotomayor Torres C M, Portal J C, Maan J C and Stradling R A) Plenum, New York 313.
- Sah C T, Ning T H and Chopp L L, (1972) Surface Science 32, 561.

- Sakaki H, Hirakawa K, Yoshino J, Svensson S P, Sekiguchi Y, Hotta T and Nishii S (1984), Surface Science 142, 306.
- Sakaki H, Ohno H, Nishii S and Yoshino J (1983), Physics 117B and 118B, 703.
- Schubert E F and Ploog K, (1984) Appl Phys A33, 63.
- Schubert E F and Ploog K, Dambkes H and Heime K (1984) Appl Phys A33 63.
- Staromlynska J, Finlayson D M and Stradling R A (1983), J Phys C, Solid State Phys 16, 6373.
- Stern F, (1983) Appl Phys Lett 43, 974.
- Sotomayor Torres C M and Stradling R A, (1987) Semicond Sci Technol 2, 323.
- Saxena A K, (1985) Solid State Electronics 25, 127.
- Stormer H L, Dingle R, Gossard A C, Wiegmann W and Sturge M D (1979) solid State Communications, Vol 29, 705.
- Stormer H L, Gossard A C, Wiegmann W, (1982) Sol Stat Commun 41, 707.
- Stormer H L, Schlesinger Z, Chang A, Tsui D C, Gossard A G and Wiegmann W, (1983) Phys Rev Lett 51, 126.
- Takikawa M, Komero J and Ozaki M, (1983), Appl Phys Lett 43, 280.
- Theis T N and Wright S L, (1986) Appl Phys Lett 48 (20), 1374.
- Van der Pauw, Phillips L J, Res (1958) Repts 13, 1.
- Venkatesh Narayanamurti (1984), Crystalline Semiconductor heterostructures, Physics Today 24.
- Vinter B, (1984) "Two Dimensional Systems Heterostructures and Superlattices." (Eds; Bawer G, Kuchar F and Heinrich H, Springer Series in Solid State Science 53, 125.
- Walukiewicz W, Ruda H E, Logowski J and Gato S H C, (1984) Phys Rev B30, 4571.
- Wang W I, Mendez E E, and Stern F, Appl Phys Lett (1984), pp639-40.
- Wei H P, Tsui D C and Razeghi M, (1984) Appl Phys Lett 45, 666.
- Weimann G and Schlapp W (1985), Appl Phys Lett 46 (4), 411.
- Windhorn T H, Cook L W and Stillman G E, (1982) IEEE Electron Device Lett EDL-3.

Yoshivo J, Sakaki H and Hotta T (1984), Surface Science, 142, 326.

Zhu L D, Sulewski P E, Chan K T, Muro K, Ballantyne J M and Sievers A J, (1985) J Appl Phys 58, 3145.